Author:
Robarts, Hannah C

Title:
Spin and charge fluctuations in cuprate superconductors studied with resonant inelastic x-ray scattering

Spin and charge fluctuations in cuprate superconductors studied with resonant inelastic x-ray scattering

HANNAH CLARE ROBARTS

Department of Physics
UNIVERSITY OF BRISTOL

A dissertation submitted to the University of Bristol in accordance with the requirements of the degree of Doctor of Philosophy in the Faculty of Science.

DECEMBER 2019

Abstract

This thesis presents new high-resolution resonant inelastic x-ray scattering (RIXS) studies in high-T_c cuprate superconductors (HTSs). RIXS measures elementary excitations of the type which characterise the ordered phases known to exist alongside superconductivity in the cuprates. The role that these phases play in the pairing mechanism which gives rise to superconductivity remains unclear. The work in this thesis therefore presents new measurements of the excitations with the aim of helping to constrain theoretical models of pairing. Spin fluctuations are characteristic of the antiferromagnetic phase of cuprates but are also seen to persist into superconducting phases. As a result, theories based on the Hubbard model often consider spin fluctuations to be important to pairing. Charge fluctuations have now been recorded in all cuprate materials and their role, either competing or contributing to superconductivity, is also important to understand. The experimental work presented here was performed at two new RIXS spectrometers, mainly at I21 at Diamond Light Source and at ID32 at the European Synchrotron Radiation Facility. Both spectrometers are optimised to achieve high intensity and energy resolution in the soft x-ray RIXS regime, for example at the Cu L_3 edge. Measurements are presented on single layer cuprate La_2CuO_4 where consideration of the prefactors to the RIXS intensity reveals the wavevector dependence of the dynamical susceptibility in new regions of the Brillouin zone. The measurements are extended to two doped compositions of $La_{2-x}Sr_xCuO_4$, $x = 0.12$ and 0.16, which show similar wavevector dependence of the susceptibility. The spin fluctuations are characterised within a damped harmonic oscillator model which reveals the wavevector dependent anisotropy of the damping in doped compositions. New RIXS measurements in two-layer $YBa_2Cu_3O_{6+x}$ (YBCO) show similar effects. The charge order is also examined in YBCO revealing a broad wavevector dependent peak in the elastic intensity which is attributed to low energy phonon excitations. These new details may provide important physical constraints on theories of pairing. This work is also a test of RIXS as a probe of low-energy excitations in well studied cuprate materials and provides insights into the RIXS intensity by comparison with a similar probe: inelastic neutron scattering.

Acknowledgements

I would like to start by thanking my three supervisors who have been so generous with their time and support in making the work in this thesis happen. Thank you to Stephen Hayden for sharing his vast knowledge of this field, to Kejin Zhou for the education in RIXS and to Stephen Dugdale for teaching me about DFT and Compton scattering and for always encouraging me to explore new things. I am grateful for the opportunity to have worked with all of them.

I thank the members of the Centre for Doctoral Training in Condensed Matter Physics for building a community that was great to be a part of. In particular Briony Spraggon, Jude Laverock and my cohort of CDT students for their role in that.

Thank you to other members of the CES group and residents of the 4.28 office for interesting discussions and advice. Thanks especially to Tom Millichamp for patiently sharing his knowledge with me as a first year student. I am grateful to many people for contributing to experiments, particularly Maud Barthélemy for help with RIXS, Kurt Kummer for support at ID32 and to all those who contributed to Compton experiments: Jon Duffy, Sean Giblin, Jon Taylor, Dan Lagos, Dan O'Neil and Dave Billington.

There are many people to thank from the time I spent at I21. Thank you to Andrew Walters and Mirian García-Fernández for their work commissioning the beamline and for frequent support during my own experiments. Jiemin Li and Abhishek Nag have been an inspiration for their knowledge and work ethic. I am grateful to them for assistance and entertainment during long experiments. I am very grateful for technical assistance from Tom Rice on whom the functioning of I21 is very much dependent. Thanks also to friends in Oxford for making the time there, when I escaped from the lab, extra fun.

Finally, I am grateful to the friends and family who have supported me over the last few years. I am especially grateful to my parents Martin and Clare and sister Kate for their encouragement, patience and lots of love. Thanks to Sam who has encouraged me through every step of this PhD. He has provided more support, understanding and love than I ever could have asked for and I'm truly grateful to him for that.

Author's declaration

I declare that the work in this dissertation was carried out in accordance with the requirements of the University's Regulations and Code of Practice for Research Degree Programmes and that it has not been submitted for any other academic award. Except where indicated by specific reference in the text, the work is the candidate's own work. Work done in collaboration with, or with the assistance of, others, is indicated as such. Any views expressed in the dissertation are those of the author.

SIGNED: ..... DATE: .....

Contents

Chapter 1

Introduction

Superconductivity is a phase of matter characterised by zero resistance and perfect diamagnetism which allows electrons to flow with infinite conductivity. Superconductivity arises when it becomes energetically favourable for electrons to pair, forming a gap at the Fermi surface and giving rise to zero resistance. In conventional superconductors, this condition is achieved via mediation with lattice vibrations, referred to as phonons. The interactions which underlie pairing in a new class of high temperature superconductors (HTSs) continue to be debated despite over 30 years of research. In this time, a number of ordered phases have been found to exist alongside the superconductivity in cuprate materials, which are some of the most well studied of HTSs. The role that these spin and charge ordered phases play in the pairing mechanism remains unclear. This thesis makes use of high-resolution resonant inelastic x-ray scattering (RIXS) to probe the spin and charge fluctuations in cuprate materials with the aim of constraining theoretical models of pairing.

While much remains uncertain, it is generally accepted that the superconducting state arises due to strong electron correlations. In strongly correlated systems, interactions between electrons must be considered in order to explain the bulk phenomena. For most materials, however, these interactions are not important. The free-electron model describes electrons in a metal by assuming that valence electrons are free to de-localise and move throughout the material. In this model, the 'gas' of electrons is expected to dominate the physics and therefore long-range interactions with the ionic cores are neglected and instead only direct collisions with the ionic cores are considered. Under these assumptions, the energy distribution, E, of electrons is given by the Maxwell-Boltzmann distribution[1],

$$f_{\mathrm{MB}}(E) = \frac{1}{\mathrm{e}^{(E-E_F)/k_B T}} \tag{1.1}$$

where E_F is the Fermi energy and T is temperature.

Although the scattering mechanism assumed by this model is known to be inaccurate, resulting in a number of discrepancies with observation, the model was able to predict some bulk properties of metals, including the form of Ohm's law, with remarkable accuracy.

Some of the known discrepancies were tackled in the quantum version of the free-electron model which was developed by Sommerfeld in 1927, building on the classical model by combining it with the new discoveries of quantum theory [2]. Chiefly, the Pauli exclusion principle which allows only one electron to occupy a state, therefore $0 < n < 1$. This principle requires electrons to follow the Fermi-Dirac distribution,

$$f_{\mathrm{FD}}(E) = \frac{1}{1 + \mathrm{e}^{(E-E_F)/k_B T}}. \tag{1.2}$$

As well as this change, the Sommerfeld model was also able to examine the results of the free electron model in the new language of quantum mechanics. The Schrödinger equation in three-dimensions can be expressed as,

$$-\frac{\hbar^2}{2m_e}\nabla^2\psi(\mathbf{r}) = E(\mathbf{r}), \tag{1.3}$$

where $\psi(\mathbf{r})$ is the electron wavefunction and E is its energy eigenvalue. Solutions can be found to Eqn. 1.3 by confining the electrons to a volume V and introducing the electron wave-vector $\mathbf{k}$ which, in the absence of a periodic potential, is any vector which is an eigenvalue of the momentum $\mathbf{p} = \hbar\mathbf{k}$,

$$\psi(\mathbf{r}) = \frac{1}{\sqrt{V}}\mathrm{e}^{i\mathbf{k}\cdot\mathbf{r}}, \tag{1.4}$$

with energy,

$$E(\mathbf{k}) = \frac{\hbar^2\mathbf{k}^2}{2m_e}. \tag{1.5}$$

Each $\mathbf{k}$ corresponds to a discrete solution to Eqn. 1.3. In a Fermi electron gas, spacing between allowed electron states is simply the volume of the space between k and $k + dk$ multiplied by the $\mathbf{k}$-density and spin degeneracy, $g_s = 2$ [2]. Therefore in a gas of free-electrons, the N lowest states are filled up to the Fermi energy,

$$E_F = \frac{\hbar^2}{2m_e}\left(\frac{3\pi^2 N}{V}\right)^{3/2}, \tag{1.6}$$

where E_F is the highest filled energy level. In a free-electron gas, the locations in k-space where $E = E_F$, referred to as the Fermi surface, is a sphere. However, for periodic crystal structures it can have a much more complicated shape.

The nearly free-electron model continues to neglect electron-electron interactions but considers electron-ion interactions by introducing a periodic potential, $v(\mathbf{r}) = v(\mathbf{r}+\mathbf{R})$, as in crystalline materials with spacing $\mathbf{R}$. This potential further constrains solutions to the Schrödinger

equation which becomes,

$$\left(-\frac{\hbar^2}{2m_e}\nabla^2 + v(\mathbf{r})\right)\psi(\mathbf{r}) = E\psi(\mathbf{r}) \tag{1.7}$$

$$\psi_{\mathbf{k}}(\mathbf{r}) = \frac{1}{\sqrt{V}}u_{\mathbf{k}}(\mathbf{r})\mathrm{e}^{i\mathbf{k}\cdot\mathbf{r}}, \tag{1.8}$$

where $u_{\mathbf{k}}(\mathbf{r})$ is a function with the same periodicity as the lattice, $u_{\mathbf{k}}(\mathbf{r}) = u_{\mathbf{k}}(\mathbf{r}+\mathbf{R})$, and $\psi_{\mathbf{k}}(\mathbf{r})$ are referred to as Bloch functions.

Introducing a periodic potential removes the requirement that Bloch wavefunctions are eigenstates of the momentum, and $\hbar k$ is referred to as the crystal momentum, defined only in the first Brillouin zone. Allowed $\mathbf{k}$-values plotted as a function of energy reveal lines representing allowed energy states, referred to as energy bands.

This model provides a good basis for introducing interactions between particles. Fermi liquid theory tackles this case by considering, instead of a sea of electrons, a sea of elementary excitations or quasiparticles which are modified by electron-electron and electron-phonon interactions. The quasiparticles are fermions which can be experimentally explored with spectroscopic techniques such as angle-resolved photoemission spectroscopy (ARPES). At low temperature, the quasiparticles act in a similar way to free electrons with properties such as conductivity and specific heat governed by the effective mass, $m^\star$. This mass renormalisation is due to the quasiparticle interactions which can be considered as creating a fluid of quasiparticles. The model has had success in explaining some properties of heavy fermion materials and metals. However, strongly correlated electron systems such as superconducting and charge density wave states are not explained within Fermi liquid theory. In these materials, electron-electron interactions dominate the physics. In both states, the electron interactions cause a gap to form at the Fermi surface resulting in a ground state which exhibits unexpected behaviours. In both cases, quasiparticles are thought to play a role in mediating the electron interactions. This thesis considers the elementary excitations, spin and charge fluctuations which are signatures of strongly correlated states, with the aim of understanding the interactions which underlie their behaviour. Chapter 2 introduces the concepts of superconductivity and the spin and charge fluctuations which accompany it in the cuprates.

The experimental work in this thesis makes use of the inelastic scattering of synchrotron x-rays to understand the charge and spin fluctuations in cuprates. Charged particles accelerating perpendicular to their direction of travel produce x-rays suitable for scattering experiments through the process of synchrotron radiation. Although this process was not demonstrated until 1947 it was theoretically predicted as far back as the discovery of the electron in 1897. Alfred

Lieńard showed that for an electron with kinetic energy E_k, radiated power is produced,

$$P = \frac{(E_k/m_e c^2)^4}{R^2}, \tag{1.9}$$

for a particle travelling with a radius of curvature R [3]. First experimental observations of this effect occurred during early scattering experiments using direct electron beams. This loss of power was initially considered a nuisance but was later utilised as a suitable source for scattering experiments itself. Experiments with synchrotron radiation have developed considerably since the early experiments and are now typically performed at dedicated facilities such as Diamond Light Source (DLS) and the European Synchrotron Radiation Facility (ESRF) where the experiments described in this thesis were performed. Chapter 3 gives a more detailed description of RIXS which is the principle experimental method used in this thesis.

The work in this thesis has two overarching aims. The first is to contribute to the understanding of superconductivity in cuprate materials. In particular, to further characterise the persistent magnetic excitations in cuprates with the aim of constraining spin fluctuation mediated theories of pairing. Charge fluctuations are not believed to be strong enough to be the sole mechanism underlying pairing but could contribute to another dominant process. Characterising the prominent charge fluctuations which are now understood to be a common feature of the cuprate phase diagram is therefore an important goal. The second aim of this thesis is to understand RIXS as a probe of elementary excitations. A significant portion of the work of this thesis was performed at the new I21 RIXS beamline at DLS as well as several experiments at ID32 at the ESRF. These experiments were mostly performed with energy resolution, $\Delta E \sim 37$ meV which allows for good characterisation of the range of excitations which are observed at the Cu L_3-edge. In particular careful consideration has been made of the resonant prefactors to the RIXS intensity including self-absorption effects and contributions from RIXS matrix elements.

To achieve these aims several RIXS studies have been performed. Chapter 4 describes RIXS experiments in the cuprate parent material La_2CuO_4 (LCO) which is a good test case for considering the RIXS intensity profile. LCO has a relatively simple single-layered crystal structure and as an insulator, simple calculations can be made of the local contributions to the RIXS cross-section. These calculations are shown to be in good agreement with inter-orbital *dd* excitations and hence are eventually used to normalise the magnetic RIXS intensity and isolate the long-range spin fluctuations which characterise the antiferromagnetic (AFM) order. This provides new measurements of the spin susceptibility which are compared to the significant previous work performed with inelastic neutron scattering (INS). Combined, these bodies of work point to significant deviations from linear spin-wave theory.

A simpler approach is taken in Chapter 5 where the RIXS measurements are extended to two doped compositions of $La_{2-x}Sr_xCuO_4$ (LSCO): underdoped $x = 0.12$ and optimally doped $x = 0.16$. In the superconducting compositions the AFM order is suppressed but the spin fluctuations remain. They are seen to be well described by a damped harmonic oscillator (DHO) model which reveals the wavevector dependence of the damping. The relative intensity of the spin fluctuations is presented by comparing RIXS and INS measurements of the parent compound. These new measurements of the spin susceptibility in doped compositions again show strong wavevector dependence. The measurements are shown to be phenomenologically similar to the predictions of spin fluctuation mediated theories based on the Hubbard model.

Chapter 6 describes RIXS experiments in underdoped $YBa_2Cu_3O_{6+x}$ (YBCO). YBCO is a two-layered cuprate material which has previously been well studied with RIXS and INS. The focus of the chapter is the charge density wave order which is measured with RIXS via an enhancement at incommensurate wavevectors. Following previous work, the new measurements show a sharp charge-density wave (CDW) peak at low temperature and a broad peak which appears as a precursor to the low temperature order. The new measurements track the two regimes as a function of temperature above and below the superconducting critical temperature, T_c, and the pseudogap temperature, $T^\star$. The spin fluctuations in YBCO are also parameterised with the DHO model exhibiting similar behaviour to LSCO. Some evidence is seen for an interaction between the spin fluctuations and the charge order.

Finally, Chapter 7 provides some concluding remarks and an outlook on the future of work in this field.

Chapter 2

Superconductivity, spin and charge fluctuations

Of the phenomena produced by strongly correlated electrons, superconductivity is one of the most well known. Superconductivity refers to a phase of matter characterised by zero electrical resistivity, occurring below a transition temperature, T_c, often at low temperature. Onnes first recorded the effect in mercury in 1911 [4] and in the following years cryogenic technology revealed a spate of metals also able to exhibit the effect. However, it took more than 50 years for a theory to be proposed that explained the phenomena on a microscopic level.

The BCS theory, put forward by Bardeen, Cooper and Schrieffer in 1957 [5], describes a coherent many-body ground state for bound electrons. These electrons, known as Cooper pairs, form the basis of the theory and are shown to pair as a result of a weak attractive potential between them, mediated by virtual phonons. The paired electrons act as a superfluid and flow without losing energy to the lattice. The BCS theory proved successful for all newly found superconductors for the next 20 years, until 1986 when the discovery of superconductivity in $La_{2-x}Ba_xCuO_4$ (LBCO) proved unable to fit the model [6]. Unlike previous superconductors, LBCO and a number of swiftly-discovered similar materials are layered ceramics with flat copper oxide planes, intercalated with dopant materials. This family of materials, referred to as cuprates, were found to have significantly higher transition temperatures than their conventional counterparts (eventually up to 133 K in $HgBa_2Ca_2Cu_3O_{8-\delta}$ (Hg-1223) [7]) and cannot be explained by conventional BCS theory. A number of further unconventional or high temperature superconductors (HTSs) have since been discovered, including iron-based pnictide superconductors [8, 9], a range of materials in the heavy fermion family [10, 11], and in several materials under high pressure [12, 13]. The failure of BCS theory to explain high temperature superconductivity

has stimulated a large amount of research aiming to provide an answer. One thing that has become clear is that superconductivity frequently exists alongside other ordered phases. This chapter introduces the properties of superconductors and our current understanding of the mechanisms which govern conventional and high-temperature superconductors and the role that spin and charge fluctuations might play in pairing.

2.1 Properties of superconductivity

The superconducting phase is characterised firstly by exactly zero resistance and secondly by the Meissner-Ochsenfeld effect, a complete expulsion of magnetic field from the bulk of the material. The Meissner state is achieved by screening currents at the surface of the superconducting material which produce magnetic fields equal and opposite to the external magnetic field. The complete screening of applied magnetic field means that superconductors are perfect diamagnets. The specific response to such an applied magnetic field divides superconducting materials into two distinct types. Type I, observed in most elemental superconductors, is characterised by surface currents which screen out magnetic flux within a distance $\lambda(T)$, known as the Ginzburg-Landau penetration depth. The same occurs in type II materials up to a critical field H_{c1}, after which magnetic flux quanta are able to penetrate into the bulk until the onset of an upper critical field, H_{c2}, when superconductivity is destroyed. London [14] predicted that single quanta of magnetic flux $\Phi_0 = h/2e$ are able to enter the material above H_{c1}, a prediction which was verified by observations in 1961[15, 16]. The penetrating lines of flux are referred to as vortices and form a range of complex lattice structures. With the increase of applied magnetic field, the superconducting state is eventually destroyed.

2.2 Conventional superconductivity

Extensive descriptions exist in the literature of the theories that have developed to explain the microscopic mechanism governing conventional superconductivity. References [17, 18, 19] give detailed descriptions of their origin and derivation. This section provides a brief summary of the background and main results of these theories.

2.2.1 The London equations

The first theory attempting to explain the superconducting phase was put forward by London and London in 1935. The London theory built on the model of superfluid ^{4}He in which some

percentage of particles become superfluid, with zero viscosity and entropy, while the rest remain in a normal state. Reflecting this, the London theory proposed that in superconductors, a small number of superconducting electrons, n_s are able to flow with zero resistance. It is now understood that this is not the microscopic mechanism in superconductors but two key equations which were developed from it are still believed to quantitatively describe their behaviour. The London equations are derived phenomenologically by applying the limit of zero scattering to the momentum-dependent conductivity expected from the Drude model and describing the behaviour of the electric and magnetic fields. The equations can be written in a single form which correctly describes the current density in all superconductors, by defining a magnetic vector potential **A**,

$$\mathbf{j} = -\frac{1}{\mu_0 \lambda_L^2}\mathbf{A}, \tag{2.1}$$

where λ_L is the London penetration depth, or the distance that an external magnetic field is able to penetrate before being screened. This demonstrates a key success of the London equations in being able to correctly explain the Meissner effect.

2.2.2 Ginzburg-Landau theory

A second piece of the puzzle was revealed in 1950 when Ginzburg and Landau presented a theory to explain the phase transition to the superconducting state. Landau had previously observed that second-order phase transitions are usually associated with a change in the symmetry of a system which in superconductivity he described with an order parameter [20],

$$\Psi(\mathbf{r}) = |\Psi(\mathbf{r})|^2 \mathrm{e}^{i\psi(\mathbf{r})}. \tag{2.2}$$

2.2.3 BCS theory

Building on these observations and theories, in 1957 Bardeen, Cooper and Scrieffer proposed a theory for the microscopic mechanism underlying the superconducting state [5]. Qualitatively, a material enters a superconducting state when the Gibbs free energy of the superconducting system is lower than a free-electron state at the same temperature. This suggests that an attractive interaction must exist to overcome the repulsive inter-electron interactions. This requires the electrons to be treated as quasiparticles interacting with the lattice vibrations which can be considered as a separate quasiparticle: a phonon. Cooper introduced this problem by considering electrons outside of an occupied Fermi surface at $T = 0$ and showed that in the presence of an applied attractive potential V_{eff}, the lowest energy is achieved with a bound state of the electron pairs [21].

To understand this phenomenon we follow the derivation of Annett in reference [17] and consider an electron in Bloch state $\psi_{\mathbf{k}}(\mathbf{r})$ moving through a crystal lattice experiencing a periodic modulation of potential. The electron can interact with the lattice, producing a phonon with crystal momentum $\hbar\mathbf{Q}$, resulting in the electron Bloch state $\psi_{n\mathbf{k}'}(\mathbf{r})$ with a crystal momentum $\hbar\mathbf{k}' = \hbar\mathbf{k} - \hbar\mathbf{Q}$. If a second electron interacting with the lattice later absorbs this momentum, the electrons effectively interact. BCS theory makes a simple approximation of this complex interaction by estimating the frequency of the phonon as the Debye frequency, ω_D, and introducing an effective interaction vertex g_{eff} representing the strength of the electron-phonon interaction,

$$\begin{aligned} V_{\text{eff}}(\mathbf{Q},\omega) &= |g_{\text{eff}}|^2 \frac{1}{\omega^2 - \omega_D^2} \\ &= -\frac{g_{\text{eff}}^2}{\omega_D^2} \text{ for } |\omega| << \omega_D. \end{aligned} \tag{2.3}$$

It is assumed that electrons involved with pairing must have energy within $k_B T$ of the Fermi energy and for the temperature scale relevant to superconductivity this is a lot less than $\hbar\omega_D$. This means we are interested only in attractive interactions and the second form of Eqn. 2.3 is sufficient to describe the interaction in conventional superconductors.

Cooper next considered the effect of the attractive potential on electrons inside and outside the occupied Fermi sea. The total wavefunction of paired electrons, $\mathbf{k}$ with position $\mathbf{r}_1, \mathbf{r}_2$ and spin states σ_1, σ_2, can be approximated by a product of their spin ϕ and spatial ψ components,

$$\Psi(\mathbf{r},\sigma) = \prod_{\mathbf{k},\sigma} \psi(\mathbf{r}_1 - \mathbf{r}_2)\phi(\sigma_1,\sigma_2). \tag{2.4}$$

In the simplest form, which is assumed by BCS theory, the spatial wave function is described as a sum over free-electron Bloch waves,

$$\psi(\mathbf{r}_1 - \mathbf{r}_2) = \sum_{\mathbf{k}} \psi_{\mathbf{k}} e^{i\mathbf{k}(\mathbf{r}_1 - \mathbf{r}_2)}. \tag{2.5}$$

The spin wavefunction must therefore be a spin singlet which we can define in terms of the spin states $\uparrow$and $\downarrow$,

$$\phi(\sigma_1,\sigma_2) = \frac{1}{\sqrt{2}}(|\uparrow\downarrow\rangle - |\downarrow\uparrow\rangle). \tag{2.6}$$

To satisfy the Pauli exclusion principle for Fermions, the total wavefunction must be antisymmetric such that $\Psi(\mathbf{r}_1,\mathbf{r}_2,\sigma_1,\sigma_2) = -\Psi(\mathbf{r}_2,\mathbf{r}_1,\sigma_2,\sigma_1)$. As the spin singlet state is odd, the spatial wavefunction, ψ must be even and so the expansion coefficient, $\psi_{\mathbf{k}}$, must be equal to $\psi_{-\mathbf{k}}$. Applying these two components to Eqn. 2.4 allows the total wavefunction to be written as a sum of Slater determinants [17],

$$\Psi(\mathbf{r},\sigma) = \sum_{\mathbf{k}>k_F} \psi_{\mathbf{k}} \begin{vmatrix} \psi_{\mathbf{k}_\uparrow \mathbf{r}_1} & \psi_{\mathbf{k}_\downarrow \mathbf{r}_2} \\ \psi_{-\mathbf{k}_\uparrow \mathbf{r}_1} & \psi_{-\mathbf{k}_\downarrow \mathbf{r}_2} \end{vmatrix}. \tag{2.7}$$

This equation describes electrons $\mathbf{k}$ with spin $\downarrow$ pairing with electrons -$\mathbf{k}$ with spin $\uparrow$.

The full BCS theory makes use of the language of second quantisation to express occupied states with creation, $c^{\dagger}_{\mathbf{k}_\uparrow}$, and annihilation $c_{\mathbf{k}_\uparrow}$ operators which respectively increase or decrease the number of particles in a given state. In this notation a pair creation operator must create two electrons with opposite spin and momentum, $\hat{P}^{\dagger}_{\mathbf{k}} = c^{\dagger}_{\mathbf{k}_\uparrow} c^{\dagger}_{-\mathbf{k}_\downarrow}$. An exact wavefunction can be constructed by creating Cooper pairs for all $\mathbf{k}$ in an occupied band, however as the $\mathbf{k}$ states are all eigenstates of the Fermi sea, the total BCS wavefunction can be defined as a product of the average occupancy of a state,

$$|\Psi_{\mathrm{BCS}}\rangle = \prod_{\mathbf{k}} (u^{\star}_{\mathbf{k}} + v^{\star}_{\mathbf{k}} P^{\dagger}_{\mathbf{k}}) \left|\psi_0\right\rangle, \tag{2.8}$$

where $|u^{\star}_{\mathbf{k}}|^2$ and $|v^{\star}_{\mathbf{k}}|^2$ describe the probability of the state being unoccupied or occupied respectively. It was later demonstrated that in the vicinity of T_c, the BCS wavefunction recovers the Ginzburg-Landau equations, where Ψ_{BCS} is the order parameter associated with the phase transition [22].

The pairing Hamiltonian associated with states $\mathbf{k}_\uparrow$ and $\mathbf{k}_\downarrow$ is a sum over all states with energy $E_{\mathbf{k}}$ within $\hbar\omega_D$ of the Fermi energy where the total energy is the pairing potential subtracted from the kinetic energy,

$$\hat{H} = \sum_{\mathbf{k},\sigma} E_{\mathbf{k}} c^{\dagger}_{\mathbf{k}\sigma} c_{\mathbf{k}\sigma} - |g_{\mathrm{eff}}|^2 \sum_{\mathbf{k},\mathbf{k}'} \hat{P}^{\dagger}_{\mathbf{k}} \hat{P}_{\mathbf{k}'}. \tag{2.9}$$

$\hat{P}$ are creation and annihilation operators for electron pairs. The total energy E of the system can be expressed in terms of the wavefunction, $E = \langle \Psi_{\mathrm{BCS}} | \hat{H} | \Psi_{\mathrm{BCS}} \rangle$. In the limit where $|u_{\mathbf{k}}|^2 + |v_{\mathbf{k}}|^2 = 1$ (i.e. the state must be either occupied or unoccupied) this produces,

$$E = \sum_{\mathbf{k}} E_{\mathbf{k}} \left(|v_{\mathbf{k}}|^2 - |u_{\mathbf{k}}|^2 + 1 \right) - |g_{\mathrm{eff}}|^2 \sum_{\mathbf{k}\mathbf{k}'} v_{\mathbf{k}} v^{\star}_{\mathbf{k}'} u_{\mathbf{k}} u^{\star}_{\mathbf{k}'}. \tag{2.10}$$

Differentiating the energy of the system with respect to $v^{\star}_{\mathbf{k}}$ and $u^{\star}_{\mathbf{k}}$ produces two linear equations which can be expressed in matrix form,

$$\begin{pmatrix} \xi_{\mathbf{k}} & \Delta_{\mathbf{k}} \\ \Delta^{\star}_{\mathbf{k}} & -\xi_{\mathbf{k}} \end{pmatrix} \begin{pmatrix} u_{\mathbf{k}} \\ v_{\mathbf{k}} \end{pmatrix} = E_{\mathbf{k}} \begin{pmatrix} u_{\mathbf{k}} \\ v_{\mathbf{k}} \end{pmatrix}. \tag{2.11}$$

$\xi_{\mathbf{k}}$ is the energy relative to the Fermi energy and we define the gap parameter, the energy gap between the occupied and unoccupied states, $\Delta_{\mathbf{k}} = |g_{\mathrm{eff}}|^2 \sum_{\mathbf{k}} \langle \hat{P}_{\mathbf{k}} \rangle$.

The matrix Eqn. 2.11 can be manipulated to directly express the energy as a function of the gap,

$$E_{\mathbf{k}} = \left(\Delta^2_{\mathbf{k}} + \xi^2_{\mathbf{k}} \right)^{1/2}. \tag{2.12}$$

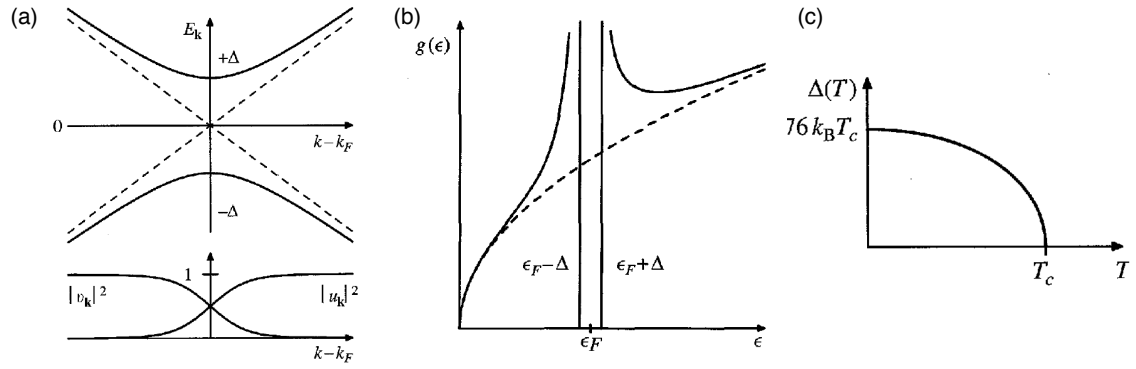

Figure 2.1: Characteristics of the superconducting gap in BCS theory showing (a) energy eigenvalues as a function of $\mathbf{k}$ close to the Fermi energy showing (solid lines) the hybridised energy states which lead to the gap, $\Delta_{\mathbf{k}}$. Panel (b) shows the BCS gap as a function of energy and panel (c) shows the gap as a function of temperature. Figure reproduced with permission from reference [17].

Fig. 2.1 (a) shows the energy eigenvalues E_k plotted as a function of $\mathbf{k}$ close to the Fermi energy $\mathbf{k}_F$, the dashed lines show the energy levels in a normal metal and the solid line shows the hybridised superconducting energy levels which give rise to the gap, $\Delta_{\mathbf{k}}$. We can evaluate the eigenvector $(u_{\mathbf{k}}, v_{\mathbf{k}})$ to find expressions for the probabilities $|u_{\mathbf{k}}|^2$ and $|v_{\mathbf{k}}|^2$

$$|u_{\mathbf{k}}|^2 = \frac{1}{2}\left(1+\frac{\xi_{\mathbf{k}}}{E_{\mathbf{k}}}\right) \tag{2.13}$$

$$|v_{\mathbf{k}}|^2 = \frac{1}{2}\left(1-\frac{\xi_{\mathbf{k}}}{E_{\mathbf{k}}}\right), \tag{2.14}$$

which are also plotted in Fig. 2.1 (a) as a function of $\mathbf{k}$ close to $\mathbf{k}_F$. This gives an expression for the probabilities in terms of the energy and gap,

$$u_{\mathbf{k}} v_{\mathbf{k}}^{\star} = \frac{\Delta_{\mathbf{k}}}{2E_{\mathbf{k}}}. \tag{2.15}$$

The above three equations can be solved self-consistently to express the gap as a function of the energy,

$$\Delta_{\mathbf{k}} = |g_{\text{eff}}|^2 \sum_{\mathbf{k}} \frac{\Delta_{\mathbf{k}}}{2E_{\mathbf{k}}}. \tag{2.16}$$

The existence of an energy gap is one of the main predictions of BCS theory. Fig. 2.1 (b) shows the gap energy as a function of energy. It shows that even at the Fermi surface where $\xi = 0$ there is a minimum energy E_k which can be thought of as a quasi-particle excitation.

Assuming that the interactions occur in a shell within $\hbar\omega_D$ of the Fermi surface, the gap can be evaluated at zero temperature by introducing an electron-phonon coupling constant $\lambda = |g_{\text{eff}}|^2 g(E_F)$ where $g(E_F)$ is the density of states at the Fermi energy,

$$|\Delta_{\mathbf{k}}| = 2\hbar\omega_D \mathrm{e}^{-1/\lambda}. \tag{2.17}$$

The result is only valid in the weak coupling limit $\lambda \ll 1$. Finite temperatures are considered by noting that the occupation is governed by the Fermi-Dirac distribution function, $f(E_{\mathbf{k}})$ at $E_{\mathbf{k}}$, $f(E_{\mathbf{k}}) = \left(e^{E_{\mathbf{k}}/k_B T} + 1\right)^{-1}$.

In the strong coupling limit, where λ is less than but close to 1, interactions between electrons and phonons become important. The Eliashberg function describes an extension to BCS theory which accounts for this by considering the screened Coulomb repulsion between pairs of electrons. This approach assumes coupling between electrons and phonons defined by a coupling matrix element, $\alpha(\omega)$, and the phonon density of states $F(\omega)$. The Eliashberg function is therefore given by,

$$\lambda_{\text{el-ph}} = 2\int_0^\infty \frac{F(\omega)\alpha^2(\omega)}{\omega} d\omega. \tag{2.18}$$

This derivation has followed the BCS simplification that $|\omega| < \omega_D$, which allows us to describe the pairing interaction with a constant g_{eff}. However, the same approach can be applied to derive a pairing interaction which depends on the wavevector, $\mathbf{Q}$, and energy, ω, of the quasiparticles which mediate the interaction, giving $V_{\mathbf{Q},\omega}$. Expressing Eqn. 2.16 in terms of such an interaction between electrons $\mathbf{k}$ and $\mathbf{k}'$ gives a wavevector dependent gap equation,

$$\Delta_{\mathbf{k}} = -\frac{1}{2}\sum_{\mathbf{k}'} \frac{V_{\mathbf{k}\mathbf{k}'}\Delta_{\mathbf{k}'}}{E_{\mathbf{k}'}} \left[1 - 2f(E_{\mathbf{k}'})\right], \tag{2.19}$$

It is clear that the symmetry of the gap reflects the symmetry of the underlying pairing interaction $V_{\mathbf{k}\mathbf{k}'}$. BCS theory makes the assumption that the interaction potential takes the form,

$$V_{\mathbf{k}\mathbf{k}'} = \begin{cases} -V & \text{if } |E_{\mathbf{k}}| \text{ and } E_{\mathbf{k}'}| < \hbar\omega_D \\ 0 & \text{otherwise.} \end{cases} \tag{2.20}$$

It should be noted that this form restricts the allowed symmetry of the gap equation to be negative. Observations that point to different symmetry in unconventional superconductors are taken as a key indicator of their deviation from BCS theory.

The predictions of BCS theory are well reproduced by observations in conventional superconductors as seen in the experimental measurements of $\Delta_{\mathbf{k}}$ which are generally in good agreement with that predicted by Eqn. 2.17 [18]. The success of the theory is also seen in its prediction of the Josephson effect and the process of Andreev scattering in which an electron tunnels into a superconducting material by forming a Cooper pair. Observations of a tunnelling current which is twice what it would have been if $\Delta_{\mathbf{k}} = 0$ is taken as evidence that a positively charged hole is produced with momentum opposite to the incident electron due to the production of a Cooper pair in the superconductor. BCS theory also explains the isotope effect in which isotopes of the same element with mass M have varying transition temperatures as $T_c \propto M^{-1/2}$

[23]. The BCS model effectively predicts this relationship due to the $\hbar\omega_D$ thickness of the shell around the Fermi surface in which pairing takes place. The predictions made by the strong coupling extension to BCS theory have also been shown to be successful in materials such as Pb and Nb [24, 17]. However, the discovery of superconductivity in LBCO and the subsequent discovery of unconventional superconductors proved incompatible with BCS theory. The next section discusses attempts which have been made to address this.

2.3 High-temperature superconductivity

Signatures of electron pairing was reported in the high T_c cuprate superconductor, $YBa_2Cu_3O_{7-\delta}$ (YBCO), soon after the discovery of HTS through the observation of quantised flux in a superconducting ring [25]. Andreev reflection was also observed [26] suggesting HTS superconductors retain some of the hallmarks of BCS theory [20]. However, measurements in several cuprates indicated the lack of an expected isotope effect with doping [27, 28]. This combined with unexpectedly high T_c led to the suggestion that although Cooper pairs are likely to exist in unconventional superconductors, the pairing mechanism is different.

2.3.1 Pairing symmetry

One consequence of BCS theory is that the spin wavefunction takes a spin-singlet form. In fact, the requirement is only that the overall wavefunction remains antisymmetric. Therefore if the orbital angular momentum l is even, $S = 0$ and the spin wavefunction will be a spin singlet as in Eqn. 2.6 but if l is odd, we must have $S = 1$ and the spin wavefunction will take the triplet form,

$$\phi(\sigma_1,\sigma_2) = \begin{cases} |\uparrow\uparrow\rangle \\ \frac{1}{\sqrt{2}}(|\uparrow\downarrow\rangle + |\downarrow\uparrow\rangle) \\ |\downarrow\downarrow\rangle \end{cases} . \tag{2.21}$$

The orbital angular momentum l can in fact be 0, 1, 2, 3, ... giving gap functions with symmetry referred to as s, p, d and f-wave respectively.

As discussed in section 2.2.3, materials which follow BCS theory develop a superconducting gap Δ which is constant in $\mathbf{k}$. The symmetry of the BCS wavefunction can be described by $l = 0$ giving the orbital part of the wavefunction s-wave symmetry. However, where strong electron-electron repulsion is not overcome by electron-phonon coupling, the energy is minimised when the pair wavefunction is equal to 0 when $\mathbf{r}_1 = \mathbf{r}_2$. To achieve this the gap is required to change sign over the Fermi surface leading to nodes where $\Delta_k(\mathbf{r}) = 0$. Fig. 2.2 shows a comparison

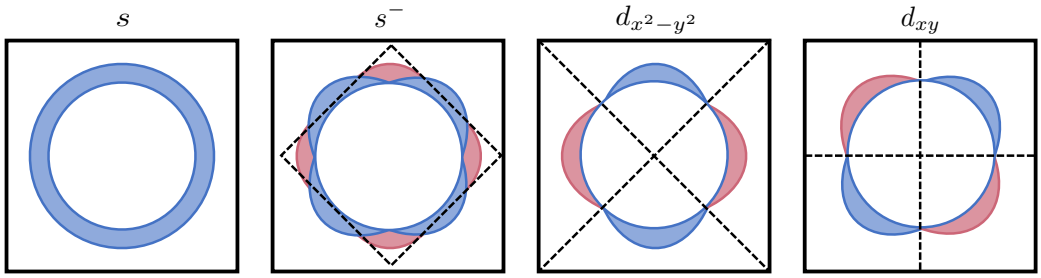

Figure 2.2: Gap wavefunctions for a tetragonal crystal with a square Fermi surface showing various possible gap symmetries $s, s^-, d_{x^2-y^2}$ and d_{xy}. The sign of the gap is indicated in pink for positive and blue for negative. Nodal directions where the sign changes are indicated with dashed lines.

of the s and d-wave pair wavefunctions for a tetragonal crystal structure with a square Fermi surface. Pure s-wave symmetry, as in the BCS case, leads to a constant spherically symmetric gap function. An extended s^- symmetry can be achieved with a constant function for all symmetries with a varying gap with 8 nodal points where the sign changes (indicated by the dashed lines in Fig. 2.2). Materials with d-wave symmetry show spatial variation in the wavefunction which is not symmetrical and gives 4 nodes.

By convention, materials with symmetry of the orbital wavefunction of $l \neq 0$ or of the spin wave function $S \neq 0$ are referred to as unconventional superconductors to differentiate them from those which obey BCS theory.

Identifying the gap-symmetry in real superconductors is an important tool for developing theories to explain the origin of pairing. This can be achieved by observing the excitation of quasiparticle states below the Fermi surface which can only occur along the nodal directions. In cuprate superconductors, singlet symmetry is observed giving possible orbital symmetries s, $s^-, d_{x^2-y^2}$ or d_{xy} [29]. The electronic properties are dominated by interactions in the CuO_2 planes resulting in a highly two-dimensional Fermi surface and possible gap wavefunctions as shown in Fig. 2.2. Experimental measurements sensitive to the phase of the superconducting order parameter suggest $d_{x^2-y^2}$ is the most likely symmetry in cuprates [30, 20]. This manifests as symmetry in the CuO_2 plane with nodes along the Cu-Cu positions and a maximum gap along the Cu-O positions. d-wave gap symmetry cannot be achieved without positive components of $V_{\mathbf{kk}'}$ which is not possible within phonon mediated theories (see Eqn. 2.20) and hence there has since been a search for a suitable mechanism. Section 2.4 provides details of some of the possible candidates for mediating superconductivity in unconventional superconductors.

Another key feature of HTS not seen in conventional superconductors is the pseudogap $2\Delta^\star$ which occurs in the normal phase. NMR [31] and subsequent ARPES measurements [32]

have confirmed the existence of a partial energy gap of the same magnitude and symmetry as the superconducting gap but above T_c. The pseudogap is generally considered to occur due to interaction between spin and charge density wave order which result in preformed pairs below a temperature $T^\star$ which become Cooper pairs below T_c [33].

2.4 Spin fluctuations

In many HTS materials, superconductivity is observed close to antiferromagnetic (AFM) order which has led to speculation into the role of magnetic order in pairing. This section briefly introduces some of the concepts which underlie the magnetic interactions in AFM materials.

2.4.1 Exchange interactions

The single band Hubbard model describes magnetic systems by considering the competition between electrons which hop between sites i and j with hopping constant t_{ij} and the on-site Coulomb repulsion U ,

$$H = -\sum_{ij\sigma} t_{ij}(c^\dagger_{i\sigma} c_{j\sigma}) + U\sum_i n_{i\uparrow} n_{i\downarrow}, \tag{2.22}$$

where $c^\dagger$ and c represent the creation and annihilation of an electron with polarisation $\sigma = \uparrow$ or $\downarrow$, and n is the occupation number of the site with spin $\uparrow$ or $\downarrow$. The $t-J$ model is a specific extension of the Hubbard model to deal with systems with long-range order described by the parameter J as a sum over the spin operators $\mathbf{S}$,

$$H = -t\sum_{ij\sigma} c^\dagger_{i\sigma} c_{j\sigma} + \sum_{ij}\left(\mathbf{S}_i \cdot \mathbf{S}_j - \frac{n_i n_j}{4}\right). \tag{2.23}$$

Long-range magnetic order can occur in crystals due to the exchange interaction as a result of an effective interaction between pairs of spins. Exchange interactions occur where atomic orbitals are able to exchange electrons resulting in the degeneracy between spin states being destroyed [34]. The spin wavefunction can therefore take either a triplet (Eqn. 2.21) or singlet (Eqn. 2.6) state and an energy difference J is revealed between the two states $J = E_s - E_t$. The Heisenberg Hamiltonian is a specific form of the Hubbard model that describes the magnetic state of a spin-1/2 system,

$$H = \sum_{i,j} J\mathbf{S}_i \cdot \mathbf{S}_j. \tag{2.24}$$

In the case of cuprates, $E_s > E_t$ and the energy gain from the exchange overcomes the Coulomb repulsion between sites, making AFM ordering energetically favourable.

In practice, direct exchange occurs between overlapping orbitals of magnetic ions and is typically the case in only a few materials such as in transition metal oxides where the magnetic

orbitals are sufficiently closely packed. Indirect processes can also lead to exchange such as in the case of superexchange interactions, where intervening non-magnetic ions mediate the process of exchange [35, 36]. Chapter 4 describes the superexchange interactions which contribute to AFM order in the cuprate parent compound La_2CuO_4 (LCO).

2.4.2 The role of spin fluctuations in pairing

Elementary excitations from the antiferromagnetic ground state are called magnons. These excitations are sometimes referred to as spin fluctuations and are eigenstates of the antiferromagnetic ground state Hamiltonian which is described above. Chapter 4 gives a description of the spin fluctuations in relation to the AFM ground state in LCO. However, in a number of HTSs, including the cuprates, spin fluctuations persist into superconducting phases where the AFM order is suppressed. A possible explanation for this is that the order remains due to the localisation of the doped holes into fluctuating spin stripes, however, the nature of possible stripe order continues to be debated [37, 38]. In any case, the persistence of the spin fluctuations into superconducting phases has sparked significant research into their possible connection with pairing.

Early theoretical calculations based on persistent AFM spin fluctuations were able to reproduce the type of pairing symmetry observed in both cuprate [39] and heavy fermion materials [40, 41]. In these and subsequent spin fluctuation meditated models, electrons on neighbouring sites pair with a magnetic coupling constant I. An approximate AFM pairing potential is given by, [42],

$$V_{\mathbf{k}\mathbf{k}'} \approx I^2 \chi'(\mathbf{Q}) = \frac{I^2}{\pi} \int \frac{\chi''(\mathbf{Q},\omega)}{\omega} d\omega, \tag{2.25}$$

where the real part of the susceptibility, $\chi'(\mathbf{Q})$ at $\omega = 0$, is related to the imaginary part, χ'', by the Kramers-Kronig relation,

$$\chi'(\mathbf{Q}) = \frac{1}{\pi} \int_{-\infty}^{\infty} \frac{\chi''(\mathbf{Q},\omega)}{\omega}\, d\omega. \tag{2.26}$$

This form of the pairing potential gives rise to a gap,

$$\Delta_{\mathbf{k}} = -\frac{1}{2} \sum_{\mathbf{k}'} \frac{V_{\mathbf{k}\mathbf{k}'} \Delta_{\mathbf{k}'}}{E_{\mathbf{k}'}} \left[1 - \frac{2}{\exp(E_{\mathbf{k}'}/k_B T + 1)} \right], \tag{2.27}$$

which favours states that change sign over the Fermi surface characteristic of d-wave pairing. Inelastic neutron scattering measurements have observed strongly enhanced magnetic susceptibility in the spin fluctuations of AFM materials at $(1/2, 1/2)$, referred to as the antiferromagnetic wavevector $\mathbf{Q}_{\mathrm{AFM}}$ [43, 44] which can lead to d-wave pairing [45, 42].

The first theory proposed to explain pairing in HTSs was the resonating valence bond (RVB) theory which developed out of a description of $S = 1/2$ antiferromagnetically coupled spins [46]. The discovery of HTS in cuprates, which are characterised by 2-dimensional layers of CuO_2 square lattice of the kind described by RVB, led to the suggestion that this could be the mechanism for pairing [47]. In this model the strong Coulomb repulsion is taken into account by modelling the band as a Fermi sea where each site has a single spin. The on-site spins would then bond as singlet pairs, forming "a liquid of pair bonds" [48]. In fact, cuprates are not metals but charge-transfer insulators, and instead display long-range AFM order. However, the suggestion from the RVB model that the AFM spin singlet pairs could be responsible for pairing has remained important. Several possible models have been proposed on this basis [42].

Flux-phase RVB theory is an extension of RVB in which the high energy spin fluctuations are fractional quasiparticles with $S = 1/2$ [49, 50]. These fractional quasiparticles are often referred to as spinons in 1D and are characterised by a rotation of the spin order in an AFM chain where long-range ordering breaks down. Dalla Piazza *et al.* [51] demonstrated the success of these theories in 2D to explain deviations from the expected behaviour of magnons in square lattice $S = 1/2$ systems.

A large amount of theoretical work has considered the influence of spin fluctuations on superconductivity within the Hubbard model. A comprehensive review of these theories is given in reference [52]. In light of these theories, neutron scattering and more recently resonant inelastic x-ray scattering (RIXS) has been used to study the spin response in many superconducting materials. Extensive characterisation has been made of the spin fluctuations in superconducting materials which has been used to make the case for a connection between magnetism and superconductivity [53]. As defined in Eqn. 2.25, the susceptibility of the spin fluctuation, $\chi''(\mathbf{Q},\omega)$, is predicted to be an indicator of the strength of the pairing potential, $V_{\mathbf{kk}'}$. INS and RIXS measure the response of the system via the dynamic structure factor, $S(\mathbf{Q},\omega)$ which is proportional to the susceptibility (more details of the relationship between $S(\mathbf{Q},\omega)$ and $\chi''(\mathbf{Q},\omega)$ in RIXS are given in Chapter 3). Fig. 2.3 shows the dynamical susceptibility from dynamical quantum Monte Carlo (DQMC) calculations based on the Hubbard model where the calculated energy dispersion is shown to match well with INS data [54]. The structure factor is predicted to evolve strongly with doping as shown in Fig. 2.3 (B). Chapter 5 examines this scenario in $La_{2-x}Sr_xCuO_4$ (LSCO).

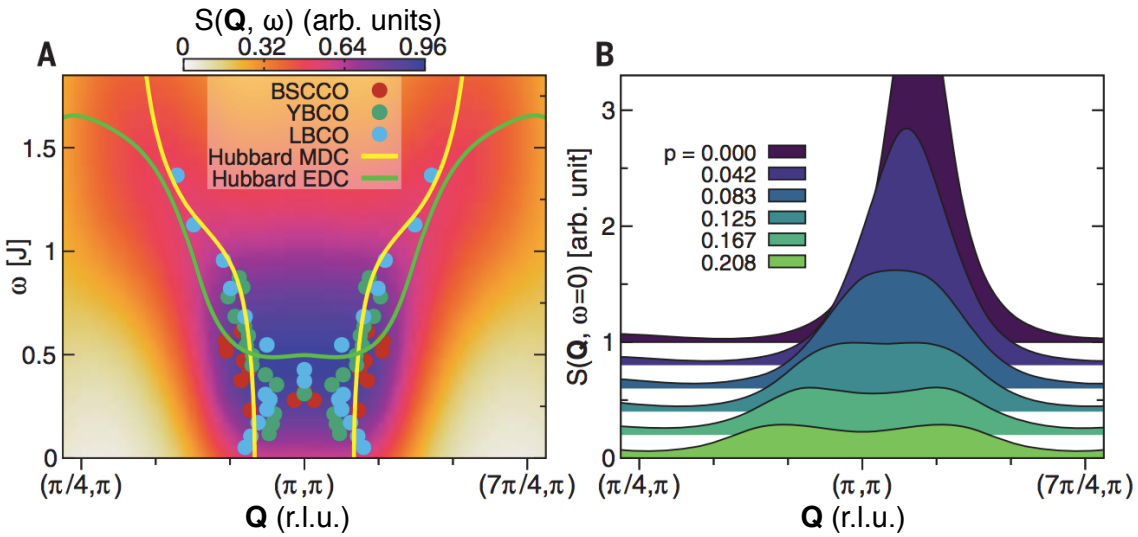

Figure 2.3: The dynamical structure factor of spin fluctuations in the cuprates from dynamical quantum Monte Carlo calculations based on the Hubbard model. Panel (A) shows the structure factor and energy and momentum distribution curves (EDC/ MDC) of the DQMC calculation compared to measurements made with INS (indicated with circles). Panel (B) shows the calculated evolution of the structure factor with doping. Figure reproduced with permission from reference [54].

2.5 Charge and spin order

High temperature superconductivity frequently emerges as AFM systems are doped with charge carriers. As the system is doped, the Hubbard model breaks down as dopants increasingly tend to delocalise and additional charge and spin ordered phases are possible, including spin and charge density waves (SDW/ CDW). This section briefly summarises the mechanisms which underlie these ordered states.

2.5.1 Charge density wave order

A CDW is a particular form of charge order resulting from periodic modulations in the charge density of valence electrons. Peierls was the first to predict that such a phase could exist in a 1D chain of metallic atoms [55]. He predicted that a modulation of the atomic positions x of the form $\delta x_n = \delta x \cos(Q + \phi)$ at $\mathbf{Q}$ equivalent to the Fermi wavevector k_F, would result in an energy gap forming at E_F. The magnitude of the gap Δ is related to an order parameter $\Psi = \Delta e^{i\phi}$. The CDW phase becomes the preferred ground state if the energy to modulate the atomic positions is less than the gain in electronic energy. Where this is the case the energy of occupied states below E_F is reduced and a gap forms at the Fermi surface[56]. Fig. 2.5 shows a schematic of a Peierls distortion leading to the formation of a gap in a 1D chain of atoms. Peierls predicted that the phase becomes energetically favourable in 1D metals below what is referred to as the Peierls

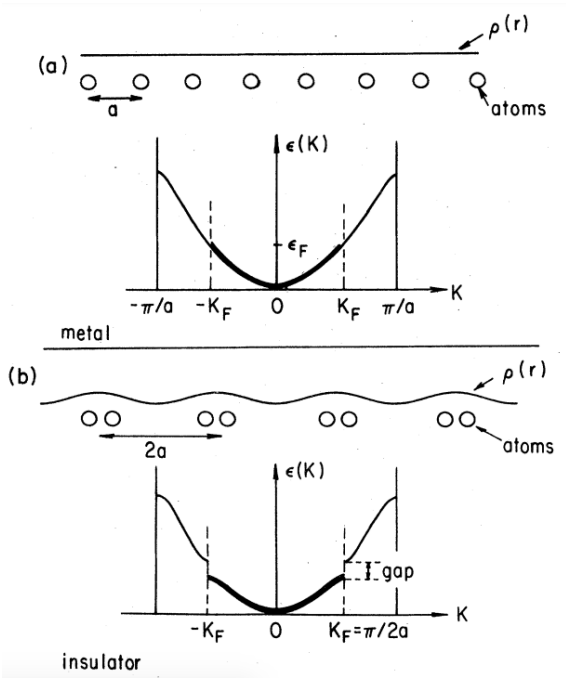

Figure 2.4: Schematic of the formation of a Peierls instability in a 1D chain of atoms showing (a) a chain of atoms giving rise to the energy distribution of a metal and (b) a periodically modulated chain giving rise to the gapped energy distribution of the ordered state. Figure reproduced with permission from reference [57] .

transition temperature T_P.

A theoretical picture of the ordered phase is achieved by applying periodic lattice displacements of $\mathbf{Q} = 2k_{\mathrm{F}}$ to the Fröhlich Hamiltonian which describes the interaction between an electron and the lattice [58],

$$H = \sum_{\mathbf{k}} E_{\mathbf{k}} a^{\dagger}_{\mathbf{k}} a_{\mathbf{k}} + \sum_{\mathbf{Q}} \hbar\omega_{\mathbf{Q}} b^{\dagger}_{\mathbf{Q}} b_{\mathbf{Q}} + \sum_{\mathbf{k},\mathbf{Q}} g_{\mathbf{Q}} a^{\dagger}_{\mathbf{k}+\mathbf{Q}} a_{\mathbf{k}} (b^{\dagger}_{-\mathbf{Q}} + b_{\mathbf{Q}}), \tag{2.28}$$

where $a^{\dagger}$ and $b^{\dagger}$ are creation operators for the electron and phonon respectively and g is an electron-phonon coupling constant [59]. This system becomes unstable towards lattice distortion, referred to as a Peierl's instability, where the displacement condition is met. This can be seen by considering the response of the charge density $\rho(\mathbf{R})$ to an external perturbation in 1D,

$$\rho(\mathbf{R}) = \int_{\mathbf{Q}} \rho(\mathbf{Q}) \mathrm{e}^{i\mathbf{Q}\cdot\mathbf{R}} d\mathbf{Q}, \tag{2.29}$$

which is related to the perturbing potential $\phi(\mathbf{Q}) = \rho(\mathbf{Q})/\chi(\mathbf{Q})$ where $\chi(\mathbf{Q})$ is the Lindhard response function,

$$\chi(\mathbf{Q}) = \int \frac{f_{\mathbf{k}} - f_{\mathbf{k}+\mathbf{Q}}}{E_{\mathbf{k}} - E_{\mathbf{k}+\mathbf{Q}}} \frac{d\mathbf{k}}{(2\pi)^d}. \tag{2.30}$$

The response becomes large when an external perturbation is applied with period $\mathbf{Q} = 2\mathbf{k}_{\mathrm{F}}$. The Lindhard function is also strongly temperature dependent due to its relationship to the Fermi function.

The lattice distortion having periodicity of $2k_F$ can be incommensurate to the underlying lattice and in reality can exist in 2 and 3D systems where the condition $E(k+\mathbf{Q}) = -E(k)$ is met. In antiferromagnetic systems, elastic distortion of the lattice can also occur but it is necessary to account for the exchange coupling of the spins in the lattice. A magnetoelastic ordering can occur because the lattice distortions modify the spin Hamiltonian. To account for this, we add a spin-phonon coupling term to the Heisenberg Hamiltonian which gives rise to a spin-Peierls (SP) transition [60]. In systems with AFM exchange coupling the theoretical basis for the SP transition is more complex due to interactions between pseudo-fermions [61].

As shown in Eqn. 2.28 the electronic response of the system to the instability is considered to be coupled to the underlying lattice via electron-phonon coupling, hence, the phonon spectra exhibits a Kohn anomaly in the presence of a CDW. The response of the phonon is seen by considering the equation of motion of a chain of atoms with coordinate R and mass M at a given wavevector $\mathbf{Q}$ [56],

$$\ddot{R}_{\mathbf{Q}} = -\omega_{\mathbf{Q}}^2 R_{\mathbf{Q}} - g\left(\frac{2\omega_{\mathbf{Q}}}{M\hbar}\right)^{1/2}, \tag{2.31}$$

where the second term contains the phonon coupling constant g for a phonon with frequency $\omega_{\mathbf{Q}}$. In the presence of the response function $\chi(\mathbf{Q},T)$ the charge density of the phonon $\rho_{\mathbf{Q}}$ and hence also the frequency $\omega_{\mathbf{Q}}$ must be renormalised,

$$\rho_{\text{norm}}(\mathbf{Q},T) = \chi(\mathbf{Q},T)g\left(\frac{2M\omega_{\mathbf{Q}}}{\hbar}\right)^{1/2} R_{\mathbf{Q}}, \tag{2.32}$$

$$\omega_{\text{norm}}(\mathbf{Q},T) = \omega_{\mathbf{Q}}^2 + \chi(\mathbf{Q},T)\frac{2g^2\omega_{\mathbf{Q}}}{\hbar}. \tag{2.33}$$

In practice, this renormalisation results in a temperature-dependent softening of the coupled phonon mode around $\mathbf{Q} = 2\mathbf{k}_F$.

In general, the theoretical basis and resulting ordered state of the CDW phase has a number of similarities to superconductivity. In both, the total energy of the system is reduced resulting in a gap at the Fermi energy. In the case of superconductivity the gap arises due to electron-electron pairing and in the case of the CDW phase it arises due to electron-hole pairing.

2.5.2 Spin density wave order

A spin-density wave is an equivalent periodic modulation in the spin density of the valence electrons. Overhauser was the first to demonstrate that the paramagnetic state of an electron gas is unstable to the creation of a spin density wave phase [62]. An SDW ground state forms when exchange interactions, driven by a sufficiently large U, fulfil the Stoner criterion $\chi^0(\mathbf{Q})U = 1$.

The total susceptibility can be expressed in relation to the paramagnetic susceptibility χ_P as,

$$\chi(\mathbf{Q}) = \frac{\chi_P f(\mathbf{Q}/2k_F)}{1 - U(E_F) f(\mathbf{Q}/2k_F)}. \tag{2.34}$$

If $\mathbf{Q} = 0$, the system is ferromagnetic, for commensurate wavevectors, $\mathbf{Q} = \pi/a$, it is antiferromagnetic and for incommensurate wavevectors, $\mathbf{Q} = 2k_F$, the ground state is a SDW. In this case, a Kohn anomaly appears in the susceptibility leading to a periodic modulation of the magnetisation of $2\pi/\mathbf{Q}$. A gap can open at the Fermi surface and reduce the energy of the system, making it unstable to the creation of an SDW [63].

SDW order can be driven by Fermi surface nesting in which one part of the Fermi surface can be directly translated onto another with wavevector $\mathbf{Q}$. A gap can form in the nested region and a spin-density wave is created with wavector $\mathbf{Q}$ [64].

Despite the different microscopic origins, a periodic modulation in spin density manifests in a similar way to the CDW, both are related to the Peierls instability which opens a gap at the Fermi surface. However with SDW it is necessary to consider the difference between the spin density of up and down polarised spins $\rho_\uparrow$ and $\rho_\downarrow$ which are out of phase by π. The total modulation in spin density is therefore given by,

$$\rho_\pm(x) = \frac{\rho_0}{2}(1 \pm \rho_1 \cos(\mathbf{Q}x)), \tag{2.35}$$

where ρ_0 is the constant component and ρ_1 is a modulated component of the spin density [65].

2.5.3 Competition with superconductivity

Interest in the role of competing charge ordered phases in HTS arose following the observation of a dip in the superconducting transition temperature of LBCO [66]. To explain this it was proposed that the spin and charge are arranged in a modulated order in which the AFM occurs in static stripes separated by domain walls which contain the majority of the charge carriers [67, 68]. Theoretical models of this state suggest that it is associated with a separated charge and spin density wave phase. Incommensurate charge and spin Bragg peaks are clear signatures of these phases and are observed with neutron diffraction in $La_{1.6-x}Nd_{0.4}Sr_xCuO_4$ at a doping level associated with anomalous suppression of the superconductivity [69]. Fig. 2.5 (c) and (d) show the signatures of the spin and charge order detected with neutron scattering [69].

Signatures of stripe order were also observed in LBCO with neutron diffraction and it was later found that the stripe phase occurs at temperatures below a structural transition from orthorhombic to tetragonal symmetry [70]. This transition is associated with anisotropy between the a and b axes which is believed to be the mechanism that pins the stripe order to the lattice.

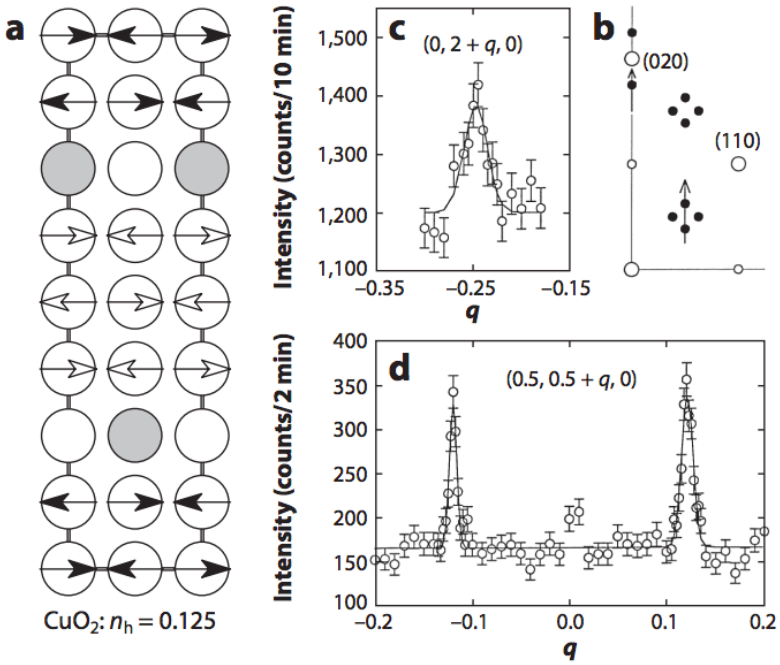

Figure 2.5: Details of stripe order in cuprates showing (a) the real space organisation of Cu sites (circles) in the $a-c$ axis of cuprate materials. The location of charge from doped holes is shown in grey and spins are indicated with arrows. Panel (b) shows the resulting location of charge and spin Bragg positions in the reciprocal lattice and panels (c) and (d) show the signatures of the charge and spin order detected with neutron scattering [69]. Figure reproduced with permission from reference [72].

Fig. 2.5 (a) shows the real space organisation of charge and spins on the Cu sites in stripe ordered cuprates and (b) shows the resulting location of charge and spin Bragg positions in the reciprocal lattice. The stripes are seen to align along the Cu-O bond direction which alternate in orientation between CuO_2 layers in the c-axis. This rotation leads to superposition of the order which prevents interlayer coupling and inhibits phase coherence. It has been hypothesised that this is the mechanism which suppresses the superconductivity [71].

Charge ordered phases were thought to be confined to the La-based family of cuprates until relatively recently when quantum oscillations measurements identified signatures of charge density wave order in the Fermi surface of $YBa_2Cu_3O_{6.5}$ [73]. Small Fermi surface pockets were identified which correspond to Fermi surface reconstruction by a CDW. A CDW phase was identified by x-ray diffraction which is considered to be the source of reconstruction in the Fermi surface [74].

CDW phases have been observed in many other cuprate materials [75, 76, 77, 78, 79, 80] as well as pnictide [81, 82] and heavy fermion [83] superconductors. Due to the observation of CDW order in many high-T_c materials and their co-existence with superconductivity at low temperatures, the question of competition between ordered phases has been widely considered [76]. The characteristics of the CDW order in YBCO have been measured with a range of

techniques at different temperatures and magnetic fields. However, the exact nature of the phase remains an open question which is discussed further in Chapter 6.

2.6 Cuprates

This thesis focuses on the cuprate family of superconductors which are among the most well studied of the HTSs. The proximity of the superconducting phase to antiferromagntism and charge order makes them useful to investigate the effect of spin and charge fluctuations. This section briefly introduces the family and relates the theories of superconductivity to observations in cuprates.

The properties of cuprate materials have also been extensively studied in the normal state [19]. Cuprates exhibit strong temperature dependence in electrical resistivity $\rho(T)$ measured parallel to the copper-oxide planes. In underdoped and optimally doped cuprates ($x \leqslant 0.15$) a large linear dependence, $\rho(T) \propto T$, extends even beyond the transition temperature. With doping, the T dependence gradually changes to T^2. According to the Weidemann-Franz (WF) law the ratio of thermal and electrical conductivities must be proportional to T. Therefore, this anomalous temperature dependence, relating to the quasiparticle scattering rate τ^{-1}, suggests that part of the doped phase is fundamentally incompatible with Fermi liquid theory [84]. Additionally, significant directional anisotropy has been observed in the $\rho(T)$ of layered cuprates when measured perpendicular and parallel to the copper oxide planes [85] again violating Fermi liquid theory.

2.6.1 Physical properties

Cuprates form a layered structure with distinctive CuO_2 planes, typically intercalated with rare earth elements. Electronic interactions within the CuO_2 planes are many orders of magnitude stronger than the inter-plane interactions leading to an essentially 2D nature. Every Cu^{2+} ion has four in-plane O^{2-} neighbours in a square plaquette as shown in Fig. 2.6 (a). The resulting nuclear Brillouin zone is indicated with a solid line in Fig. 2.6 (b). The magnetic Brillouin zone is defined as the repeating unit of the aligned spins as indicated with the dashed line in Fig. 2.6 (b). The intercalated elements provide dopants which control the net charge in the system, adjusting the valence of the Cu^{2+} ion and provide the charge carriers necessary to induce superconductivity.

Many of the interesting properties of the cuprates come from the character of holes in the Cu3d and O2p bands. The electronic configuration of the Cu^{2+} ions $3d^9$ is shown in Fig. 2.7 (a) where the crystal field splitting of the electron states is given by the O2p orbital resulting in a half

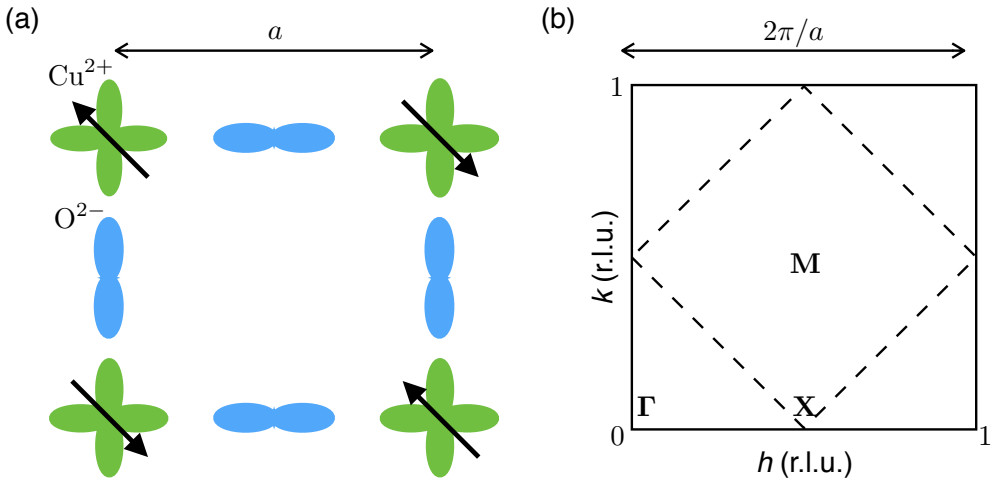

Figure 2.6: Structural properties of the hole doped cuprates showing (a) the location of the Cu^{2+} and O^{2-} ions in the CuO_2 plaquette and the orientation of the Cu^{2+} spins and (b) the resulting Brillouin zone (BZ) in reciprocal lattice units, indicating the structural BZ with a solid line and the magnetic BZ with a dashed line.

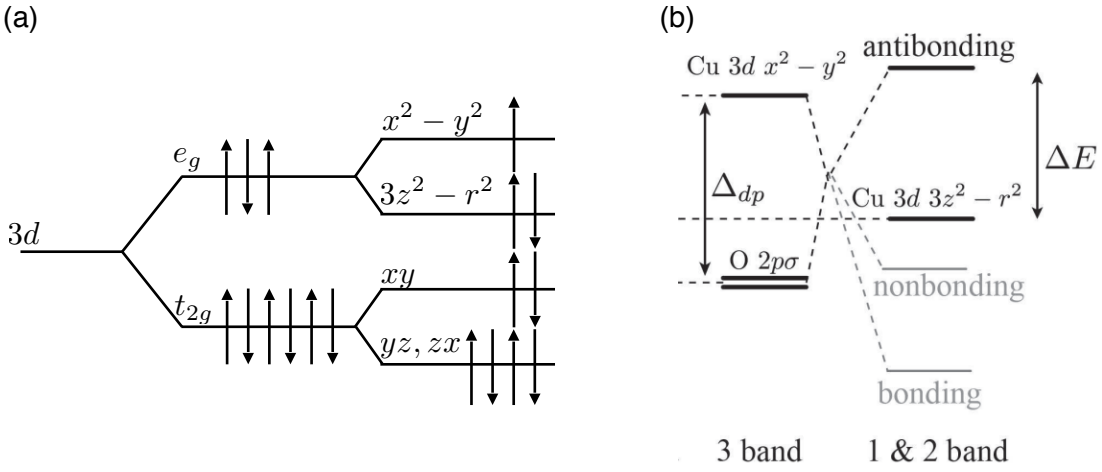

Figure 2.7: Electronic properties of the hole doped cuprates showing (a) the energy levels produced by crystal field splitting of the Cu^{2+} orbitals and (b) the energy levels produced by hybridisation with the O2p orbitals, figure reproduced with permission from reference [86].

filled $d_{x^2-y^2}$ band. All of the even, and some odd orbitals of Cu3d and O2p are hybridised due to the formation of bonding and antibonding molecular orbitals. The hybridisation of the Cu3d and O2p orbitals removes the degeneracy of the states and reduces the spherical symmetry. Fig. 2.7 (b) shows the energy level of the hybridised orbitals in a 1, 2 and 3 band picture based on the Hubbard model [86]. More details of the orbital states in La_2CuO_4 and their characterisation with RIXS are given in Chapter 4.

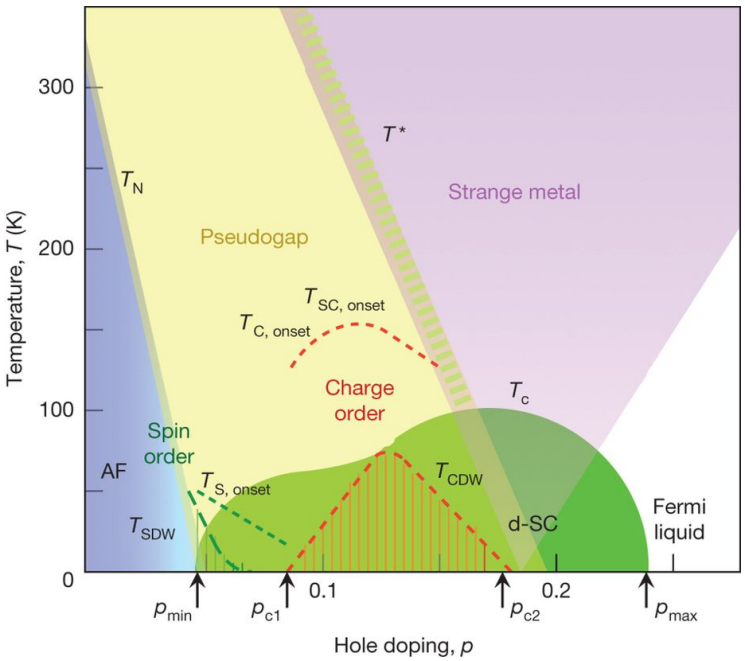

Figure 2.8: The generic phase diagram of the hole doped cuprates. Figure reproduced with permission from reference [87].

2.6.2 The cuprate phase diagram

The resulting phases and their properties are summed up in the phase diagram of the hole-doped cuprates, a generic example of which is shown in Fig. 2.8. It is clear that superconductivity in the cuprates exists alongside a number of other phases. The extent to which superconductivity competes with or is driven by these other phases has become a significant question in the search for an explanation for HTS pairing.

Antiferromagnetism

With one unpaired electron in the $d_{x^2-y^2}$ orbital, the single-electron model incorrectly predicts a metallic state in the undoped cuprates. The insulating state is in fact favoured due to electron-electron interactions. It is generally accepted that the energy gain t from adding a second electron is resisted by the strong on-site Coulomb repulsion U which results in a Mott insulating state [47, 88, 89, 90, 91]. Some theories of HTS suggest that the interactions are not strong enough to induce a Mott transition and therefore assume the insulating state is itself induced by AFM order [92].

AFM order occurs in undoped cuprates due to exchange processes between Cu^{2+} ions with spin-1/2 via the non-magnetic oxygen orbitals. Mixing of the atomic orbitals allows the indirect exchange of kinetic energy [35] which results in an AFM state below the Néel transition temperature, typically around 300 K. Fig. 2.6 shows the orientation of the spins along [110]

direction. Further details of the origin of the AFM state of La_2CuO_4 and its description via a 2D Heisenberg model are given in Chapter 4.

Spin fluctuations from the AFM state have been extensively measured in cuprate materials with the aim of revealing the exact nature of the ground state. Of particular interest is the persistence of these spin fluctuations into the superconducting states despite the complete suppression of Néel order.

Superconducting state

The suppression of the AFM state with doping, p, results in the emergence of a superconducting dome between $0.05 \lesssim p \lesssim 0.26$. The temperature and doping dependence of the dome has been carefully mapped with transport measurements demonstrating the strong doping dependence of T_c. The peak of the dome at $p \simeq 0.16$ is referred to as optimally doped, compositions with $p < 0.16$ are underdoped and those with $p > 0.16$ are overdoped. With the increased addition of charge carriers with doping beyond $p \simeq 0.26$ the superconductivity is eventually destroyed.

Charge order

Charge density wave order is now considered a near ubiquitous feature of the cuprate phase diagram[70, 75, 74, 76, 77, 78, 79, 80], therefore detailed measurements of the charge fluctuations are desirable to characterise their relationship with the superconducting phase. Chapter 6 contains further discussion of the charge order in YBCO and details of our RIXS measurements on the compound.

Quantum criticality

Several different states are observed in cuprates above the superconducting transition temperature, including strange metal, Fermi liquid and pseudogap phases. Smooth transitions are observed between all of these phases and recent work has hypothesised that the intersection of the pseudogap and Fermi liquid phase is a quantum critical point (QCP) below the superconducting dome. Quantum criticality refers to phase transitions which occur at 0 K. At zero temperature, fluctuations associated with the phase transition must be quantum in nature because their characteristic energy will always be greater than the classical thermal energy. Attempts have been made to understand this via transport measurements performed in high magnetic fields to suppress the superconductivity and reveal the underlying behaviour [93, 94]. Close to optimal doping the normal state is characterised by a marginal Fermi-liquid

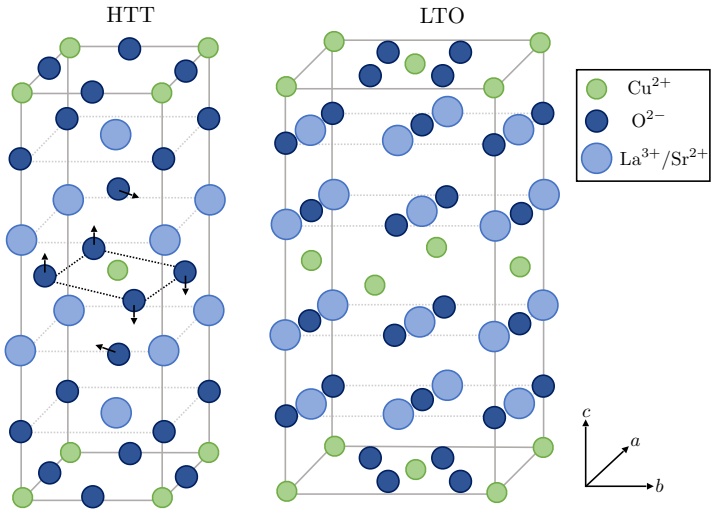

Figure 2.9: The crystal structure of La_2CuO_4 showing (left) the high-temperature tetragonal phase with spacegroup $I4/mmm$ and (right) the low-temperature orthorhombic phase with spacegroup $Bmab$.

state referred to as a strange metal. The state exhibits behaviour similar to a regular Fermi gas coupled to strongly-temperature dependent excitations resulting in T-linear resistivity. It has been suggested that the strange behaviour of this state could be driven by the QCP [94]. Beyond a critical amount of doping the superconductivity is fully suppressed and the normal Fermi liquid state re-emerges.

2.6.3 $La_{2-x}Sr_xCuO_4$

The first cuprate material studied in this thesis is La_2CuO_4 (LCO) which exhibits superconductivity when doped with Sr, forming $La_{2-x}Sr_xCuO_4$ (LSCO). The superconducting phase is observed on cooling LSCO below $T_c = 39$ K for optimally doped compositions. LSCO is referred to as single layer due to the repetition of the crystal structure between all CuO_2 layers as shown in Fig. 2.9 and for this reason is often considered one of the cuprate materials with the simplest structure.

Undoped LCO displays antiferromagnetism below a Néel temperature of $T_N \simeq 325$ K [95]. The undoped compound also undergoes a structural transition to a low temperature orthorhombic (LTO) phase below $T_{\mathrm{LTO}} \simeq 525$ K. The LTO phase is further suppressed with doping before totally disappearing at $x = 0.21$. The phase transition is driven by condensation of the zone-boundary phonons resulting in the CuO_6 octahedra rotating around the orthogonal axis as indicated by the arrows in Fig. 2.9 (left) [96]. In this thesis the high-temperature tetragonal (HTT) crystal structure notation has been used to allow comparison between different compounds. The lattice constants for the HTT structure of LCO are $a_t = b_t = 3.80$ Å and $c_t = 13.117$ Å at $T = 10$ K [97]. Cooling through the structural transition can result in two equally likely struc-

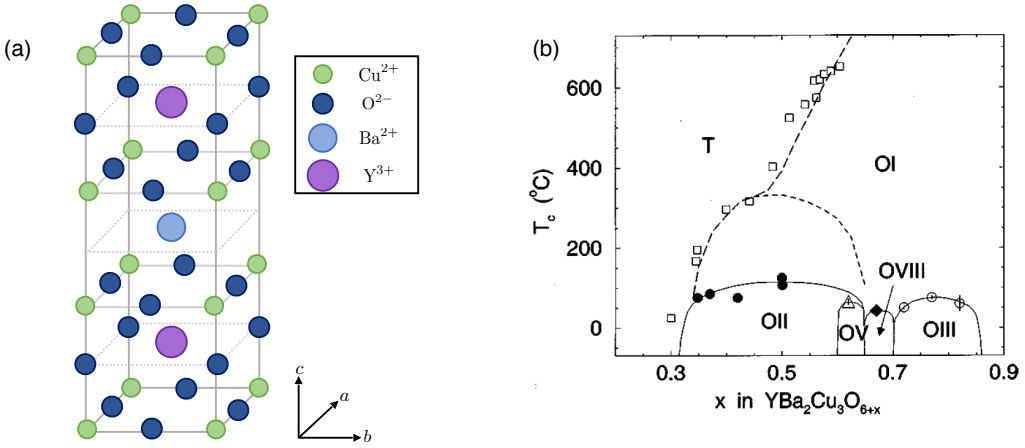

Figure 2.10: The crystal structure of $YBa_2Cu_3O_{6+x}$ showing (a) the structure at $x = 0$ where the structure is tetragonal with spacegroup $P4/mmm$ and (b) the structural phase diagram reproduced with permission from reference [100] .

tures where a and b are reversed. As a result, orthorhombic LCO is often twinned as sections of the crystal contain either the a or b orientation separated by defined domain boundaries [98]. LCO crystals can be de-twinned by cooling through the transition under uniaxial pressure along one of the orthorhombic directions [99]. Magnetic measurements in combination with neutron diffraction have confirmed that superconductivity persists in both the HTT and LTO structural phases and the transition between phases does not seem to have an effect on the superconducting transition temperature [97].

2.6.4 $YBa_2Cu_3O_{6+x}$

$YBa_2Cu_3O_{6+x}$ (YBCO) is both more complex than LCO structurally, having an alternating layered structure, and more complex in its structural phase diagram. At $x = 0$, the crystal structure is tetragonal with alternating Y and Ba ions intercalating the CuO_2 planes as shown in Fig. 2.10. A Cu-O chain structure is observed along the b axis with periodicity ma which acts as a charge-reservoir providing holes to the CuO_2 planes [100]. Four different chain superstructures are observed depending on the amount of oxygen, x. At low oxygen stoichiometry, the structure remains tetragonal up to doping $x = 0.35$ where it transitions to one of several orthorhombic structures depending on x and T: ortho-II with $m = 2$, ortho-III with $m = 3$, ortho-V with $m = 5$ and ortho-VIII at $m = 8$. Fig. 2.10 (b) shows the structural phase diagram of YBCO.

The lattice parameters for orthorhombic YBCO at $x = 0.67$ (the composition measured in

this thesis) and $T = 2\ K$ are approximately $a \simeq 3.81$ Å, $b \simeq 3.87$ Å, $c \simeq 11.72$ Å [76]. Optimally doped YBCO has a transition temperature $T_c = 93$ K.

Chapter 3

Resonant inelastic x-ray scattering

The significant progress made in resonant inelastic x-ray scattering (RIXS) in the past ten years has brought it into the range of experimental techniques able to make detailed studies of elementary excitations. The rapid improvement in energy resolution and an increase in the availability of high-brilliance x-ray radiation now allows RIXS experiments to measure a wide range of energy transfers with both energy and momentum resolution. Such improvements allow RIXS experiments to be performed in areas where inelastic neutron scattering (INS) was previously the only tool available, giving advantages such as tolerance of smaller sample sizes and potentially faster count rates. However, RIXS remains a relatively new approach in comparison to INS, which makes detailed comparison of the two techniques desirable.

RIXS emerged as an extension of Raman scattering where the measurement of small energy transfers from materials with optical light was extended to the x-ray regime [101]. The availability of tunable x-ray sources at synchrotron facilities in the 1970's introduced the possibility of x-ray Raman as a probe of excitations, and studies in materials such as copper proved the effectiveness of the technique [102, 103]. The principal limitation of these early RIXS experiments was the energy resolution, limited by the intensity of the tunable x-ray source and the instrumentation required to resolve scattered photons. Improvements in both of these areas have been significant over the past 15 years [104]. As a result, RIXS at the Cu-L_3 edge has been well established as an ideal probe of excitations in the copper-oxides sparking a renewed interest in the magnetic and charge excitations of cuprates [105, 106, 107, 108, 109, 110, 111, 112].

This chapter provides an introduction to the RIXS technique. It introduces the RIXS scattering mechanism with a particular focus on processes at the Cu-L_3 edge in cuprates and briefly considers ongoing questions related to the RIXS cross-section. In section 3.3 details are provided of a typical new soft x-ray RIXS beamline using the I21 spectrometer at Diamond Light Source

as an example.

3.1 Theoretical outline

In an x-ray scattering experiment, the intensity of photons scattered from a sample are measured as a function of incident and scattered momentum, $\mathbf{k}$ and $\mathbf{k}'$, and incident and scattered energy, E and E'. The energy transfer between the photon and the system is defined as,

$$\hbar\omega = E - E' = c\,|\mathbf{k}| - c\left|\mathbf{k}'\right|, \tag{3.1}$$

and the momentum transfer is,

$$\mathbf{Q} = \mathbf{k} - \mathbf{k}'. \tag{3.2}$$

Here $\mathbf{Q}$ is the scattering vector which is also defined in relation to the crystal axes of the sample,

$$\mathbf{Q} = h\mathbf{a}^* + k\mathbf{b}^* + l\mathbf{c}^*, \tag{3.3}$$

where $\mathbf{a}^* = 2\pi/a$ etc. in reciprocal lattice units (r.l.u.).

The scattering cross-section, σ, describes the total number of photons which scatter from a sample in relation to the incident flux Φ. The differential scattering cross-section, $d\sigma/d\Omega$, is a useful measure of the number of scattering events which occur within a solid angle Ω. The partial differential cross-section also considers the final energy of the photon, $d^2\sigma/d\Omega dE_f$. It can be defined in terms of the dynamic structure factor $S(\mathbf{Q},\omega)$ which describes the materials' response to the probe,

$$\frac{d^2\sigma}{d\Omega dE} = \frac{k'}{k} S(\mathbf{Q},\omega). \tag{3.4}$$

RIXS is an example of photon-out spectroscopy technique in which the energy and momentum transfer from a material can be measured. Resonance refers to the fact that the incident energy is tuned to the excitation edge of a chosen element in the material, enhancing the x-ray cross section and providing a site specific probe of the excitations. RIXS sees excitations over a wide energy transfer range which yields information about energy, momentum and polarization.

In the RIXS process, as described above, an x-ray photon interacts with a sample in initial state $\mathbf{k}$ and excites it into final state $\mathbf{k}'$. The process can be associated with a transfer of energy from the photon to the sample $\hbar\omega = \hbar\omega_{\mathbf{k}} - \hbar\omega_{\mathbf{k}'}$ and a transfer of angular momentum resulting in a change of polarisation from ϵ to ϵ'. This energy and angular momentum is transferred to the sample, leaving it in an excited state, therefore the scattering process directly probes the excitations. Fig. 3.1 shows a schematic of the RIXS process showing the incoming and outgoing photons relative to the core and valence bands and the resulting valence excitation.

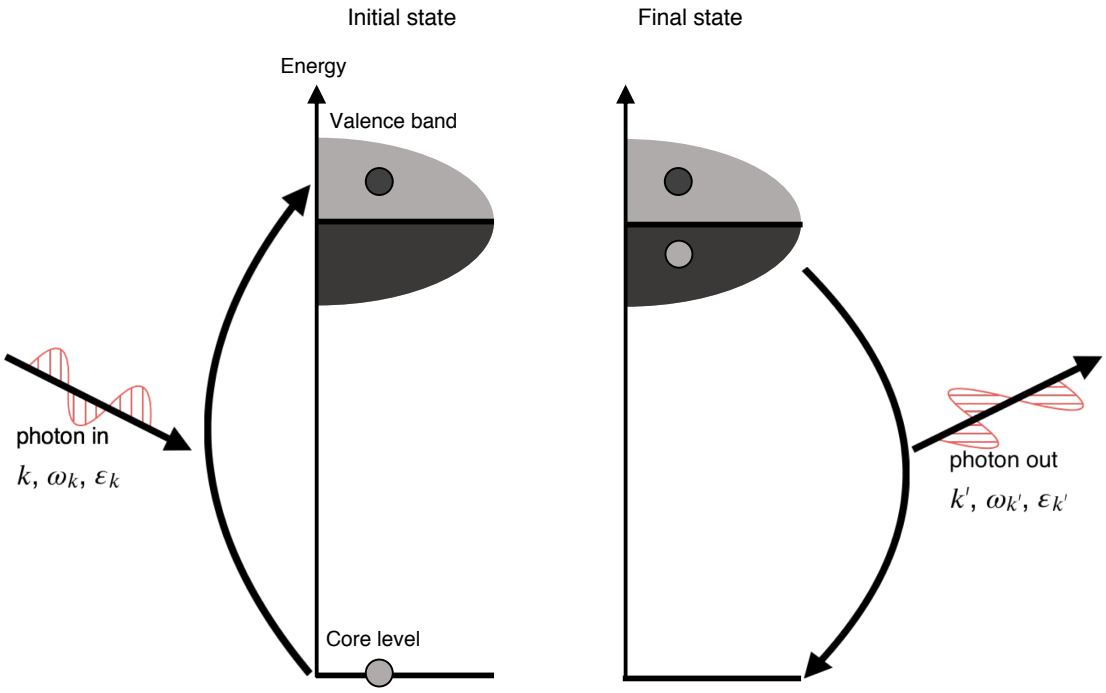

Figure 3.1: Schematic of the direct RIXS process. An incoming photon excites an electron to the valence band then an electron from the occupied state returns to the core level, emitting a photon, leaving a final excited state. Figure is based on reference [104]

.

3.1.1 The Kramers-Heisenberg dispersion formula

Generic calculations of the scattering amplitude in spectroscopic x-ray techniques come from the Kramers-Heisenberg formula. The formula accounts for the interaction of a photon's electromagnetic field with the material it is probing. Reference [113] describes these interactions and derives the Kramers-Heisenberg formula for various scattering techniques with a particular focus on the interaction with magnetic materials. In RIXS, the initial energy, E describes the system in a ground state g with energy E_g and the final state energy E' describes the system in final state f with energy E_f. The RIXS intensity I_{raw} can be expressed in terms the ground and final state energies and a scattering amplitude $\mathscr{F}$,

$$I_{\text{raw}}\left(\mathbf{k},\mathbf{k}',\boldsymbol{\epsilon},\boldsymbol{\epsilon}',\omega_{\mathbf{k}},\omega_{\mathbf{k}'}\right)=\sum_f\left|\mathscr{F}_{f,g}\left(\mathbf{k},\mathbf{k}',\boldsymbol{\epsilon},\boldsymbol{\epsilon}',\omega_{\mathbf{k}},\omega_{\mathbf{k}'}\right)\right|^2\times\delta\left(E_f+\hbar\omega_{\mathbf{k}'}-E_g-\hbar\omega_{\mathbf{k}'}\right). \tag{3.5}$$

The scattering amplitude describes which excitations are probed as a function of wavevector, polarisation and energy. In this section we will discuss the scattering amplitude in RIXS following the derivation by Ament *et al.* in reference [104].

The Kramers-Heisenberg formula is derived by applying a second order perturbation to the studied system, describing both the perturbation due to the creation of a hole in the core level and due to the emission of a photon and return to the ground state. For this purpose we

construct a Hamiltonian H describing a system of N electrons which is split into an electron-photon interaction part H' and a non-interacting part H_0 then treat H' as a perturbation to H_0.

The general Hamiltonian H can be written in terms of the interaction of individual electrons i with an electromagnetic field with vector potential $\mathbf{A}(\mathbf{r})$,

$$\begin{aligned} H = \sum_i^N \Bigg(& \frac{\left[\mathbf{p} + e\mathbf{A}(\mathbf{r})\right]^2}{2m} - e\phi(\mathbf{r}) + \frac{e\hbar}{2\left[2mc\right]^2}\boldsymbol{\sigma} \cdot \left[\mathbf{E}(\mathbf{r}) \times \left\{\mathbf{p} + e\mathbf{A}(\mathbf{r})\right\} - \left\{\mathbf{p} + e\mathbf{A}(\mathbf{r})\right\} \times \mathbf{E}(\mathbf{r})\right] \\ & + \frac{e\hbar}{2m}\boldsymbol{\sigma} \cdot \mathbf{B}(\mathbf{r})\Bigg) + \frac{e\hbar^2\rho(\mathbf{r})}{8(mc)^2\epsilon_0} + \sum_{\mathbf{k},\boldsymbol{\epsilon}} \hbar\omega_{\mathbf{k}} \left(a^\dagger_{\mathbf{k},\boldsymbol{\epsilon}} a_{\mathbf{k},\boldsymbol{\epsilon}} + \frac{1}{2} \right), \end{aligned} \tag{3.6}$$

where $\mathbf{p}$ and $\mathbf{r}$ are momentum and position operators and $\boldsymbol{\sigma}$ are the Pauli matrices for electron i. The first term is the kinetic energy of the electrons in relation to the electromagnetic field. The second term is the Coulomb repulsion given by the electric potential $\phi(\mathbf{r})$. The third term is spin-orbit coupling due to photon electric field $\mathbf{E}(\mathbf{r}) = -\nabla\phi - \frac{\partial \mathbf{A}(\mathbf{r})}{\partial t}$. The fourth term is Zeeman splitting in the presence of the photon magnetic field $\mathbf{B}(\mathbf{r}) = \nabla \times \mathbf{A}(\mathbf{r})$. The fifth term is the Darwin term which smears out the electrostatic interaction between the electron and the nucleus over short distances, hence only applying for s orbitals. The sixth term describes the creation $a^\dagger$ and annihilation a of photons in initial state $\mathbf{k}$ with energy $\hbar\omega_{\mathbf{k}}$ and polarisations ϵ. This Hamiltonian is valid in the case of non-relativistic photons and in the limit where the photon and electron potentials are small compared to the electron mass.

The non-interacting Hamiltonian H_0 is constructed from the terms in H which do not contain $\mathbf{A}(\mathbf{r})$ and the remaining interacting terms give H'. The RIXS process is described by a transition from the ground state wavefunction $\left|g\right\rangle$ to a final state $\left|f\right\rangle$, both of which are eigenstates of H_0. Fermi's golden rule allows us to write the transition rate w in terms of these states for a range of intermediate states $|n\rangle$,

$$w = \frac{2\pi}{\hbar} \sum_f \left| \left\langle f \right| H' \left| g \right\rangle + \sum_n \frac{\left\langle f \right| H' \left| n \right\rangle \left\langle n \right| H' \left| g \right\rangle}{E_g - E_n} \right|^2 \times \delta(E_f - E_g). \tag{3.7}$$

The first term generally dominates except when the energy of state n, E_n, is close to the ground state energy, E_g, for example when the incoming photon energy $\hbar\omega_{\mathbf{k}}$ is close to an absorption edge in the material. In this case the incoming photon creates a core hole and the second order terms are greatly enhanced. Hence, terms in H' which are quadratic in $\mathbf{A}$ give rise to first order perturbations which result in nonresonant scattering and terms linear in $\mathbf{A}$ give rise to second order perturbations, resulting in resonant scattering. This resonant enhancement was first observed in x-ray magnetic scattering measurements by Gibbs *et al.* [114] and has since been used to enhance magnetic signals in a range of x-ray techniques [115, 116].

In RIXS, the resonant part of the scattering amplitude is expanded to include an intermediate state lifetime broadening Γ which accounts for non-radiative processes which shorten the lifetime of the core hole. Considering only this resonant part, the double differential cross-section is obtained from the density of states in solid angle $d\Omega$ which allows Eqn. 3.5 to be re-expressed as,

$$I_{\text{raw}}\left(\mathbf{k},\mathbf{k}',\boldsymbol{\epsilon},\boldsymbol{\epsilon}',\omega_{\mathbf{k}},\omega_{\mathbf{k}'}\right) = \left(\frac{e^2}{4\pi\epsilon_0 m_e c^2}\right)^2 m_e^2 \omega_{\mathbf{k}'}^3 \omega_{\mathbf{k}} \sum_f |\mathscr{F}_{f,g}\left(\mathbf{k},\mathbf{k}',\boldsymbol{\epsilon},\boldsymbol{\epsilon}',\omega_{\mathbf{k}},\omega_{\mathbf{k}'}\right)|^2 \times \delta\left(E_f + \hbar\omega_{\mathbf{k}'} - E_g - \hbar\omega_{\mathbf{k}'}\right). \tag{3.8}$$

Where the Kramers-Heisenberg scattering amplitude is,

$$\mathscr{F}_{f,g}\left(\mathbf{k},\mathbf{k}',\boldsymbol{\epsilon},\boldsymbol{\epsilon}',\omega_{\mathbf{k}},\omega_{\mathbf{k}'}\right) = \sum_n \frac{\left\langle f\right|\mathscr{D}'^{\dagger}\left|n\right\rangle\left\langle n\right|\mathscr{D}\left|g\right\rangle}{E_g + \hbar\omega_{\mathbf{k}} - E_n + i\Gamma}, \tag{3.9}$$

where $\mathscr{D}$ is a transition operator for the RIXS cross-section. For soft x-ray RIXS experiments we can make the dipole approximation because the wavelength of incident photons is much greater than the inter-atomic spacing, so the transition operator is expressed as,

$$\mathscr{D} = \boldsymbol{\epsilon} \cdot \sum^{N} \mathrm{e}^{i\mathbf{k}\cdot\mathbf{R}}\mathbf{r}, \tag{3.10}$$

where $\mathbf{R}$ is the distance from the electron to the ionic core.

A more complex approach is needed in the hard x-ray limit where a multipole expansion is required. The Kramers-Heisenberg dispersion formula in Eqn. 3.9 is valid in the case of direct RIXS processes, however, in indirect RIXS we must add an additional term for the core hole as excitations occur due to Coulomb interactions between the core hole and the valence electrons. This thesis deals only with direct RIXS processes, hence Eqn. 3.9 is valid.

3.1.2 The RIXS cross-section

Solving the Kramers-Heisenberg formula for real systems is a complex problem requiring the eigenstates and eigenvalues for the ground, intermediate, and final states to be evaluated [117]. Significant work has been directed at achieving this in the cuprates in order to isolate prefactors to the RIXS cross-section.

Exact diagonalisation methods in doped cuprates are highly complex as a large number of possible configurations of the basis exist when electron correlations are considered. Kotani and Shin [118] review efforts to characterise the cross-section through exact diagonalisation with increasing levels of electron correlations up to transition metal compounds.

In the antiferromagnetic cuprate parent compounds, the cross-section at the Cu L-edge can be evaluated by a single ion model in which transitions are calculated between the $2p^6 3d^9$ and

$2p^5 3d^{10}$ states [106, 119]. The transition must account for Coulomb effects, spin-orbit coupling and crystal-field splitting and are calculated on the basis of the surrounding oxygen ligands. An example of these calculations for La_2CuO_4 (LCO) is given in Chapter 4.

In doped cuprate compounds, electron correlations become significant and the single-ion model does not capture the ground state. Solving the Kramers-Heisenberg equation therefore requires more complex estimations. The work of Jia *et al.* [120, 121, 122] describes numerical evaluations of the RIXS cross-section in cuprates using exact diagonalisation (ED) techniques. Calculations in doped cuprates which capture the correlation effects remain an area of significant ongoing research which will have important consequences for the RIXS community.

3.1.3 Relationship to the structure factor

One purpose of understanding the exact nature of the RIXS cross-section is to relate the intensity of the scattered photons to the structure factor of the excitations that they create, removing effects due to the nature of the probe. The circumstances in which the RIXS cross-section can be related to the electronic structure factor $S(\mathbf{Q},\omega)$ are the subject of significant ongoing research and debate. Van den Brink *et al.* [123] first described the RIXS cross-section in terms of an intrinsic correlation function which accounts for the core-hole lifetime. They developed the ultrashort core-hole lifetime (UCL) approximation which estimates the cross-section by assuming the core-hole potential is the dominant interaction [124, 125]. In direct RIXS the intermediate state dynamics are neglected and the transition operators can be calculated.

On the basis of the UCL approximation, Ament *et al.* [104] describe the theoretical approximations within which the RIXS cross-section is believed to be proportional to S($\mathbf{Q}$, ω). In these situations it is possible to describe the RIXS scattering amplitude, which for simplicity we define I_{raw}, as being proportional to $S(\mathbf{Q},\omega)$ multiplied by a resonant prefactor f,

$$I_{\text{raw}}(\mathbf{k},\mathbf{k}',\epsilon,\epsilon') = f(\mathbf{k},\mathbf{k}',\epsilon,\epsilon')S(\mathbf{Q},\omega). \tag{3.11}$$

Both I_{raw} and f are dependent on the incoming and outgoing wavevector $\mathbf{k}$ and polarisation ϵ. Experimental Chapters 4, 5 and 6 detail attempts to characterise f in order to establish $S(\mathbf{Q},\omega)$.

In cuprates, calculations of the RIXS scattering amplitude have been tested against experimental work. In parent compounds, good agreement with calculation has been reported by taking these effects into account [126]. Calculations on doped compounds using the exact diagonalisation method [122] agree qualitatively with RIXS measurements in the cross-polarised channel, that is, where the polarisation of the photon is flipped during the scattering process from horizontal to vertical linear polarisation. The agreement is not seen in the opposite parallel

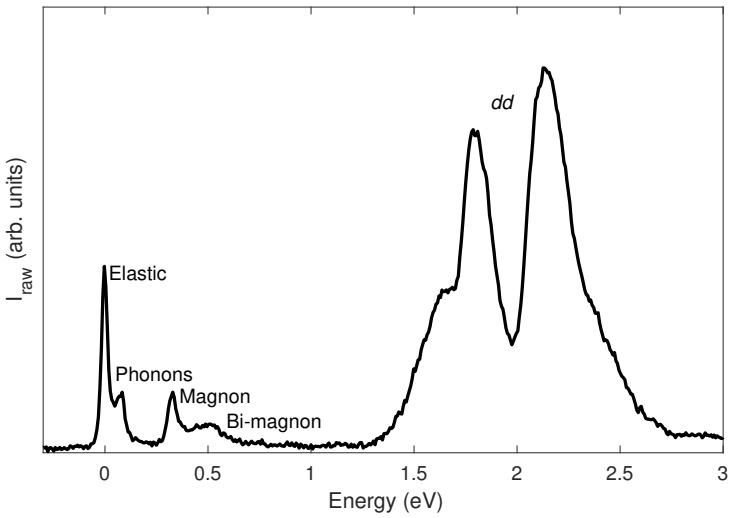

Figure 3.2: A typical RIXS spectrum measured on La_2CuO_4 at $\mathbf{Q} = (0.38, 0)(r.l.u.)$ at the Cu L_3 edge. The spectrum was measured for 10 minutes allowing a range of excitations to be measured including phonons, magnons and *dd*-excitations.

channel where the polarisation is unflipped. This suggests the UCL approximation may miss some of the excitations which can occur when $\Delta S = 0$.

3.2 Excitations

In RIXS experiments, energies transferred to the sample are measured by recording the relative energy loss experienced by the photons, hence the full range of excitations which are excited are seen in a single energy-dependent spectrum. This section gives details of some of the excitations which are captured with RIXS. Early work performed on instruments with energy resolution ΔE generally around 1 eV focused on interband excitations in insulating materials. These excitations arise due to an electron being excited into an empty conduction band and the creation of an electron-hole pair. With similar energy resolution charge transfer excitations can also be observed in metals due to charge screening of the core-hole. In recent years, energy resolutions of $\Delta E < 100$ meV have become available which has allowed a range of mid and low energy excitations to be clearly resolved [127]. A RIXS spectrum typical of the type described in this thesis is shown in Fig. 3.2 indicating the range of excitations which are resolved.

3.2.1 Orbital excitations

dd excitations are created due to the presence of a local crystal-field which splits the orbital d states in materials such as the $3d$ transition-metal oxides. In materials with half-filled d bands, unpaired electrons can be in any of the orbitals and RIXS measures a transfers of energy

between the states. The excited electron can decay into a different state and the resulting energy difference is measured as a *dd* excitation. *dd*-excitations measured with RIXS can generally be well described by considering a single-ion in a crystal-field and calculating the relative energy of the orbitals.

Tanaka and Kotani [128] made the prediction that RIXS could be used as a probe of orbital excitations in the cuprates by directly measuring the transition between $2p$ and $3d$ states. Subsequent RIXS measurements performed by Ghiringhelli *et al.* [105] in several cuprate materials verified this prediction and identified *dd* excitations due to local transitions. The excitations are broadened due to electron-hole excitations especially in the doped cuprates.

In the new RIXS measurements at the Cu L-edge of cuprate materials, *dd*-excitations are observed at approximately 2 eV. Crystal field splitting in the Cu $3d$ band is well understood and transitions between these orbitals are allowed with RIXS. The incoming photon excites an electron to a higher energy orbital where it remains bound to the core hole. The excitation produces a local exciton, hence, when it de-excites an excited state can be measured.

3.2.2 Electron-phonon coupling

Lattice vibrations can be measured with many inelastic probes. With RIXS, phonon excitations are measured where the phonon couples to an electron. The excitation can be thought of as coupling to the transient change in the samples charge distribution. Phonon excitations in RIXS are due to electron-phonon coupling at the resonant edge at the site where the scattering process occurs, hence, unlike other common probes of phonons such as IXS and Raman Scattering, the observed phonons are site-specific. RIXS also measures momentum transfer to phonon excitations as the energy of incident photons is much higher than in Raman scattering.

In $3d^9$ Cu orbitals a hole resides in the $x^2 - y^2$ orbital which is thought to be coupled to several phonons. Phonons have only recently been routinely resolved from the elastic peak in RIXS spectra as shown in the high resolution measurements of LCO performed at the Cu L-edge by Braicovich *et al.* [107]. Clearly resolved phonons are seen in the new RIXS measurements with typical energy of less than 100 meV. Devereaux *et al.* [129] make calculations of the RIXS response in the cuprates and show that three momentum dependent phonons are in principle excited at $\approx$ 10, 40 and 80 meV.

Ament *et al.* [130] describe how the electron-phonon coupling (EPC) strength can be extracted from measurements of phonons with RIXS by determining their differential cross-section. The RIXS process can also produce a "two-phonon" excitation in which two phonons with op-

posite momenta are created. The ratio of the energy of the single phonon and two-phonon excitations can also be used to extract the EPC strength M from the Fröhlich Hamiltonian which is the typical description of electron-phonon interactions,

$$H = \sum_{\mathbf{k},\mathbf{Q},\lambda} M_{\mathbf{Q},\lambda} d^{\dagger}_{\mathbf{k}-\mathbf{Q}} d_k (b^{\dagger}_{\mathbf{Q}\lambda} + b_{-\mathbf{Q}\lambda}), \tag{3.12}$$

where the electrons and phonons are described by the operators d and b respectively and λ indicates the number of the phonon branch. The theoretical work describes an expansion under the UCL approximations which proposes that the ratio of a one and two phonon intensity, $A^{(1)}$ and $A^{(2)}$ is related to the EPC strength as $A^{(2)}/A^{(1)} = \sqrt{2}M/z$, where z is a detuning factor from the resonance. Yavaş *et al.* [131] discuss how the multiple phonon excitations are suppressed due to the fast decay of the core-hole which does not allow the system to respond to changes in charge density. However, RIXS is in principle a direct probe of the EPC strength.

Ament *et al.* [130] describe a second approach to extract the EPC strength from the scattering cross-section of a single phonon. The technique, which has recently been developed and tested by Rossi *et al.* [132], involves measuring the intermediate state lifetime Γ and EPC matrix element M as a function of the detuning energy Ω. The phonon signal increases with both M and Γ and therefore the phonon scattering cross-section depends on their ratio, M/Γ. Intuitively, Γ can be thought of as the width of the Cu L_3 resonance, hence as the energy is detuned away from the resonance by an amount Ω, the available states decrease, and Γ decreases. Equally, M is extracted from the phonon intensity and is detuned with Ω. In this way, the EPC strength can be obtained when only a single phonon harmonic is detected.

Braicovich *et al.* [133] gives a detailed comparison of the two approaches to extract the EPC strength, describing how in the detuning approach, the relative intensity of a single phonon mode can be very accurately measured with the energy resolution of current advanced RIXS instruments. Obtaining the intensity of two harmonics of the same phonon is currently very difficult with RIXS as the second harmonic is strongly suppressed, however, this approach has the advantage of cancelling resonant prefactors to the phonon intensity.

3.2.3 Charge order

RIXS is fundamentally a scattering probe, however, when there is a periodic modulation such as Bragg diffraction of the lattice, enhanced elastic spectral weight is measured. This feature has been used to identify charge and spin modulations at wavevectors associated with the spacing of charge stripes [134, 135]. Recently RIXS has also been shown to have high sensitivity in detecting

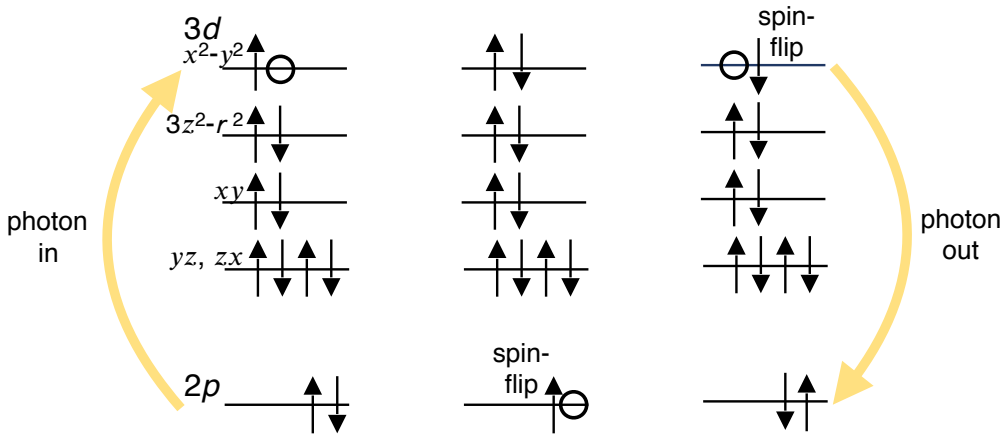

Figure 3.3: The RIXS process responsible for magnetic excitations at the Cu L_3-edge.

the short-range charge density wave or charge density fluctuations which are now believed to exist in almost all hole-doped cuprates [74, 136, 112].

In this regard, RIXS is a complementary probe to resonant x-ray diffraction which has been used to study charge density wave order in several cuprate materials [76, 77, 137, 138]. RIXS has the advantage of being able to separate inelastic contributions to the measured response and has therefore been used to extract information about the effect CDW order has on phonon excitations [74, 112]. Additionally, RIXS is more able to attribute spectral weight to the elastic intensity so can identify contributions which result purely from fluctuations in the charge density.

3.2.4 Magnetic excitations

In cuprates, magnetic excitations are collective spin-fluctuations of the antiferromagnetic state in the CuO_2 planes. The resulting measured excitations are referred to as magnons and can be thought of as eigenstates of the antiferromagnetic state. Magnetic excitations can be observed in the RIXS process by measuring a transfer of angular momentum. This is achieved indirectly by spin-orbit coupling of the intermediate core-hole state such as at the Cu L_3-edge. Photons with angular moment L = 1 can measure $\Delta L_z = 0$, 1 or 2 [139]. When an excitation takes place, the total angular momentum of the intermediate state is $j = 3/2$ and therefore orbital and spin-angular momentum can be exchanged providing a probe of excitations with total angular momentum transfer $\Delta S = 0, 1, ...$ thus providing a probe of spin-flip in the system. A schematic of this process is shown in Fig. 3.3. This transition has been studied theoretically by considering local spin operators and their selection rules to establish that a pure spin-flip transition can only occur in the $3d_{x^2-y^2}$ orbital when spin is not parallel to z [140, 141, 106, 142].

Following these predictions Braicovich *et al.* [143] were the first to measure single magnon excitations with angular momentum transfer $\Delta S = 1$ in La_2CuO_4. With improved energy resolution, many RIXS studies have since experimentally confirmed the presence of these spin-flip processes in cuprates [105, 107, 143, 120, 121, 110, 122].

The RIXS process also allows the simultaneous creation of two magnons which are referred to as bimagnon excitations. Bimagnons are associated with a two-site double spin-flip and can occur for both $\Delta S = 0$ and 1 [144, 145]. In the Heisenberg description of antiferromagnetism, bimagnons are associated with a fluctuation parallel to the ordered moment and are measured in the longitudinal susceptibility with inelastic neutron scattering measurements. With RIXS, bimagnon excitations were first measured at the O K-edge by Harada *et al.* [146] and then at the Cu K-edge by Hill *et al.* [147]. At the Cu L-edge, where single magnon excitations are allowed, bimagnon excitations are seen as a broad shoulder to the sharp single magnon excitations which makes separation of the first and higher order components more challenging. Bisogni *et al.* [148] argue that the various RIXS edges probe different parts of a wide multimagnon continuum.

3.3 RIXS at the I21 spectrometer at Diamond Light Source

As described in section 3.1, the resonant enhancement seen in RIXS is a second order process and therefore requires high photon intensities to achieve usable count-rates. With the advent of third generation synchrotron sources this has become increasingly accessible. The second piece of the puzzle is in the availability of sufficiently high-density gratings and large spectrometer arms to provide the kind of energy resolution needed for resolving low-energy excitations in RIXS. The issue of energy resolution is particularly important for low incident energy experiments (soft x-ray RIXS) and as such the instrumentation for hard and soft RIXS are typically very different. Fig. 3.4 shows the significant gain in instrumental energy resolution for soft x-ray RIXS spectrometers in recent years showing the improvement in energy resolution at the Cu L_3-edge. This thesis deals exclusively with experiments on soft x-ray RIXS beamlines, therefore this section contains descriptions of typical instrumentation for these experiments.

A number of dedicated soft x-ray RIXS beamlines have been developed over the past few years including SAXES at the ADRESS beamline at the Swiss Light Source (SLS) [150], the ERIXS/ ID32 beamline at the European Synchrotron Radiation Facility (ESRF) [151, 149], the SIX beamline at Brookhaven National Laboratory (BNL) [152], beamline 41A at the Taiwan Photon Source[153, 154] and the Veritas beamline at MAX IV [155]. This section describes the soft x-ray RIXS I21 beamline at Diamond Light Source (DLS) [156] which began user operation in

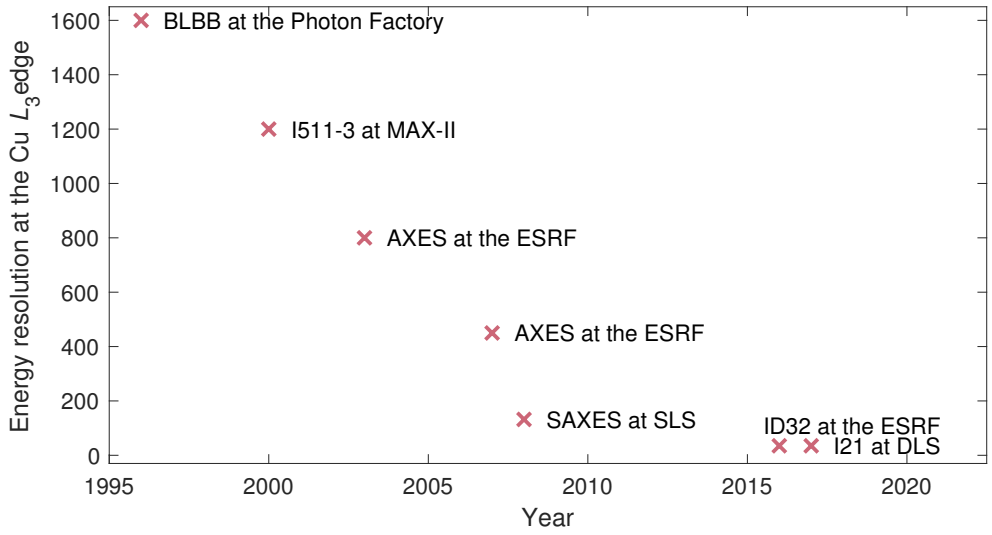

Figure 3.4: The improvement in energy resolution at the Cu L_3-edge for some of the RIXS spectrometers developed in the last decade. Energy resolution values from references [104, 149].

September 2017.

3.3.1 Diamond Lightsource

Diamond Light Source is a third generation x-ray synchrotron at the Rutherford Appleton Laboratory in the UK. The synchrotron accelerates electrons to 3 GeV in a storage ring consisting of 24 bending magnets. Synchrotron radiation is directed to beamline endstations by passing the accelerated electrons through insertion devices producing x-rays of the required wavelength. Insertion devices are formed of magnetic arrays which manipulate the electron beam to produce synchrotron radiation through acceleration perpendicular to their direction of travel. Insertion devices are typically divided into two categories, wigglers which produce high energy radiation and undulators which can be tuned to a specific energy by varying the separation of the magnetic arrays producing bright monochromatic beams.

3.3.2 The I21 beamline

Synchrotron radiation is directed to the I21 endstation through a 5m helical undulator which produces tunable photon beams with energy between 250 and 3000 eV (currently in use up to 1500 eV). The incident photons can also be linearly polarised with the electric vector of the photon oriented either horizontal (LH/ π-polarisation) or vertical (LV/ σ-polarisation) to the direction of the beam by movement of the undulator gap.

As photon intensity is of particular importance to soft x-ray RIXS experiments the I21 instrument has been designed with as few optical elements as possible to minimise the flux lost

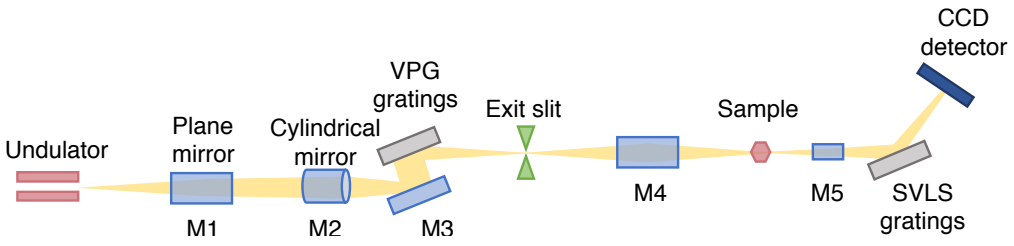

Figure 3.5: Schematic of the I21 beamline optics showing the path of photons from the undulator to the sample and then to the detector [156].

to reflection. Fig. 3.5 shows the beam path through the optical components of the beamline. Starting at the undulator, the beam passes through mirrors and variable line-density plane (VPG) gratings to shape and monochromatise the beam resulting in a spot-size at the sample position of approximately 30 μm in the horizontal axis and 2 μm full-width half maximum (FWHM) in the vertical.

3.3.3 The RIXS spectrometer

Manipulator

The sample sits within a large ultra-high vacuum (UHV) chamber with minimum pressure to 10^{-10} mbar. The scattering geometry is controlled by the orientation of the sample to the beam which can be rotated with 6 degrees of freedom controlled by the sample manipulator. The sample is placed in the centre of the sample chamber and can be cleaved in-situ to present highly clean surfaces to the beam. This is particularly important in the soft x-ray regime where the beam does not penetrate particularly far into the sample (in LCO, the penetration depth is $\sim 0.1\mu$ m at the Cu L_3 edge). For low temperature experiments, the entire sample chamber is cooled with liquid He and has a base temperature of approximately 14 K.

A unique aspect of the I21 spectrometer is the location of the M5 collecting mirrors inside the sample chamber. This feature allows the collecting mirrors to be placed very close to the sample and collect as much of the scattered beam as possible resulting in higher flux than in previous designs. The design requires careful optimisation of the beam position on the mirrors as the sample is rotated.

Gratings

Photons scattered from the sample are refocused with the collecting mirrors onto a spherical variable-line-spacing (SVLS) grating. The gratings act as analysers of the scattered beam by

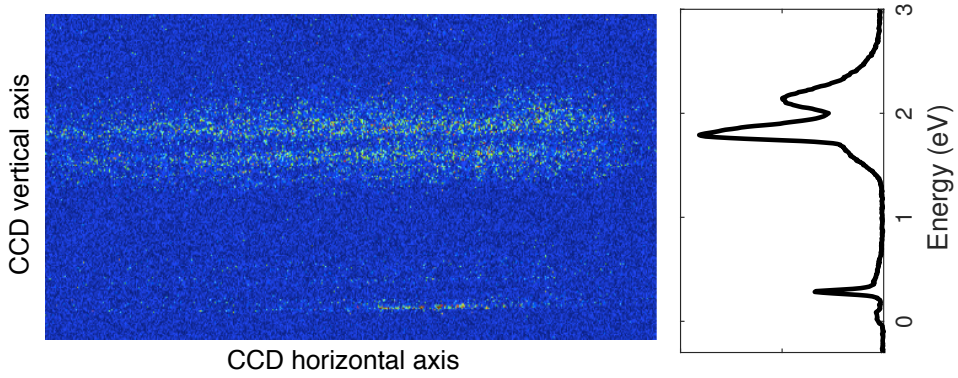

Figure 3.6: The RIXS intensity captured at the CCD detector showing in the left panel a 2D RIXS image measured on LCO. Photons are scattered to the detectors as a function of energy in the vertical axis and intensity in the horizontal axis. The right panel shows the RIXS spectra which is produced by integrating the CCD image along the vertical axis.

dispersing light to the detectors based on wavelength. The variable-line-spacing grating has a fixed curvature which minimises optical aberrations. The extremely fine density of lines on the SVLS gratings is what gives the spectrometer its resolving power of 10000-40000 at 1000 eV. I21 has two different SVLS gratings which provide optimal energy resolution for different energy ranges giving energy resolution of up to 35 meV at the Cu L-edge and 20 meV at the O K-edge.

Detector

The SVLS gratings serve the secondary purpose of focusing the scattered light onto the detector. The detector arm has variable length up to 15 m in order to analyse as well as focus the scattered photons at the detector. The entire spectrometer can be rotated by 150^{o} to measure excitations in a large range of **Q**-space.

The grating monochromatise the photons vertically according to their energy and are collected on a 2D position sensitive charge coupled device (CCD) detector. As shown in Fig. 3.6, integrating along the horizontal axis gives the total RIXS intensity as a function of vertical pixel. The relationship between pixel and energy is calibrated by measuring an elastic peak for a series of incident energies which allows the spectra to be plotted as a function of energy.

Practically, the beamline requires significant space to accommodate the complex instrumentation and is housed in a separate building next to the synchrotron where the detector arm is freely rotated on large marble and granite supports. Fig. 3.7 shows a schematic of components which make up the spectrometer.

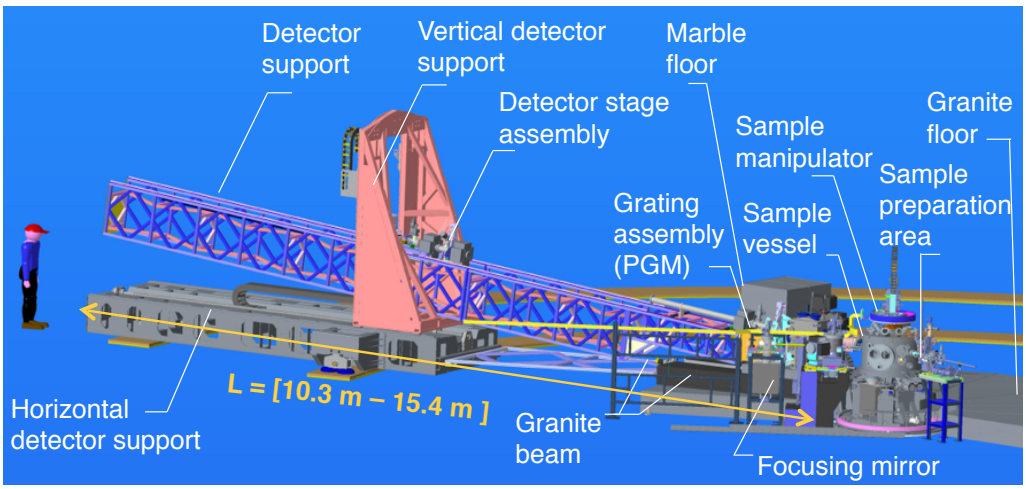

Figure 3.7: The I21 RIXS spectrometer.

3.3.4 Sample preparation

The majority of samples used for the work in this thesis were cut into posts from larger rods of material using a diamond saw. The posts have dimensions approximately 1 x 1 x 2 mm with the c axis along the long edge. The orientation is found using Laue diffraction which uses broad spectrum incident radiation to produce diffraction peaks from many crystal directions at once. The symmetry of the resulting Laue pattern can be used to orient the crystal as shown in Fig. 3.8 (a). Following cutting, the posts are glued on a sample plate with conductive epoxy. The c-axis is oriented normal to the sample plate and the orientation is rechecked with Laue. Any misalignment between the plate and the crystal axes is measured and can be offset by rotating the sample manipulator. The alignment can be confirmed by performing diffraction at the beamline within the constraints of energy and rotation. At the Cu L-edge in $La_{2-x}Sr_xCuO_4$ (LSCO) it is typically only possible to measure the [002] diffraction peak. To ensure the samples cleave in the correct orientation, a notch is cut in the c-axis and a cleave-post is attached to the top as shown in Fig. 3.8 (b). The samples are placed in the sample chamber in ultra-high vacuum and cleaved to expose a clean $a-b$ surface to the beam.

3.3.5 Typical experimental geometry

Fig. 3.9 shows the typical geometry of the RIXS experiments on cuprate materials which are described in this thesis. Samples are oriented to expose the $a-b$ surface to the beam resulting in momentum transfer $\mathbf{Q}$ in the (h,k) plane. The excitations of interest in this thesis, namely the spin fluctuations in cuprates, are dispersive predominantly in (h,k) due to the two-dimensional nature of the CuO_2 planes, it is therefore assumed that there is negligible dispersion due to

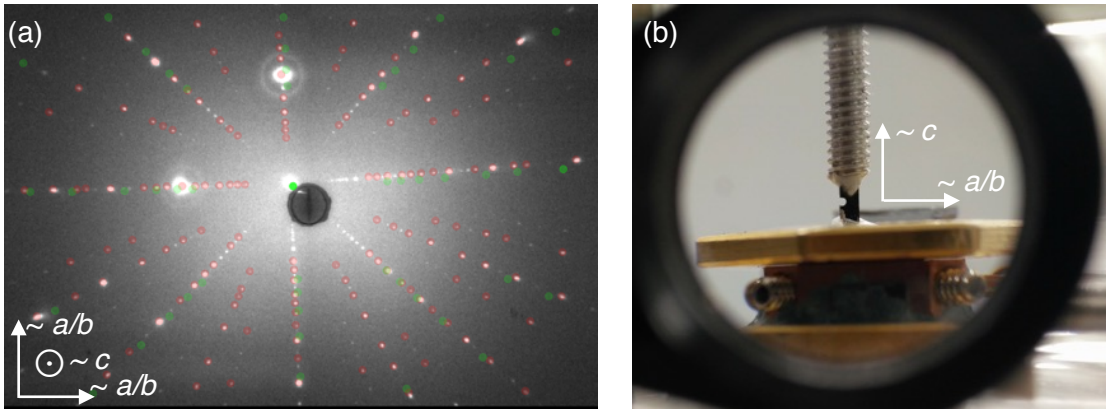

Figure 3.8: Alignment procedure for RIXS experiments showing (a) a typical Laue image (showing here a LSCO $x = 0.16$ sample) for a mounted sample with a/b and c axes identified and (b) a sample mounted on a sample plate with cleave-post and notch.

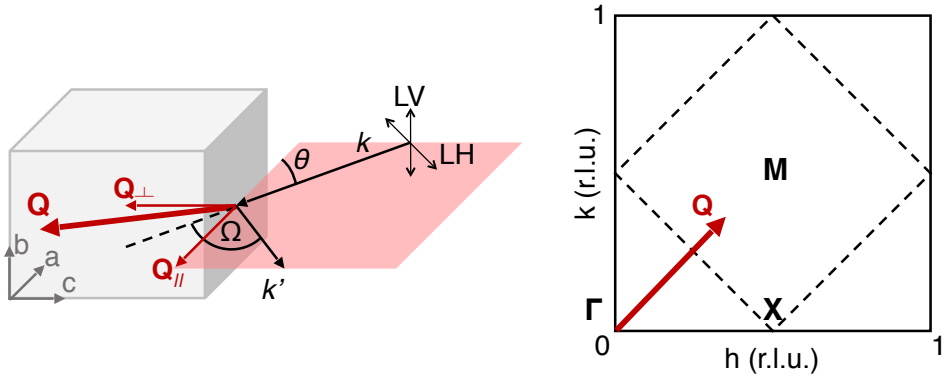

Figure 3.9: The typical experimental geometry for the RIXS experiments described in this thesis showing the relationship between the crystal axes and the scattering plane and the subsequent trajectory in the Brillouin zone.

variation in l. In the new RIXS experiments the total scattering angle, Ω, and the incoming beam position are fixed and the incident angle, θ, is varied by rotating the sample. In most of the experiments described in this thesis, we measure the parallel projection of $\mathbf{Q}$ ($\mathbf{Q}_{||}$ in Fig. 3.9) which at the Cu L-edge in LCO exposes the $a-b$ plane between $(0,-0.5)$ and $(0,0.5)$ or between $(-0.35,-0.35)$ and $(0.35,0.35)$. The perpendicular projection, $\mathbf{Q}_{\perp}$, can also be measured.

3.3.6 Data processing

The RIXS images are integrated along the detector horizontal edge to give a RIXS spectrum at each $\mathbf{Q}$. A dark-image background is subtracted and the spectra are normalised by time. The

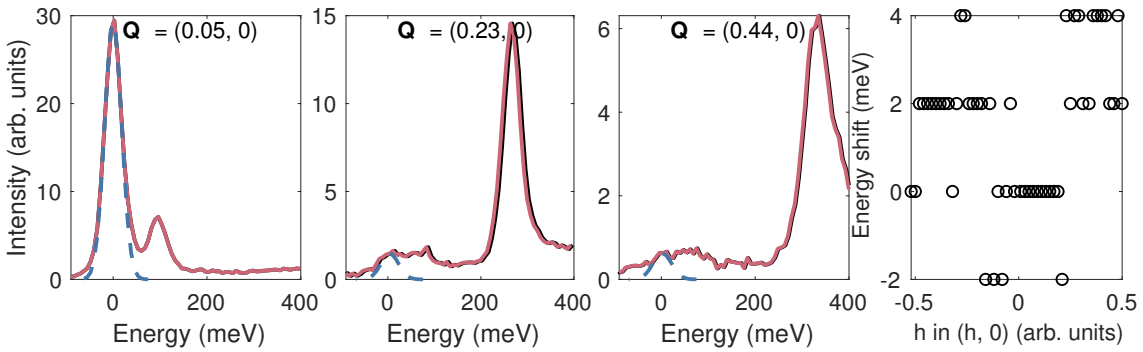

Figure 3.10: Examples of the second procedure which is used to align the zero-energy position of the RIXS spectra. The original energy scale from alignment to a purely elastic reference is shown in black, which is aligned to a Gaussian function with FWHM of the experimental resolution shown in dashed blue and the resulting shifted energy spectrum is shown in pink. The final plot shows the absolute shift in energy as a result of this procedure for RIXS spectra measured on LCO in the $\mathbf{Q} = (h, 0)$ direction with π polarisation.

zero-energy position of the spectra is established roughly by comparison to a purely elastic peak from a carbon tape reference below the sample. Then more precisely by aligning to the elastic peak in the spectra by comparing to a Gaussian function with width limited to the experimental resolution. Fig. 3.10 shows examples of this procedure showing data with the roughly estimated zero energy position in black compared to the resolution function indicated with dashed blue lines and the corrected data in pink. The figure shows that the spectra are typically well aligned from the first procedure and the second procedure provides further fine tuning of the order of a few pixels. It is clear from Fig. 3.10 that this process is much easier close to the specular position ($\mathbf{Q} = 0$ in the standard orientation) where the elastic peak becomes large. To reflect this, the error in the energy correction is established by the error in fitting a Gaussian peak convolved with a Bose function $n(\omega) + 1$ to the region around the elastic peak. The right plot in Fig. 3.10 shows the energy shift, that is the difference between the zero peak established from the carbon tape and from fitting the elastic peak, are plotted as a function of $\mathbf{Q}$ for example LCO data. The energy shifts remain within 10 meV and are broadly consistent across the $\mathbf{Q}$-range, therefore it is assumed that the procedure is consistent regardless of the intensity of the elastic peak.

3.3.7 Self-absorption

The connection between the RIXS cross-section and the dynamic structure factor $S(\mathbf{Q}, \omega)$ remains an area of continued debate. As discussed in Section 3.1.3, Ament *et al.* [125, 104] describe the conditions in which the measured RIXS intensity can be proportional to $S(\mathbf{Q}, \omega)$ multiplied by a resonant prefactor, $f(\mathbf{k}, \mathbf{k}', \epsilon, \epsilon')$ (see Eqn. 3.11).

One component of the cross-section f is given by the self-absorption of photons within the

material before and after the RIXS process. Self-absorption is dependent on the angle, polarisation and energy of incident and scattered photons and as such the effect of self-absorption varies considerably depending on the experiment. This section describes the method used to calculate self-absorption in the RIXS experiments described in this thesis.

The literature contains many studies discussing methods of estimating the self-absorption effect in RIXS [157, 138, 158, 159]. The three factors affecting self-absorption are described as follows. A geometrical component based on the path of the photon through the material. Polarisation, due to the orientation of the photon's electric field to the orbitals in the material - this is particularly significant where a transfer of angular momentum occurs, as in magnetic excitations. And finally the proximity of the photon to an absorption edge, known as the resonance effect.

Starting with the simplest case, the intensity of a photon travelling distance T through a crystalline material experiences absorption proportional to,

$$I \propto \mathrm{e}^{-\mu T}. \tag{3.13}$$

where μ is a linear absorption coefficient [160]. In the quasi-2D case, a scattered photon will travel a distance with projection x and y into the sample before scattering and has absorption coefficients μ_i and μ_f before and after scattering respectively (see Fig. 3.11 (a)). The absorption can be estimated by integrating over these scattering distances such that,

$$I_{\mathrm{SA}} \propto I_{\mathrm{raw}} \int \exp\left(\frac{\mu_i y}{\sin\theta}\right) \exp\left(\frac{\mu_f y}{\sin(\Omega-\theta)}\right) dx dy \sin\theta, \tag{3.14}$$

where θ is the angle between the sample and the incident photons and Ω is the total scattering angle, therefore the angle between the sample and the scattered photons is $\Omega-\theta$. x is integrated between the limits $x_{\mathrm{min}} = \frac{y}{\tan\theta}$ and $x_{\mathrm{max}} = \frac{y}{\tan\theta} + \frac{\delta}{\sin\theta}$ and in y between 0 and ∞ which can be rearranged to give,

$$I_{\mathrm{SA}} \propto I_{\mathrm{raw}} \frac{\sin(\Omega-\theta)}{\mu_i(\omega,\theta,\sigma)\sin(\Omega-\theta) + \mu_f(\omega,\theta,\sigma)\sin\theta}. \tag{3.15}$$

In practice, the absorption coefficients are energy, angle and polarisation dependent, hence this equation should capture the full variation of the self-absorption.

Geometry

In our geometry, the scattering angle Ω is fixed at approximately 150^{o}, and the sample is rotated in θ. With increasing θ, the sample orientation moves from "grazing-in" to "grazing-out" as shown in Fig. 3.11 (b) and (c) where the effect on the incoming and outgoing beam is seen to be

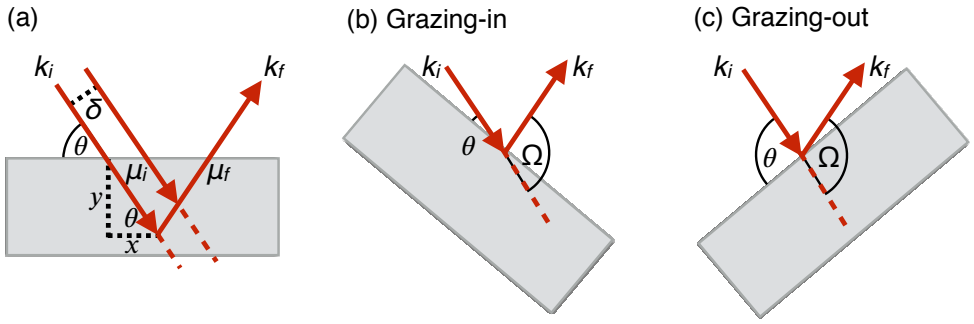

Figure 3.11: Scattering geometry for RIXS experiments showing (a) the projected distances x and y that the photon penetrates into the sample before scattering and the extreme scattering angles (b) grazing-in and (c) grazing-out.

very different. The absorption coefficients μ are also θ dependent for π polarisation in cuprates due to the orientation of the photon electric vector to the Cu orbitals.

Polarisation

The impact of the photon polarisation is contained within the absorption coefficients μ. The interaction of x-rays with materials is a complex problem which is well discussed in reference [113]. Here the elements relevant to the experiments are briefly discussed.

In RIXS experiments the incident photon beam is typically linearly polarised with either π or σ orientation. The total polarisation of the beam is described by the Stoke's vector **P** which is composed of P_1, P_2 and P_3 coefficients which describe the extent of polarisation of the beam. Perfect linear polarisation is achieved when $P_2 = 0$ and $P_1 + P_3 = 1$ (in real systems, the photon beam is likely to contain a mix of states and so $P_1 + P_2 + P_3 < 1$). Coefficients of **P** are matrix elements of **G**, the scattering amplitude operator in which diagonal elements are amplitudes where the initial and final polarisation are the same, $\sigma \rightarrow \sigma$ and $\pi \rightarrow \pi$ and the off-diagonal elements are amplitudes where the polarisation changes, $\sigma \rightarrow \pi$ and $\pi \rightarrow \sigma$.

Certain RIXS processes, such as single magnon spin fluctuations, are associated with a transfer of angular momentum. In these instances, the angular momentum of the photon is also changed and the self-absorption is calculated under the assumption that the polarisation of the scattered photon is flipped. In practice, the exact polarisation state of the scattered photon is not known. Recent experiments have made use of polarisation analysis on the scattered beam to fully separate charge and magnetic excitations. Peng *et al.* [161] describe polarisation analysis on the magnetic excitations of the $(Bi,Pb)_2(Sr,La)_2CuO_{6+\delta}$ cuprate family. The intensity of the

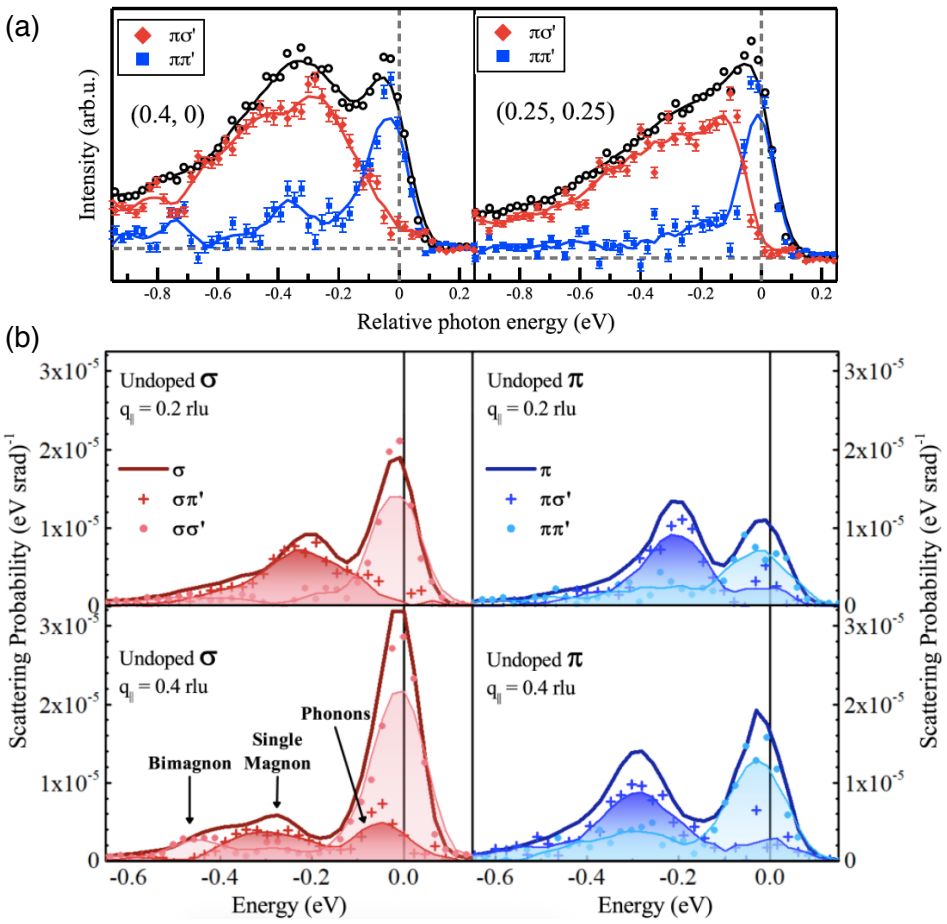

Figure 3.12: RIXS polarisation analysis showing (a) the polarisation dependence of the magnetic excitations in $(Bi,Pb)_2(Sr,La)_2CuO_{6+\delta}$ (reproduced with permission from reference [161]) and (b) $NdBa_2Cu_3O_{7-\delta}$ (reproduced with permission from reference [162]). Both plots show energy transfer from the reference frame of the photon hence excitations are shown with negative energy. For the remainder of this thesis, the opposite convention is used, where energy transfer is referred to in the reference frame of the excitations which are hence shown with positive energy.

magnetic excitations which they measure is shown in Fig. 3.12 (a) and is seen to be composed of spectral weight mostly in the cross-polarisation channel (82% in the range 150–600 meV). This is seen to be the case for excitations across the Brillouin zone with charge excitations composing a background, elastic and phonon contribution. A similar trend is seen in doped and undoped $NdBa_2Cu_3O_{7-\delta}$ measured by Fumagalli *et al.* [162] as shown in Fig. 3.12 (b). These results are taken as evidence that RIXS at the Cu L_3 edge is probing predominantly magnetic excitations in this region.

The resonance effect

The self-absorption experienced by a photon is also strongly energy-dependent. This is clearly important in RIXS as the incident energy is tuned to an absorption edge in the material. Ap-

proaching the resonant energy, absorption sharply increases. Where a photon is scattered from an excitation with large energy, such as the *dd*-excitations, the incident photons experience much larger self-absorbtion than the scattered photons. This effect is referred to as the resonance effect. As with the polarisation, the resonance effect is captured in Eqn. 3.15 within the absorption coefficients, μ.

Estimating the self-absorption

In practice, the absorption coefficients μ_i and μ_f are estimated from x-ray absorption spectroscopy (XAS) which can be performed prior to the RIXS measurements by measuring the total electron yield from the sample as the incident energy is varied. In XAS the photon form factor $f_{pq}(\omega)$ is defined as,

$$f_{pq}(\omega) = \frac{e^2}{\hbar^2 m_e^2 c^2} |\mathbf{A}|^2 \sum_{i,f} \frac{\langle \psi_i | p_q | \psi_f \rangle \cdot \langle \psi_f | p_p | \psi_i \rangle}{\omega - \left(\omega_f - \omega_i\right) + i\Lambda_{if}}, \tag{3.16}$$

where p is the electron momentum operator for direction p and q [163]. For Cu L-edge XAS in the geometry of our experiments the atomic form factors can be broken down into their directional components,

$$\mathbf{F_{Cu}} = \begin{pmatrix} f_a(\omega) & 0 & 0 \\ 0 & f_b(\omega) & 0 \\ 0 & 0 & f_c(\omega) \end{pmatrix}.$$

In linear vertical (σ) polarisation for a sample aligned with surface normal to the (001) direction as shown in Fig. 3.9, the polarisation of the photon is always perpendicular to the Cu^{2+} orbitals and therefore f_a is proportional to σ XAS intensity. In linear horizontal (π) polarisation a projection of the Cu^{2+} orbitals is measured which is dependent on the incident angle such that π XAS intensity is proportional to $f_a \sin\theta + f_c \cos\theta$. It is therefore possible to estimate f_c by measuring the π XAS at low θ to minimise the projection of f_a. To check the veracity of this estimation, the π spectra were measured at $\theta = 20^o$ to estimate f_c and the θ-dependence of the XAS intensity was calculated. Fig. 3.13 shows the XAS spectrum for σ and the calculated spectrum for π at $\theta = 90^o$ where the projection of the Cu^{2+} is the same in both polarisations and therefore the peak XAS intensity should be the same. The plot shows that the σ and π XAS spectra are indeed the same to within 5%.

This approximation allows us to estimate the incident and final absorption coefficients, μ_i and μ_f, from the components of the photon form factor as,

$$\begin{aligned} \mu_{i,\sigma} &= f_{i,a}, \qquad \mu_{i,\pi} = f_{i,a}\sin^2\theta + f_{i,c}\cos^2\theta, \\ \mu_{f,\sigma} &= f_{f,a}, \qquad \mu_{i,\pi} = f_{f,a}\sin^2(\Omega-\theta) + f_{f,c}\cos^2(\Omega-\theta). \end{aligned} \tag{3.17}$$

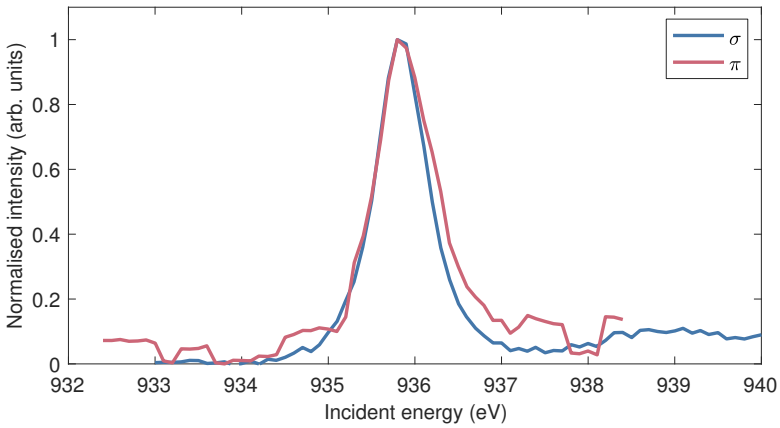

Figure 3.13: Comparison of σ and π polarised XAS spectra where the intensity of the π spectra is calculated from components of the photon form factor f_a and f_c. The XAS spectra are compared at 90^o where the projection of the Cu^{2+} orbital seen by photons of the different polarisations should be the same. The intensity of the spectra is the same to within 5%.

F has a strong energy and polarisation dependence, as shown in the XAS spectra in Fig. 3.13. When there is a difference between the energy or polarisation between the incident and scattered photons, the components of the photon form factor f_a and f_c, and therefore the absorption coefficients μ_i and μ_f, will be different. Considering all these factors, Fig. 3.14 shows the self-absorption factor calculated from Eqn. 3.15 as a function of both energy and incident photon angle θ for different combinations of incident and scattered polarisation. The plots demonstrate the significant energy, angle and polarisation-dependence of the self-absorption. The general trend of increased absorption at higher θ is due to the geometrical effect, as photons pass through more of the sample and are therefore more likely to be absorbed. In all cases, close to 0 eV energy transfer the resonance effect is dominant, where self-absorption is highest close to the resonance of the absorption edge. This effect is also highly polarisation-dependent - σ-polarised photons are seen to experience significantly more self-absorption at high θ. Photons scattered with different energy experience less absorption and at around 1.5 eV the effects of the resonance become negligible. At higher energy, in instances where the initial polarisation state is π, self-absorption has a secondary geometrical effect due to the angular dependence of the f_c component of the form factor.

It is worth noting that for all of the measurements described in this thesis, incident photons are tuned to the resonance peak of the XAS spectra and therefore scattered photons all experience less absorption than incident and unscattered photons. Excitations which fall on the energy loss part of the spectra experience self-absorption roughly linearly with energy and therefore the shape of the spectra is not significantly impacted. However, Minola *et al.* describe measurements [158] performed with a range of incident energies and the resulting non-linear

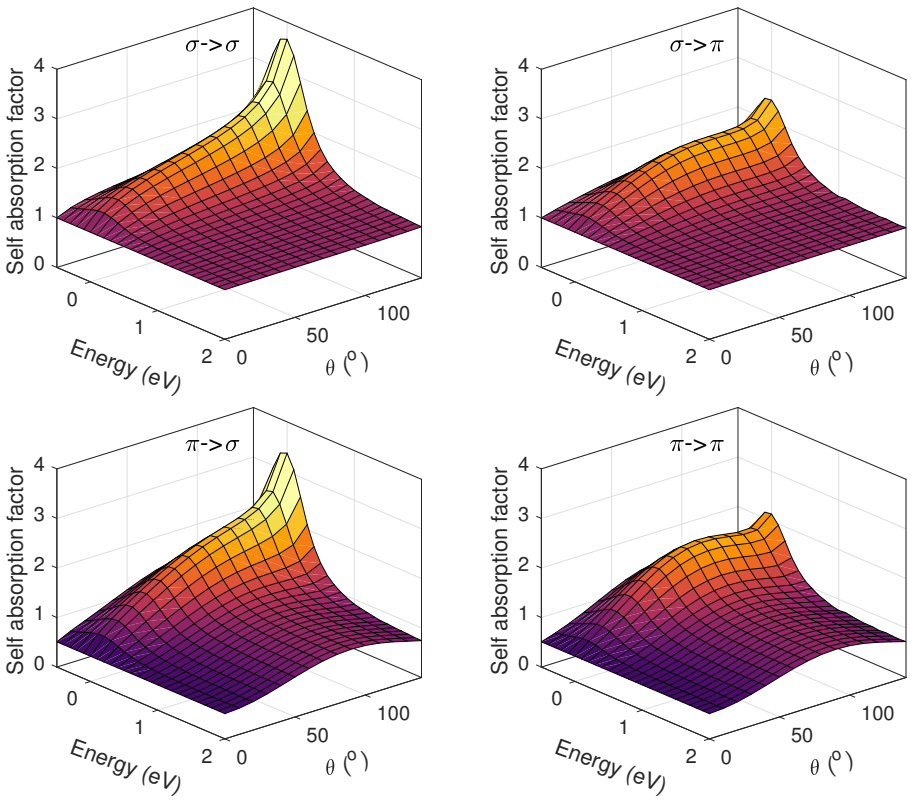

Figure 3.14: Self-absorption factors as a function of energy and incident angle θ for combinations of incident and final polarisation state.

self-absorption was calculated to significantly distort the shape of the spectra.

Chapter 4

Spin and charge fluctuations in La_2CuO_4

This chapter describes high-resolution resonant inelastic x-ray scattering (RIXS) measurements performed at beamline I21 of Diamond Light Source with the aim of fully characterising the excitation spectrum in La_2CuO_4 (LCO).

Following the overall motivations of this thesis, the work in this chapter has two main aims. The first is to study the antiferromagnetic (AFM) exchange interactions which occur in the CuO_2 planes of LCO in light of previously observed deviations from spin-wave theory (SWT). Understanding the magnetism in the AFM parent compounds of cuprate superconductors has the potential to help confine spin-fluctuation mediated theories of pairing in doped compositions. Details that can be established regarding additional excitations in LCO, such as higher order components of the magnetic response and phonon excitations, may also play a role in confining these theories.

The second motivation of this chapter is to improve understanding of RIXS as a probe of spin fluctuations by careful characterisation of the cross-section. LCO is a simple and well understood system which has been thoroughly characterised with inelastic neutron scattering [43, 44]. This makes it an ideal system in which to compare the spin fluctuations and identify prefactors to the RIXS response.

To achieve these aims, comprehensive measurements are made of the magnetic, phonon and *dd* excitations. The experimental work described in this chapter is broadly split into two sections. The first section tests an approach to correct the RIXS cross-section in the high energy *dd* excitations which have previously been well studied with RIXS [105]. Calculations are made of the self-absorption effect and the local cross-section based on a single-ion model in order to extract the intensity of the underlying excitations. Following these corrections, good agreement is seen between the experiment and theory. In the second section, the study

is extended to the low energy excitations. The same correction approach is applied to the single magnon spin fluctuations which yields measurements of the spin fluctuation intensity which are qualitatively similar to those seen with INS and establishes new details in the $(h,0)$ direction. The new measurements were performed in two different orientations which allow access further along the (h,h) direction than previous RIXS measurements. This method is a good test of the geometry dependent self-absorption and cross-section correction. The extended region probes from $(0.35,0.35)$ to $(0.4,0.4)$ in which a rapid increase is observed in the spin fluctuation intensity towards the antiferromagnetic wavevector $\mathbf{Q}_{\mathrm{AFM}} = (1/2,1/2)$. The energy dependence of the multimagnon continuum and two phonon branches is also extracted and a basic approximation of the cross-section allows an estimation of the intensity as a function of wavevector.

The principal advantage that these experiments have over previous studies is the enhanced energy resolution, around 30 meV full-width half-maximum (FWHM), in comparison to more than 100 meV in previous work on LCO. This enhanced energy resolution allows greater separation of the excitations, most obviously resolving the magnon and multimagnon branches and separating phonon excitations from the elastic peak.

4.1 Background

A common feature of the superconducting cuprates is the antiferromagnetic state which is observed in their undoped parent materials. The proximity of this state to high temperature superconductivity has lead to numerous theories relating antiferromagentic order to the pairing mechanism. A summary of some of these theories is given in references [45] and [52]. While no consensus yet exists on the nature of this relationship it is clear that some properties of the antiferromagnetic state, such as spin fluctuations, persist into doped phases [164, 165, 166, 167, 168, 110].

Significant work has focused on characterising and understanding the properties of the parent materials, in particular, the magnetic excitations from the AFM ground state that are observed as spin-waves which are collective magnetic excitations of the CuO_2 planes. This section introduces theoretical work describing the local excitations within a single-ion model picture which is used to describe the RIXS cross-section. Other theoretical calculations are also introduced which describe the spin fluctuations in terms of a Heisenberg model with next-nearest neighbour interactions. This section also describes the experimental probes, including INS and RIXS, which have been used to test this model in La_2CuO_4 (LCO).

4.1.1 Properties of La_2CuO_4

As described in Chapter 1, La_2CuO_4 is a comparatively simple, single-layer cuprate material making it a good choice for both characterising spin fluctuations and understanding the RIXS cross-section.

LCO is a typical Mott insulator with antiferromagnetic order below $T_N \sim 325$ K [95] due to exchange interactions in the CuO_2 plane. AFM order was first confirmed with neutron powder diffraction [169] confirming a magnetic order on the Cu sites along the HTT [110] direction. LCO is also an insulator due to electron-electron interactions. The first possible mechanism to explain this is the weak coupling picture, where the de Broglie wavelength λ is assumed to be less than the AFM correlation length ζ which results in the opening of a pseudogap at the Fermi level [170]. Alternatively, in the strong coupling picture, the energy gain t from adding a second electron is resisted by the strong on-site Coulomb repulsion U which gives a Mott insulator. It was originally proposed and has generally been accepted that strong-coupling is the origin of the insulating state in cuprates [47, 88, 89, 90, 91], however, some theories suggest that the interactions are not strong enough to induce a Mott transition and therefore assume the insulating state is itself induced by the AFM order [92].

4.1.2 Theoretical understanding

Single-ion model

The local interactions in LCO can be described within mean-field theory by considering a single Cu^{2+} ion and its surrounding oxygen ligands and accounting for further interactions with a constant electric field. Haverkort [171] describes calculations where a Hamiltonian matrix is used to describe a many electron basis to which the mean-field treatment is applied. Calculations can be made of both the ground state and a final state which describes the system after being probed with a spectroscopic technique. Diagonalising the Hamiltonian yields the ground state energy and wavefunction. Spectra are reproduced by calculating transitions from the ground to the final state.

In the case of LCO, we consider a Cu ion with the $3d^9$ shell interacting with neighbouring O ions with a $2p^6$ shell. The ground state Hamiltonian is constructed from two configurations Cu3d^9-O2p^6 which has 10 possible wavefunctions and Cu3d^{10}-O2p^5 which has 6 possible wavefunctions. In the case of one-electron interactions, the Hamiltonian between two wavefunctions is described as a sum of Slater determinants and the total Hamiltonian must consider interactions between all wavefunctions.

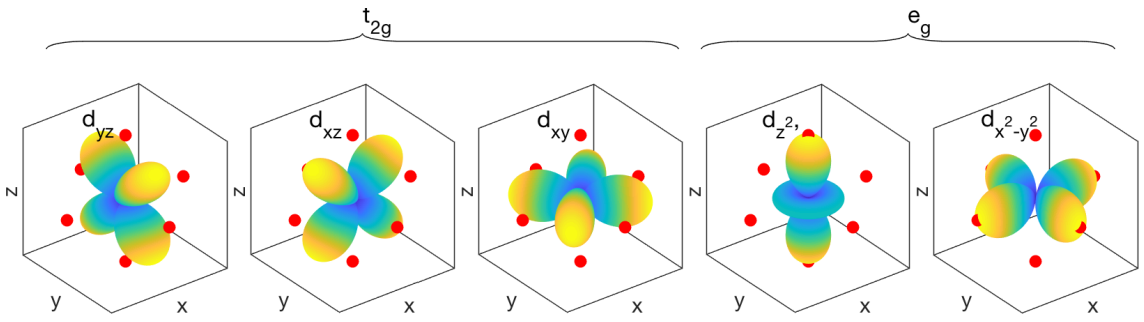

Figure 4.1: Orbitals associated with the Cu d band showing lower energy t_{2g} orbitals and higher energy e_g orbitals. The location of O ligands are shown in red.

Applying a crystal field to the system which results from the surrounding charges, has the effect of splitting the local energy levels. The total potential experienced by the ion, the Madelung potential V, can be described by spherical harmonics Y_k^m such that $\Psi = R_{n,l}Y_k^m$,

$$V = \sum_{k=0}^{\infty}\sum_{k=-m}^{k} A_{k,m} r^k \sqrt{\frac{4\pi}{2k+1}} Y_k^m(\theta,\phi), \tag{4.1}$$

where r,θ and ϕ describe the coordinates of the distribution and A is a Taylor expansion in r. The matrix elements of the interaction Hamiltonian can be constructed from the potential over all the possible wavefunctions,

$$H_{i,j} = \sum_{k=0}^{\infty}\sum_{k=-m}^{k} A_{k,m} \left\langle Y_{li}^{mi}(\theta,\phi)\right| \sqrt{\frac{4\pi}{2k+1}} Y_k^m(\theta,\phi) \left|Y_{lj}^{mj}(\theta,\phi)\right\rangle \left\langle R_{ni}^{li}\right| r^k \left|R_{nj}^{lj}\right\rangle. \tag{4.2}$$

The exact potential therefore depends on the symmetry of the orbital. In LCO the crystal field parameters have been determined from local density approximation calculations with a fixed potential (LDA+U) [171]. The Cu d orbitals have 5 possible configurations which are shown in Fig. 4.1. The t_{2g} orbitals are oriented away from the O ligands hence have the lowest energy. The e_{eg} orbitals have higher energy as they point along the direction of the O ligands. The $d_{x^2-y^2}$ orbitals have the greatest degree of overlap with the O ligands and are therefore the highest energy and half-filled [172].

Excitation spectra are calculated by considering all the possible final state wavefunctions Φ_f and calculating the probability of transition from the occupied initial states Φ_i. This gives a set of Dirac-delta functions corresponding to the excitation spectra which can be compared to spectra obtained from x-ray absorption spectroscopy (XAS).

Another paper by Haverkort [142] considers the specific case of calculating magnetic excitations measured with RIXS. As discussed in Chapter 3, the RIXS cross-section contains a large resonant pre-factor, which is partly due to interactions in the intermediate state. Haverkort proposed that the RIXS cross-section can be described by calculated XAS spectral functions. This approach yields an exact solution for the magnetic excitations as a product of local spin

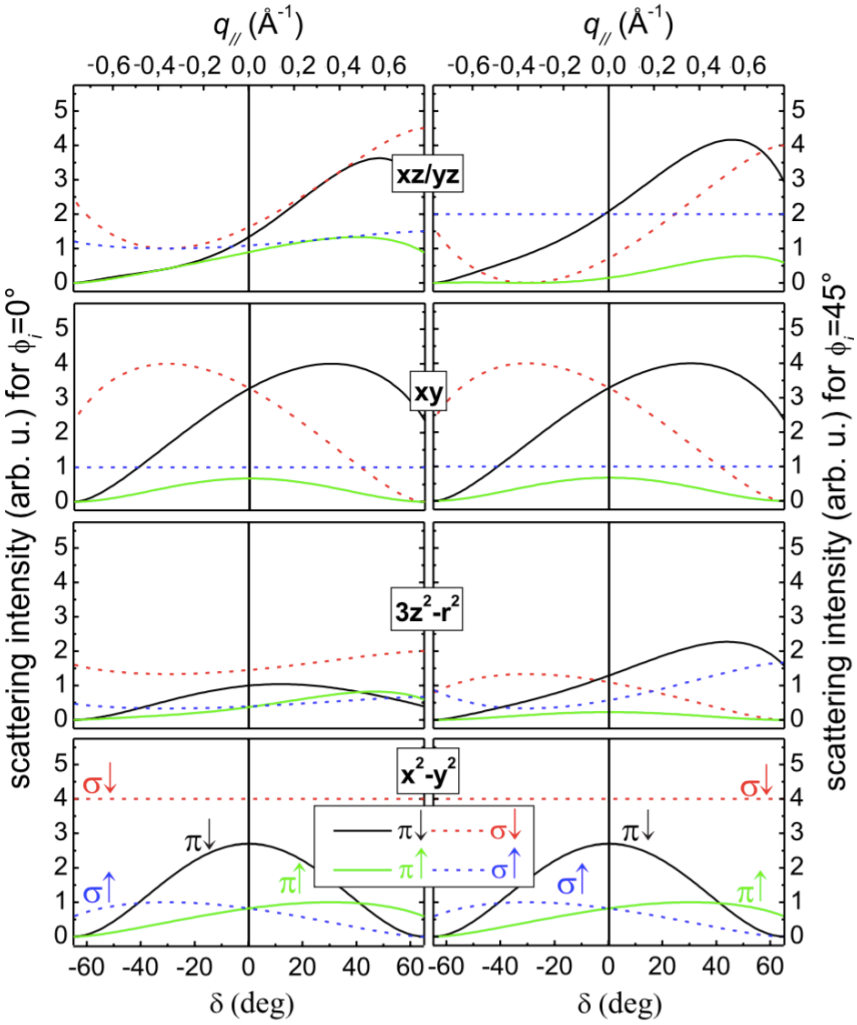

Figure 4.2: Calculated scattering intensity of *dd*-excitations at the Cu L_3-edge in LCO as a function of scattering angle δ (this is equivalent to θ in our experiments) and wavevector $\mathbf{Q}$ showing spin-flip and non-spin-flip states for initial polarisations σ and π. The left panels show $\psi_i = 0$ which is equivalent to $\mathbf{Q} = (h, 0)$ and the right panels show $\psi_i = 45$ which is equivalent to $\mathbf{Q} = (h, h)$. Figure reproduced from reference [119].

operators and x-ray absorption spectral functions. Such calculations have proved successful in modelling experimental RIXS data, recreating orbital and magnetic excitations measured with RIXS in TiOCl [173]. A similar approach has successfully described orbital interactions in LCO, Fig. 4.2 shows the orbital intensities at the Cu L_3-edge calculated on a single ion basis by Moretti *et al.* [119]. Fig. 4.3 shows an example spectrum calculated at incident scattering angle $\theta = 0$ with σ polarisation compared to a RIXS spectrum. The agreement between the experiment and theory is good but the resolution of the RIXS experiments is not good enough to fully separate the orbitals.

Haverkort *et al.* [174] point out that the single-ion approach can be useful to calculate the local properties of a system without considering long-range interactions and that these can be calculated with exact diagonalisation relatively easily. The local properties which can be

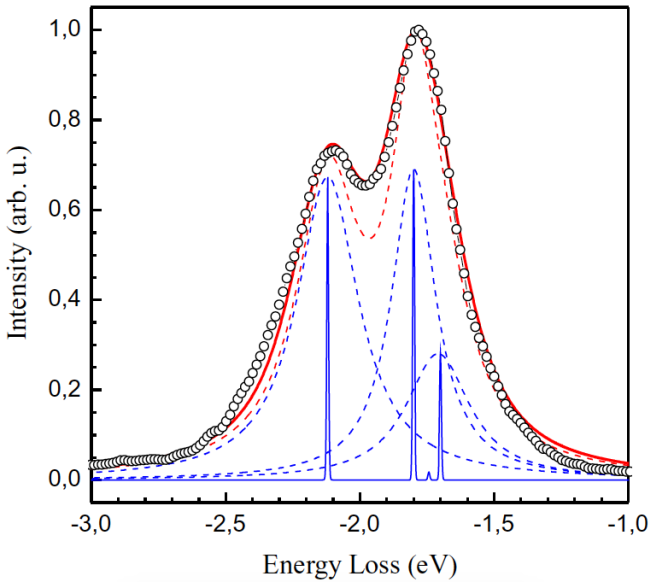

Figure 4.3: Calculated scattering intensity of *dd*-excitations at the Cu L_3-edge for an example spectra with $\theta = 0$ and polarisation = σ. The individual excitations are shown in blue, the sum of the excitations convolved with a Gaussian in red compared to measurements with RIXS indicated with black circles. Figure reproduced from reference [119].

well described by this approach include crystal-field, excitonic and core-level excitations [175]. In this chapter, the single-ion model calculations are used to describe the local effects in LCO and therefore calculate the transitions which contribute to the RIXS cross-section. Full cluster calculations which account for electron correlations involving multiple sites are also possible but extremely time consuming.

In this chapter transitions measured by RIXS are calculated using the Quanty package written by Maurits W. Haverkort and coworkers. General descriptions of how RIXS orbitals are calculated in Quanty are given in the following references [174, 176, 177]. In Section 4.3 calculated transitions between orbital states are compared to the *dd* excitations measured in RIXS and in Section 4.4, calculations of the local magnetic excitations are used to estimate the resonant prefactor to the RIXS cross-section.

Spin-wave theory

Non-local magnetic interactions have been studied for some time in LCO starting with a description of the antiferromagnetism. As discussed in Chapter 2, exchange interactions are responsible for the AFM state in LCO including interactions which go beyond direct exchange, known as superexchange. A theoretical description of the superexchange interaction was first established by Anderson in the early 1950's [35, 36] and classical spin wave theory (SWT) was quickly developed to describe the antiferromagnetic order in the ground state. Anderson approximated

the antiferromagnetic ground state in various simple structures and found long-range ordering in cubic and square lattices [178]. In LCO, the Cu $3d$ bands are half filled and magnetic order occurs in essentially 2D Cu^{2+} plaquettes, hence the spin dynamics can be understood as a 2D lattice of spin-1/2 particles. Systems of this type have been studied extensively and their basic characteristics are captured in the Hubbard model, namely the electron filling and the ratio between the electron hopping parameter t and the on-site Coulomb repulsion U which can be interpreted as a penalty for double occupancy of a site [47]. The $t-J$ model extends the Hubbard model to describe correlated systems giving exchange constants J, which for half-filling is referred to as the Heisenberg model.

Various methods have been used to derive a Heisenberg Hamiltonian which fully describes the physics of a spin-1/2 square lattice. Kubo [179] and Oguchi [180] describe methods using the Holstein Primakoff formalism which describes spin operators as a series of Bosonic creation and annihilation operators. Here we follow the derivation of Headings *et al.* [44] in which the same formalism is used to express the simple Heisenberg Hamiltonian introduced in Chapter 1 for two sublattices,

$$H = J\sum_{i,j}\mathbf{S}_i\cdot\mathbf{S}_j + h_1\sum_i\mathbf{S}_i + h_2\sum_j\mathbf{S}_j, \tag{4.3}$$

describing the antiferromagnetism, with magnetic fields h_1 and h_2. As before, J is the superexchange constant and S is the spin on site i and j. The spins are expanded in terms of creation and annihilation operators a and b for the two sublattices A and B,

$$S_i^+ = \sqrt{2S}f_i(S)a_i, \qquad S_i^- = \sqrt{2S}a_i^\dagger f_i(S), \qquad S_i^z = S - a_i a_i^\dagger, \tag{4.4}$$

$$S_j^+ = \sqrt{2S}b_i^\dagger f_j(S), \qquad S_j^- = \sqrt{2S}f_j(S)b_j, \qquad S_j^z = S - b_j b_j^\dagger. \tag{4.5}$$

$f(S)$ is an expansion such that $f(S) = (1-\frac{n}{2S})^{1/2}$. It is useful to re-express the creation and annihilation operators in terms of their Fourier transform in order to allow distinction between the sublattices,

$$a_\mathbf{Q} = \sqrt{2/N}\sum_i \mathbf{e}^{-i\mathbf{Q}j}a_i, \qquad a_\mathbf{Q}^\dagger = \sqrt{2/N}\sum_i \mathbf{e}^{i\mathbf{Q}j}a_i^\dagger, \tag{4.6}$$

$$b_\mathbf{Q} = \sqrt{2/N}\sum_j \mathbf{e}^{-i\mathbf{Q}j}b_j, \qquad b_\mathbf{Q}^\dagger = \sqrt{2/N}\sum_j \mathbf{e}^{i\mathbf{Q}j}b_j^\dagger. \tag{4.7}$$

We next substitute these operators into Eqn. 4.3 and sum for nearest neighbours within vector δ,

$$H = -\frac{1}{2}NzJS^2 + \sum_\mathbf{Q}\left[A_\mathbf{Q}\left(a_\mathbf{Q}^\dagger a_\mathbf{Q} + b_\mathbf{Q}^\dagger b_\mathbf{Q}\right) + B_\mathbf{Q}\left(a_\mathbf{Q}b_\mathbf{Q} + a_\mathbf{Q}^\dagger b_\mathbf{Q}\dagger\right)\right]. \tag{4.8}$$

The first term is the ground state energy E_0 and the second term is the energy of the excited state where two sublattices are defined, $A_\mathbf{Q} = zJS$ and $B_\mathbf{Q} = JS\sum_\delta \mathrm{e}^{i\delta\cdot\mathbf{Q}}$. Finally, through Bogoliubov

transformation we express operators $\alpha_{\mathbf{Q}}$, $\alpha^{\dagger}_{\mathbf{Q}}$ and $\beta_{\mathbf{Q}}$, $\beta^{\dagger}_{\mathbf{Q}}$,

$$a_{\mathbf{Q}} = \alpha_{\mathbf{Q}}\cosh\theta_{\mathbf{Q}} - \beta^{\dagger}_{\mathbf{Q}}\sinh\theta_{\mathbf{Q}}, \qquad a^{\dagger}_{\mathbf{Q}} = \alpha^{\dagger}_{\mathbf{Q}}\cosh\theta_{\mathbf{Q}} - \beta_{\mathbf{Q}}\sinh\theta_{\mathbf{Q}}, \tag{4.9}$$

$$b_{\mathbf{Q}} = \beta_{\mathbf{Q}}\cosh\theta_{\mathbf{Q}} - \alpha^{\dagger}_{\mathbf{Q}}\sinh\theta_{\mathbf{Q}}, \qquad b^{\dagger}_{\mathbf{Q}} = \beta^{\dagger}_{\mathbf{Q}}\cosh\theta_{\mathbf{Q}} - \alpha_{\mathbf{Q}}\sinh\theta_{\mathbf{Q}}. \tag{4.10}$$

and express the total Hamiltonian as,

$$H = E_0 + \sum_{\mathbf{Q}} A^{-}_{\mathbf{Q}}\alpha^{\dagger}_{\mathbf{Q}}\alpha_{\mathbf{Q}} + A^{+}_{\mathbf{Q}}\beta^{\dagger}_{\mathbf{Q}}\beta_{\mathbf{Q}}. \tag{4.11}$$

Several important physical parameters can be extracted from this result. Firstly, the energy of excitations created with operators $\alpha_{\mathbf{Q}}$ and $\beta_{\mathbf{Q}}$ acting on the ground state is given by,

$$\omega_{\mathbf{Q}} = Z_c\sqrt{A^2_{\mathbf{Q}} - B^2_{\mathbf{Q}}}, \tag{4.12}$$

where Z_c is a quantum renormalisation factor. To order $1/2S$, $Z_c = 1 + \xi/2S$ where ξ is given by,

$$\xi = \frac{2}{N}\sum_{\mathbf{Q}}\left[1 - \left(1 - \gamma^2_{\mathbf{Q}}\right)^1/2\right], \tag{4.13}$$

where $\gamma_{\mathbf{Q}}$ is defined,

$$\gamma_{\mathbf{Q}} = \frac{1}{z}\sum_{\delta} e^{i\delta\cdot\mathbf{Q}}. \tag{4.14}$$

The susceptibility can also be extracted from the SWT model. Perpendicular to the spin lattice, the susceptibility is dominated by the response to the staggered magnetisation. The perpendicular susceptibility $\chi_{\perp}$ is therefore expressed,

$$\chi_{\perp} = Z_{\chi}\frac{1}{2zJ}, \tag{4.15}$$

where Z_{χ} is another renormalisation constant. The transverse dynamical susceptibility is dominated by the spin-waves which for single-magnon creation is expressed as,

$$\chi''_{\perp}(\mathbf{Q},\omega) = Z_d(\mathbf{Q})\frac{\pi}{2}g^2\mu_B^2 S\left(\frac{A_{\mathbf{Q}} - B_{\mathbf{Q}}}{A_{\mathbf{Q}} + B_{\mathbf{Q}}}\right)^2\delta(\omega \pm \omega(\mathbf{Q}). \tag{4.16}$$

As the spin-waves disperse to higher energy, spectral weight is reduced which is accounted for with a normalisation parameter $Z_d(\mathbf{Q})$ which is related to the perpendicular susceptibility and energy renormalisation parameters as $Z_d(\mathbf{Q}) = Z_{\chi}Z_c$.

In reality, single spin-waves are not the only response allowed, the quantum fluctuations lead to a full multimagnon continuum. Two-magnon scattering is allowed in antiferromagnetic SWT by the creation of two independently propagating spin waves with $\Delta m_s = \pm 1$. Higher order processes are also theoretically allowed: odd terms in the expansion are recorded in

the transverse susceptibility and even terms in the longitudinal susceptibility. The dynamical susceptibility of two-magnon creation therefore dominates the longitudinal response,

$$\chi''_{\perp}(\mathbf{Q},\omega) = Z_{2M}\frac{\pi g^2\mu_B^2}{2N}\sum_{\mathbf{Q}_1,\mathbf{Q}_2} f(\mathbf{Q}_1,\mathbf{Q}_2)\delta(\omega-\omega_{\mathbf{Q}_1}-\omega_{\mathbf{Q}_2})\delta(\mathbf{Q}-\mathbf{Q}_1-\mathbf{Q}_2), \tag{4.17}$$

where $f(\mathbf{Q}_1,\mathbf{Q}_2)$ is the two-magnon structure factor,

$$f(\mathbf{Q}_1,\mathbf{Q}_2) = \frac{1}{2}\left[\cosh(\theta_{\mathbf{Q}_1})\sinh(\theta_{\mathbf{Q}_2}) - \cosh(\theta_{\mathbf{Q}_2})\sinh(\theta_{\mathbf{Q}_1})\right]^2. \tag{4.18}$$

Again the renormalisation parameter Z_{2M} accounts for the loss of spectral weight to higher multimagnon processes.

Anisotropic exchange terms

A number of additional anisotropic exchange terms contribute to the magnetism in LCO. Magnetisation measurements report a small out-of-plane ferromagnetic state which was explained by the presence of a Dzyaloshinskii-Moriya (DM) interaction [181]. The DM interaction contributes a small antisymmetric component to the exchange interaction. Moriya first described how DM anisotropic exchange interactions come about by extending the Anderson model of exchange to include the effects of spin-orbit coupling [182]. The resulting interaction contributes an additional exchange term $\mathbf{D}_{ij}$ to the Hamiltonian between two neighbouring spins,

$$H_{DM} = \mathbf{D}_{ij}\cdot(\mathbf{S}_i \times \mathbf{S}_j). \tag{4.19}$$

The DM interaction favours slight canting of the spins which leads to ferromagnetic order along the c-axis. In the presence of an external magnetic field, the ferromagnetic order aligns parallel to the field.

The pseudodipolar (XY) interaction, an additional anisotropic exchange term, is also present in LCO. The XY interaction arises due to second order, symmetric terms in the spin-orbit coupling in the exchange interaction [182]. In LCO the interaction can occur due to the exchange of spin between the x^2-y^2 orbital and zx orbital. The following terms are contributed to the Hamiltonian,

$$H_{XY} = \mathbf{S}_i\overleftrightarrow{\mathbf{\Gamma}}_{ij}\mathbf{S}_j, \tag{4.20}$$

where $\overleftrightarrow{\mathbf{\Gamma}}_{ij}$ is the pseudodipolar tensor between sites.

In LCO, the anisotropic exchange interactions have a number of effects on the measured magnetic properties. In contrast to that expected by the simple Heisenberg model, the out-of-plane magnetic susceptibility has been shown to be highest as a result of the anisotropic exchange processes and spin-gaps form in the in- and out-of-plane excitation spectra. Silva

Neto *et al.* [183] explain these properties in relation to the anisotropic exchange interactions, DM and XY. In high magnetic fields, displacement of the apical oxygen atoms results in a small monoclinic distortion away from the orthorhombic crystal structure [98]. However, the pure spin-spin exchange interactions dominate the magnetism in the CuO_2 planes and are considered to be solely responsible for the high energy spin fluctuations that are measured with RIXS.

4.1.3 Experimental studies

Inelastic neutron scattering

Soon after the discovery of HTS, inelastic neutron scattering (INS) was used to map spin fluctuations in many cuprate systems[184, 185, 186, 164, 187, 188, 189, 190]. Like RIXS, INS is an inelastic scattering technique in which energy transfer from the probe is used to investigate excitations in a material.

Neutrons have several advantages as a probe of condensed matter systems. Firstly, lacking electronic charge, neutrons interact primarily with atomic nuclei, allowing them to penetrate into a sample without scattering from electrons, thus making them an effective bulk probe. However, practically this means that larger samples are required to measure significant counts compared with x-ray scattering. Secondly, neutrons have their own spin moment allowing them to interact with local magnetic fields, such as unpaired electrons. Finally, at typical energies for neutron experiments, neutrons have a de Broglie wavelength of the order of atomic spacing, hence neutron diffraction is well suited to studying material structures. Inelastically scattered neutrons at the same energy can typically measure energy transfers of the order of excitations in condensed matter with energy resolution of less than 1 meV.

Another specific advantage of INS over RIXS is that the scattering cross-section of inelastically scattered neutrons is well understood and can be directly connected to the dynamical susceptibility of a system χ''. For magnetic scattering from electrons, the neutron cross-section is related to the spin-spin correlation function. In the case of a 2D antiferromagnet, where all directional components of the susceptibility are assumed to be the same, the double differential neutron cross-section can be expressed as [99],

$$\frac{d^2\sigma}{d\Omega dE} = \frac{k_f}{k_i}(\gamma r_e)^2 \left(\frac{g_J F(\mathbf{Q})}{2}\right)^2 [n(\omega)+1] \frac{2}{\pi g^2 \mu_B^2} \chi''(\mathbf{Q},\omega). \tag{4.21}$$

Here k_i and k_f are the incident and final wavevectors, γ is the neutron gyromagnetic ratio, r_e is the radius of the electron and $F(\mathbf{Q})$ is the magnetic form factor. As discussed in Chapter 3, the

exact nature of the RIXS cross-section is not well understood and is particularly hard to calculate for complex systems with excess charge such as doped cuprates.

In time-of-flight neutron measurements, where the energy of scattered neutrons is determined by the time between the neutron pulse and the neutron reaching the detector, the neutron beam is "chopped" into a monochromatic fixed incident energy in order to measure energy transfers in a system. Excitations can therefore only be reliably measured as a ratio of the incident energy and as such, measuring spin-fluctuations which disperse over $\simeq$ 300 meV is likely to require multiple incident energy measurements with different energy resolution. In a time-of-flight spectrometer, neutrons reaching the detector are also spatially scattered hence a large region of $\mathbf{Q}$ space is probed simultaneously, however, variations in the magnetic form factor mean the scattered intensity is significantly reduced at certain $\mathbf{Q}$, including the (1/2, 1/2) position in reciprocal lattice units.

Early INS measurements in LCO discovered long-range spin-fluctuations in the CuO_2 planes that persist above the Neèl temperature [184] and to some extent into the doped phases [185, 186]. Subsequent INS measurements resolved propagating spin-waves up to the experimental limit of 140 meV and extracted an exchange constant of 136 meV at 5 K [191, 192]. The full dispersion was revealed in measurements to higher energies up to a maximum 312 meV along $(h,0)$ [193, 165, 194]. This work was later extended across the Brillouin zone to characterise dispersing spin fluctuations up to 314 meV at (1/2,0) and up to 292 meV at (3/4, 1/4) which require the inclusion of longer than nearest-neighbour interactions to be understood in the framework of SWT [43]. Including interactions up to order t^4 in the Hamiltonian gives,

$$\begin{aligned} H = & J\sum_{i,j}\mathbf{S}_i\cdot\mathbf{S}_j + J'\sum_{i,i'}\mathbf{S}_i\cdot\mathbf{S}'_i + J''\sum_{i,i''}\mathbf{S}_i\cdot\mathbf{S}''_i \\ & + J_c\sum_{i,j,k,l}(\mathbf{S}_i\cdot\mathbf{S}_j)(\mathbf{S}_k\cdot\mathbf{S}_l) + (\mathbf{S}_i\cdot\mathbf{S}_l)(\mathbf{S}_k\cdot\mathbf{S}_j) - (\mathbf{S}_i\cdot\mathbf{S}_k)(\mathbf{S}_j\cdot\mathbf{S}_l), \end{aligned} \tag{4.22}$$

where J, J' and J'' are exchange constants for the first, second and third nearest neighbour interactions respectively and J_c is the exchange constant for a ring exchange, Fig. 4.4 shows these interactions within the CuO_4 plane. The exchange constants are related to the hopping parmeters as $J = 4t^2/U - 24t^4/U^3$, $J' = J'' = 4t^4/U^3$ and $Jc = 80t^4/U^3$ where the parmeters were found to be $t = 0.33 \pm 0.02$ eV and $U = 2.9 \pm 0.4$ eV. Further high energy INS measurements performed on LCO by Headings *et al.* [44] measured the exchange constants to be J =143 meV, $J' = J''$ =2.9 meV, and J_c = 58 meV. The spin-wave dispersion measured by Headings *et al.* is shown in Fig. 4.5.

These results in LCO established the importance of longer-range interactions in understand-

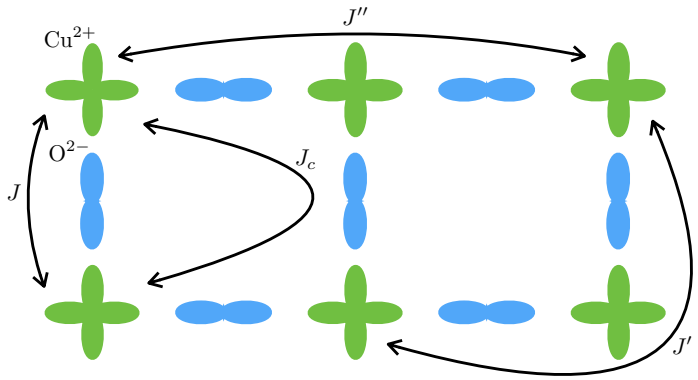

Figure 4.4: Exchange constants in SWT which account for the interactions in the CuO_2 plane in LCO.

ing the spin fluctuations in cuprates within the bounds of SWT. The higher order exchange interactions take place between multiple sites, such as the next and next-next nearest neighbours. Cyclic or ring-exchange interactions couple the spins in corners of the square plaquette and were first proposed to explain the magnetism in ^{3}He at low temperatures [195, 196]. The existence of the ring-exchange term in LCO was subsequently verified with polarised neutron scattering measurements which are better able to extract the excitations from the background [197, 198]. These measurements were compared to calculations of the spin fluctuations based on the Hubbard model and shown to indicate that the magnetic exchange terms are sensitive to higher order parameters that give rise to ring-exchange [197].

Measurements of the Fermi surface in lightly doped LCO with angle-resolved photoemission spectroscopy (ARPES) [199, 200, 201, 202] and band structure calculations [203, 204] reveal a large pseudogapped Fermi surface with a quasiparticle band, referred to as a Fermi arc, crossing at (π,π). Fitting these observations in the 2D single-band tight-binding model requires consideration of higher order hopping constants t' and t''. Delannoy *et al.* [205] point out that introducing t' and t'' parameters, good agreement with the INS results can be achieved resulting in a larger U, also more in line with the ARPES measurements.

The intensity of the spin-fluctuations has been found to be greatest at $(1/2,1/2)$ which is the location of the repeating unit of the AFM order, referred to as the antiferromagnetic wavevector $\mathbf{Q}_{\mathrm{AFM}}$ [43, 44]. The enhanced intensity of the magnetic excitations at $\mathbf{Q}_{\mathrm{AFM}}$ has been hypothesised to indicate that these excitations are important for pairing.

Headings *et al.* [44] also measured an anomalous broadening in the lineshape of the spin fluctuations at $(1/2,0)$ which cannot be explained in SWT. Softening is also seen in the excitation energy at the same wavevector as shown in Fig. 4.5. These anomalies suggests the $(1/2,0)$ excitations are more strongly coupled to other excitations than elsewhere in the zone. Such

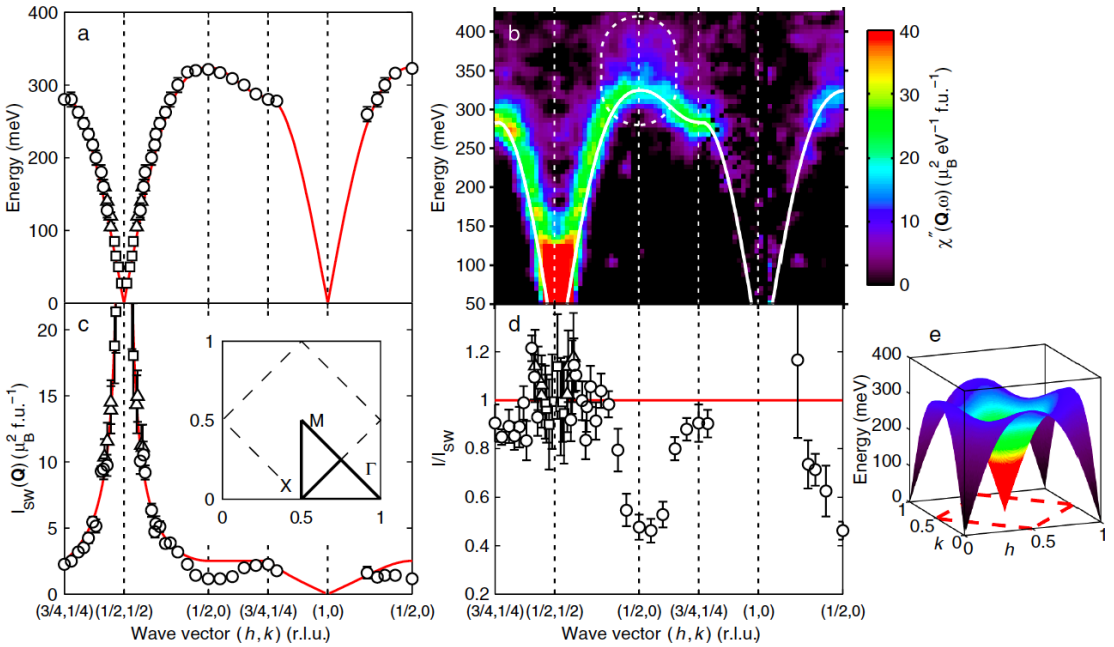

Figure 4.5: Spin fluctuations in LCO measured with INS showing the wavevector dependence of (a) the excitation energy (b) the susceptibility (c) the neutron response and (d) the deviation from SWT. Square data points indicate measurements performed with incident energy 160 meV, triangles indicate 240 meV, and circles indicate 450 meV. Panel (e) shows a model of the SWT dispersion in 3D. Figure reproduced with permission from reference [44].

additional spin correlations have been hypothesised to be spinons which, as described in Chapter 2, are predicted to occur in some RVB models of the cuprates [206].

Quantum Monte Carlo (QMC) calculations suggest that some of the increase in intensity towards $\mathbf{Q}_{\mathrm{AFM}}$ is connected to enhanced spectral weight in the multimagnon continuum [207]. Unpolarised INS experiments are not expected to separate single and two magnon scattering hence the spectral weight measured is expected to contain both 1+2M (one plus two magnon). Models of 1+2M scattering generally match well with the experimental data but do not account for the enhanced spectral weight at $\mathbf{Q} = (1/2, 0)$.

RIXS

RIXS was first used to probe high energy excitations in the cuprates following the prediction of Tanaka and Koti [128] that resonant x-ray emission could yield direction information about the transition between $2p$ and $3d$ states. These orbital excitations in LCO are measured at energy transfers of several eV and as such have been within the range of resolvable excitations for some time.

Ghiringhelli *et al.* [105] measured the orbital excitations in LCO identifying both local, *dd* excitations, and non-local, charge transfer excitations within the RIXS spectra. Little *et al.*

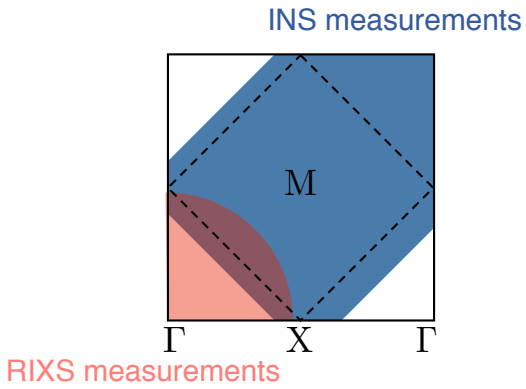

Figure 4.6: Typical region of the Brillouin zone probed by RIXS and INS in cuprates.

subsequently argued that the energy of the *dd* excitations measured with RIXS in $Tl_2Ba_2CaCu_2O_8$ match models of phonon coupling implying that they may be important for a full description of the pairing mechanism [208]. Further, higher resolution measurements on cuprates including LCO by Moretti *et al.* [119] have confirmed the energies of the *dd* excitations are too high to be involved with pairing. The *dd* excitations were also found to be in good agreement with theoretical cross-sections calculated using a single-ion model.

Similarly, Cu K-edge RIXS was used by Abbamonte *et al.* [209] to relate the orbital excitations in LCO to $S(\mathbf{Q},\omega)$. Their work estimates the effects of a resonant prefactor using a perturbative approach. Later a similar approach was taken to estimate the resonant prefactor following the work of Ament *et al.* [125]. The work produced good agreement between $S(\mathbf{Q},\omega)$ obtained from elipsometry measurements of the dielectric loss function and high resolution RIXS [126]. Further measurements at the K-edge show momentum-dependent charge excitations to be in good agreement with the Hubbard model [210].

More recently, RIXS has been established as a complementary probe to INS in measuring the spin-fluctuations in cuprates. At the Cu L-edge, RIXS measures a symmetrical region around Γ which corresponds to a region of overlap with INS, but allows investigation of the portion of the Brillouin zone where the spectral weight in INS is greatly reduced. Fig. 4.6 shows the regions of the Brillouin zone probed by the two techniques.

With x-ray scattering techniques, the x-ray photon interacts with the electron field of the sample allowing direct measurement of the electronic properties. As a result, the photons generally penetrate less far into the sample than with INS. In RIXS at the Cu L-edge, incident photons have energy around 930 eV which means they have a penetration depth $\sim 0.1\mu$ m into the sample at 90^o (less at lower or higher incident angle). As a side effect of this, the required sample sizes are typically much smaller for RIXS than with INS allowing investigation

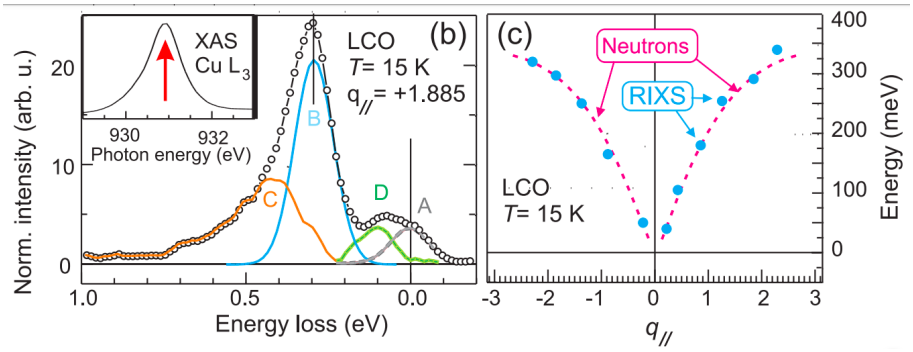

Figure 4.7: Spin fluctuations in LCO measured with RIXS by Braicovich *et al.* showing an example RIXS spectrum with the quasielastic peak indicated at A, single magnon at B, multimagnon at C and phonons at D. The right panel shows the single magnon dispersion compared to the INS of reference [44]. Figure reproduced with permission from reference [143].

of materials which would otherwise be too difficult to grow in large proportions.

Unlike in INS, the photon does not generally directly interact with the electron spin of the sample. However, as described in Chapter 3, Ament *et al.* [125] made the prediction that RIXS could indirectly measure excitations in which a transfer of angular momentum occurs via spin-orbit coupling. Braicovich *et al.* [143] demonstrated that RIXS can indeed measure single and bimagnon excitations at the Cu L-edge in LCO. An example of their measured RIXS spectra and the single magnon dispersion is shown in Fig. 4.7, their work shows good agreement with INS in the measured region to approximately $\mathbf{Q} = (1/3, 0)$ along the $(h, 0)$ direction.

Large numbers of RIXS measurements have since been performed on the spin excitations in parent and doped cuprates, generally showing good agreement with INS. In LCO, Dean *et al.* [211] observed spin fluctuations even in single-layer samples which was interpreted as indicating a lack of out of plane coupling. The authors note that the spin fluctuations appear to disperse to a slightly higher energy than is observed with INS which can be partially attributed to the presence of a higher energy magnetic continuum, however, the excitations are not fully separated. This higher energy spectral weight is described in SWT as longitudinal multimagnon scattering. Follow up studies to $(0.4, 0)$ in $(h, 0)$ and $(0.32, 0.32)$ in (h, h) confirmed the presence of dispersive multimagnon excitations in LCO [211, 111].

RIXS measurements on LCO at the Cu K-edge [147] and O K-edge [148], where transfers of angular momentum cannot be measured, identify non-dispersive multimagnon excitations. They suggest that the two experiments probe different parts of the multimagnon continuum and hence show that RIXS experiments performed at different edges can yield unique information.

With enhanced instrumental energy resolution, low energy phonons (< 100 meV) are now just about resolvable with RIXS in LCO. Devereaux *et al.* [129] predict that RIXS is sensitive to at

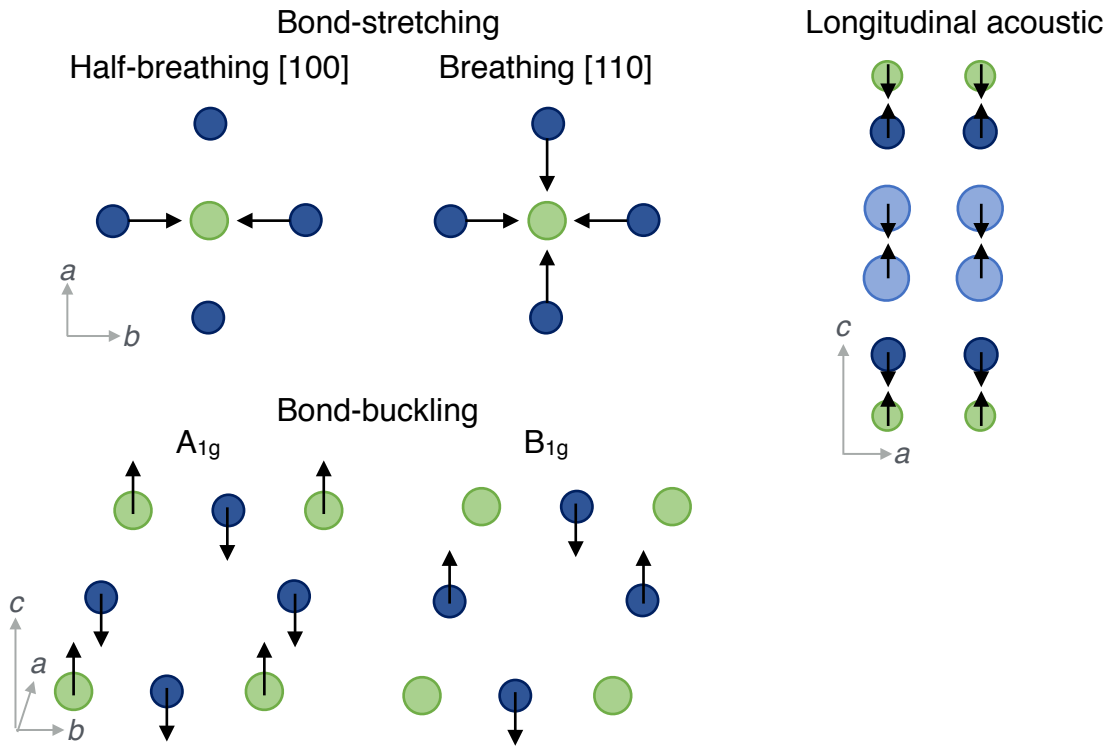

Figure 4.8: Phonon modes which RIXS is predicted to be sensitive to at the Cu L_3-edge showing the orientation of the lattice vibrations to the CuO_2 planes. Cu, O and La ions are shown in green, light blue and dark blue respectively.

least three phonon modes in this range at the Cu L_3-edge. These modes show similar dependence to early neutron measurements in $YBa_2Cu_3O_{6+x}$ (YBCO) [212, 213] and are identified as a longitudinal acoustic, bond-buckling (A_{1g} and B_{1g}) and bond-stretching (half-breathing in [100]-direction and breathing in [110]) mode at approximately 10, 45 and 70 meV respectively. A diagrammatic representation of these modes is shown in Fig. 4.9 and their intensity and dispersion predicted in reference [129] are shown in Fig. 4.8. In several recent experiments phonon excitations have been present as a shoulder to the quasi-elastic peak [211, 111] and show minimal dispersion for wavevectors above $\mathbf{Q} = 0.1$ (r.l.u.). Below this, the intensity of the elastic peak generally dominates over the phonons. Clear phonon excitations have been observed in cupric oxide CuO which shares the CuO_4 plaquette structure of the high T_c cuprates [131].

In LCO, Bisogni *et al.* [148] point out that the currently available energy resolution is sufficient to measure phonons in LCO. As described in Chapter 3, the electron-phonon coupling (EPC) strength can be determined from RIXS data via two approaches either from the ratio of a single and two-phonon harmonic or from the electron-phonon interaction matrix element M and intermediate state lifetime Γ.

The first approach has been demonstrated in several cuprate materials at the O K-edge [214,

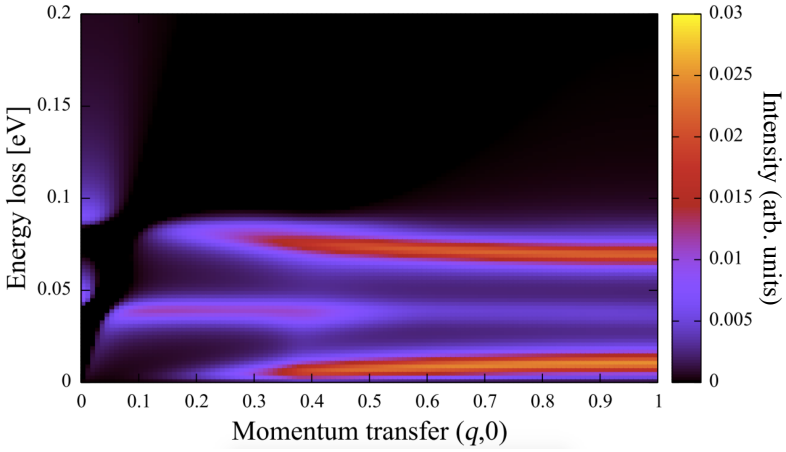

Figure 4.9: The sum of phonon modes predicted to contribute to the RIXS signal at the Cu L_3-edge. The intensity is in arbitrary units. Figure reproduced with permission from reference [129].

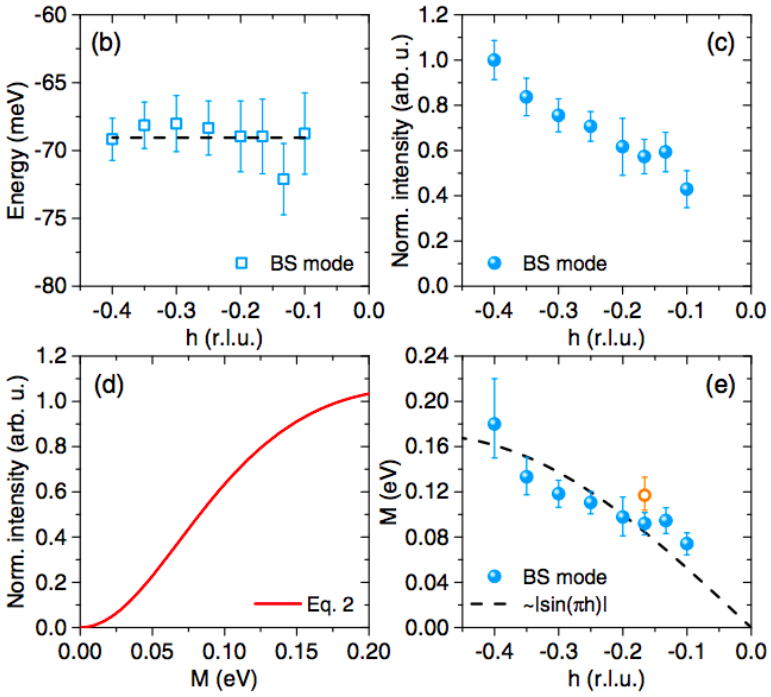

Figure 4.10: Details of the approach to extract the electron-phonon coupling strength from phonon intensity measured with RIXS. Showing the energy and normalised intensity of the breathing (bond-stretching) phonon mode and the extracted EPC strength, M. Figure reproduced with permission from reference [132].

215]. Recent RIXS experiments have verified the use of the second approach in $Nd_{1+x}Ba_{2-x}Cu_3O_{7-\delta}$ (NBCO) [133]. Braicovich *et al.* [133] identify two phonon branches, a breathing and buckling mode, and measure energy dispersions which match well with the theoretical predictions of reference [129] shown in Fig. 4.8. They obtain momentum dependent EPC constants for both phonon modes using the energy detune method described above and find similar results to calculations based on the ratio of the one and two phonon intensity. Using the same approach, Rossi *et al.* [132] report that the EPC strength in NBCO increases towards the Brillouin zone boundary reaching 0.17 eV at $\mathbf{Q} = -0.4$. Fig. 4.10 is reproduced from reference [132] showing the breathing mode phonon and its extracted EPC strength.

These results match reasonably well with calculations based on the Hubbard model [216, 217] and confirm that the EPC strength is not of high enough energy to be solely responsible for the pairing but that it may play some contributing role. In $La_{2-x}Sr_xCuO_4$ (LSCO), estimates of the electron-phonon coupling strength have been made by measuring the Eliashberg function with optical spectroscopy techniques [218]. Calculations which assume that phonons give rise to enhancements to another dominant pairing interaction, assumed to be spin-fluctuation mediated, have been shown to match well with these measurements [219]. In general, the doping evolution and temperature dependence of superconductivity in the cuprates point to the importance of phonon interactions. Recent work also indicates that RIXS is beginning to be seen as a useful tool for measuring phonons.

4.2 Measurement details

This section describes the new Cu L-edge RIXS measurements which were performed on LCO at the I21 beamline of Diamond Light Source.

4.2.1 Sample preparation

The samples of single-crystal LCO were grown via the travelling-solvent floating zone technique (TSFZ) in Bristol by previous group member Neil Headings [99] . TSFZ is a well-established technique for the growth of large single crystals of the type which are necessary for low-flux neutron-scattering experiments [220]. Crystals are formed in a molten zone between a polycrystalline feed material and a seed crystal. The zone is translated along the feed rod and cooled with a solvent. The as-grown crystals were annealed in an Argon atmosphere to remove excess oxygen and detwinned by applying uniaxial pressure along an orthorhombic direction. Full details of the growth of crystals studied in this thesis are available in the thesis of Neil Headings

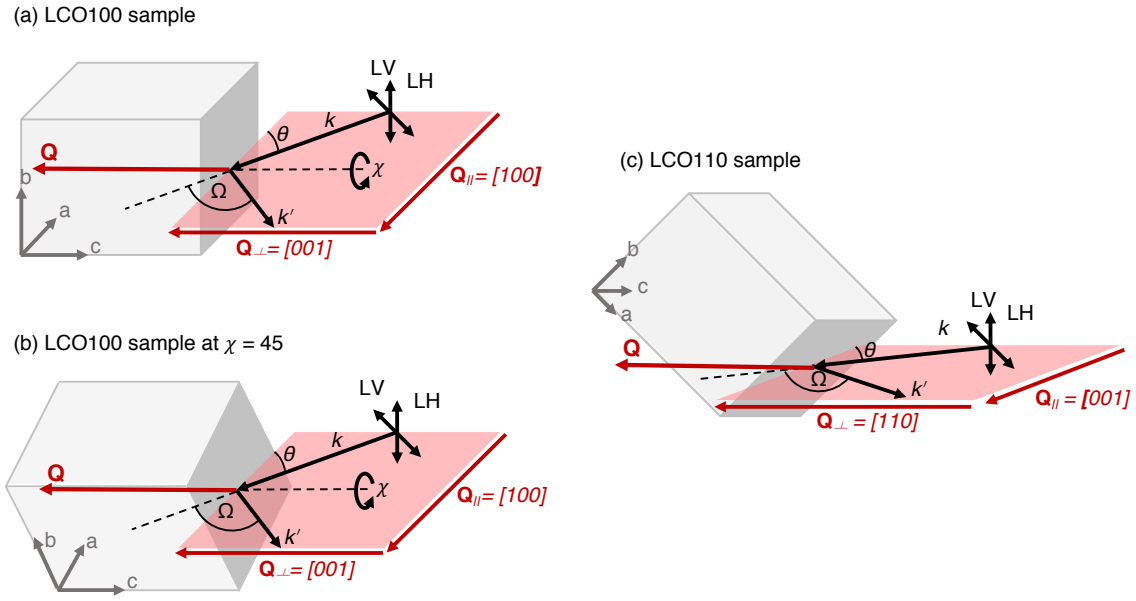

Figure 4.11: Sample orientation for RIXS experiments performed on LCO at beamline I21 at Diamond Light Source. The scattering plane is indicated in red showing the orientation to the crystal axes of the sample in grey.

[99]. The crystals were previously used in the neutron scattering measurements described in reference [44]. The samples were stored in a desiccator to prevent contamination and SQUID measurements were performed prior to the RIXS experiments to confirm that the samples remain undoped.

As noted previously, LSCO forms a low-temperature orthorhombic (LTO) crystal structure below T_{LTO} 240 K, however to allow later comparison between the three compounds in Chapter 5, the high-temperature tetragonal (HTT) I/4mmm crystal structure notation is used in which $a = b \simeq 3.8$ Å, $c \simeq 13.2$ Å. The momentum transfer is therefore $\mathbf{Q} = h\mathbf{a}^\star + k\mathbf{b}^\star + l\mathbf{c}^\star$ in reciprocal lattice units (r.l.u.). The effects of twinning or a small differences between the a and b axes are not resolvable within the energy resolution of the experiments described in this chapter.

4.2.2 Experimental setup

The experiments were all performed at the Cu L_3 edge with an incoming beam energy $\simeq$ 932 eV. RIXS spectra were measured from grazing-in to grazing-out orientation with linear horizontal (LH) / π and linear vertical (LV) / σ polarisation. The samples were cleaved in vacuum and the measurements were performed at $T = 20$ K.

Two different samples were measured in these experiments, Fig. 4.11 shows the orientation

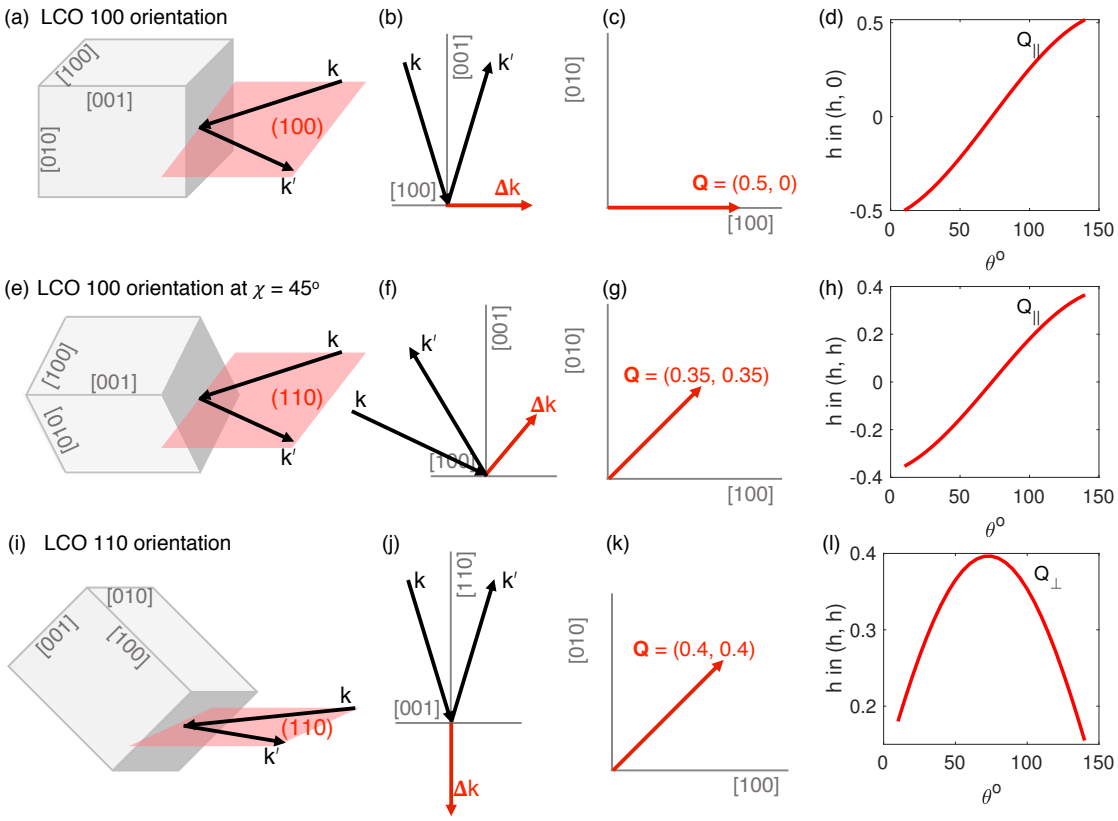

Figure 4.12: Details of the LCO100 and LCO110 samples and the experimental geometries which are accessed with them showing in panels (a), (e) and (i), the scattering plane (red) in relation to the crystal axes of the samples (grey). Panels (b), (f) and (j) show the projection of the scattering vector to the high symmetry directions. Panels (c), (g) and (k) show the region of the Brillouin zone which is probed and panels (d), (h) and (l) show the wavevector-transfer $\mathbf{Q}$ measured in (h,h) for the range of incident angles θ that were probed.

of the scattering plane, indicated in red, to the crystal axes for each orientation measured with the samples. The first, "LCO100" sample, uses the typical RIXS geometry described in Section 3.3.5, the crystals were cut into posts measuring approximately 1mm x 1 mm x 2mm with the c-axis of the crystal along the long edge. The samples were glued perpendicular to the beam, exposing the planes $\mathbf{Q}_\perp = [001]$ and $\mathbf{Q}_\parallel = [100]$ as shown in Fig. 4.11 (a). This sample is optimised to measure the [100] plane where the sample is aligned along the $\mathbf{Q}_\parallel$ plane which allows access to $(h,0)$ from $(-0.5,0)$ to $(0.5,0)$ as shown in Fig. 4.12 (a-c). However, rotating χ around the c-axis in this sample also gives access to (h,k) from $(-0.35,-0.35)$ to $(0.35,0.35)$, as shown in Fig. 4.11 (b) and Fig. 4.12 (e-g). In the second, "LCO110" sample, the crystals were cut with the same dimensions but with the a-axis along the long edge and were glued on a wedge exposing a face at 45° to the beam. This exposes the planes $\mathbf{Q}_\perp = [110]$ and $\mathbf{Q}_\parallel = [001]$ as shown in Fig. 4.11 (c). In this orientation, the $\mathbf{Q}_\perp$ projection is chosen in which momentum transfers are accessed further along the (h,k) direction to $(h,k) = 0.4$, as shown in Fig. 4.12 (i-k).

Fig. 4.12 (d), (h) and (l) show the range in $\mathbf{Q}$-transfer which can be probed in the two

orientations for the range of θ that is measured. In the LCO110 orientation **Q** varies sinusoidally with incident angle θ,

$$k_\perp = 4\pi\lambda \sin\left(\frac{\Omega}{2}\right)\sin\left(\frac{\pi+\Omega}{2}-\theta\right). \tag{4.23}$$

The self-absorption and RIXS cross-section can therefore be different for neighbouring points in **Q** which makes dealing with these prefactors particularly important. The following sections describe methods to remove the effects of self-absorption and the RIXS cross-section to reveal the underlying excitations.

4.3 Results: orbital excitations

All of the spectra measured in the RIXS experiments are plotted together in a RIXS intensity map as a function of energy and **Q** in Fig. 4.13 showing the full excitation range. The data are dominated by strong orbital excitations between 1.5 and 3 eV with low energy excitations visible below 0.5 eV. Data from the LCO110 orientation in the right panels of Fig. 4.13 demonstrate the importance of correcting the prefactors to the RIXS intensity. The data are plotted at a function of **Q** but the prefactors vary as a function of the scattering angle θ, this is particularly important in the LCO110 sample as **Q** does not vary linearly with θ (as shown in Fig. 4.12) and hence the prefactors to the intensity can vary considerably between neighbouring **Q**-points. The effect of the prefactors can also be seen in the asymmetry between negative and positive **Q** and data measured with different incident polarisation.

4.3.1 Crystal field theory calculations

The RIXS intensity of the *dd*-excitations can be compared to well understood values of the orbital intensities calculated on a single-ion basis with crystal field theory (CFT). The calculations are made using the Quanty package described in Section 4.1.2 [177].

The theoretical basis of the Quanty package is described in Section 4.1.2. In practice, the LCO system is approximated as a single ion in an effective electric potential formed by the crystal field. The calculations are performed by defining a basis and operators for the Cu^{2+} $2p$ and $3d$ states and calculating RIXS transitions between them. The Cu^{2+} basis has D4h symmetry and transitions are defined from the Cu $3d$ hole in the $d_{x^2-y^2}$ orbital to the d_{z^2}, d_{xy}, d_{xz} and d_{xy} orbitals. The interaction tensors which act on the basis are defined as follows. U_{dd} describes the on-site Coulomb repulsion between $3d$ electrons,

$$U_{dd} = \sum_{i\neq j}\frac{1}{2}\frac{e^2}{|r_i - r_j|}, \tag{4.24}$$

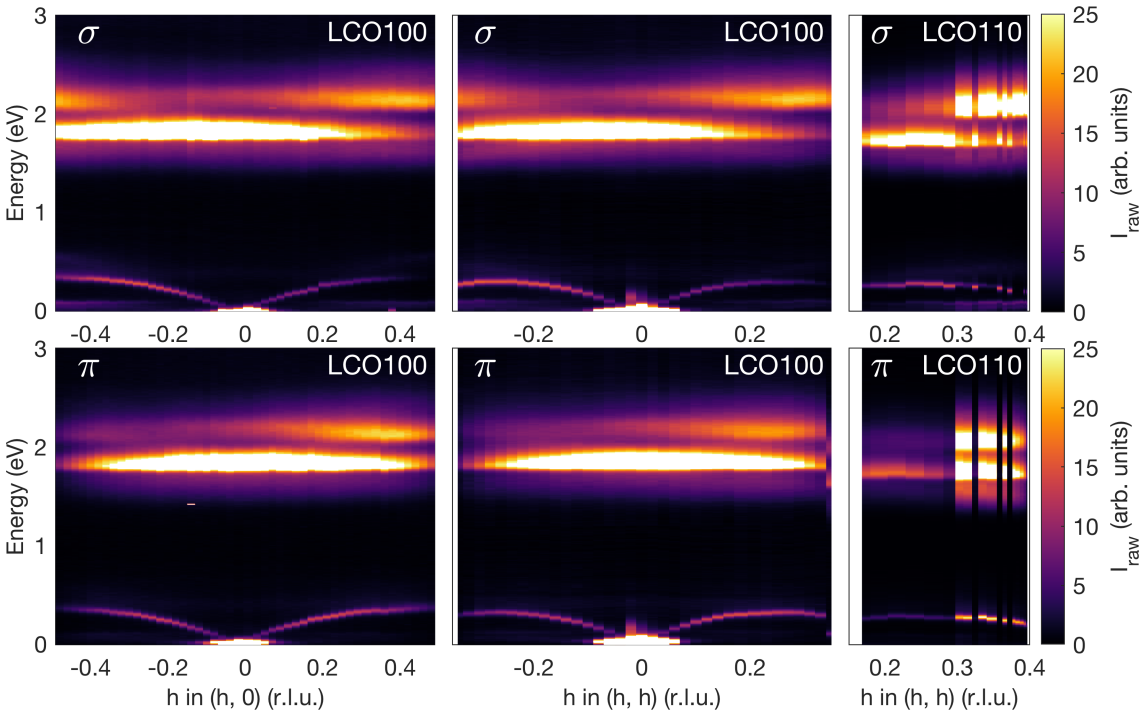

Figure 4.13: RIXS intensity maps as a function of energy and **Q** showing measurements on LCO along the $(h,0)$ and (h,k) direction with σ and π polarisation in the LCO110 and LCO100 orientation showing the full excitation range. Jumps in the LCO110 data reflect the non-linear dependence of prefactors to the RIXS cross-section.

defined as a sum over all electrons i and j. This can be expanded as a sum of spherical harmonics which for the simple case of Coulomb repulsion within one shell includes a single radial component F_{r_i,r_j}. The Coulomb repulsion can therefore be defined,

$$U_{dd} = \sum_{k,m} Y_{\theta_i,\phi_i} Y^{\star}_{\theta_j,\phi_j} F_{r_i,r_j}. \tag{4.25}$$

The angular part can be solved analytically but, F_{r_i,r_j}, must be defined with three Slater integrals, F^0 which is the interaction between two d electrons and F^2 and F^4 which represent interactions with a transfer of angular momentum 2 or 4. F^0_{dd}, F^2_{dd}, F^4_{dd} are known energy differences between multiplets in the d bands given in Table 4.1.

The next interaction is spin-orbit coupling in the respective $3d$ bands which is defined as an interaction between orbital and spin operators, l and s,

$$H_{\mathrm{SO}} = \zeta \sum_i l_i \cdot s_i. \tag{4.26}$$

ζ is an atom dependent constant which can be approximated as a spherical potential defined for the d electrons as ζ_d in Table 4.1.

All of these parameters are defined for both the ground state, $2p^6 3d^9$ and excited state, $2p^5 3d^{10}$. A summary of the parameters used in the model is given in Table 4.1 where the values for the Slater integrals are from reference [171].

	F^0_{dd}	F^2_{dd}	F^4_{dd}	F^0_{pd}	F^2_{pd}	G^1_{pd}	G^3_{pd}	ζ_d	ζ_{2p}
$2p^6 3d^9$	0	12.854	7.980					0.102	
$2p^5 3d^{10}$	0	13.611	8.457	0	8.177	6.169	3.510	0.124	13.498

$d_{x^2-y^2}$ (eV)	d_{z^2}(eV)	d_{xy} (eV)	d_{xz}(eV)	d_{yz}(eV)
0	1.5	1.8	2.1	2.1

Table 4.1: Parameters used in the single-site multiplet crystal field theory calculations of the local interactions in LCO. Parameters are from references [171] and [119].

The crystal field is defined by the energies of the d orbitals providing a potential which removes the degeneracy of the electrons. The crystal field Hamiltoniam can be described by expanding the potential on spherical harmonics giving,

$$H_{\mathrm{CF}} = \sum_{\tau_1,\tau_2} \sum_{k,m} A_{k,m} \left\langle Y_{l_1,m_1} \right| C_{k,m} \left| Y_{l_2,m_2} \right\rangle a^\dagger_{\tau_1} a_{\tau_2}, \tag{4.27}$$

where τ represents the quantum numbers n, l and m and spin σ. Each orbital has different relationships between the expansion coefficients, hence Quanty takes the relative energies of the orbitals, which are known from spectroscopic experiments[119], and expands them on the relevant spherical harmonics. This allows us to define a potential, $A_{k,m}$, for the $D4_h$ symmetry. The orbitals energies used for these calculations are shown in Table 4.1 and are from reference [119].

Finally, a magnetic field is applied in the (110) direction of magnitude to account for the AFM ordering, this is simulated by applying an energy difference of 0.03 meV between the two directions. The total Hamiltonian for the ground states is therefore,

$$\begin{aligned} H_{\mathrm{ground}} =& F^0_{dd} \cdot F^0 + F^2_{dd} \cdot F^2 + F^4_{dd} \cdot F^4 + \zeta_d \sum_i (l_i \cdot s_i) \\ &+ \sum_{\tau_1,\tau_2} \sum_{k,m} A_{k,m} \left\langle Y_{l_1,m_1} \right| C_{k,m} \left| Y_{l_2,m_2} \right\rangle a^\dagger_{\tau_1} a_{\tau_2} + B \cdot (2S_x \cdot L_x) + B \cdot (2S_y \cdot L_y). \end{aligned} \tag{4.28}$$

Energy dependent spectra are calculated via the Green's function,

$$G(\omega) = \left\langle \psi_i \right| T^\dagger \frac{1}{\omega - H + i\Gamma/2} T \left| \psi_i \right\rangle, \tag{4.29}$$

where T is a transition operator that depends on the spectroscopic technique. Here the spectroscopic data are approximated by calculating transitions between the two ground states. In RIXS we must include core-hole interactions which occur in the intermediate state and effect the energy of the excitations. H is therefore defined as the x-ray absorption spectroscopy (XAS) Hamiltonian which is defined as,

$$H_{\mathrm{XAS}} = H_{\mathrm{ground}} + \frac{e}{m} p \cdot A + \frac{e^2}{2m} A \cdot A. \tag{4.30}$$

This Hamiltonian describes the interaction between the system in the ground state and the incident photon with vector field A. Equivalently to the definitions above, the Coulomb interaction between the $3d$ electrons and the $2p$ core-hole is described by the interaction tensor U_{pd} defined by Slater integrals F^0_{pd}, F^2_{pd}, G^1_{pd} and G^3_{pd}. The additional G integrals represent the exchange Coulomb interaction which occurs between the $2p$ and $3d$ orbitals in the intermediate state. As before, spin-orbit coupling between the $2p$ and $3d$ in the intermediate state is given by ζ_{2p}. The total Hamiltonian for the XAS spectra is therefore,

$$H_{\mathrm{XAS}} = H_{\mathrm{ground}} + F^0_{pd} \cdot F^0 + F^2_{pd} \cdot F^2 + G^1_{pd} \cdot G^1 + G^3_{pd} \cdot F^2 + \zeta_{2p} \sum_i (l_i \cdot s_i). \tag{4.31}$$

For RIXS it is necessary to also include resonant effects which are approximated as a third order Green's function of the form of Eqn. 4.29.

Using the method outlined above, the intensity of each orbital is calculated for each set of experimental conditions: horizontal and vertical polarisation in the $(h,0)$ and (h,h) directions for the LCO100 and LCO110 samples.

Fig. 4.14 (a) shows the energy of the d orbitals relative to the $d_{x^2-y^2}$ ground state. Fig. 4.14 (b) shows the relative intensity of the dd orbitals, showing first calculated CFT (broadened by 150 meV, the fitted FWHM of the dd-excitations in experimental data) and measured RIXS peaks for an example spectra at $\theta = 120°$ along the $(h,0)$ direction with σ polarisation. The peaks are identified as the d_{z^2} orbital in blue, d_{xy} in green and d_{xz}/d_{yz} in pink. The orbitals are split due to the presence of a magnetic field in the (h,h) direction and spin-orbit coupling of the d_{z^2} orbital. Fig. 4.14 shows that the new RIXS measurements are generally able to separate the orbital excitations more clearly than previous work such as that in Fig. 4.3.

The CFT and RIXS spectra are modelled with 6 pseudo-Voigt functions which we define as,

$$PV(\omega) = \frac{1}{2} A \mathrm{e}^{-\frac{(\omega-\omega_0)^2}{2\sigma^2}} + \frac{1}{2} \frac{A\sigma^2\sqrt{2\ln 2}}{(\omega-\omega_0)^2 + (\sigma\sqrt{2\ln 2})^2}, \tag{4.32}$$

where A is the shared peak height and σ is the width where the full-width half maximum FWHM $= 2\sigma\sqrt{2\ln 2}$. In the RIXS spectra, significant spectral weight is present at higher energy centred at 2.4 eV. This peak is seen in previous work and has been attributed to oxygen vacancies which alter the ligand field acting on the Cu ions [119]. This peak is fitted with an additional pseudo-Voigt function and is shown in yellow. The calculated and measured spectra for all directions, polarisations and orientations are shown with their fit functions in Appendix A.

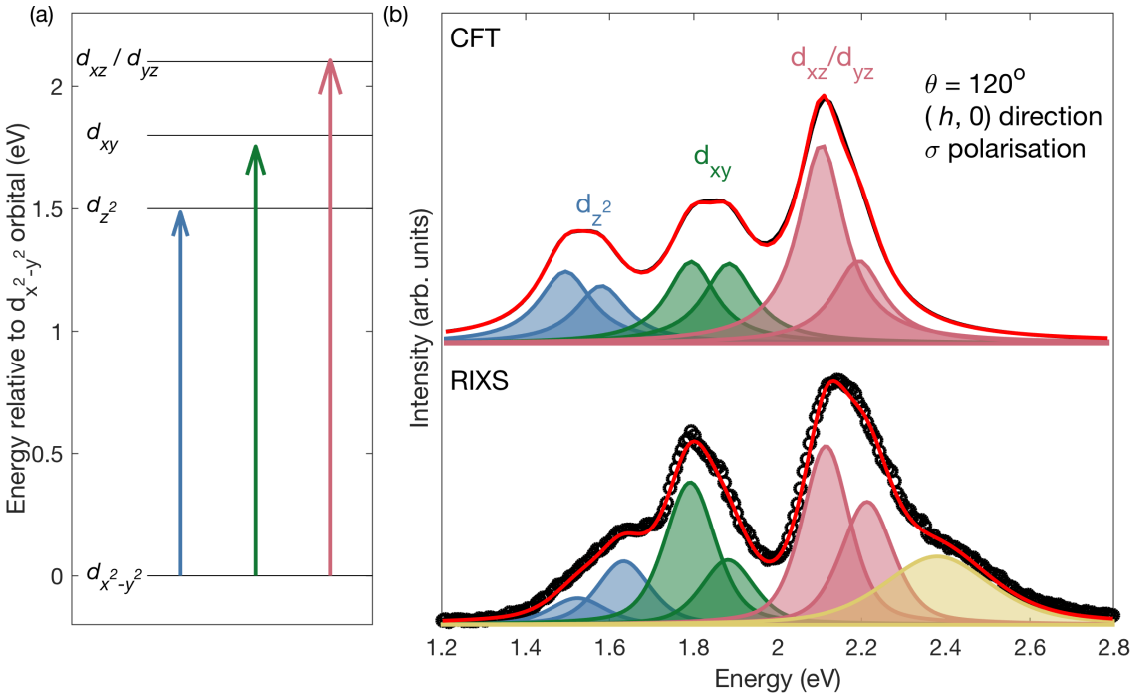

Figure 4.14: Comparison of the *dd* intensity calculated from crystal field theory and measured with RIXS, showing (a) the origin of the *dd* transitions between orbital states and (b) the *dd* peaks calculated from CFT and RIXS (in black) and the Pseudo-Voigt functions which are used to fit the individual orbitals (in blue, green, pink and yellow). The spectra are offset for clarity.

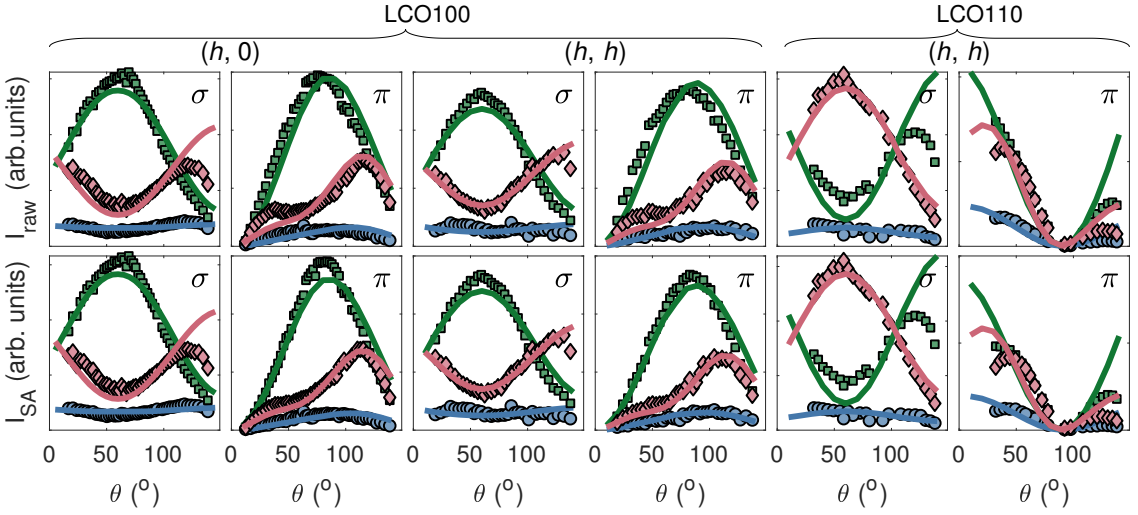

Figure 4.15: *dd*-excitation orbital intensities as a function of incident photon angle θ showing the dependence for the $(h,0)$ and (h,h) directions for σ and π polarisation in the LCO100 and LCO110 sample. Solid lines show the intensities calculated from crystal field theory and shapes from RIXS measurements. The d_{z^2} orbital is indicated with blue circles, d_{xy} with green squares and d_{xz}/d_{yz} with pink diamonds. The top panels show un-normalised data and the bottom panels show data normalised using the self-absorption correction.

4.3.2 Self-absorption correction

Next, the intensity of the measured and calculated *dd* excitations is compared. This serves as a test of the self-absorption correction method described in Chapter 3. In this instance the self-absorption calculation assumes that the polarisation of the scattered photons is unchanged. This does not reflect the full complexity of the excitations recently reported by Fumagalli *et al.* [162], however, the total absorption at this energy is low and the effect of polarisation is small and therefore it is assumed that this approximation is suitable for our purposes.

Fig. 4.15 shows a comparison of the measured and calculated *dd* excitation intensity. For simplicity the plot shows the sum of the intensity for each orbital. The top panels show the un-normalised intensities and the bottom panels shows the intensity after accounting for self-absorption effects. It can be seen that the scattered photons are not strongly self-absorbed in the energy range of the dd excitations hence there is not much difference between the two rows in Fig. 4.15, however, both rows match the data fairly well. Instances where the measured and calculated data do not fully align are likely to be due to inaccuracies in the self-absorption correction. However, agreement is generally good.

Fig. 4.15 shows that there are strong geometrical contributions to the intensity of the *dd*-excitations. This is due to the orientation of the incident photon to the orbitals shown in Fig. 4.1. The agreement between the calculated and measured data suggests that the single-ion model can capture this geometrical dependence well.

It should be noted that in Fig. 4.15 the calculated orbital intensities have been separately scaled to their respective orbitals to more clearly illustrate the effect of the self-absorption correction. The relative intensity of the orbitals is therefore not shown. In fact, the calculation consistently overestimates the relative intensity of the d_{z^2} orbital as seen in the example spectra in Fig. 4.14. Fig. 4.16 shows the calculated and measured orbital intensities, including both crystal-field-split states, where the total intensity of the measured orbitals is scaled to the total intensity of the calculated orbitals. The plot clearly shows the persistent over-estimation of the intensity of the d_{z^2} orbital in the calculations in comparison to the measured data.

The relative intensities of the orbital excitations is likely to be dependent on the fit as the proximity of the peaks makes it difficult to attribute spectral weight to the correct orbital. However, the orbital excitations broadly follow the same θ-dependence in the calculated and measured data.

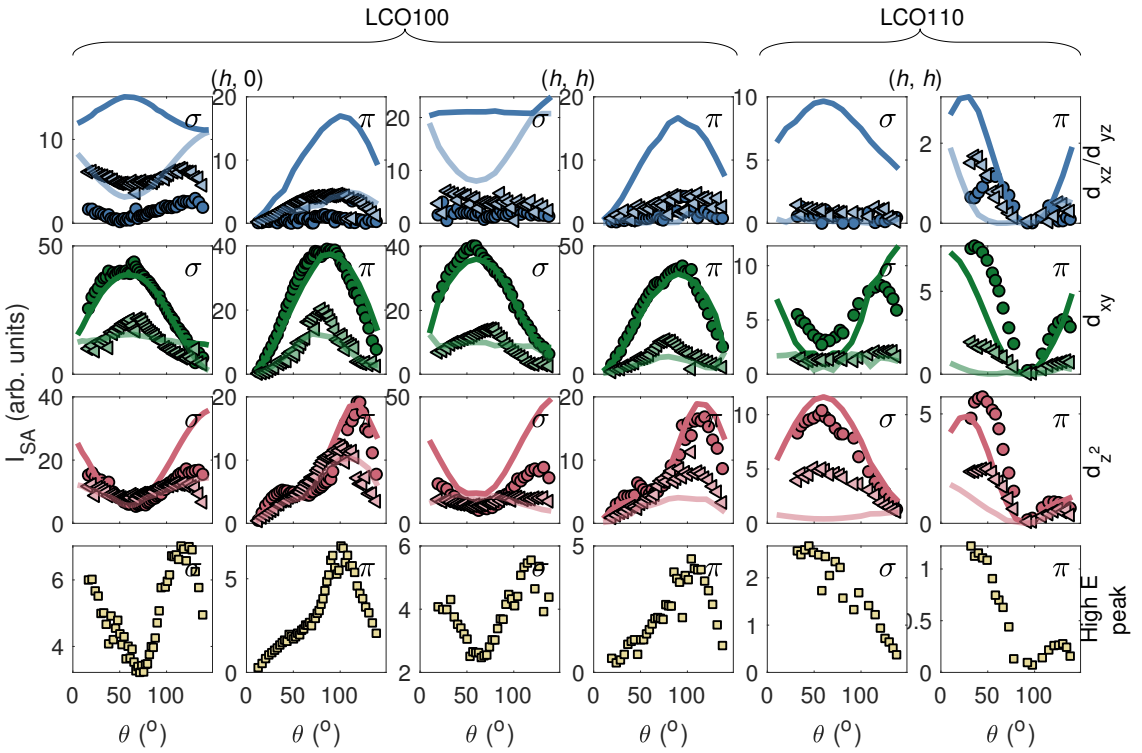

Figure 4.16: *dd*-excitation orbital intensities as a function of incident photon angle θ showing the dependence for the $(h,0)$ and (h,h) directions for σ and π polarisation in the LCO100 and LCO110 sample. Solid lines show the intensities calculated from crystal field theory and shapes from RIXS measurements. The d_{xz}/d_{yz} orbital is indicated in blue, d_{xy} in green and d_{z^2} in pink. The lower and higher energy of each *dd* orbital is plotted with darker circles and lighter triangles respectively. The additional peak is indicated with yellow squares. All data are adjusted using the self-absorption correction.

4.4 Results: low energy excitations

Having demonstrated the approximate agreement between local single-ion model calculations and self-absorption corrected RIXS data, we next move on to the low energy excitations. Fig. 4.17 shows the un-normalised RIXS spectra at low energy plotted as a function of **Q** where the intensity corresponds to the RIXS response. In the low energy region, sharp resolution limited peaks dominate the spectra between 0 and 400 meV which are identified as single magnon excitations. Broader peaks are also seen at higher energy (up to 600 meV) which are interpreted as multimagnons. The excitations are identified by comparison with INS measurements. The spectra also show phonon excitations below 100 meV, most clearly in σ-polarised spectra where charge scattering is favoured and in which two phonon branches can be resolved. The spectra contain elastic peaks, which have particularly high intensity at θ = 70 (**Q** $\simeq$ 0 in the LCO100 orientation and **Q** $\simeq$ 0.4 in the LCO110 sample) due to the specular reflection.

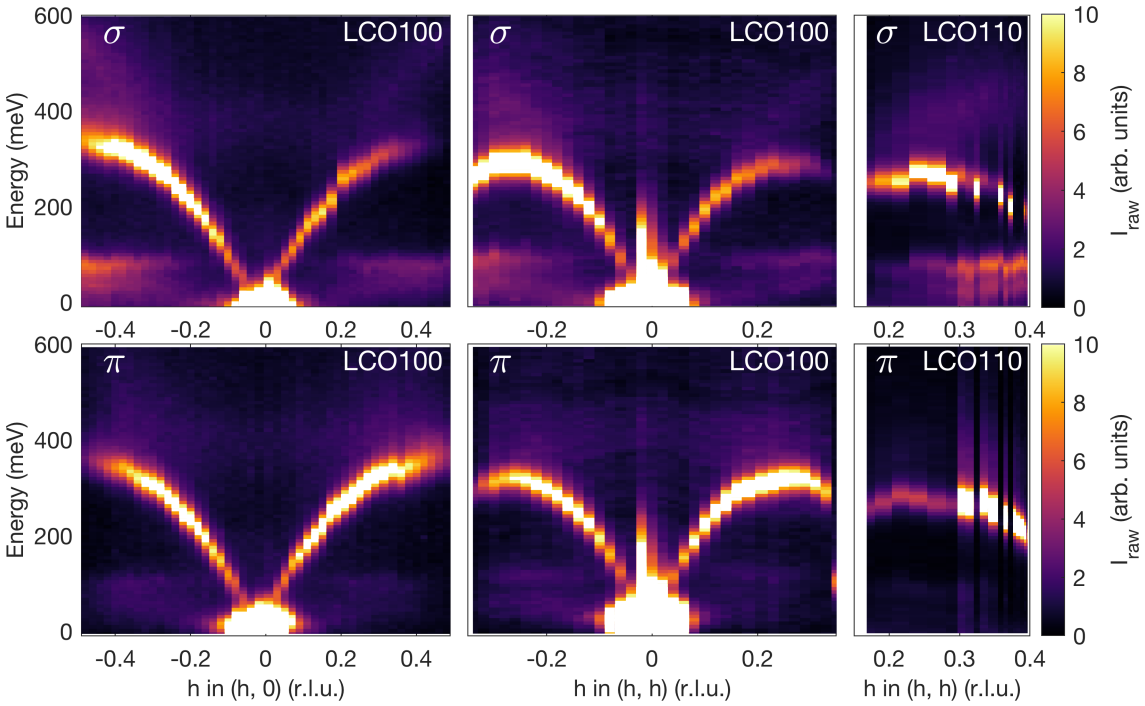

Figure 4.17: Low energy RIXS intensity maps as a function of energy and **Q** showing measurements on LCO along the $(h,0)$ and (h,k) direction with σ and π polarisation for the LCO110 and LCO100. Jumps in the LCO110 data reflect the non-linear dependence of prefactors to the RIXS cross-section.

4.4.1 Data fitting

In order to capture the variety of excitations which are observed, the data are modelled between –80 and 800 meV. The elastic peak and phonons are modelled with Gaussian peaks and the magnetic excitations are modelled with the response function of a damped harmonic oscillator (DHO).

Damped Harmonic Oscillator model

Lamsal and Montfrooij [221] point out that using a Lorentzian function to fit the magnetic excitations, as has been common in previous RIXS work, imposes a limitation on the damping factor γ which requires $\gamma/2$ to be less than ω_0, the frequency of the undamped excitation. This assumption is not always valid for the doped cuprates as is discussed in Chapter 5. Although the undoped compositions described in this chapter exhibit excitations which can be described with a function well within the Lorentzian limit, a generic DHO model is used to describe the data in order to perform consistent analysis and allow for later comparison between compositions. This approach has been adopted by several recent RIXS studies in cuprates [109, 222, 221, 161]. In a mechanical system, the DHO equation is given by [223],

$$\ddot{x} + \omega_0^2 x + \gamma \dot{x} = f/m. \tag{4.33}$$

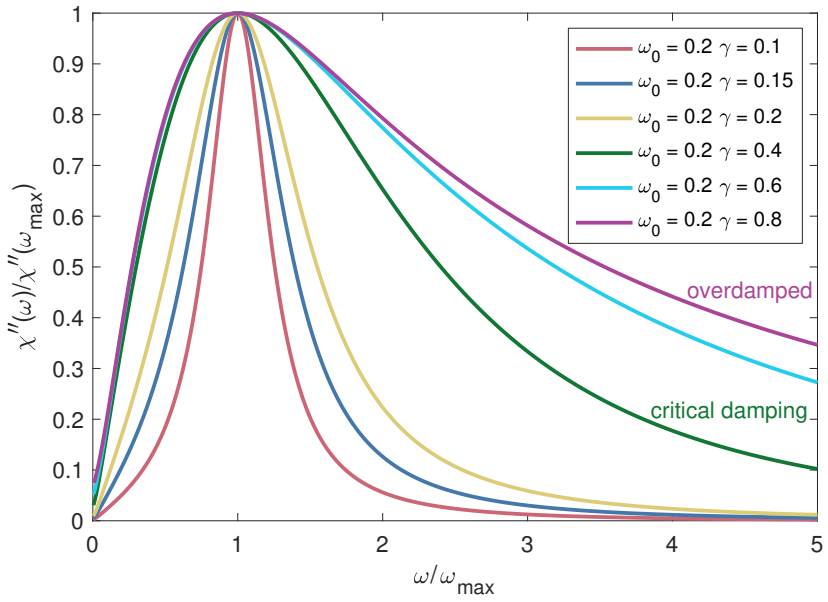

Figure 4.18: The form of the damped harmonic oscillator response for a range of γ showing that the function spans the phase from under to overdamped behaviour. The DHO response function is normalised the peak maximum position $\omega_{\max}$

The solutions of this equation are two poles,

$$\omega = \pm\left[\omega_0^2 - \left(\gamma^2/4\right)\right]^{\frac{1}{2}} = \pm\omega_1 - \frac{i\gamma}{2}. \tag{4.34}$$

Unlike the Lorentzian model, these solutions span the entire parameter space for ω_0 and γ. If $\omega_0 \geq \gamma/2$, ω_1 is real and describes the frequency of a propagating pole. If $\omega_0 \leq \gamma/2$, ω_1 is imaginary and the system is overdamped.

In the case of an excitation with wavevector $\mathbf{Q}$, the imaginary part of the response function is given by,

$$\chi''(\mathbf{Q},\omega) = \frac{\chi'(\mathbf{Q})\,\omega_0^2(\mathbf{Q})\,\gamma(\mathbf{Q})\,\omega}{\left[\omega^2 - \omega_0^2(\mathbf{Q})\right]^2 + \omega^2\gamma^2(\mathbf{Q})}, \tag{4.35}$$

where $\chi'(\mathbf{Q})$ is the real part of the susceptibility at zero frequency.

As the multimagnon peak contains multiple orders of the spin response its shape is not well defined. $\omega_{\max}$ therefore describes the peak position of the total excitation spectral weight,

$$\omega_{\max} = \frac{1}{6}\sqrt{12\omega_0^2 - 6\gamma^2 + 6\sqrt{\gamma^4 - 4\gamma^2\omega_0^2 + 16\omega_0^4}}. \tag{4.36}$$

Fig. 4.18 shows imaginary part of the response, $\chi''(\mathbf{Q},\omega)$ calculated from Eqn. 4.35 normalised to the response calculated with $\omega_{\max}$. The response is plotted as a function of $\omega/\omega_{\max}$ for a range of γ spanning the range of damping seen in the measurements in this thesis. In LCO, ω_0 is generally greater than $\gamma/2$ and Eqn. 4.35 takes a form similar to a Lorentzian function, such as the pink line in Fig. 4.18. As described above, the model also allows damping up to and beyond

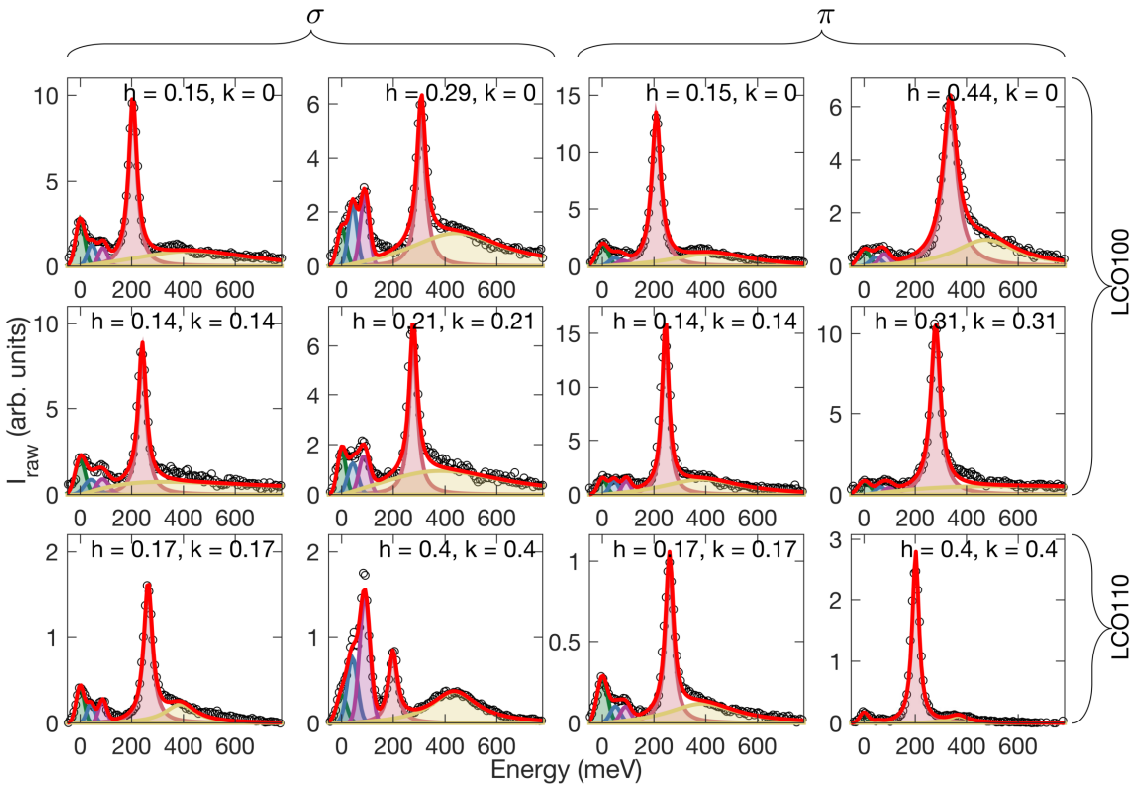

Figure 4.19: Example fits to the low energy excitations in LCO showing the total fit in red with the constituent parts beneath: the elastic peak and phonons are fit with Gaussian functions, shown in green, blue and purple respectively. The magnetic excitations are fit with a damped harmonic oscillator function, shown in pink for the single magnon and yellow for the multimagnon.

critical damping, $\omega_0 = \gamma/2$, which has a shape as shown in the green line in Fig. 4.18. This is important in the analysis of data from damped compositions as in Chapters 5 and 6.

Example fits for the different direction, polarisations and orientations are shown in Fig. 4.19 and full data are displayed in Appendix A.

4.4.2 Magnetic excitations

Energy dispersion

The energy dispersion extracted from the fits is shown in Fig. 4.20. Clearly dispersive excitations are resolved for both the single-magnon (pink) and multimagnon (yellow). The energy of the magnon pole, ω_0, extracted from the RIXS data is compared to the single magnon energy calculated from a next-nearest neighbour SWT model (Eqn. 4.12) as parametrised with INS [44]. The parameters used in the SWT model are summarised in Table 4.2. In the (h,h) direction, agreement is very good, however, in the $(h,0)$ direction the RIXS measurements appear to observe the spin fluctuations dispersing to a higher energy in the positive **Q** branch but not the negative branch, this may indicate a slight misalignment of the crystal axes. Fig. 4.21 shows a

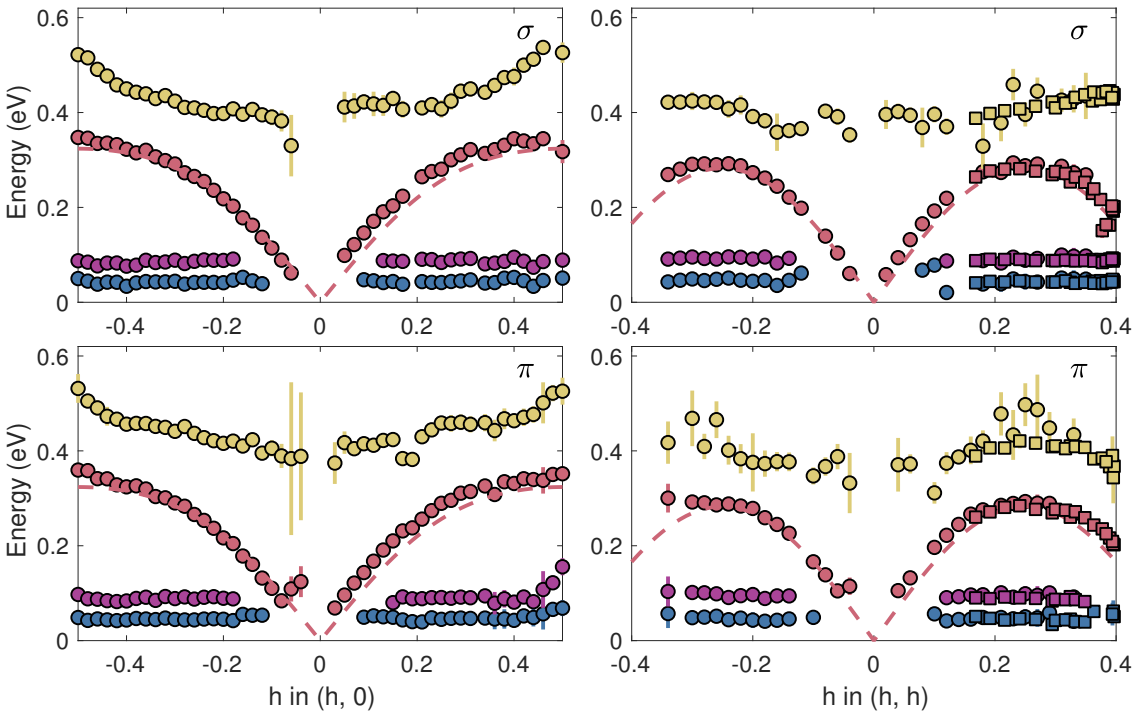

Figure 4.20: Energy dispersion for all the low energy excitations measured in LCO with RIXS. ω_0 from the magnon fit is indicated in pink, the energy position of the phonons in blue and purple and $\omega_{\max}$ of the multimagnons in yellow. Excitations measured in the LCO100 and LCO110 samples are shown as circles and squares respectively. A plot of the single magnon energy calculated from a next-next-nearest neighbour SWT model modified to fit INS data [44] is shown as a dashed line.

Exchange constant	Energy (meV)
J	143
J'	2.9
J''	2.9
J_c	58

Table 4.2: Exchange constants used in the spin-wave theory model of the spin fluctuations in LCO, parameters established from INS [44].

comparison of the lineshape of the excitation measured with RIXS and INS in which the RIXS spectra is seen to have significantly more spectral weight at a higher energy but the rising edge of the excitation is closely matched. From this it can be concluded that the energy dispersion of the excitations is broadly the same as measured by the two techniques but the distribution of spectral weight may be different.

Dynamical spin susceptibility

This section describes calculations to extract the intensity of the spin fluctuations by considering the two components which preface the magnetic excitations. Firstly, the self-absorption which is accounted for as in Eqn. 3.15 yielding I_{SA} and secondly, the RIXS cross-section due to local

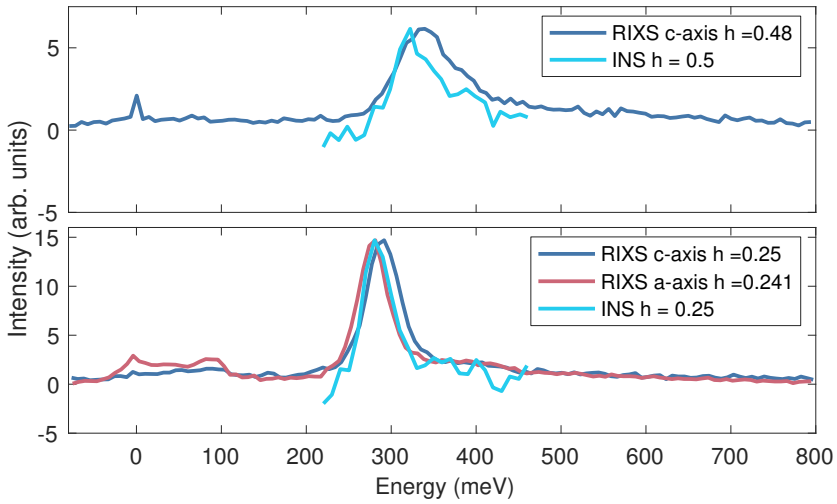

Figure 4.21: Comparison of the magnon lineshape measured with RIXS in the LCO100 (dark blue) and LCO110 (pink) orientation and with INS (light blue) [44], showing spectra measured close to (1/2,0) and (1/4,1/4).

spin-flip matrix element, σ_{CFT}, which is calculated with CFT calculations of the local magnetic interactions. This gives an approximation of the underlying spin fluctuation measured with RIXS,

$$I_{\mathrm{RIXS}} = \frac{I_{\mathrm{SA}}}{\sigma_{\mathrm{CFT}}}. \tag{4.37}$$

In the low energy regime the effect of self-absorption is particularly significant making it more important to correctly account for the polarisation of the scattered photons. For the single magnon excitations the polarisation of the scattered light is assumed to be flipped due to transfer of angular momentum to the excitation. While the exact interaction of the photon polarisation with the angular momentum of the magnetic excitations is unclear, there is experimental evidence that the single magnetic excitations are indeed associated with a change of linear polarisation [224, 162]. As discussed in Chapter 3, recent work suggests that the majority of spectral weight in the region of the magnon is associated with magnetic excitations. Any charge component remaining after this analysis is likely to be small but would result in an overestimation of the susceptibility.

On this basis, Fig. 4.22 (a-f) shows the magnon intensity which is an integration of the fitted magnon function yielding I_{raw}. I_{raw} is shown in white and the self-absorption corrected intensity, I_{SA}, is shown in pink. The calculated RIXS spin-flip cross-section is shown in black. The overall shape of the cross-section matches the self-absorption corrected data remarkably well. The envelope of the RIXS response is well captured in the calculation.

The final step to remove the RIXS prefactors is to divide the magnon intensity by the local RIXS spin-flip cross-section, σ_{CFT}, and assume the remaining intensity is due to the long-range

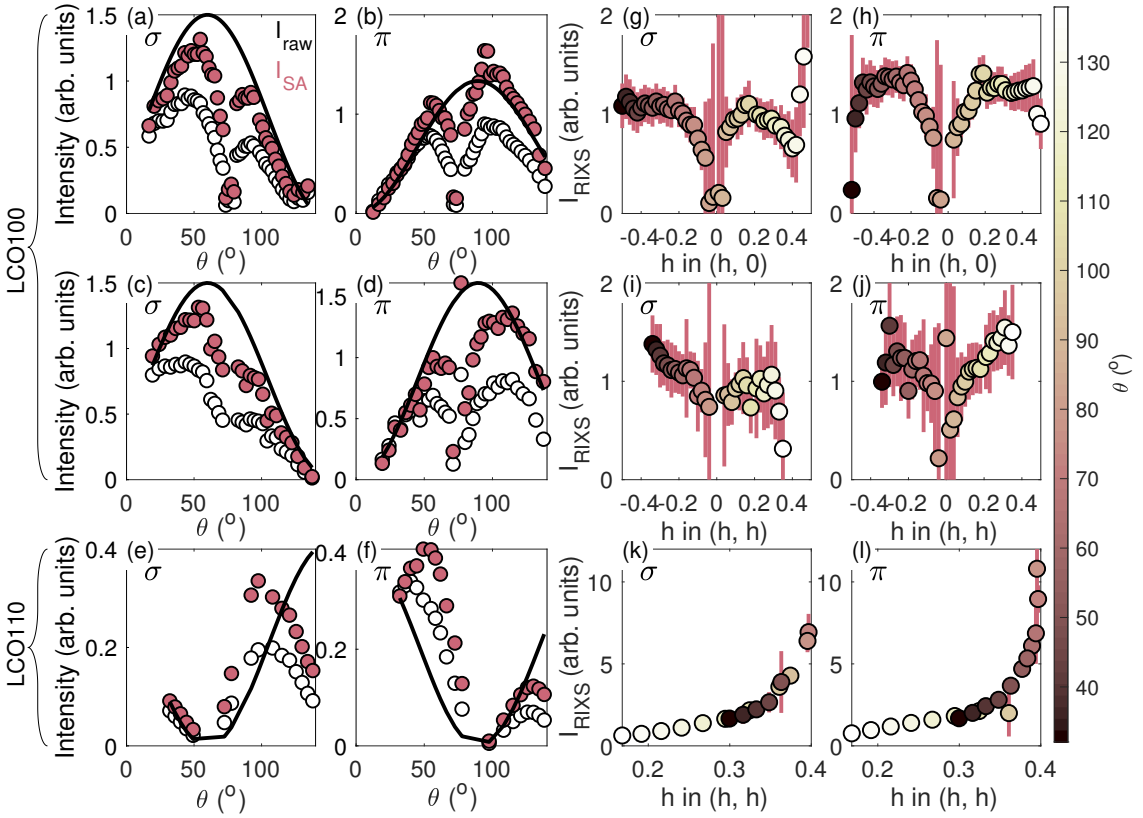

Figure 4.22: Intensity of the magnetic excitations in LCO. Panels (a-f) show the raw magnon intensity in white, extracted from the peak of a damped-harmonic oscillator fit to RIXS data and data corrected for the effects of self-absorption in pink. The solid black line shows the expected RIXS spin-flip cross-section of the magnetic excitations calculated from crystal field theory. Panels (g-l) show the data divided by the local RIXS cross-section. The colour of the data point shows the incident scattering angle θ.

spin fluctuations. Fig. 4.22 (g-l) shows the spin fluctuation intensity, I_{RIXS}, following this correction.

As mentioned above, the situation is more complex for the LCO110 data because the relationship between the perpendicular projection of the wavevector $\mathbf{Q}_\perp$ and incident angle θ is sinusoidal. Therefore the same value of $\mathbf{Q}_\perp$ is measured at multiple incident angles, as shown in Fig. 4.12 (h). I_{RIXS} is therefore plotted as a function of $\mathbf{Q}$ in Fig. 4.22 where the marker colour indicates θ. This plot shows that equivalent $\mathbf{Q}$ points measured at different θ have closely matching intensities suggesting that the correction procedure is effective.

Another indicator of the success of the correction technique is the relative symmetry which is achieved between the negative and positive $\mathbf{Q}$ values and between measurements made with σ and π polarisation. After removing the effects of geometry, polarisation and local spin interactions, reasonably good agreement is seen between the negative and positive branches and σ and π polarisations.

The correction method results in particularly large error bars where the RIXS cross-section

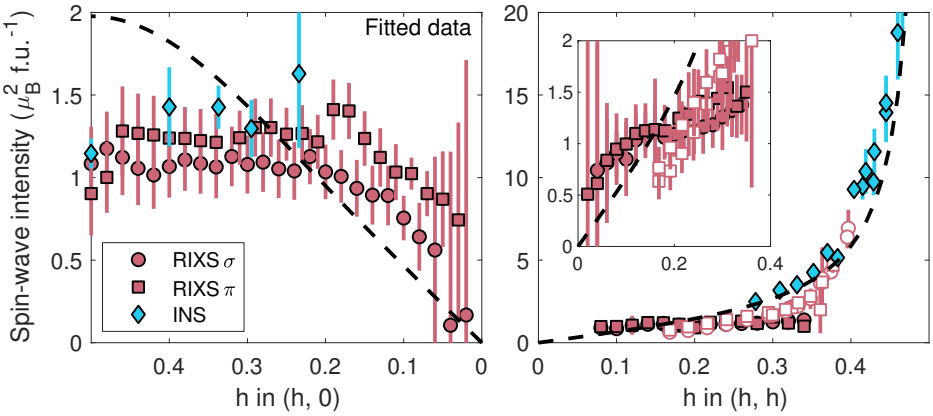

Figure 4.23: The spin-wave intensity extracted from fits to RIXS measurements. The data are corrected for the effects of self-absorption and the local magnetic cross-section. RIXS data from the LCO100 are indicated in pink and LCO110 in white, σ and π polarisation is indicated with circles and squares respectively. The data are compared to INS data by Headings *et al.* [44] (blue diamonds) as well as a next-next nearest neighbour spin-wave intensity modelled from the INS data (black dashed line).

approaches zero. It is therefore assumed that in the AFM scheme, excitations in **Q** are equivalent to -**Q**. This allows only the regions of high intensity to be selected in the remaining analysis, these are σ grazing-in, π grazing-out for the LCO100 data and σ grazing-out and π grazing-in for the LCO110 data.

The absolute intensity of the spin fluctuations is next scaled to SWT calculations (Eqn. 4.16 using the exchange constants in Table 4.2). This scale factor allows the RIXS data to be related to the absolute spin susceptibility and quoted in absolute units $\mu_B^2 f.u.^{-1}$. The scale factor is not **Q**-dependent therefore the relative intensity of the excitations that are measured with RIXS is preserved. In Fig. 4.23, the fully corrected magnon intensity is compared to the intensity measured with INS [44]. The region of the Brillouin zone which RIXS probes has a particularly low scattering intensity in the INS measurements so there are only a few equivalent points, hence the SWT calculation is also shown.

The new RIXS measurements match the INS data reasonably well in the $(h,0)$ direction with both showing a levelling of the intensity close to $(1/2,0)$ which is unexplained in SWT. In (h,h), the LCO110 data clearly shows the sharp increase in intensity approaching $(1/2,1/2)$. This is beginning to become apparent in the LCO100 measurements, however, the measurements do not access far enough along the (h,h) direction to clearly see the trend. This shows that the LCO110 experiment is uniquely able to access the region of rapidly increasing intensity towards $\mathbf{Q}_{\mathrm{AFM}}$.

At low **Q**, RIXS generally observes greater spectral weight than INS. This may be because the magnon fit contains some of the additional intensity from the specular reflection. The error

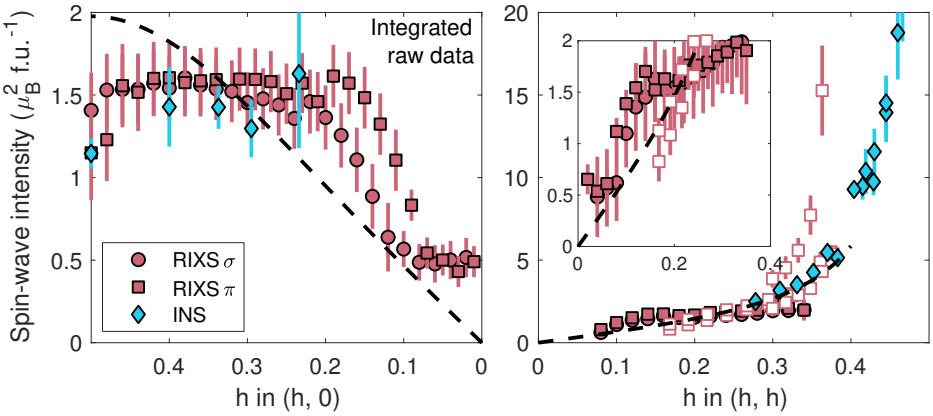

Figure 4.24: The spin-wave intensity extracted from an integration of RIXS data between 150 and 450 meV. The data are corrected for the effects of self-absorption and the local magntic cross-section. Showing a comparison to INS and SWT from reference [44]. Data are labelled as in Fig. 4.23.

bars are generally larger around $\mathbf{Q} = 0$ reflecting the uncertainty in fitting the magnon.

Consistently higher intensity is seen in the data measured with π polarisation. This is likely to be due to a failure of the self-absorption method to fully correct the data. To investigate this further, the magnon intensity extracted from an integration in the energy range 150 meV to 450 meV is plotted in Fig. 4.24. The same correction procedures are applied as in Fig. 4.23. This analysis removes any uncertainty which occurs in the fit of the data allowing direct comparison of the effect of the correction procedures. In the region $\mathbf{Q} = 0.1$ to 0.2, the discrepancy between σ and π polarisation is seen but not at higher $\mathbf{Q}$. This analysis demonstrates the difficulty of fully accounting for the cross-section. However, it is concluded that the discrepancy is within the error bars of the experiment.

Two-magnon continuum

As described in Section 4.1.2, higher order spin fluctuations can be created from the AFM ground state. The dominant higher order process is two-magnon, where two independently propagating magnetic excitations are created. Some of the processes in the two-magnon continuum are associated with a double spin flip, hence the total angular momentum is unchanged and the excitation is identified by a longitudinal response in the susceptibility. However, two-magnon processes with $\Delta S = 1$ are also possible. Two-magnon processes have been readily identified in several AFM materials, including in the $S = \frac{1}{2}$ system $Cu(DCOO)_2{\cdot}4D_2O$ (CFTD), which is analogous to LCO. This is achieved by separating the transverse and longitudinal components of the susceptibility [51]. Multimagnon processes have also been identified in LCO with RIXS at energy loss greater than the single magnon [148, 211, 111]. The higher energy magnetic

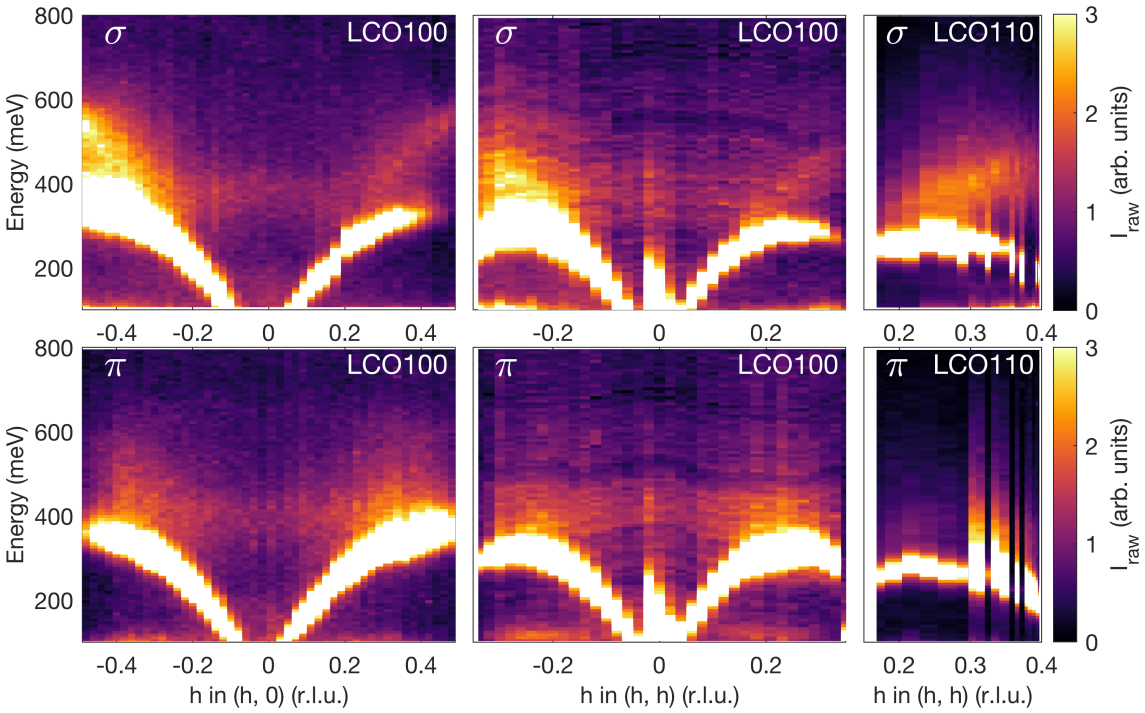

Figure 4.25: RIXS intensity map as a function of wavevector in the energy range associated with the multimagnon excitations.

continuum may also contain contributions from spinon excitations which are discussed further in Section 4.5.1. In the following sections the high energy magnetic excitations are referred to as multimagnons as higher order processes cannot be separated, however, it is assumed that the excitations are predominantly two-magnon in character.

In the RIXS data, the multimagnon peak can be well separated from the single-magnon. This is demonstrated most clearly in Fig. 4.25 where the energy and intensity range is focused on the multimagnon and a clear continuum of excitations is observed above the sharp, high intensity single magnon dispersion. However, extracting the true intensity of the multimagnon excitations is complicated because of uncertainty in both the exact nature of the self-absorption and the RIXS cross-section.

Fumagalli *et al.* [162] perform polarisation analysis on $NdBa_2Cu_3O_{7-\delta}$ (NBCO) and find that the spectral weight of the multimagnon continuum is mixed in character resulting from both $\Delta S = 0$ and $\Delta S = 1$ processes. On this basis, an approximate self-absorption correction can be made assuming that 50% of the excitations are due to spin-flip processes and 50% are unflipped.

Full calculations of the multimagnon cross-section require multiple-site calculations to account for the simultaneous creation of two magnons which are beyond the scope of this thesis. The multimagnon cross-section is therefore estimated from the single-site multiplet calculations. As a further approximation, it is assumed that the multimagnon cross-section is comprised

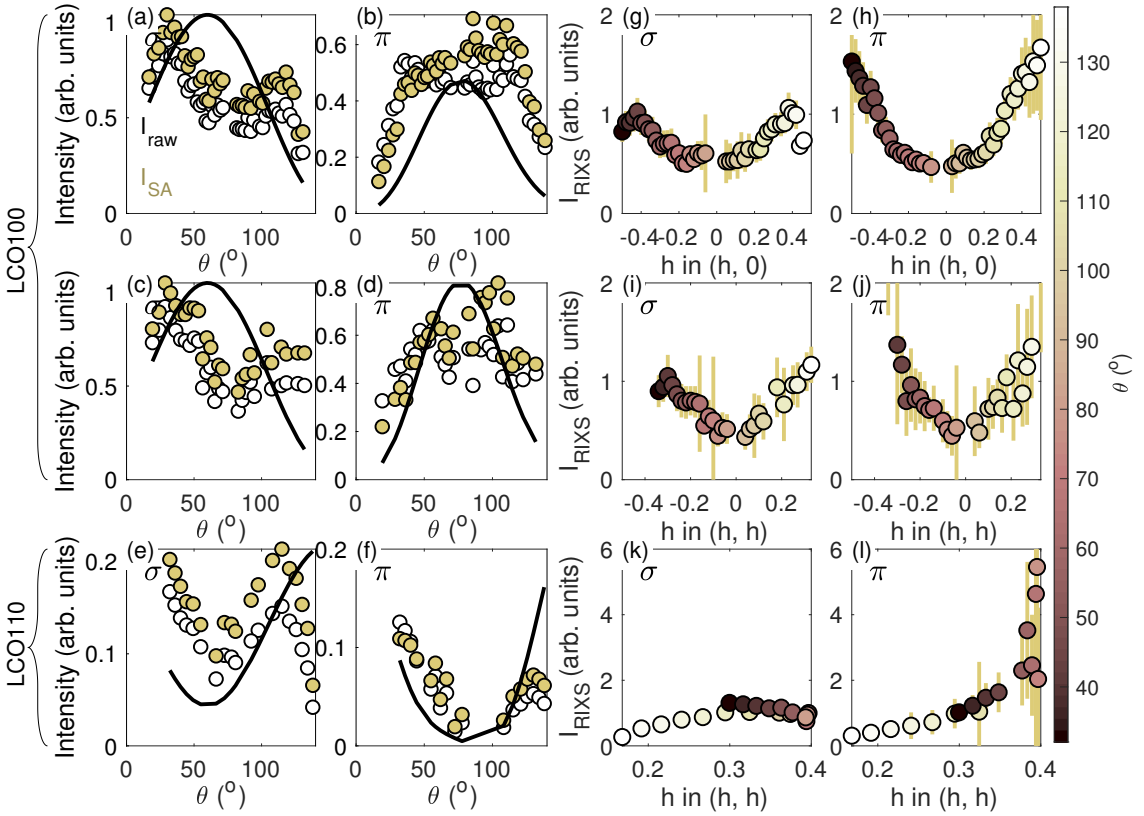

Figure 4.26: Intensity of the multimagnon excitations in LCO. Panels (a-f) show the raw multimagnon intensity in white, extracted from the peak of a damped-harmonic oscillator fit to RIXS data and data corrected for the effects of self-absorption in yellow. The solid black line shows the approximate spin/ charge cross-section of the magnetic excitations calculated from crystal field theory. Panels (g-l) show the data divided by the local RIXS cross-section. The colour of the data point shows the incident scattering angle θ.

50% of the single-magnon spin-flip cross-section and 50% of the charge cross-section. Both of these approximation are purely phenomenological and were tuned to achieve reasonably good symmetry in the data.

Following these approximations, the intensity of the multimagnon is plotted in white in Fig. 4.26 (a-f) and the self-absorption corrected data are shown in yellow. The approximated cross-section is shown as the black line and appears to reflect the shape of the data relatively well. Fig. 4.26 (g-l) shows the θ and **Q**-dependence of the fully corrected multimagnon intensity after accounting for self-absorption and the RIXS cross-section. The corrections result in reasonably good symmetry and agreement between different θ. This suggests the approximation accounts for the cross-section reasonably well.

As with the single magnon analysis, the grazing-in/ grazing-out and σ/ π polarised data are combined and datasets where the cross-section is particularly low are removed. Fig. 4.27 shows the multimagnon intensity as a function of **Q**. The corrected plots show significantly enhanced spectral weight at high **Q** in both the $(h,0)$ and (h,h) directions. As seen in the single magnon

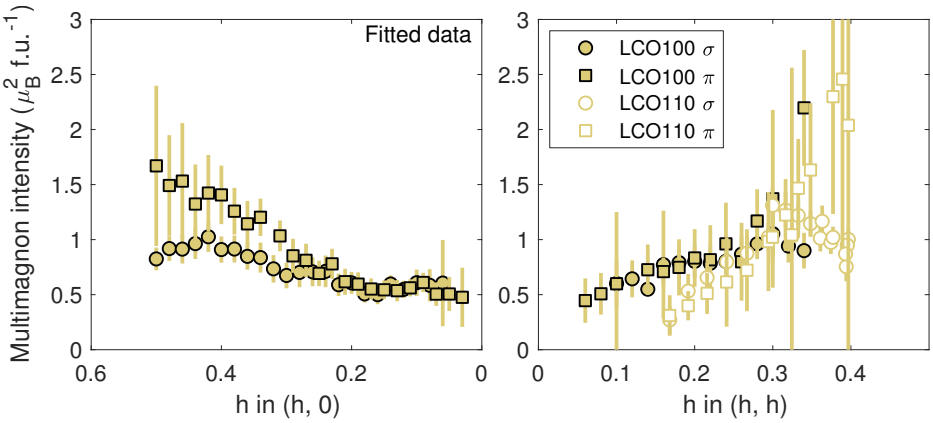

Figure 4.27: The multimagnon spin-wave intensity measured by RIXS following correction for the effects of self-absorption and local magnetic effects. The data are scaled to the spin fluctation intensity of single magnons measured with INS [44]. RIXS data from the LCO100 are indicated in yellow and LCO110 in white, σ and π polarisation is indicated with circles and squares respectively.

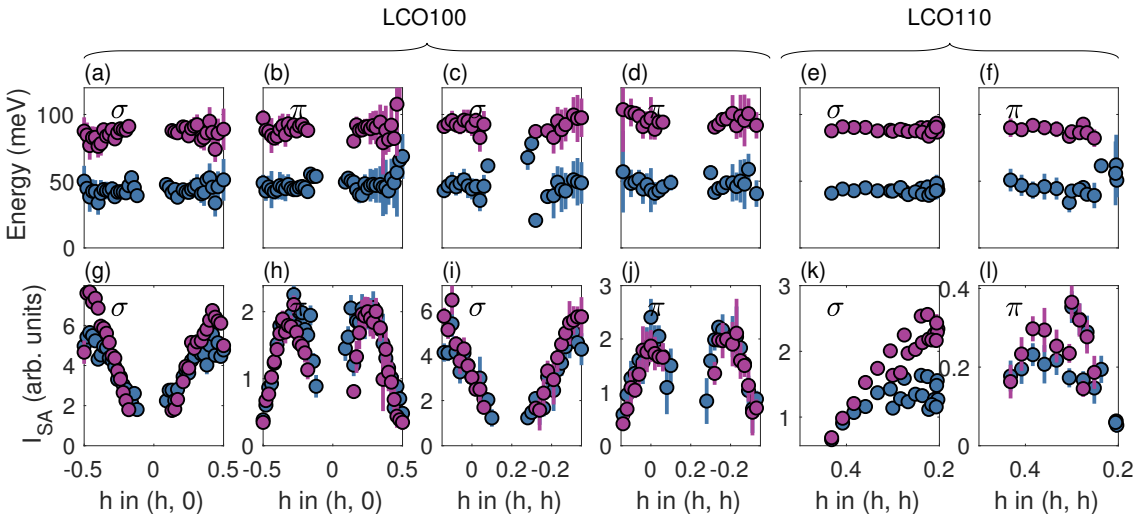

Figure 4.28: Characteristics of the phonon excitations in LCO showing (a-f) the energy and in (g-l) the intensity corrected for the effects of self-absorption.The bond-stretching mode is shown in purple and the bond-buckling mode in blue.

plot, the difference between σ and π close to $\mathbf{Q} = (1/2, 0)$ is likely due to a failure to fully correct the self-absorption. In this instance, the approximate correction procedure is not good enough to fully account for the prefactors to the RIXS intensity.

4.4.3 Phonons

In recent studies Cu L-edge RIXS studies of phonons in the cuprates, the two resolvable phonons have generally been attributed to bond-breathing (stretching) and bond-buckling (bending) phonon modes [129, 132, 133]. Fig. 4.28 (a-f) show the energy of the extracted phonons which we also attribute to a stretching and buckling mode. Both phonons appear to be nondispersive for the resolvable wavevectors, however, at low $\mathbf{Q}$, it is not possible to separate the phonon

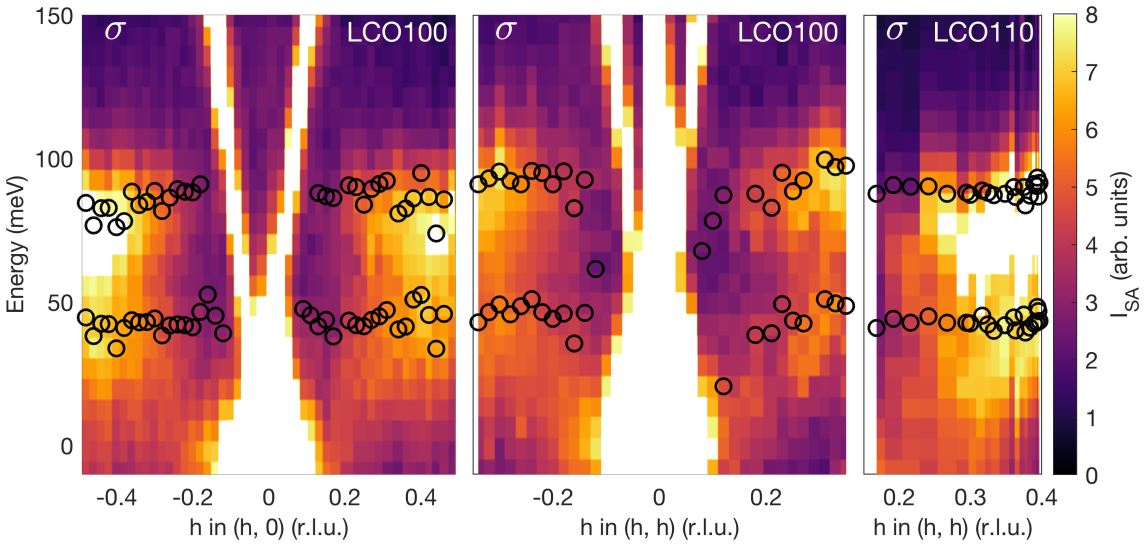

Figure 4.29: RIXS intensity map as a function of wavevector in the energy range associated with the phonon excitations. Black markers indicate the energy centres of Gaussian fits to the phonons.

excitations from the elastic or magnetic peaks. There is some suggestion that both phonons soften close to $\mathbf{Q} = (0,0)$ but the experimental geometry is not optimised to verify this as the specular reflection dominates at the elastic peak making the phonons impossible to resolve. In the non-dispersive region, the energy of the modes are also slightly different to those reported elsewhere at approximately 45 and 90 meV.

Fig. 4.28 (g-l) shows the intensity of the two resolved phonons. The intensity in Fig. 4.28 (g-l) is corrected for the effects of self-absorption, assuming no change of polarisation. The matrix elements of the RIXS cross-section are assumed to be independent of wavevector in $\sigma \rightarrow \sigma$ polarisation but not with $\pi \rightarrow \pi$ polarisation. In general, the excitations are symmetrical in $\mathbf{Q}$ but show significant differences with polarisation, these differences indicate the contribution of the matrix element in π polarisation, hence data measured with σ polarisation is the most reflective of the underlying excitations. In these data, the two phonon modes have very similar wavevector dependent intensity and both decrease approaching Γ. This is in contrast to previous calculations and measurements which show strongly wavector-dependent phonon intensities with opposite trends: the buckling mode intensity increases towards Γ whereas the breathing mode intensity decreases as shown in Fig. 4.8 [212, 213, 129, 132, 133]. A summary of the phonon measurements in LCO is shown in Fig. 4.29 in a RIXS intensity map in the region of the phonon excitations. The RIXS intensity is normalised for the effects of self-absorption showing data from σ only. The phonon excitations are clearly separated in the data and, as is reflected in the fits, the higher energy phonon increases in intensity towards the zone boundary. The low energy phonon does not show evidence for an increase in intensity towards Γ.

4.5 Discussion and conclusions

One aim of the work in this Chapter is the characterisation of the RIXS cross-section. Towards this, the new measurements provide comprehensive details of its evolution in a range of orientations. This tests the proposal of Haverkort *et al.* [142] that x-ray absorption spectral functions are a good description of RIXS transitions. The agreement between the calculated orbital transitions and measured *dd* excitations is generally very good and the qualitatively similar character of the spin fluctuations measured with RIXS and INS is a promising sign for this technique.

Despite the significant amount of previous work measuring excitations in LCO, the work described in this chapter has contributed a number of new insights.

- The relative intensities of the orbital excitations are verified but note unexpectedly high intensity in the d_{z^2} orbital.
- In the low energy range, measurements of χ' are extended from $\mathbf{Q}$= $(1/2,0)$ to $(0,0)$ which equates to X to Γ. In this region the deviation from SWT is verified at $(1/2,0)$ and the reduction in χ' towards $(0,0)$ is confirmed.
- New details are provided of the multimagnon excitations and following approximate correction their rapid increase towards $\mathbf{Q}$ = $(1/2,1/2)$ is reported.
- High energy resolution phonons are resolved which show a somewhat different wavevector dependent intensity than in other recent RIXS experiments on the cuprates.

This section provides some additional discussion of these new insights.

4.5.1 Divergence from spin-wave theory

The spin fluctuations measured by Headings *et al.* [44] show remarkably good agreement with calculations from SWT. However, two key discrepancies were identified, damping of excitations at $\mathbf{Q}$ = $(1/2,0)$ and softening of the excitations between $\mathbf{Q}$ = $(1/4,0)$ and $(1/2,0)$. This second result is seen in only a small number of points in the INS data and has not been widely discussed. The new RIXS results complement the INS data by providing some overlapping points in $\mathbf{Q}$ and a higher density of points in this region. These measurements verify the INS results and provide further details of the observed discrepancies.

Fig. 4.20 includes the energy dispersion of the spin fluctuations showing overlapping points with INS via the SWT calculation. The agreement is generally very good except at $\mathbf{Q}$ = $(1/2,0)$ where the spin fluctuations measured with RIXS disperse to $\hbar\omega_0 = 355 \pm 25$ meV compared to $\hbar\omega_0$

= 322 ± 6 meV measured with INS [44]. As shown in Fig. 4.21, this may be due to the lineshape of the excitation, greater spectral weight is seen at higher energy in the RIXS measurement. In general, the RIXS data agrees with the INS observation of enhanced damping at close to **Q** = (1/2, 0).

Q-dependent quantum re-normalisation

One explanation for the discrepancy is that the quantum renormalisation does not fully account for the fluctuating moment. Renormalisation is performed in quantum field theory to account for fluctuations which alter the total of known physical quantities. In the spin-wave theory calculations described in Section 4.1.2, the susceptibility is renormalised to account for fluctuations which reduce the total magnetic moment. In previous work [43, 44], the renormalisation is performed by integrating across the whole Brillouin zone as shown in Eqn. 4.13. This static renormalisation gives good agreement for the majority of data measured with INS and RIXS except between **Q** = (0, 0) and **Q** = (1/2, 0).

The measured excitation spectrum can be approximately described by a wavevector dependent $Z_d(\mathbf{Q})$ such that,

$$Z_d(\mathbf{Q}) = \begin{cases} Z_d \sin(h\pi), & \text{if } h < \frac{1}{4} \\ Z_d \sin\left(\frac{\pi}{4}\right), & \text{if} h \geq \frac{1}{4}. \end{cases} \tag{4.38}$$

In practice, this means the susceptibility at the anomalous wavevector **Q** = (1/2, 0) is approximately 50% lower than expected in SWT. To provide a physical description of this reduction, Dalla Piazza [225] presents work to examine the **Q**-dependence of the renormalisation which accounts for the fluctuations more rigorously than the static normalisation which has previously been used. Their work involves renormalising charge fluctuations from the Hubbard model as part of a perturbative effective theory which gives a renormalised susceptibility,

$$\chi'(\mathbf{Q},\omega) = \frac{1}{4}(u_{\mathbf{Q}} + v_{\mathbf{Q}})^2 \left\{ 1 - 4\frac{t^2}{U}\left[1 - \frac{\cos(\mathbf{Q}_x) + \cos(\mathbf{Q}_y)}{2} \right] \right\}^2 \delta(\omega - \omega_{\mathbf{Q}}), \tag{4.39}$$

where $v_{\mathbf{Q}}$ and $u_{\mathbf{Q}}$ are matrices which account for interactions in a single layer of CuO_2. The susceptibility is modelled assuming $t/U = 0.14$ resulting in a reduction in the intensity at (1/2, 0) of 5%. This suggests that the **Q**-dependence of the susceptibility is not drastically changed by accounting for $Z_d(\mathbf{Q})$ and this approach cannot reproduce the 50% reduction from SWT at (1/2, 0) that is observed in the new RIXS data.

Spinon creation

Another explanation for the divergence from SWT is that the wavevector $\mathbf{Q} = (1/2, 0)$ is associated with the creation of a spinon pair. Dalla Piazza *et al.* [51] have studied the spin excitations in square lattice $S = \frac{1}{2}$ system CFTD. CFTD is analagous to LCO but with lower energy exchange couplings which make polarised neutron scattering possible and hence they are able to separate components of the response which are longitudinal and transverse to the ordered moment. Similar deviations from SWT are also seen in this system and they identify transverse "spin-isotropic" continuum of excitations at $\mathbf{Q} = (1/2, 0)$. They explain these observations as being signatures of pairs of fractional quasiparticles described as 2D analogues of spinons. Within this model, the fractional quasiparticles are bound at other wavevectors and recreate the typical magnon continuum. Headings *et al.* [44] point out that the lineshape of the excitations in LCO can be modelled with a power law function which shows a similar dependence to other systems in which spinons have been measured [226, 227].

Some theoretical descriptions of the cuprates based on the Heisenberg model contain spinons. A mean field strong-coupling theory recreates the d-wave symmetry and spin-gap which is seen in the cuprates [228]. Within weak-coupling theory spinons are predicted within the RVB state and in particular predict enhanced spectral weight at high energy at $\mathbf{Q} = (1/2, 0)$ [50]. This work provides additional constraints to these theories as the results appear to point to spinon creation as the likely cause of the deviations from SWT.

4.5.2 Multimagnon creation

The new results demonstrate that RIXS resolves a separate multimagnon continuum in a band of spectral weight at higher energy than the single magnon response. The energy dependence of this continuum shown in Fig. 4.20 indicates that $\mathbf{Q}= (1/2, 0)$ corresponds to a region with a small energy separation between the single and multimagnon which is an important consideration when analysing discrepancies from SWT.

Although full polarisation analysis is needed to rigorously extract the multimagnon intensity, some tentative remarks can be made about the approximate intensity that is extracted. Namely that the intensity follows the single magnon and increases towards $\mathbf{Q}$=$(1/2, 0)$. This seems to be in agreement with measurements based on linear SWT for multimagnon excitations as described by Headings [99].

4.5.3 Electron-phonon coupling strength

Extracting phonon excitations has only recently become possible with the improved energy resolution now available at soft x-ray RIXS spectrometers. It should be noted that the RIXS experiments reported in this chapter are not optimised for this task as the specular reflection dominates the low energy spectrum at low $|\mathbf{Q}|$. It would be possible to design experiments in which the specular position is rotated such that phonon excitations are easier to resolve throughout the **Q**-range. Energy detune measurements were also not performed. However, two phonon modes are extracted which are attributed to a buckling and breathing mode. The energy of the both modes appears to be non-dispersive beyond the low-**Q** region.

Regarding the intensity of the phonons, the measurements made with σ polarisation are expected to be the most reliable as they do not contain contributions from the RIXS matrix elements. The data measured in σ polarisation show that the intensity of the two phonon modes is approximately the same except at high **Q** where the intensity of the breathing mode phonon is increased. This is quite different to the predictions made by Devereaux *et al.* [129] that the buckling mode phonon increases towards Γ. RIXS measurements which confirm this prediction have been made in $Nd_{1+x}Ba_{2-x}Cu_3O_{7-\delta}$ (NBCO) [133] and $La_{2-x}Ba_xCuO_4$ (LBCO) [229].

INS has been used extensively to measure phonons in YBCO. The energy resolution of INS experiments make it generally better optimised to resolve low energy phonons and a range of phonon modes have been reported below 80 meV [230]. The breathing and buckling modes have also been characterised with INS. Reznik *et al.* also see an opposite dependence of the electron phonon coupling strength and also report a slight softening ($\approx$ 15 meV) of the breathing mode towards the zone boundary [231] which is not seen in the RIXS data. The discrepancies reported here suggest that further RIXS measurements optimised to extract details of the two phonon modes would be valuable.

Chapter 5

Anisotropic damping and susceptibility in the spin fluctuations of $La_{2-x}Sr_xCuO_4$

This chapter reports new resonant inelastic x-ray scattering (RIXS) studies on doped compositions of high temperature superconductor $La_{2-x}Sr_xCuO_4$ (LSCO). The aims of this work are similar to those described in Chapter 4. As before, this study hopes to provide insights into RIXS as a technique by isolating the prefactors to the spin-fluctuation intensity. Secondly, this work aims to characterise the spin fluctuations in doped LSCO and in particular provide details of their damping and spin-susceptibility $\chi''(\mathbf{Q},\omega)$. Understanding the evolution of these parameters into doped compositions has the potential to constrain theories which describe the mechanisms underlying high temperature superconductivity (HTS).

To achieve these aims, high resolution RIXS measurements have been performed on two doped compositions of LSCO, $x = 0.12$ and 0.16 which are compared to the undoped parent material La_2CuO_4 (LCO). The new RIXS measurements exhibit high energy spin fluctuations similar to those seen previously with inelastic neutron scattering (INS) and RIXS. The spin fluctuations are well described by a damped harmonic oscillator (DHO) model which reveals the anisotropic nature of the excitations. Enhanced damping is observed at close to $\mathbf{Q} = (0.2, 0.2)$ in both doped compositions. These measurements are extended in (h,k) to a full quadrant of the Brillouin zone where the anisotropy is clearly seen.

To analyse the intensity, a new approach is taken to account for the RIXS cross-section by comparing the spin-fluctuations of LCO measured with RIXS and INS. From this comparison a normalisation constant is established which is used to correct the intensity of the doped compositions. This approach avoids having to calculate the full spin cross-section, as in Chapter 4, which becomes prohibitively more complex in LSCO compared to LCO. The new analy-

sis allows us to present measurements of the wavevector dependent magnetic susceptibility $\chi''(\mathbf{Q},\omega)$ which is seen to rapidly increase towards the antiferromagnetic (AFM) wavevector $\mathbf{Q}_{\mathrm{AFM}} = (1/2, 1/2)$ for all compositions. In particular, the wavevector dependent susceptibility is greater in LSCO compared to LCO. The region probed by RIXS contains some points of overlap with previous INS measurements in LSCO and in comparison to these measurements, RIXS measures greater susceptibility. This is attributed to spectral weight at higher energy that is cut off in the INS experiments.

These measurements provide a number of details which could constrain theories which relate the AFM spin fluctuations in cuprates to the superconducting pairing mechanism. This chapter briefly discusses the importance of these observations to spin fluctuations theories based on the Hubbard model.

5.1 Background

Doping LCO with strontium rapidly suppresses the long-range AFM order and gives rise to the superconducting state. As holes are introduced into the system, the tendency for spins to delocalise and hop between sites is increased, hence the hopping constant t increases in relation to the on-site Coulomb repulsion U and AFM order breaks down. Despite the suppression of long-range AFM order, it is now well established that strong, short-range spin fluctuations persist in doped compositions across the phase diagram. It has been hypothesised that this order arises due to fluctuating spin stripes [38]. Analogous to the charge stripe picture which describes the collection of doped holes in charged domains, pockets of remaining AFM order could give rise to the short range spin fluctuations [232].

The nature and importance of the spin-fluctuations have long been considered in theoretical pictures of pairing in HTS. However, the main experimental probe of the spin fluctuations, INS, is better suited to characterising the fluctuations at low-energy rather than at high-energy where excitations associated with the AFM order are located. These excitations are significantly broadened in doped compositions making the INS signal difficult to separate from the background. In a limited section of the Brillouin zone, this gap has since been filled with RIXS but the exact nature of the RIXS cross-section remains a barrier to understanding the susceptibility of the spin-fluctuations. In general, the two techniques have revealed significant structure in the spin-fluctuations and evidence of strong evolution with doping. Specifically, the high-energy spin fluctuations are phenomenologically similar to those observed in the parent compounds but softened and damped with doping

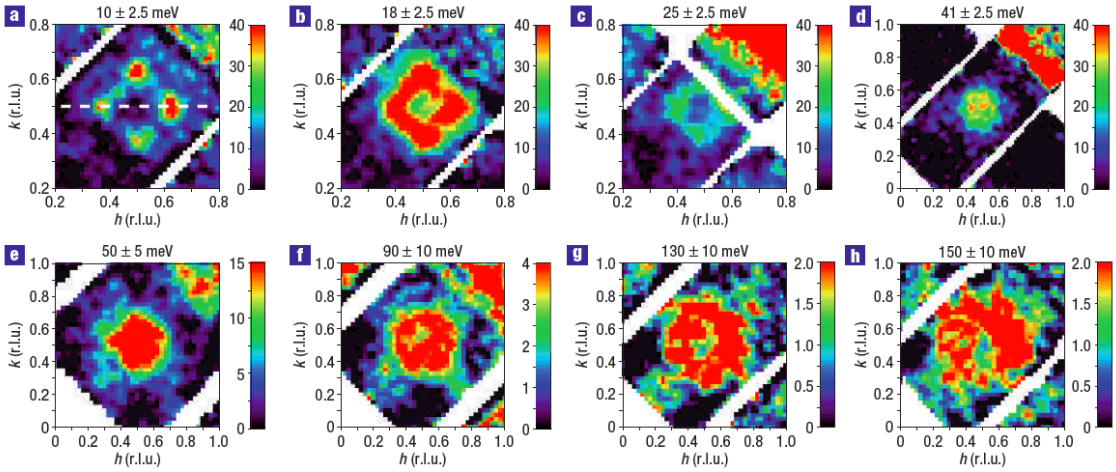

Figure 5.1: Wavector dependence of $\chi''(\mathbf{Q},\omega)$ in optimally doped LSCO as measured with inelastic neutron scattering, reproduced with permission from reference [233].

How AFM spin-fluctuations exist alongside doped holes in the superconducting state remains an open question. LSCO lacks the low-temperature tetragonal phase that appears to trigger stripe order in other La-based cuprates [69]. More recently, superconductivity has been shown to exist alongside a dynamic charge density wave (CDW) in LSCO [77]. It remains unclear how this phase is linked to magnetic order.

5.1.1 Previous INS measurements

As discussed in Chapter 4, INS is a highly effective probe of collective excitations in superconducting materials. INS is able to probe spin fluctuations in doped cuprates due to the interaction of the neutron moment with local magnetic fields which gives a direct measurement of the susceptibility of the system, $\chi''(\mathbf{Q},\omega)$. This puts INS in a strong position to verify and constrain the predictions made by theoretical models. LSCO has been one of the most well studied cuprates with INS due to its relatively simple structure and the availability of large crystals.

INS has been used to perform careful characterisation of the excitations at low energy in LSCO. For $\hbar\omega \lesssim 25$ meV, an incommensurate structure has been observed in optimally doped compositions offset from the antiferromagnetic wavevector $\mathbf{Q}_{\mathrm{AFM}}$ by a vector δ which increases with doping. The incommensurate susceptibility is peaked at 18 meV in the optimally doped compound and shifts to lower energy in under and over doped compositions [168, 233, 234] . Below the peak, a spin-gap is observed and at very low doping, a disordered spin-glass state with periodicity incommensurate to the lattice which is characterised by low energy magnetic correlations [235].

In optimally doped compositions, a broad component has been seen to dominate the mid-

energy range at $\hbar\omega \simeq 40$ to 70 meV [236, 233]. The excitations disperse inwards towards the remaining incommensurate peaks resulting in an "hourglass" dispersion at low energy which is similar to the low energy dispersion first seen in $YBa_2Cu_3O_{6+x}$ (YBCO) [237, 238, 239]. In heavily overdoped compositions, $x = 0.22 - 0.25$ the additional structure is suppressed [240, 168]. In Fig. 5.1 **Q**-dependent energy slices up to 150 meV show the evolution of the low energy excitations.

Hayden *et al.* [165] performed the first INS study on the high energy spin fluctuations in doped LSCO in an $x = 0.14$ compound finding spin fluctuations with similar characteristics to the AFM phase, persisting into the doped compositions. They observe high-energy spin fluctuations above $\hbar\omega \approx 250$ meV, on the Brillouin zone boundary at $\mathbf{Q} = (3/2, 0)$ and report the strongest response at $\mathbf{Q}_{\mathrm{AFM}} = (1/2, 1/2)$ at intermediate energies ($\hbar\omega = 0 - 150$ meV). Subsequent measurements on LSCO [236, 233, 240, 168, 234] confirmed the persistence of the spin fluctuation response has comparable intensity to LCO but with excitations that are considerably broadened [193, 43, 44]. Persistent, broadened spin fluctuations have been observed in many other doped cuprate materials including in YBCO [237, 238]. It should be noted that measuring broad excitations at high energy, $\hbar\omega > 200$ meV, can be difficult with INS due to the difficulty of capturing the full excitation from incident energy slices. The energy resolution depends on the incident energy and hence is generally worse for high energy excitations. Additionally, characterising the background in inelastic neutron scattering experiments is difficult and is usually done by subtracting from a region of the Brillouin zone where the excitations of interest are suppressed. A significantly enhanced background is observed when measuring doped compositions due to charge scattering which makes extracting the underlying spin fluctuations particularly difficult.

5.1.2 Previous RIXS measurements

The advent of high-resolution RIXS has proved an important breakthrough in measuring the spin fluctuations in doped cuprates. While RIXS spectrometers do not currently have sufficient energy resolution to measure the low-energy spin-fluctuations, they are more easily able to measure the broad high-energy fluctuations above 50 meV. The low incident energy used in Cu L-edge RIXS means measurements are restricted to a circular region around Γ which is complementary to the region accessible to INS.

Dean *et al.* [109] measured the spin fluctuations in various dopings of LSCO along the $(h, 0)$ direction confirming the persistence of the spin fluctuations as seen with INS and noting that the dispersion is slightly softened with doping. Meyers *et al.* [111] subsequently extended the

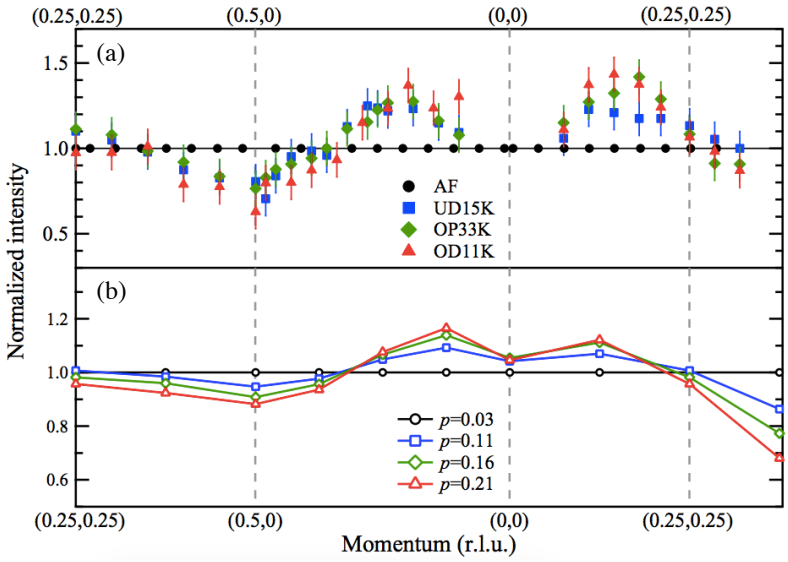

Figure 5.2: Spin fluctuation intensity in doped cuprates showing (a) the intensity measured with RIXS and (b) the intensity from DQMC calculations based on the Hubbard model. In both plots, the intensity is normalised to the intensity measured in the AFM parent compound. Figure reproduced with permission from reference [161].

measurements to the (h,h) direction finding the softening is even greater and the excitations are more strongly damped with doping. Studies in heavily overdoped composition $x > 0.23$ confirm that the excitations become overdamped [222, 80].

A number of recent studies have focused on the intensity of the spin-fluctuations measured with RIXS. Peng *et al.* [161] study the doping dependence in $(Bi,Pb)_2(Sr,La)_2CuO_{6+\delta}$ finding anisotropic behaviour in both the damping and intensity of the excitations. In their analysis they divide the intensity of the spin fluctuations of three doped compositions by the intensity in the undoped parent compound. The relative intensity is seen to increase in (h,h) towards $(1/4,1/4)$ and in $(h,0)$ the intensity initially increases before decreasing towards $(1/2,0)$. Fig. 5.2 shows the normalised spin-fluctuation intensity presented in reference [161] showing comparison to Determinantal quantum Monte Carlo (DQMC) calculations based on the Hubbard model.

5.1.3 Theoretical models

Measurements of the spin-fluctuations in doped cuprates are motivated by understanding high T_c superconductors and their description based on spin-fluctuation mediated theories. The simplest theories are based on the single and multi-band Hubbard model which, as discussed in the previous chapters, capture much of the important physics in the cuprates. Scalapino [52] reviews the theoretical studies of pairing which have been made based on the spin fluctuation Hubbard model and their ability to reproduce measured parameters in superconducting materials. This section gives a brief introduction to some of this theoretical work.

Determinantal quantum Monte Carlo (DQMC) calculations based on the Hubbard Model reproduce the long range AFM order in LCO with parameters $U \approx 8t$ [241]. This is referred to as the intermediate coupling regime where U is approximately equal to the bandwidth.

Extending these calculations to the doped cuprates is complicated and hence is generally restricted to small lattices. Calculations have been made based on both a weak and strong coupling picture. Calculations made by Scalapino [52] suggest that doped cuprates exhibit intermediate coupling as in the parent compounds, and optimal doping is achieved where the system has both local and itinerant properties. An earlier paper by Scalapino [45] makes the case for $d_{x^2-y^2}$ pairing based on NMR [242] and optical conductivity [243] measurements which point to the importance of spin fluctuations. Calculations which therefore assume that spin-fluctuation exchange is the mechanism for pairing find that an attractive electron-electron interaction arises in the $d_{x^2-y^2}$ singlet channel. Signatures of $d_{x^2-y^2}$ pairing have been observed in various measurements where nodes in the gap indicative of $d_{x^2-y^2}$ symmetry are seen. These include phase sensitive magnetometry measurements [30] and a characteristic variation in the specific heat as $H^{1/2}$ with magnetic field [244] which is predicted by calculations based on the Hubbard model [245].

Another prediction of the Hubbard model is that the wavevector-dependent pairing interaction V_{eff} is proportional to $\chi'(\mathbf{Q},\omega)$,

$$V_{\text{eff}} \simeq \frac{3}{2}U^2\chi'(\mathbf{p}'-\mathbf{p}), \tag{5.1}$$

where $\mathbf{p}$ and $\mathbf{p}'$ are the wavevectors of Cooper pair electrons. This equation indicates the importance of establishing $\chi'(\mathbf{Q},\omega)$ in constraining these theories.

Huang *et al.* [38] perform DQMC numerical studies based on the two-dimensional Hubbard model with an additional next nearest neighbour hopping parameter t' and are able to qualitatively reproduce the slowly-evolving high-energy magnetic excitations. DQMC calculations based on the 3-band Hubbard model match well with calculations of the relative intensity of the spin fluctuations at a range of dopings as measured with RIXS [161].

Other models have also had success, calculations based on a doped RVB model reproduce the shape of the spin-excitation spectrum [246] and self-consistent calculations based on local and itinerant characteristics show a good match with RIXS and INS data [247]. Monte Carlo calculation based on Green's functions describing the $t-t'-J$ model have also been able to reproduce AFM and superconducting properties [248].

The spin operators in the Heisenberg model result in an overall symmetry which is described by the $SO(3)$ vector representation. It has been suggested that an $SO(5)$ model is also able

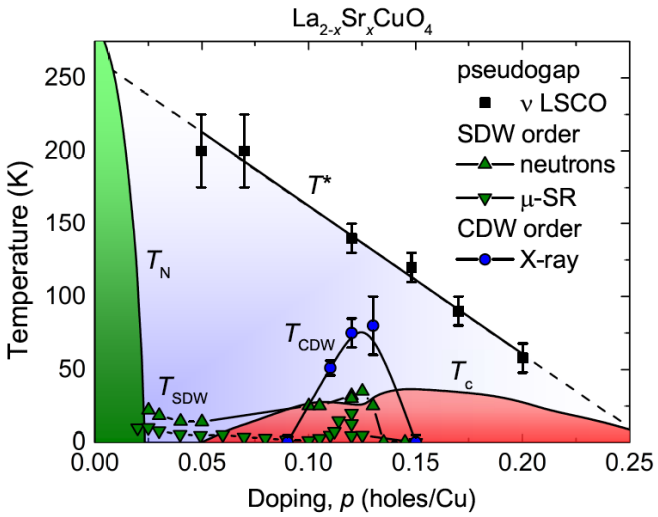

Figure 5.3: Phase diagram of LSCO showing the AFM phase in green, superconductivity in red, the pseudogap phase in blue and the strange metal/ Fermi liquid phase in white. Reproduced from reference [250].

to unite the antiferromagnetic order and superconductivity [249]. The $SO(5)$ model successfully predicts a low energy collective excitation which is especially strong at $\mathbf{Q} = (1/2, 1/2)$ as experimentally observed in YBCO and other cuprates.

In general, theoretical approaches with a range of approximations have made predictions for the physical properties of the cuprates with varying success. In general, as the system is doped the spin fluctuations are predicted to be phenomenologically different at $\mathbf{Q} = (0,0)$ and $(1/2,1/2)$ and not symmetric around $(1/4,1/4)$ as would be expected for a metal which is not magnetically ordered.

5.2 Measurement details

5.2.1 Experimental setup

The single crystal samples of LSCO used for the studies in this chapter were grown by previous members of the Bristol group using the travelling solvent floating zone technique as described in Chapter 4 and in references [220, 99]. These samples have been well characterised in the past and used for previous neutron [44, 233, 168] and x-ray [77] scattering studies. SQUID magnetometry measurements were used to verify the composition of the samples, relative to known phases, as shown in the phase diagram in Fig. 5.3. Fig. 5.4 shows the SQUID measurements and the approximate transition temperatures of the samples.

This chapter describes experiments on three compositions of LSCO, $x = 0$ - the AFM parent compound, underdoped $x = 0.12$ and optimally doped $x = 0.16$. The $x = 0.12$ composition is

	T_N (K)	T_c (K)	T_{CDW} (K)
$x = 0$	320 [44]	-	-
$x = 0.12$	-	28	75 [77]
$x = 0.16$	-	35	-

Table 5.1: Phases of LSCO and their associated transition temperatures for the three compositions measured. The T_c values were measured with SQUID.

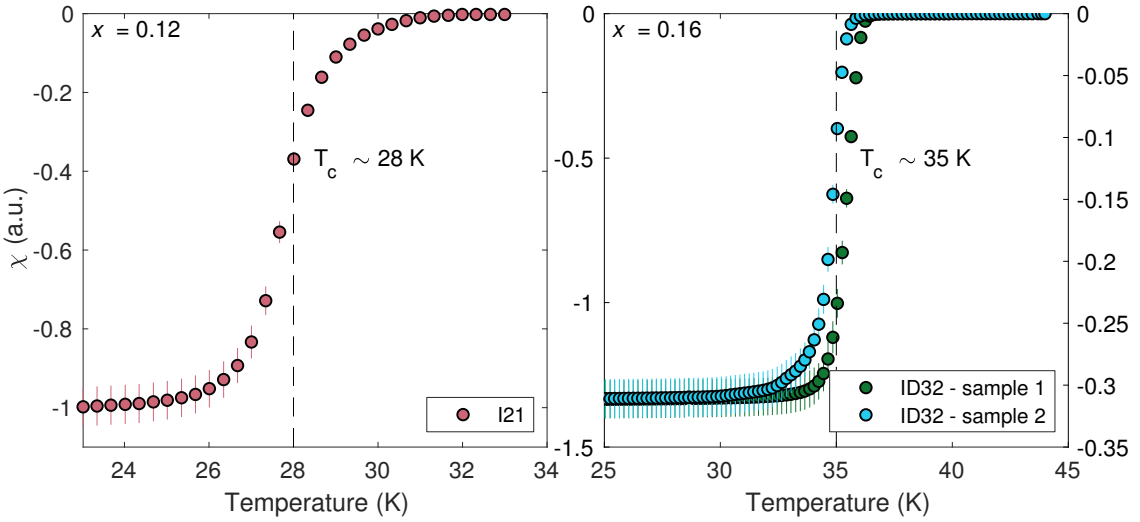

Figure 5.4: SQUID magnetometry measurements performed on the single crystal samples of LSCO $x = 0.12$ and 0.16. The samples were cooled in zero field and measured in an applied field of 3 Oe.

close to optimal doping for the CDW phase (the fluctuations associated with the CDW in LSCO are not discussed in this thesis). Table 5.1 gives the ordering temperatures of the three compositions and Fig. 5.3 show the phase diagram for LSCO. In this chapter the high-temperature tetragonal (HTT) I/4mmm crystal structure notation is used where the lattice parameters $a = b \simeq 3.8$ Å, $c \simeq 13.2$ Å.

The RIXS experiments were performed at I21 of Diamond Light Source and at ID32 of the European Synchrotron Radiation facility. RIXS measurements were performed at both spectrometers at the Cu L-edge with energy resolution $\Delta E \sim 37$ meV. The incident photons were tuned to ~ 932 eV and polarised horizontal to the propagation direction (LH/ π). The experiments were performed with the typical experimental geometry described in Chapter 3 and spectra were collected between $\mathbf{Q} = (0,0)$ and $(0,0.5)$ and between $(0,0)$ and $(0.35,0.35)$. On the $x = 0.12$ and 0.16 samples, data were additionally collected in a grid of points with spacing $\mathbf{Q} = 0.05$ throughout the whole accessible region of the Brillouin zone. The $x = 0$ and 0.12 measurements were performed at I21 and the $x = 0.16$ at ID32 in two separate experiments. All of the grid measurements were performed at ID32. These measurements have energy resolution $\Delta E \simeq 50$ meV which yields higher flux and hence a shorter count time. Data from the grid

measurements are subject to a weighted average with each of their nearest neighbours in **Q** to account for the lower quality of data taken at each individual point.

All samples were cleaved *in-situ* apart from the $x = 0.12$ sample used to measure the grid data at ID32. This sample was polished with aluminium oxide abrasive strips with increasingly small grain sizes between 60 and 0.3 μm following the procedure in Croft *et al.* [77]. It is interesting to note that the cleaved $x = 0.12$ sample, produced an elastic peak in the region close to the specular that measures approximately 15 times smaller than the polished sample. The lineshape, intensity and energy of the magnetic excitations is the same in both datasets but the low energy, low **Q** excitations are difficult to extract in the data from the polished sample so are only used in the map plots. These results confirm the usefulness of cleaving samples in vacuum to prevent surface contamination.

5.2.2 Analysis

The spectra are integrated and aligned using the standard approach described in Section 3.3.6. To compare spectra from different samples, the first step of the analysis is performed by normalising the intensity of the raw data $I_{\text{raw}}(\mathbf{k},\mathbf{k}',\epsilon,\epsilon')$ to an integration over the range of the *dd* excitations obtained from the same spectrum, between 1 eV and 4 eV. It is assumed that the intensity of the *dd* excitations is described by a function $g(\epsilon,\epsilon',\mathbf{k},\mathbf{k}')$ and therefore the normalised intensity is defined as,

$$I_{\text{RIXS}} = \frac{I_{\text{raw}}}{g(\epsilon,\epsilon',\mathbf{k},\mathbf{k}')}. \tag{5.2}$$

It was not possible to perform x-ray absorption spectroscopy (XAS) in all experimental geometries so the self-absorption cannot be fully accounted for with calculations. The *dd* normalisation analysis accounts for the geometrical component of the self-absorption but not the energy or polarisation dependent part. However, this approach is sufficient for analysing the dispersion and damping of the magnetic excitations. This point is returned to in Section 5.4.1 when the intensity is considered.

The data are modelled in the region –80 to 800 meV. As in Chapter 4, the $x = 0$ data are described with Gaussian functions to account for the elastic and phonon peaks and with damped harmonic oscillator (DHO) functions (Eqn. 4.35) to account for the spin fluctuations. In LCO, two DHO functions are used to account for the one and two magnon. In the doped compositions a single DHO function is used to model the broadened spin fluctuations which are assumed to contain higher order components of the magnetic response. As in LCO, the elastic peak and phonons are modelled with a Gaussian function but the charge broadening means only one

phonon branch can be resolved in the doped compositions. Charge transfer also broadens the *dd* excitations such that they contribute a background to the spectra in the region of interest for doped compositions. This is modelled with a linear function crossing the intensity axis at 0 eV. The gradient of the line is found by fitting to the data at low **Q** where the magnetic excitations are absent from the spectra at ~ 800 meV then fixing this gradient for all spectra of the same composition. This approach prevents the background changing as the lineshape of the magnetic excitations evolves with **Q**.

The lineshape of the spin fluctuations evolves considerably with doping and the full range is captured within the DHO model. When $\omega_0 \geq \gamma/2$, ω_1 is real and the system is described by two propagating poles ω_0 and ω_1. When $\omega_0 \leq \gamma/2$, ω_1 is imaginary and the system is overdamped. Analysis shows that in the doped compositions, γ is significantly increased and at some **Q** the excitations enter the overdamped regime. The DHO response fully describes this case but the lineshape of the function evolves slowly with changes in γ and ω_0 hence the error bars become large. At low **Q**, the excitations become critically damped as ω_0 tends to 0. Here $\chi''(\mathbf{Q},\omega)$ can be approximated as a Lorentzian centred at the origin which allows Eqn. 4.35 to be described by just two parameters,

$$\chi''(\mathbf{Q},\omega) = \frac{\chi'(\mathbf{Q})\Gamma(\mathbf{Q})\omega}{\omega^2 + \Gamma^2(\mathbf{Q})}. \tag{5.3}$$

In this regime the DHO response has two poles. One of the poles decays very rapidly and is neglected leaving a single pole that decays with Γ [223]. χ' is the same as in Eqn. 4.35 and the damping parameters can be related as $\Gamma = \omega_0^2/\gamma$. This function is referred to as the overdamped harmonic oscillator (ODHO).

5.3 Results: spin fluctuation dispersion and damping

Intensity maps

A comparison of the spectra measured at **Q** = (0.25, 0) for the three compositions is shown in Fig. 5.5. The *dd* excitations dominate the spectra at high **Q**. The broadening due to charge transfer excitations is clearly visible in the $x = 0.12$ and 0.16 compositions.

At low energy, the magnetic excitations are seen to dominate the spectra. With increased doping the sharp resolution limited magnon peaks become broad. The individual spectra can be combined in map plots showing the RIXS intensity as a function of energy and **Q**. Fig. 5.6 shows map plots in the low energy region. The anisotropic dispersion is clear as the excitations disperse to approximately 400 meV in $(h,0)$ and approximately 300 meV in (h,h). The phonons

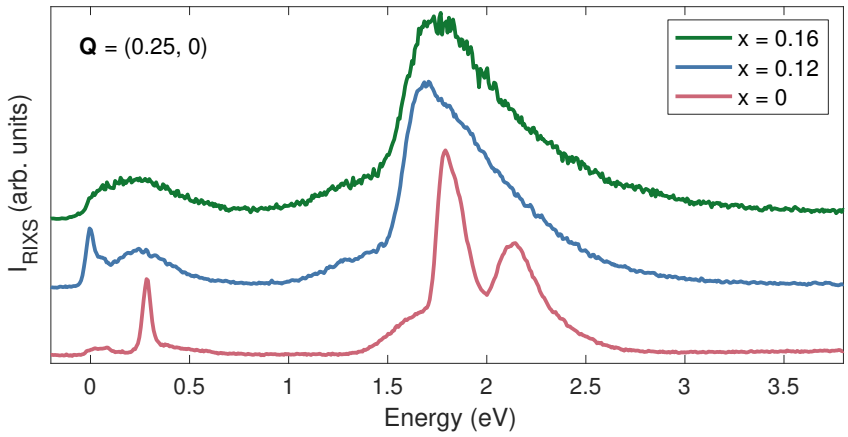

Figure 5.5: Example RIXS spectra at $\mathbf{Q} = (0.25, 0)$ measured on LSCO $x = 0, 0.12$ and 0.16. Data measured with π polarisation at I21, I21 and ID32 respectively.

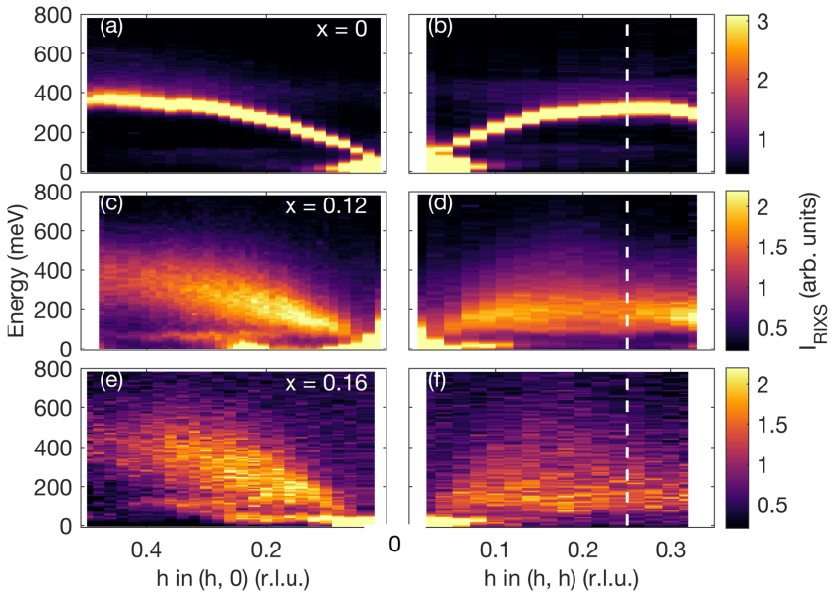

Figure 5.6: Example RIXS spectra at $\mathbf{Q} = (0.25, 0)$ measured on LSCO $x = 0, 0.12$ and 0.16 with π polarisation.

and multimagnons are also visible. In $x = 0.12$, the CDW order results in enhanced spectral weight in the elastic peak at $\mathbf{Q}_{\mathrm{CDW}} \simeq 0.21$ as shown in Fig. 5.6 (c).

The grid measurements allow the intensity to be plotted as a function of h and k throughout the Brillouin zone as shown in Fig. 5.7. The intensity shows the evolving nature of the excitations for a range of energy slices. At low energy, $E = 50 \pm 12.5$ meV, the largest intensity is due to the elastic peak, this is the case at all values of $\mathbf{Q}$ but especially close to $\mathbf{Q} = (0,0)$ due to specular reflection. Note here the much increased intensity of the elastic peak in the $x = 0.12$ sample which was polished rather than cleaved as described above. With increasing energy, the magnetic excitations emerge forming a band around the Γ point, $\mathbf{Q} = (0,0)$, and disperse towards the Brillouin zone boundary. At low energy, the (h,h) and $(h,0)$ directions have equal intensity but

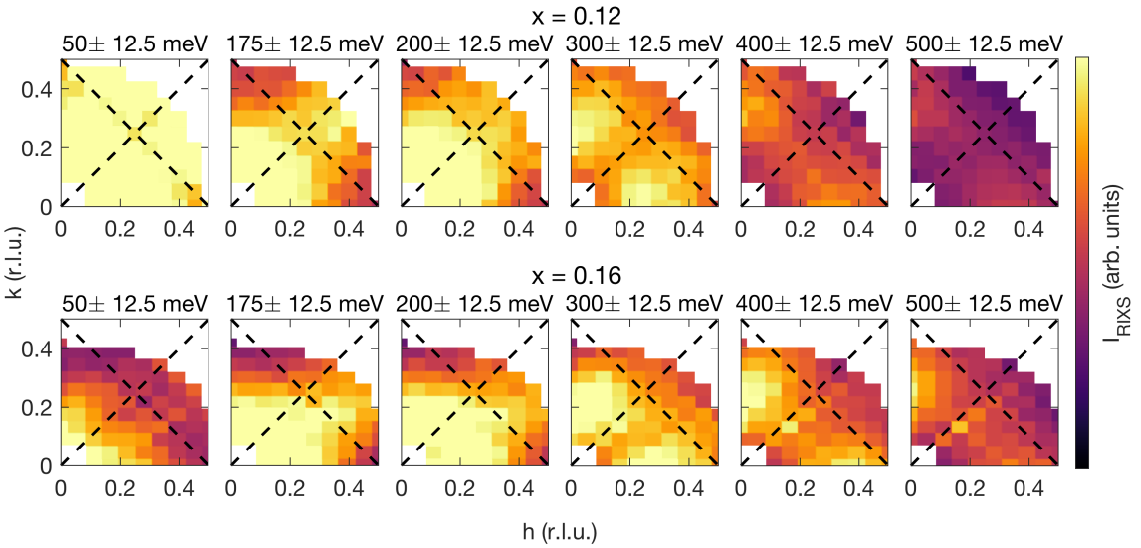

Figure 5.7: RIXS intensity as a function of h and k showing the total intensity in energy slices of the spectrum. Showing data from LSCO $x = 0.12$ and 0.16 where the $x = 0.16$ data has been rotated by 8^o to correct misalignment in the measurement. Data measured with π polarisation.

at higher energy the $(h,0)$ excitations dominate, reflecting the anisotropic dispersion. It should be noted that the absolute RIXS intensity still contains prefactors to the RIXS cross-section from both the energy and polarisation dependent self-absorption and from local interactions.

One advantage of presenting the data in this way is that it allows easy comparison with the INS data such as that in Fig. 5.1, where the neutrons are scattered to position sensitive detectors. The INS measurements were performed with a time of flight instrument so the excitations are presented in energy slices which are qualitatively similar to the observations with RIXS. This presents a new opportunity for comparison between RIXS and INS data.

Data fitting

Examples of fitted RIXS spectra are shown for low **Q** points in Fig. 5.8 and for high **Q** points in Fig. 5.9. The figures show the underlying fit functions including the elastic peak, phonons, single magnon DHO function, multimagnon DHO function and the linear background. The energy resolution of the measurements generally allows the elastic peak, phonons, single and multimagnons to be well separated. The phonon peaks are more prominent in spectra along the $(h,0)$ direction due to coupling to the charge density wave phase. The DHO function is able to describe the magnon peak well for the range of spectral lineshapes which are observed.

The damping parameters ω_0 and γ are extracted from the fits and plotted as a function of **Q** in Fig. 5.10. The grey shaded region identifies the area where Eqn. 5.3 is used to fit the data and the single parameter Γ is shown. Outside this region, $\gamma/2$ is plotted to readily identify the regions

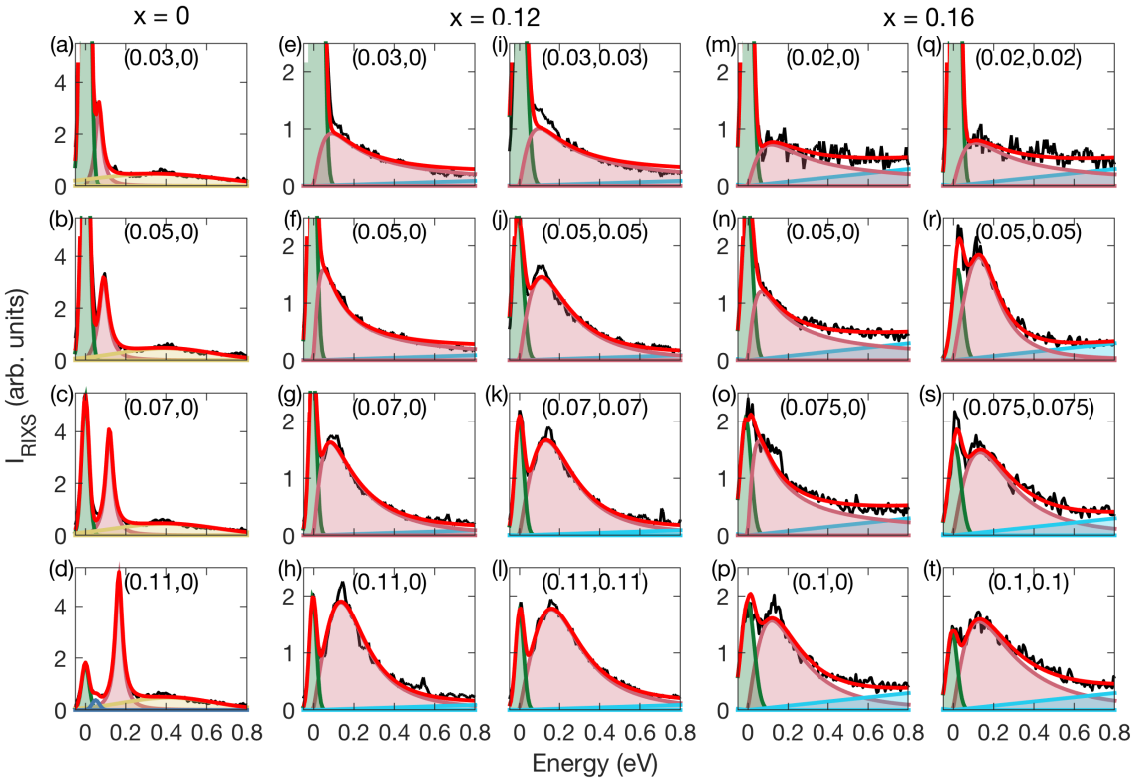

Figure 5.8: Example low **Q** RIXS spectra showing data from $x = 0, 0.12$ and 0.16 measured with π polarisation. The data are shown in black with the total fit function in red and the underlying fit functions beneath, showing the elastic peak in green, phonons in blue and purple, the single magnon DHO function in pink, multimagnon DHO function in yellow and the linear background in light blue. The slope and intercept of the linear background are fixed for each data set after fitting to a low-**Q** example spectrum. Data in panels (e), (f), (i), (j), (m), (n), (o) and (q) are fitted with the ODHO function.

where $\gamma/2 < \omega_0$. It should be noted that the instrument resolution function $\Delta E \simeq 35$ meV has not been deconvolved from the data which means γ is increased by approximately 5% across all **Q**. This is investigated further in Chapter 6.

The dispersion of ω_0 is similar to that previously reported with RIXS and INS. However, no softening of ω_0 is seen in either the $(h,0)$ or (h,h) direction. At $(1/2,0)$ $\omega_0 = 354 \pm 43$ meV for $x = 0$, and $\omega_0 = 396 \pm 54$ meV for $x = 0.16$. At $(1/4,1/4)$, $\omega_0 = 289 \pm 27$ for $x = 0$, and $\omega_0 = 313 \pm 29$ for $x = 0.16$.

In the parent compound, the magnon peaks are sharp and resolution limited, therefore γ is small compared to ω_0. There is a slight increase in γ close to $(h,0)$ which is associated with the anomalous broadening in LCO which is discussed extensively in Chapter 4. However, this increase is small compared to the enhancement seen in the doped compounds. In the data from $x = 0.12$ and 0.16, $\gamma/2$ is significantly increased. As has been noted before [109, 110, 222, 111], the damping is anisotropic as a function of **Q** showing greater broadening along (h,h). In particular, a peak is observed in γ at approximately (0.2, 0.2), which does not reflect the symmetry of the

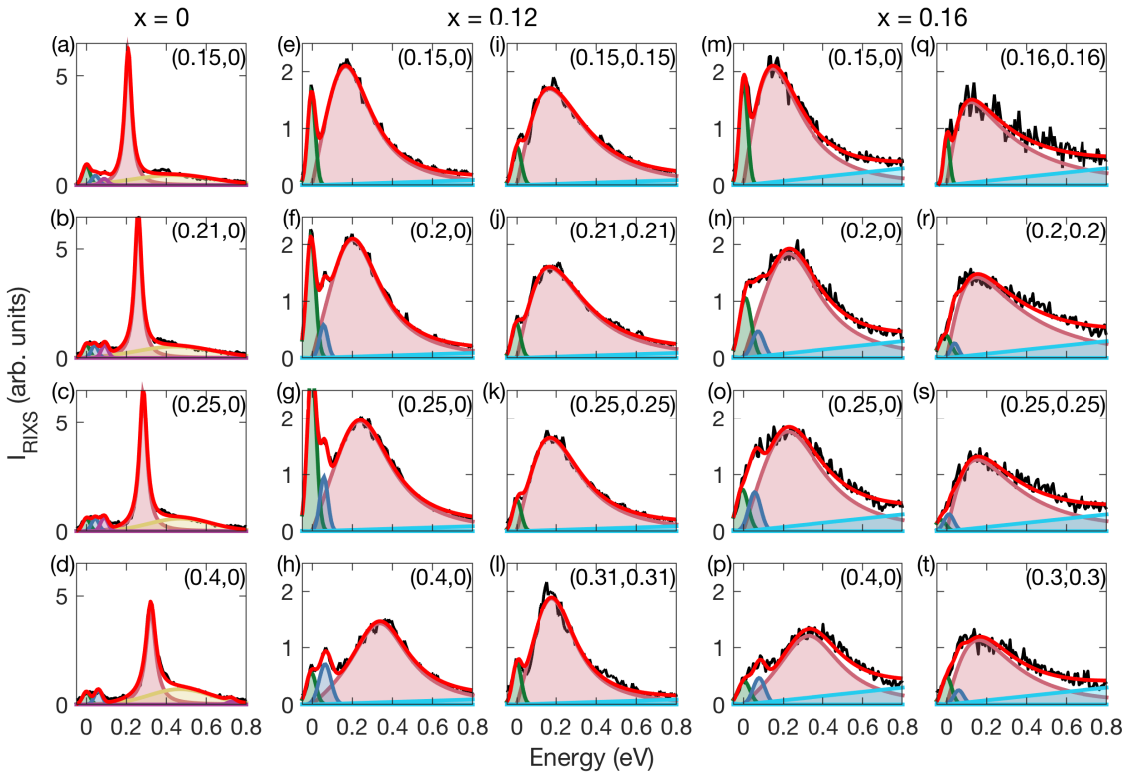

Figure 5.9: Example high **Q** RIXS spectra showing data from $x = 0, 0.12$ and 0.16 measured with with π polarisation. Fit functions are shown as in Fig. 5.8.

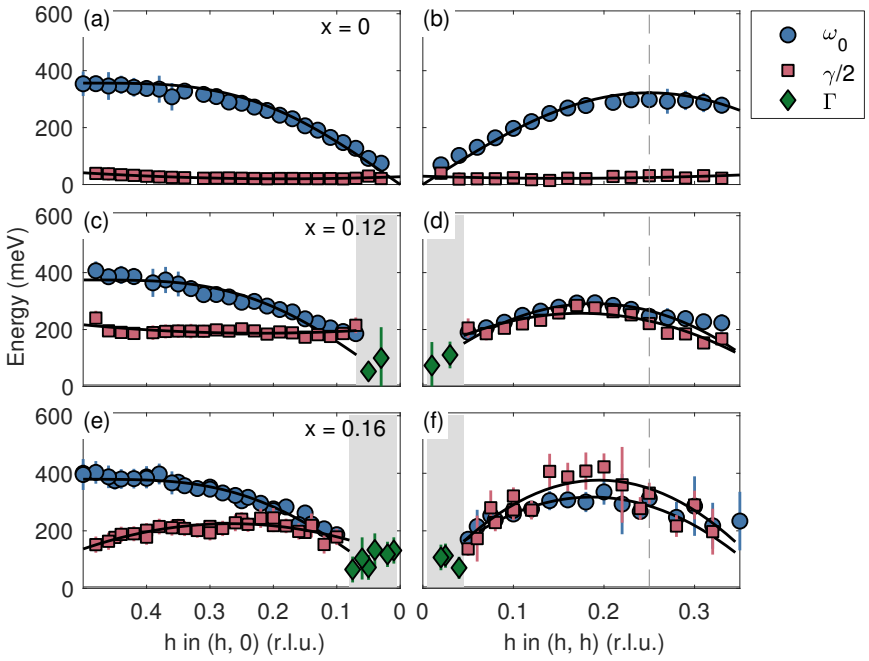

Figure 5.10: Fitted DHO parameters ω_0 (blue circles) and $\gamma/2$ (pink squares) in $(h,0)$ and (h,h) for LSCO $x = 0, 0.12$ and 0.16. The grey region indicates data where the two-parameter ODHO is used (Eqn. 5.3), the damping in this regime is described by Γ which is plotted as green diamonds. The data are fitted to a cubic polynomial fit shown as solid lines.

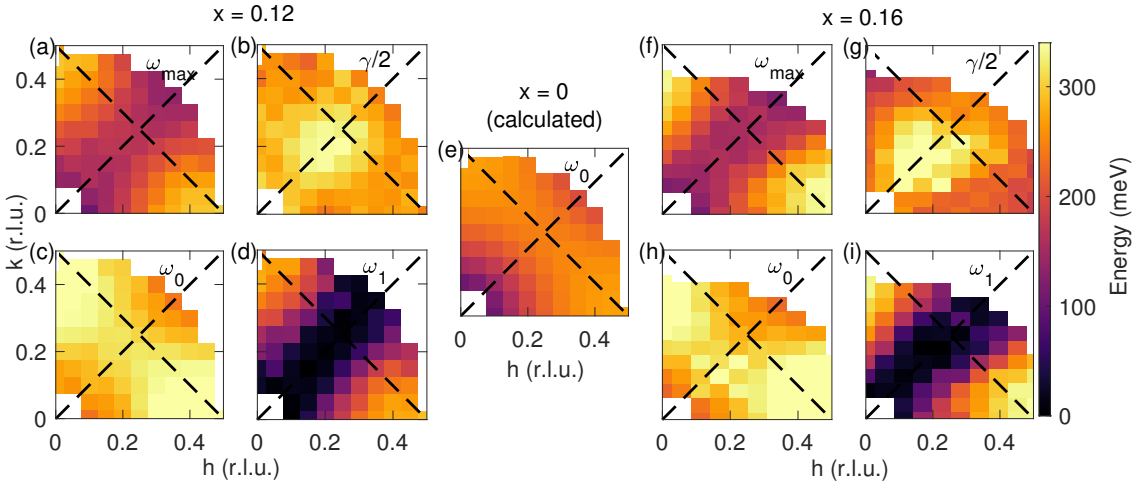

Figure 5.11: Fitted DHO parameters as a function of **Q** in the accessible quadrant of the Brillouin zone (h,k). Showing (a) and (f) $\omega_{\max}$, (b) and (g) $\gamma/2$, (c) and (h) ω_0 and (d) and (i) ω_1 for LSCO $x = 0.12$ and 0.16. Also showing ω_0 from a calculation in spin-wave theory for $x = 0$. The $x = 0.16$ data have been rotated by 8^o to ensure symmetry across (h,k).

AFM Brillouin zone. This effect is seen in both doped data sets, most prominently in $x = 0.16$ where $\gamma/2$ peaks above ω_0.

Fit parameters extracted from the grid data are shown in Fig. 5.11 for $x = 0.12$ and $x = 0.16$. Fig. 5.11 (c) and (h) show ω_0 which display the anisotropic dispersion between $(h,0)$ and (h,h). As shown in the dispersion in 3D, the doped compounds show qualitatively similar dispersion to the AFM spin fluctuations which are described by spin-wave theory (SWT). To demonstrate this, ω_0 calculated from SWT in 3D is plotted in Fig. 5.11 (e). The parameters for the SWT are as described in Chapter 4 Table 4.2. $\omega_{\max}$, shown in Fig. 5.11 (a) and (f), describes the peak of the excitation and contains both ω_0 and γ. The smooth evolution of $\omega_{\max}$ suggests the DHO model describes the data well. Fig. 5.11 (b) and (g) show $\gamma/2$, as seen in the 2D plots, there is a clear peak in the (h,h) direction centred at $\mathbf{Q} = (0.2,0.2)$.

The effect of self-absorption on γ

At this point, the effect that the normalisation method has on the results is briefly considered. It has already been noted that normalising the data to the *dd* excitations does not account for the energy or polarisation dependence of the self-absorption. While this should have no effect on the energy of the excitations, in some situations it has been shown to alter the excitation lineshape [251] and could have a corresponding effect on γ. As the self-absorption effect varies strongly with **Q**, it is important to verify that it does not affect the findings regarding the wavevector dependence of γ.

To test this, the $x = 0.12$ data are corrected for the energy and polarisation dependent self-

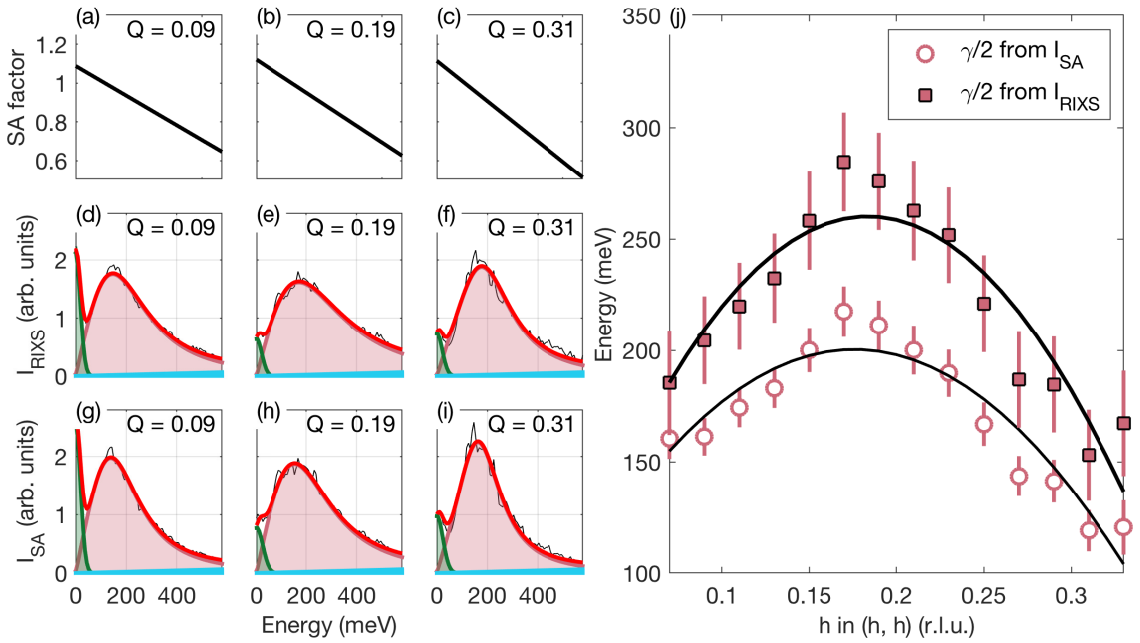

Figure 5.12: Details of the self-absorption correction in $x = 0.12$ LSCO showing the effect on three example spectra. Panels (a-c) show the calculated self-absorption factor, (d-f) show fitted spectra normalised to the *dd* excitations I_{RIXS}, (g-i) show fitted spectra normalised with the self-absorption correction I_{SA} and (j) shows the resulting **Q**-dependence in (h,h) of $\gamma/2$ for the two approaches

absorption correction. XAS measurements in the orientation of the RIXS measurements were performed during the beamtime for this composition. It is assumed that the polarisation is flipped during the magnon scattering process from π to σ. As discussed before, this assumption is based on previous polarised RIXS measurements [161, 162] which indicate that the majority of spectral weight is in the spin-flip channel. It is also assumed that the fit to the spectra is able to separate charge components.

Fig. 5.12 (a-c) show the calculated self-absorption factor as a function of energy for three representative **Q** points, showing the effect in the region of the magnon. The fitted RIXS data is shown following normalisation with the *dd* excitations in Fig. 5.12 (d-f) compared to normalisation with self-absorption in Fig. 5.12 (g-i). The resulting $\gamma/2$ values are shown in Fig. 5.12 (j). It is clear that γ is reduced for I_{SA} compared to I_{RIXS}, by an average of 28% across **Q**. However, the key result, that $\gamma/2$ is peaked at $\mathbf{Q} = (0.2, 0.2)$ is preserved.

5.4 Results: dynamical spin susceptibility

5.4.1 Normalisation procedure

This section presents parameters extracted from the RIXS data relating to the intensity of the magnetic excitations. It is clear that normalising to the *dd* excitations is not sufficient to

fully account for the **Q**-dependent RIXS cross-section and data normalised this way do not represent the underlying susceptibility. The $x = 0$ data is compared to the SWT model which is parametrised and modified with INS performed on LCO by Headings *et al.* [44]. In this way the RIXS prefactor should cancel out leaving the dynamical spin susceptibility in absolute units,

$$\langle \chi'^{\mathrm{LSCO}}(\mathbf{Q})\rangle = \chi'^{\mathrm{LSCO}}_{\mathrm{RIXS}}(\mathbf{Q}) \times \frac{\phi^{\mathrm{LCO}}_{\mathrm{SWT}}(\mathbf{Q})}{\phi^{\mathrm{LCO}}_{\mathrm{RIXS}}(\mathbf{Q})}. \tag{5.4}$$

In this equation, $\chi'(\mathbf{Q})$ is the real part of the wavevector dependent susceptibility at $\omega = 0$ extracted from the DHO model in Eqn. 4.35. $\chi'(\mathbf{Q})$ is related to $\chi''(\mathbf{Q})$ by the Kramers-Kronig relation as defined in Eqn. 2.26.

In Eqn. 5.4, $\phi^{\mathrm{LCO}}_{\mathrm{SWT}}(\mathbf{Q})$ is a wavevector dependent energy integrated spin-wave pole weight, determined from a fit of linear SWT to INS data. The SWT calculation is as described in Chapter 4 with an additional wavevector dependent renormalisation constant Z_d which phenomenologically describes the deviation from linear SWT in the $(h,0)$ direction,

$$Z_d(\mathbf{Q}) = \begin{cases} Z_d \sin(h\pi), & \text{if } h < \frac{1}{4} \\ Z_d \sin\left(\frac{\pi}{4}\right), & \text{if } h \geq \frac{1}{4}. \end{cases} \tag{5.5}$$

Unlike the INS measurements, it is assumed that RIXS is equally sensitive to the three components of the susceptibility hence $\chi = \frac{1}{3}(\chi_{xx} + \chi_{yy} + \chi_{zz}) = \frac{2}{3}\chi_{\perp}$ and $\phi^{\mathrm{LCO}}_{\mathrm{SWT}}(\mathbf{Q})$ is,

$$\phi^{\mathrm{LCO}}_{\mathrm{SWT}}(\mathbf{Q}) = \int_0^{\infty} \chi''(\mathbf{Q},\omega)\, d\omega = \frac{\pi}{3}\chi'_{\perp}(\mathbf{Q})\,\omega_0(\mathbf{Q}). \tag{5.6}$$

The final term in Eqn. 5.4 is $\phi^{\mathrm{LCO}}_{\mathrm{RIXS}}$, the integrated pole weight of fitted LCO RIXS data. This is obtained by considering Eqn. 4.35 in the limit $\omega_0 \geq \gamma/2$ (valid only for $x = 0$),

$$\chi''(\mathbf{Q},\omega) = \frac{\chi'(\mathbf{Q})}{2\omega_1(\mathbf{Q})}\left[\frac{\gamma^2(\mathbf{Q})}{4} + \omega_1^2(\mathbf{Q})\right] \times \tag{5.7}$$

$$\left\{\frac{\gamma(\mathbf{Q})/2}{\gamma^2(\mathbf{Q})/4 + [\omega - \omega_1(\mathbf{Q})]^2} - \frac{\gamma(\mathbf{Q})/2}{\gamma^2(\mathbf{Q})/4 + [\omega + \omega_1(\mathbf{Q})]^2}\right\}. \tag{5.8}$$

Finally integrating with respect to ω_0, gives $\phi^{\mathrm{LCO}}_{\mathrm{RIXS}}(\mathbf{Q})$ as a function of the fitted parameters $\omega(\mathrm{Q}), \gamma(\mathrm{Q})$ and $\chi'(\mathrm{Q})$:

$$\phi^{\mathrm{LCO}}_{\mathrm{RIXS}}(\mathbf{Q}) = \frac{\pi\chi'(\mathbf{Q})\omega_0^2(\mathbf{Q})}{\sqrt{4\omega_0^2(\mathbf{Q}) - \gamma^2(\mathbf{Q})}}. \tag{5.9}$$

Several assumptions are made in Eqn. 5.4. The first thing to note is that both $\chi'^{\mathrm{LCO}}_{\mathrm{RIXS}}(\mathbf{Q})$ and $\phi^{\mathrm{LCO}}_{\mathrm{RIXS}}(\mathbf{Q})$ are obtained by fitting to I_{RIXS}, i.e. to the intensity of the integrated *dd* excitations g, which are assumed to cancel in Eqn. 5.4. To check this, the **Q**-dependence of the integrated *dd* intensity is plotted in Fig. 5.13 (a). The trend in **Q** is broadly consistent. The second assumption is that the remaining **Q** dependent RIXS prefactor, defined by Ament *et al.* as f is also cancelled in

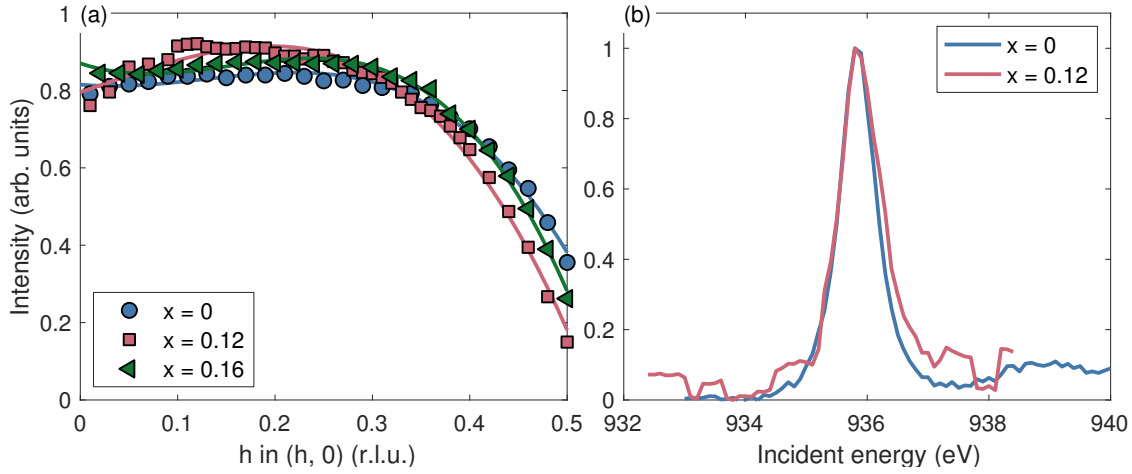

Figure 5.13: Characteristics of the LSCO RIXS and XAS spectra showing (a) the **Q**-dependence of the integrated intensity of the *dd* excitations for the three compositions and (b) the shape of the XAS spectra in the $x = 0$ and 0.12 compositions.

Eqn. 5.4. Fig. 5.13 (b) shows a comparison of the XAS spectra for the $x = 0$ and 0.12 data, showing that the energy loss edge is very similar and therefore the energy dependent self-absorption is likely to cancel out. The final assumption is that the fitted magnon excitations are entirely magnetic in nature and not due to charge. As in Chapter 4, this analysis depends on the recent polarisation analysis of Peng *et al.* [161] which shows that the single magnon excitations have spectral weight 82% in the cross-polarisation channel sensitive to single magnon excitations. The remaining 18% charge contribution is accounted for with the linear background and with fits to the phonon and elastic peak. On this basis it is assumed that the spectral weight captured in the magnon fit is mostly due to magnetic excitations. Any remaining charge contribution in the fit of the magnon in the doped composition would lead to an overestimation of $\chi'^{\mathrm{LCO}}_{\mathrm{RIXS}}(\mathbf{Q})$.

5.4.2 Susceptibility measurements

Fig. 5.14 (a) and (b) show $\chi'_{\mathrm{RIXS}}(\mathbf{Q})$ extracted from the DHO model. The $x = 0$ data contains a sum of the single and multimagnon contribution because it is assumed that higher order contributions are present in the LSCO data which cannot be separated from the single magnon. Fig. 5.14 (c) and (d) show the susceptibility corrected with Eqn. 5.4 revealing $\chi'(\mathbf{Q})$ in absolute units.

An important observation of this work is the consistently higher spectral weight measured in the doped compounds compared to the parent compound. This is seen to be the case in both the raw [Fig. 5.14 (a) and (b)] and corrected data [Fig. 5.14 (c) and (d)] so is not an artefact related to the correction procedure. Eqn. 2.26 demonstrates this effect, showing that as spectral weight is moved to lower energy a larger contribution is given to $\chi'(\mathbf{Q})$. This is seen to be the

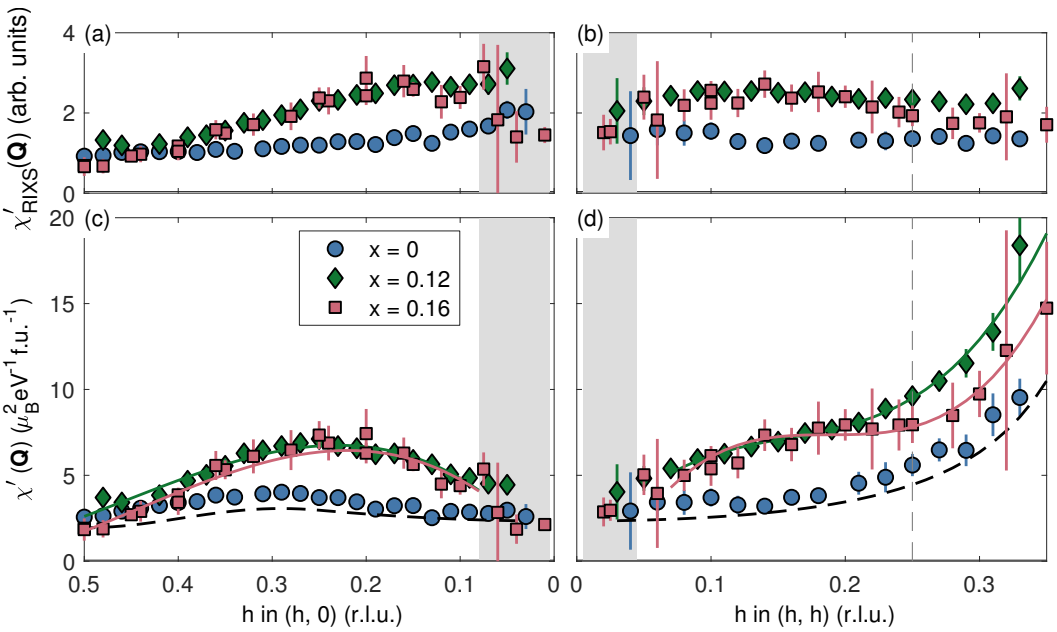

Figure 5.14: Wavevector dependent susceptibility in LSCO showing (a) and (b) $\chi'_{\mathrm{RIXS}}(\mathbf{Q})$ extracted from the DHO fits to the magnetic excitations and (c) and (d) $\chi'(\mathbf{Q})$ in absolute units corrected using Eqn. 5.4. The data are fitted to a cubic polynomial fit shown as solid lines. The grey region indicates data where the two-parameter ODHO was used (Eqn. 5.3).

case in the measurements in the example spectra in Fig. 5.9 where spectral weight in data from the doped compounds is present at lower energy in doped compositions.

The wavevector dependence reflects that seen with INS. For $x = 0$, the absolute susceptibility is forced to have the same trend as the SWT model with additional spectral weight due to the multimagnon contribution. All three compositions show a significant increase along (h,h) reflecting the INS observation of strong spin fluctuations at the AFM wavevector $\mathbf{Q}_{\mathrm{AFM}} = (1/2,1/2)$. The measurements also show a peak in intensity at $(1/4,0)$ along $(h,0)$ which reflects the reduced intensity close to $(1/2,0)$ which is a signature of the INS result.

Fig. 5.15 shows the fully modelled excitation $\chi''(\mathbf{Q},\omega)$ constructed from Eqn. 4.35 where $\omega_0(\mathbf{Q})$, $\gamma(\mathbf{Q})$ and absolute $\chi'(\mathbf{Q})$ are extracted from fits to the data in Figs. 5.10 and 5.14. The model captures the effects discussed so far in this section: the broadened lineshape of the excitations, the anisotropy of the damping and the enhanced susceptibility towards $\mathbf{Q} = (1/2,1/2)$.

5.5 Discussion and conclusions

As described above, the two motivations of this work are to further understand the RIXS cross-section through comparison with INS and to better characterise the spin-fluctuations in LSCO. Towards the first goal, the new measurements provide additional evidence that Cu-L edge RIXS is able to measure transfers of angular momentum. The spin fluctuations that RIXS observes as

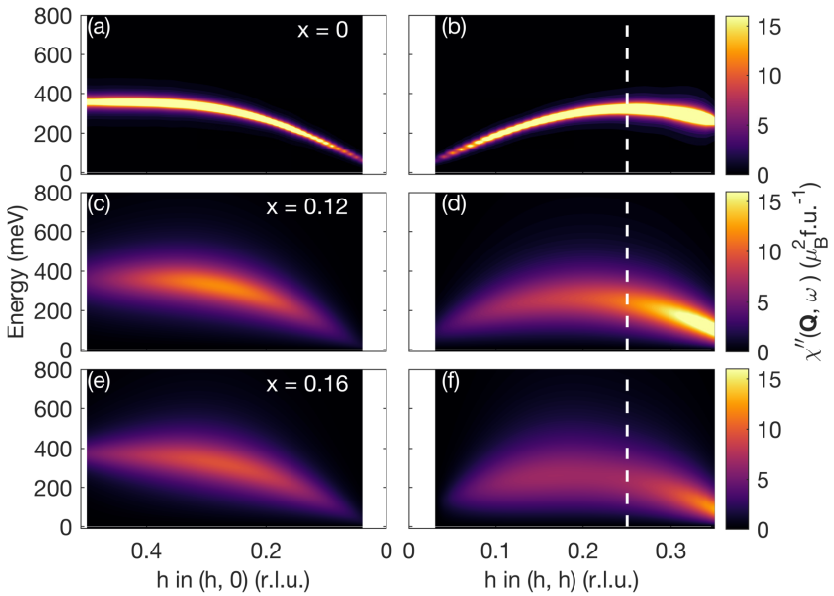

Figure 5.15: $\chi''(\mathbf{Q},\omega)$ showing the fully modelled excitation using the fitted parameters $\omega_0(\mathbf{Q})$, $\gamma(\mathbf{Q})$ from Fig. 5.10 and $\chi'(\mathbf{Q})$ corrected with Eqn. 5.4 as shown in Fig. 5.14.

a result of this mechanism appear to be the same as the excitations measured by INS. Although this chapter does not provide detail of the origin of the prefactors to the susceptibility, the difference between χ' in Fig. 5.14 (a-b) and (c-d) is an indicator of the wavevector dependence of the RIXS cross-section for LSCO. Towards the second goal, the new RIXS measurements provide a number of new details about the spin fluctuations which may be able to place further constraints on spin-fluctuation mediated theories of high-temperature superconductivity:

- The wavevector and doping dependence of the damping parameter, γ, is reported, and is seen to show a peak in the (h,h) direction close to $\mathbf{Q}$= $(0.2,0.2)$.
- 3D map plots are presented which confirm the existence of the peak in γ and show the evolution of the magnon spectral weight over a wide energy range. The maps are the first RIXS measurements which show the 3D evolution of the RIXS intensity in a symmetrical portion of the Brillouin zone.
- The wavevector and doping dependence of the susceptibility $\chi'(\mathbf{Q})$ is reported and shows that the doped compositions have greater susceptibility than the parent compound. The enhancement towards $\mathbf{Q}_{\mathrm{AFM}} = (1/2,1/2)$ appears to be preserved in the doped compositions.
- The deviations from SWT which are observed in LCO, including softening and broadening of the spin fluctuations at $\mathbf{Q} = (1/2,0)$, appear to persist into the doped compositions.

	$\chi'(\mathbf{Q})(\mu_B^2 \text{eV}^{-1}\text{f.u.}^{-1})$					
	$\mathbf{Q} = (1/2,0)$			$\mathbf{Q} = (1/4,1/4)$		
x	RIXS	RIXS <0.26 eV	INS	RIXS	RIXS <0.26 eV	INS
0	2.6 ± 0.3		2.36 ± 0.3 [44]	5.6 ± 0.6		4.5 ± 0.4 [44]
0.12	3.7 ± 0.9	1.3 ± 0.3		9.6 ± 1	5.8 ± 0.6	
0.14			~ 0.5[165]			
0.16	1.8 ± 1	0.41 ± 0.2		8.0 ± 1	4.0 ± 0.5	

Table 5.2: Doping dependence of the $\chi'(\mathbf{Q})$ in LSCO as measured with RIXS and INS.

This section briefly discusses the success of the correction procedure by comparing the results to inelastic neutron scattering and discusses the importance of the additional constraints by linking to existing theories.

5.5.1 Comparison to inelastic neutron scattering

Following the correction procedure, a comparison can be made of the absolute susceptibility measured with INS and RIXS for an equivalent point $\mathbf{Q} = (1/2,0)$. The available INS data were measured on LSCO $x = 0.14$ by Hayden *et al.* [165] which can be compared to the new RIXS data measured on the $x = 0.16$ composition. From the RIXS measurements $\chi'(\mathbf{Q}) = 1.8 \pm 0.6\mu_B^2 \text{eV}^{-1}\text{f.u.}^{-1}$ at $(1/2,0)$ and from INS $\chi'(\mathbf{Q}) \approx 0.5\mu_B^2 \text{eV}^{-1}\text{f.u.}^{-1}$. It is important to note that the RIXS result is based on an integration of the spectrum up to about 800 meV compared to only 260 meV with INS. It is also interesting to note that very similar susceptibility is observed at $\mathbf{Q} = (1/2,0)$ in all three compositions of LSCO with RIXS whereas the INS measurement is approximately four times greater in $x = 0$ ($\chi'(\mathbf{Q}) = 2.36$) compared to $x = 0.14$. This again could be attributed to the ability of RIXS to capture the full excitation whereas INS may cut off the higher energy components of the excitations measured in the doped compounds. Table 5.2 shows a comparison of the susceptibility measured with RIXS and INS at a number of different wavectors. It is clear that the wavevector dependence of the two probes is consistent but that RIXS measures greater spectral weight in the doped compositions. If it were possible to increase the integration range of INS a more comparable value is likely to be seen between the two probes. Table 5.2 contains a column showing the equivalent susceptibility which is found by integrating the doped RIXS spectra up to only 260 meV. It can be seen that this significantly reduces the value of $\chi'(\mathbf{Q})$ measured with RIXS and brings it closer to the values measured with INS.

5.5.2 Constraints on spin fluctuation mediated theories of pairing

These RIXS measurements show persistent spin-fluctuations into the doped compositions of LSCO which maintain the anisotropy of the parent compound. ω_0 shown in Fig. 5.10 shows dispersion in $(h,0)$ and (h,h) for $x = 0.12$ and 0.16 which is similar to $x = 0$. These observations are consistent with previous RIXS measurements [109, 222, 111] but the enhanced energy resolution allows more consistent separation of the magnetic excitations from phonon and elastic contributions.

The full wavevector dependence of γ also shown in Fig. 5.10 is a new result of this work. Damping increases with doping from $x = 0$ to 0.12 and again to 0.16 with a peak in γ at $\mathbf{Q} = (0.2, 0.2)$. The 3D damping maps shown in Fig. 5.11 (b) and (g) provide further details of this peak identifying the center at $\mathbf{Q} = (0.2, 0.2)$ in the Brillouin zone. Recent RIXS studies have connected the anisotropic damping and softening in doped cuprates to calculations based on a model of itinerant quasiparticles [252, 253, 222]. They develop a random phase approximation of the spin susceptibility based on modification from the Lindhard response function. The model described by Monney *et al.* [222] predicts an additional low energy branch of magnetic excitations in the (h,h) direction with a peak at the wavevector where γ is seen to be enhanced. If this is the mechanism that produces the spin fluctuations in LSCO it may provide evidence that they arise due to collective excitations from correlated itinerant electrons. Alternatively, some of these features may be reproduced by calculations within the Hubbard model. Huang *et al.* [38] present DQMC calculations which predict enhanced damping approaching $\mathbf{Q} = (1/2, 1/2)$ which is explained in relation to the importance of spin fluctuations in pairing at this wavevector. In this picture, the measurements are capturing the edge of an enhanced damping region which extends to $(1/2, 1/2)$ and the results support the suggestion that residual AFM spin fluctuations contribute to pairing.

The procedure used to normalise the RIXS intensity allows estimates of $\chi'(\mathbf{Q})$ to be presented in absolute units in Fig. 5.14 (c) and (d). As has been seen in the parent compound, the doped compositions show clear anisotropy in $\mathbf{Q}$ and $\chi'(\mathbf{Q})$ is approximately 4 times larger at $(1/4, 1/4)$ than at $(1/2, 0)$. This is somewhat explained due to the reduced $\omega_0(\mathbf{Q})$ at $(1/4, 1/4)$ shifting spectral weight to lower energy. In fact, $\chi'(\mathbf{Q})$ increases monotonically along (h,h) towards $\mathbf{Q}_{\mathrm{AFM}} = (1/2, 1/2)$ for all compositions and is consistent with INS measurements [165, 233, 240, 168, 234].

The DQMC calculations performed by Huang *et al.* also provide estimates of the imaginary part of the susceptibility $\chi''(\mathbf{Q}, \omega)$ for doped compositions. Slices in $\chi''(\mathbf{Q}, \omega)$ are extracted from

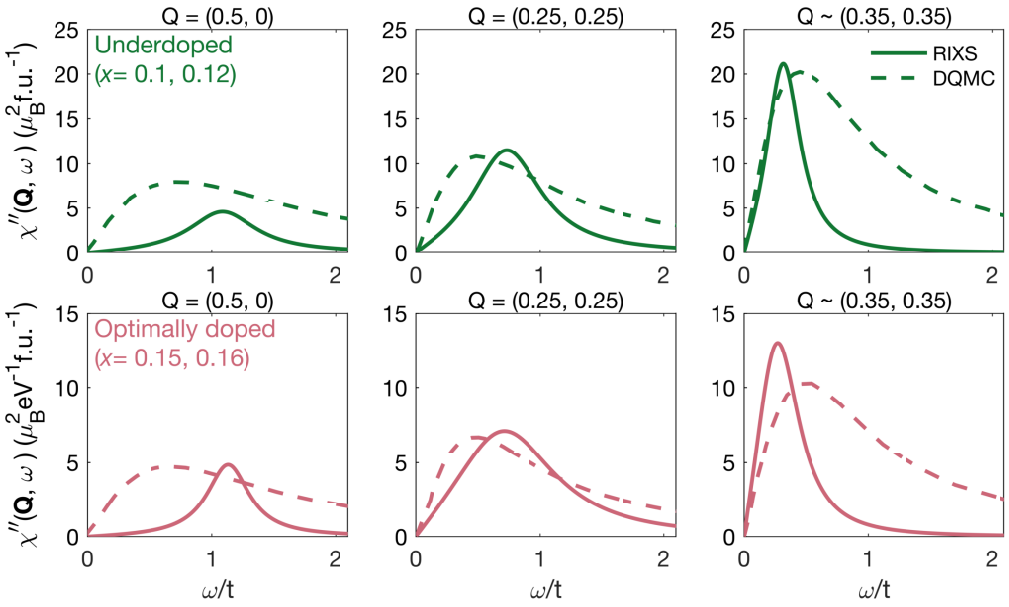

Figure 5.16: $\chi''(\mathbf{Q},\omega)$ modelled with the RIXS parameters $\omega_0(\mathbf{Q},\omega),\gamma(\mathbf{Q},\omega)$ and corrected $\chi'(\mathbf{Q})$ compared to DQMC calculations reproduced from Huang *et al.* [38]. The modelled spectra are scaled to $t = 0.33$ showing the $x = 0.12$ compound (solid green line) compared to calculations at $x = 0.1$ (dashed green line) and spectra from the $x = 0.16$ compound (solid pink line) compared to calculations at $x = 0.15$ (dashed pink line). The intensity of the DQMC data is scaled by an arbitrary fixed amount to allow comparison with the RIXS data.

the intensity plots in Fig. 5.15. A comparison of theoretical and measured $\chi''(\mathbf{Q},\omega)$ is shown in Fig. 5.16 for slices at $\mathbf{Q} = (1/2,1/2)$, $(1/4,1/4)$ and $(0.35,0.35)$. The calculations well describe the evolution of the measured susceptibility with $\mathbf{Q}$ showing that strong spin fluctuations still exist in the doped compositions towards $(1/2,1/2)$, which may reflect the importance of the spin fluctuations in this region. The calculations do not capture the change in lineshape which evolves strongly in the RIXS data but is relatively unchanged until $\mathbf{Q} = (1/2,1/2)$ in the DQMC result.

As described in Section 5.1.3, calculations based on the Hubbard model also predict that the wavevector-dependent pairing interaction V_{eff} is proportional to the susceptibility (see Eqn. 5.1) [52]. These calculations predict that the spin fluctuations contribute to pairing most strongly at $\mathbf{Q} = (1/2,1/2)$ and hence predict strongest susceptibility at this wavevector. Fig. 5.17 shows a comparison of the RIXS measurements of $\chi'(\mathbf{Q})$ to the Monte Carlo simulations of Scalapino for $x = 0.13$ [45]. The approximate agreement provides some support for this model.

A dip in $\chi'(\mathbf{Q})$ along $(h,0)$ is seen in all compositions and reflects the reduced spectral weight at $(1/2,0)$ observed in LCO with INS [44] and the RIXS measurements described in Chapter 4. The anomaly at $\mathbf{Q} = (1/2,0)$ is not predicted in the pure SWT model and has been hypothesised to arise due to the creation of a spinon pair. The results suggest that this anomaly is also present

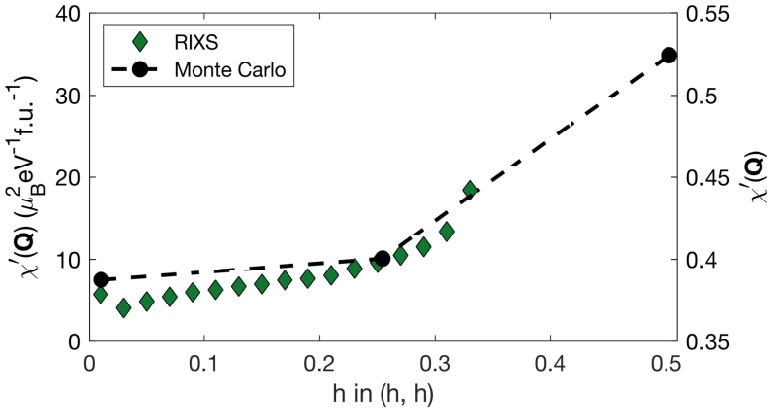

Figure 5.17: $\chi'(\mathbf{Q})$ from RIXS (green diamonds) compared to Monte Carlo calculations (dashed green line) based on the Hubbard model (from reference [45]). The RIXS is performed on an $x = 0.12$ composition and the calculations are for $x = 0.13$ The plots are scaled differently, the RIXS scale is shown on the left axis and the Monte Carlo scale is shown on the right.

in the case of the doped compositions. $\chi'(\mathbf{Q})$ measured in both $x = 0.12$ and 0.16 shows a clear decrease towards $\mathbf{Q} = (1/2, 0)$ suggesting the residual spin fluctuations also deviate from linear spin-wave theory.

Chapter 6

The interplay of charge and spin fluctuations in $YBa_2Cu_3O_{6+x}$

This chapter reports a new high resolution resonant inelastic x-ray scattering (RIXS) study on underdoped cuprate superconductor $YBa_2Cu_3O_{6+x}$ (YBCO). The main focus of this chapter is the charge density wave (CDW) order in YBCO, signatures of which are observed with RIXS as fluctuations in the local charge density. As a result, RIXS observes enhanced spectral weight in the elastic response at wavevectors close to the charge order, $\mathbf{Q}_{\mathrm{CDW}}$. The aim of this work is to characterise this order to provide insights into its relationship with high temperature superconductivity. This should help to address a number of open questions which remain about the relationship between the phases. These include uncertainty about the nature of the order in terms of its static and dynamic phase and the relationship of the order with superconductivity and the pseudogap. This chapter also briefly considers the characteristics of the spin fluctuations in YBCO which serve as a good comparison to the measurements in LSCO described in Chapter 5.

To address these questions, high resolution RIXS measurements were performed on single crystal samples of YBCO with oxygen concentration $x = 0.67$ which gives hole doping of approximately 0.12 per Cu ion. The intensity of the elastic peak is analysed to extract the strength of the charge order which is tracked as a function of temperature above the pseudogap temperature, $T^\star \approx 150$ K and below the superconducting critical temperature, $T_c \approx 65$ K. Analysis is performed to extract different components of the charge order. The impact of charge fluctuations on the inelastic part of the spectrum is also discussed.

The high energy spin fluctuations in YBCO are also characterised within a damped harmonic oscillator model and found to exhibit enhanced damping along the (h,h) direction of the

Brillouin zone.

6.1 Background

Theories which consider the mechanism driving electron pairing in HTSs typically incorporate charge or spin fluctuations. Stripe order or charge density wave order are now considered ubiquitous features of the cuprate phase diagram existing at a range of doping levels and have widely been considered in theories of HTS. On the other hand, as discussed in Chapters 4 and 5, the proximity of superconductivity to antiferromagnetic (AFM) order is another common feature in cuprates with spin fluctuations existing alongside superconductivity. It is clear that fully characterising these two phases is important in understanding the mechanisms that underlie HTS. YBCO shares many similar features with LSCO making it a useful candidate to characterise the ordered phases.

6.1.1 Charge order

Early theoretical descriptions of doped cuprates proposed that doping the AFM state with holes could produce charged magnetic domains, or stripes, in which the charged particles are concentrated [254, 68, 255]. Indeed, static stripe order was quickly detected with inelastic neutron scattering (INS) in the 214 family of cuprates including in $La_{2-x}Ba_xCuO_4$ (LBCO) [69]. In these compounds, order is characterised by intertwined out of phase spin and charge density wave phases. The onset of order appears to be associated with a phase transition from orthorhombic to "less orthorhombic" or tetragonal structure which break the Cu-O bond symmetry making the static stripe ordered phase favourable.

In contrast, for many years following their discovery, no evidence was found for charge order in the 123 cuprates such as YBCO. NMR and ultrasound measurements have since indicated that dynamic CDW order is induced in the presence of a high magnetic field [256, 257]. The order appears at the typical 1/8th doping where superconductivity is suppressed and stripe order is observed in LBCO. Quantum oscillations detected in the negative Hall coefficient of YBCO are now considered signatures of this dynamic charge ordered phase [258]. CDW order was later seen in RIXS measurements on YBCO and the closely related compound, $NdBa_2Cu_3O_{6+x}$ (NBCO), in zero field [74]. Ghiringhelli *et al.* [74] describe how RIXS is sensitive to fluctuations in the local charge density which enhance the elastic response in the presence of charge order. RIXS is particularly sensitive to these fluctuations as the energy is tuned to the absorption edge of the ions which are associated with the charge order. This increased sensitivity may explain

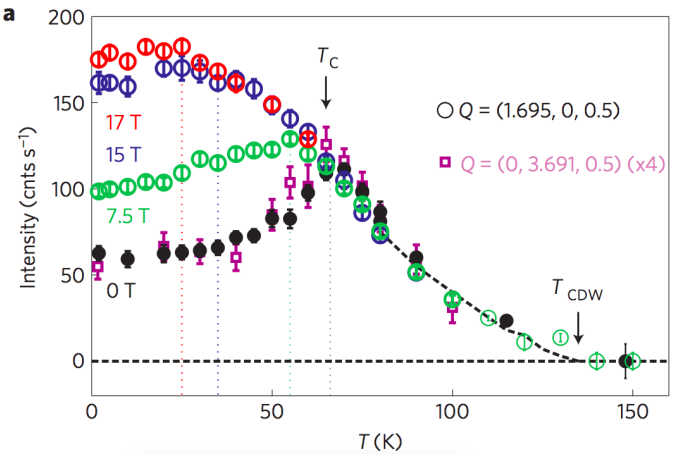

Figure 6.1: Details of the competition between superconductivity charge density wave order showing the charge order intensity as a function of temperature above and below T_c for applied fields 0, 7.5, 15 and 17 T. Figure reproduced with permission from reference [76].

why the ordered phase is observed in RIXS where it was previously not detected. In this set-up, a dynamic 3D CDW peak is identified as quasielastic to within 130 meV.

The ordered phase was observed in a crystal with ortho-II symmetry and subsequent studies observed order in an ortho-VIII crystal with hard x-ray diffraction [76] and in an ortho-III crystal with resonant elastic scattering (REXS) [259]. The ubiquity of the phase across the family of structures suggests that structural phase transitions do not drive the order.

Several measurements indicate that the charge order competes with superconductivity. In NMR measurements, the order only appears when the superconductivity is sufficiently suppressed with applied magnetic field [256]. Similarly, in scattering experiments, the charge order intensity and correlation length decrease below T_c in zero field but dramatically increases in applied field above 12 T [76, 260, 261]. The field is assumed to suppress the superconductivity which allows the intensity of the charge order to increase. Fig. 6.1 shows data from reference [76] in which the intensity of the charge order peak is seen to decrease below T_c in zero field and increase in applied fields. However, Hall effect measurements performed in high magnetic field find that the application of high hydrostatic pressure (2.6 GPa) increases T_c by up to 10 K but does not change the Hall coefficient $R_H(T)$ [262]. This is believed to indicate that the increase in pressure does not considerable change the CDW suggesting the increase in T_c should not be attributed to the suppression of the CDW.

Static and dynamic order

A large number of studies have now been performed on the CDW phase of YBCO which have revealed distinct differences between the CDW order reported at high and low magnetic field.

The high field measurements, above around 15 T, performed with NMR [256], ultrasound [257] and x-rays [260, 261] detect an inherently fluctuating CDW phase at low temperature with T_{CDW} = 150 K. Whereas in zero field, the x-ray studies report charge order at relatively high temperatures with transition T_{CDW} = 150 K [74, 76, 263].

In the low-field measurements the charge ordered phase is identified as dynamic due to the temperature dependence of the correlation length [74]. The CDW is observed parallel to the Cu-O chains along the *b* axis [263]. At high field, Gerber *et al.* [260] report x-ray measurements in pulsed fields of up to 28 T which show the 2D CDW becomes 3D above 15 T. Jang *et al.* [261] track the 3D state with field and detect no CDW in the *h* direction, concluding that the phase is unidirectional.

One explanation for this is provided by quantum oscillations measurements performed at magnetic field up to 62 T which observe small pockets in the Fermi surface [73]. It has been suggested that these pockets occur due to Fermi surface reconstruction from stripe order [264, 265]. Recent calculations by Gannot *et al.* [266] suggest that the the bidirectional CDW order reported by scattering measurements does not explain the Fermi surface reconstruction, whereas the unidirectional order reported in high fields does. This has lead to the speculation that the high-field CDW may be induced by nesting with the low-field CDW acting as a precursor to this state.

New zero-field RIXS measurements in YBCO identify two peaks associated with the charge order with distinct characteristics [136]. The first is a sharp 3D CDW peak which is shown to be suppressed below T_c and the second is a broad peak interpreted as arising due to short-range dynamical fluctuations in the charge density. The broad peak persists in the superconducting phase and above the pseudogap temperature $T^\star$. The onset of the sharp peak is in reasonably good agreement with the high-field measurements which may suggest that the same state is being observed but with an additional short-range order characterised by the broad CDW peak.

Similar behaviour has been seen in recent RIXS measurements in LBCO which indicate that dynamic order might also exist alongside the stripe phase [229, 267]. A precursor peak precedes the charge order at low temperature which is found in a range of doping with varying wavevector. Miao *et al.* [267] propose that the precursor mode originates from the CDW phase coupled with a phonon suggesting CDW order gives way to the intertwined stripe ordered state. Both modes, however, are considered to arise from the same underlying instability.

In general, the characteristics of the charge order in LBCO, YBCO and other cuprates remain unclear. However, a picture is emerging of strong 3D CDW order in low temperature and high

field competing strongly with superconductivity. It now seems likely that this phase exists alongside additional order which takes the form of stripes or short-range fluctuating order which persist over a wide range of temperatures. The relationship between these orders and why they manifest so differently in different compounds, remains an open question.

Some theoretical models of charge order qualitatively reproduced these findings. Caprara *et al.* [268] make calculations based on a single-band Hubbard model and suggest that low and high-field measurements in the cuprates can be unified by assuming the static ordered phase, which is induced by Fermi surface nesting, is suppressed by CDW fluctuations at higher temperature and doping.

Alternatively, theoretical pictures that place spin fluctuations as the dominant driver of the physics in cuprates suggest that exchange interactions play a role in the onset of charge order [269]. Comin *et al.* [163] use resonant soft x-ray scattering to probe the charge ordered electronic ground state and find that the charge is associated with the O2p orbitals in YBCO. The symmetry of the order is also found to be d wave in character, similar to the symmetry thought to be responsible for the superconductive pairing driven by antiferromagnetism.

Phonon anomalies

Another intriguing feature of CDW order in cuprates is the anomalous behaviour of phonons at the ordering wavevector. As described in Chapter 2, electron-phonon coupling plays a role in CDW formation. The order is associated with a divergence in the electronic response $\chi(\mathbf{Q})$ at the Fermi momentum $\mathbf{Q} = 2\mathbf{k}_F$ and an associated reconstruction of the phonon spectrum known as a Kohn anomaly which manifests in softening of the phonon energy. Anomalous behaviour was reported in both acoustic and optical phonon modes in cuprates even prior to the discovery of charge order[270, 271, 272]. Subsequently, Le Tacon *et al.* [137] performed detailed measurements of transverse acoustic and optical phonons with high resolution non-resonant IXS measurements, reporting softening at wavevectors associated with the charge order. Fig. 6.2 is reproduced from reference [137] showing in panels (a) and (b) the phonon energy as a function of $\mathbf{Q}$ and temperature. Both phonon modes show softening at $\mathbf{Q} \sim 0.31$. Fig. 6.2 (c) shows a sharp jump in the width of the peak at $\mathbf{Q} \sim 0.31$. Both features have a characteristic temperature scale of $\sim T_c$ rather than at T_{CDW} which may point to a link with superconductivity. However, high-resolution RIXS has since been used to measure phonon anomalies in several other cuprates [112, 229]. Chaix *et al.* [112] report that the behaviour of the phonon appears to be driven more by $T^\star$ than T_c suggesting a link with the pseudogap.

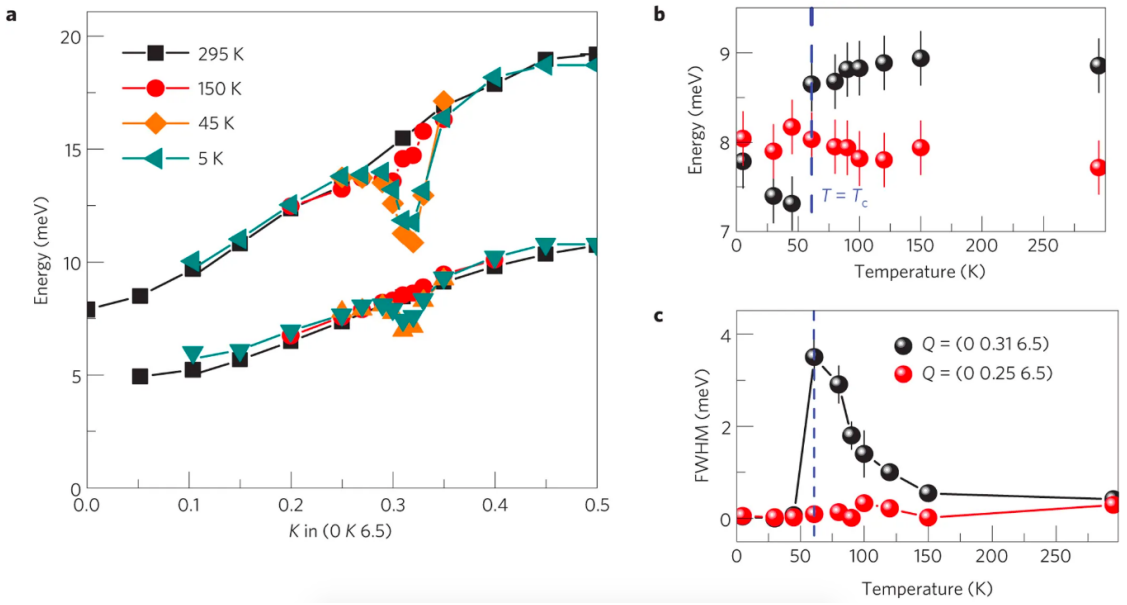

Figure 6.2: Characteristics of the phonon anomaly in YBCO showing (a) the **Q**-dependence of the phonon dispersion for a range of temperatures and (b-c) the temperature dependence of the phonon energy and width. Figure reproduced with permission from reference [137].

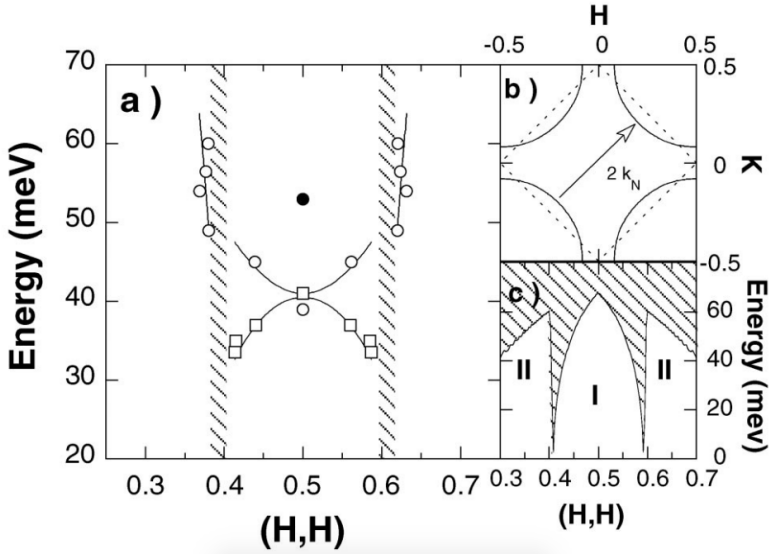

Figure 6.3: The spin fluctuations in YBCO showing in panel (a) the energy dispersion along the 110 direction measured with INS and in panel (b) the location of the measurements relative to the Fermi surface of cuprates, panel (c) shows predictions that the dispersion should reduce to zero at the nodal points of the Fermi surface. Figure reproduced with permission from reference [273].

6.1.2 Magnetic order

As in LSCO, the superconducting phase in YBCO is preceded by an antiferromagnetic phase. AFM order in the parent compound is rapidly suppressed with doping and short-range spin fluctuations are seen to remain [274, 275, 276]. Several INS studies have been made of the spin fluctuations of YBCO. At high energies, a continuum of incommensurate excitations are

observed with INS [239]. Unlike in LSCO, the excitations do not disperse to zero, making the characteristic dispersion curve quite different. Fig. 6.3 (a) shows the energy dispersion of the spin fluctuations in the 110 direction, the curve is sometimes referred to as an "hourglass" due to its shape in energy-momentum space [273, 277]. Fig. 6.3 (b) shows the dispersion in relation to the typical Fermi surface of cuprates and (c) shows that the energy of the fluctuations is predicted to go to zero at nodal points of the Fermi surface.

At low energies, a resonance peak is observed at around 40 meV close to the antiferomagnetic wavevector $\mathbf{Q}_{\mathrm{AFM}} = (1/2, 1/2)$ [278, 279]. The peak has been found to coincide with the formation of the pseudogap and is strongly enhanced in the superconducting state [238, 167]. Another key feature of the excitation spectrum is a spin-gap observed in the susceptibility of YBCO at low energy transfer [280, 166, 167, 281]. This gap has been observed in several cuprates below around 35 meV.

A number of studies have reported signatures of the impact of charge order on the spin fluctuations [282, 283, 284]. Fig. 6.4 (a) shows RIXS measurements performed by Dean *et al.* [282] on stripe ordered LBCO which show enhanced intensity in the spin fluctuations at the wavevector associated with the charge order. They also report a slight decrease in the excitation FWHM in the same region. Da Silva Neto *et al.* [284] perform similar experiments with exit-beam polarisation analysis. Their measurements on NCCO also show that additional spectral weight is observed in the spin fluctuations at the charge ordering wavevector. The enhanced elastic response observed in RIXS in the presence of charge order is shown to be associated with the cross polarisation channel. Fig. 6.4 (b) shows the intensity of the spin fluctuations at high and low temperature, in which the low temperature data show a peak close to the $\mathbf{Q}_{\mathrm{CDW}}$. They interpret this as suggesting that the dynamic response is associated with spin-flip excitations providing strong evidence for the link between charge order and spin fluctuations. It should be noted that these studies report the intensity following normalisation to the *dd*-excitations and therefore may not account for self-absorption effects or the effects of the local RIXS cross-section.

Jiang *et al.* [232] report calculations based on the Hubbard model which considers both the spin and charge fluctuations. Their model predicts that the dominant order depends on the next-nearest neighbour hopping parameter t'. When t' is tuned to zero, the superconducting correlations are suppressed and charge order dominates which they interpret as suggesting the superconductivity emerges when stripe order is suppressed.

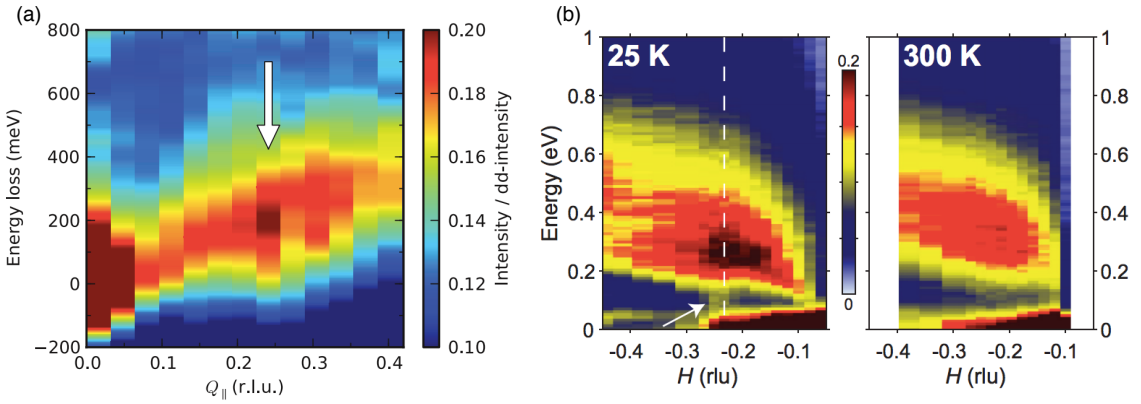

Figure 6.4: Signatures of charge order influencing spin fluctuations in (a) RIXS measurements in LBCO, reproduced with permission from reference [282] and (b) polarised RIXS measurements in NCCO, reproduced with permission from reference [284]. Both measurements show enhancements in the intensity of the spin fluctuations close to the charge ordering wavevector which is indicated with the white arrows.

6.2 Measurement details

6.2.1 Sample preparation

The single crystal samples of YBCO measured in the experiments described in this chapter were grown with the TSFZ technique by previous member of the Bristol group, Maud Barthélemy [285]. The samples were annealed in an argon atmosphere and detwinned under pressure. The oxygen content is verified with SQUID magnetometry measurements which find the transition temperature matches the expected value for the $x = 0.67$ composition (see the phase diagram in Fig. 6.5 [76]). The SQUID measurement is shown in Fig. 6.6.

The size of the YBCO samples is significantly smaller than the LSCO samples measuring less than 0.5 x 0.5 mm in the $a-b$ plane and much less along the c axis. This means the samples are difficult to cleave but the growth method results in a shiny crystal surface in their as-grown state. Fig. 6.7 compares the intensity of the elastic peak close to the specular position, $\mathbf{Q} = (0.03, 0.03)$, measured with the uncleaved YBCO samples and the cleaved LSCO samples. The intensity of the elastic peak is similar, suggesting that it is not necessary to cleave the shiny as-grown YBCO samples.

6.2.2 Experimental setup

The Cu L-edge ($\simeq$ 932 eV) RIXS measurements described in this chapter were performed at I21 at Diamond Light Source with an energy resolution $\Delta E \sim 45$ meV. The standard experimental geometry described in Chapter 3 was used for these experiments and a scan was made over the

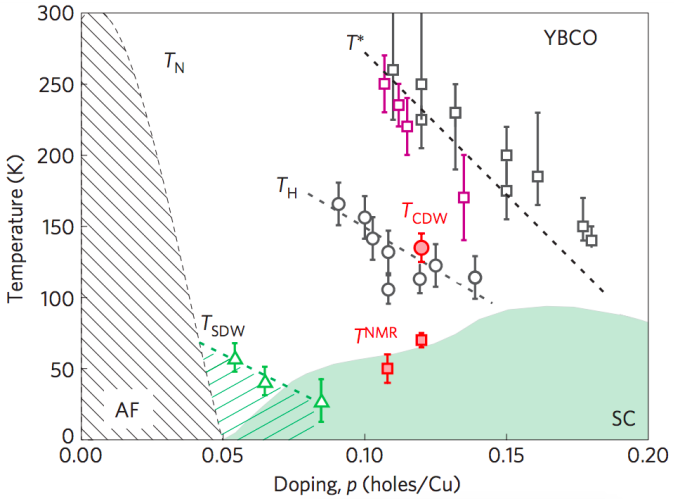

Figure 6.5: Phase diagram of YBCO showing the temperature dependence of the antiferromagnetic, superconducting, pseudogap, charge and spin ordered states. Data points are shown for the pseudogap measured with the Nernst effect (black squares) and neutron diffraction (purple squares). Measurements of the Hall coefficient were measured with the Hall effect (black circles). Spin density wave order was measured with INS (green triangles). The CDW measurements are shown in red from NMR (squares) and x-ray diffraction (circles). Figure reproduced with permission from reference [76].

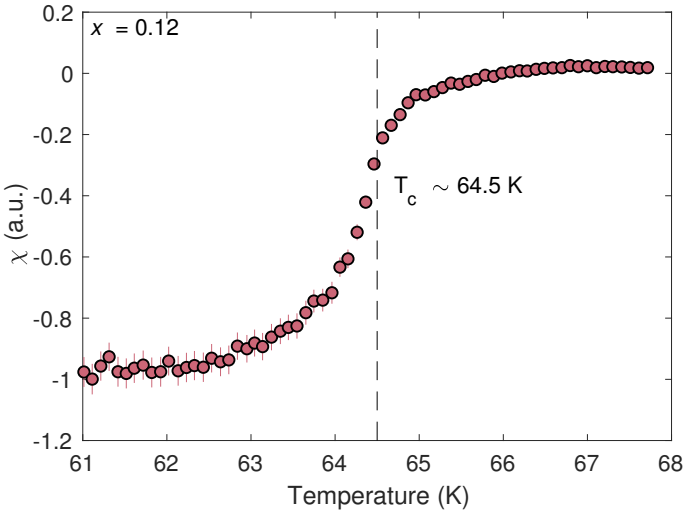

Figure 6.6: SQUID magnetometry measurements of the YBCO sample showing the transition to the superconducting state at $T_c \sim 64.5$ K. The samples were cooled in zero field and measured with an applied field of 3 Oe.

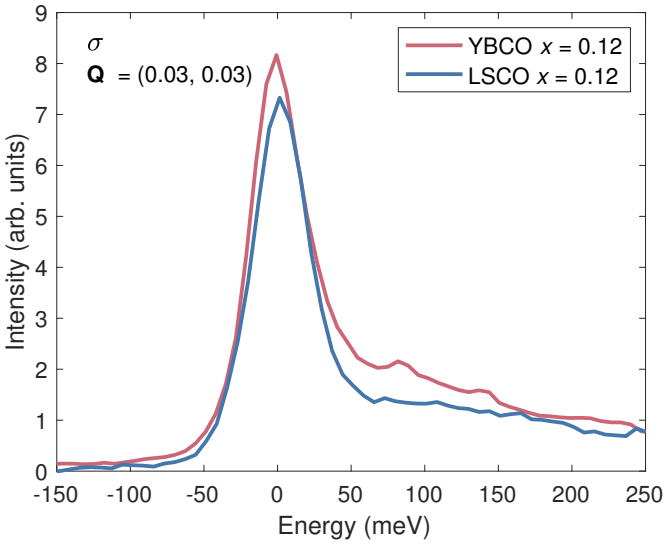

Figure 6.7: Comparison of RIXS spectra measured in YBCO $x = 0.67$ which gives hole doping of approximately 0.12 and LSCO $x = 0.12$. The measurements show that the elastic peak close to the specular position ($\mathbf{Q} = (0.03, 0.03)$ is similar in cleaved LSCO as in thin as-grown YBCO.

grazing-out region to probe positive $\mathbf{Q}$. The spin fluctuations are favoured in the π geometry – these were measured at base temperature, $T = 16$ K, in both high symmetry directions (h,h) and $(h,0)$. In the grazing-out region, σ polarisation favours the charge fluctuations – these were measured in the $(h,0)$ direction for 5 different temperatures, 16, 65, 150, 250 and 300 K. The temperatures are chosen to explore the charge fluctuations at $T_c = 65$ K and $T^\star = 150$ K and their evolution well above and below this range.

6.2.3 Data normalisation

When measuring CDW order, RIXS is sensitive to fluctuations in the charge density which contribute to the total elastic spectral weight. It is therefore able to track the strength of the CDW phase by observing changes to the elastic peak intensity. As these changes are fairly small, careful analysis of the self-absorption and other factors affecting the intensity is important. The YBCO samples are considerably smaller than LSCO and hence are particularly sensitive to movement of the beam on the sample.

To demonstrate the importance of these factors, Fig. 6.8 compares the integrated intensity of the elastic peak as a function of $\mathbf{Q}$ for a range of temperatures. Fig. 6.8 (a) shows uncorrected data, I_{raw}, (b) shows the data divided by, g, an integration over the range of the dd excitations which we redefine I_{dd} (from Eqn. 5.2) and (c) shows the data corrected via the self-absorption calculation, I_{SA} (from Eqn. 3.15) . Crucially 6.8 (d) shows that the normalisation method alters whether the charge order intensity is seen to increase or decrease below T_c. This is likely to

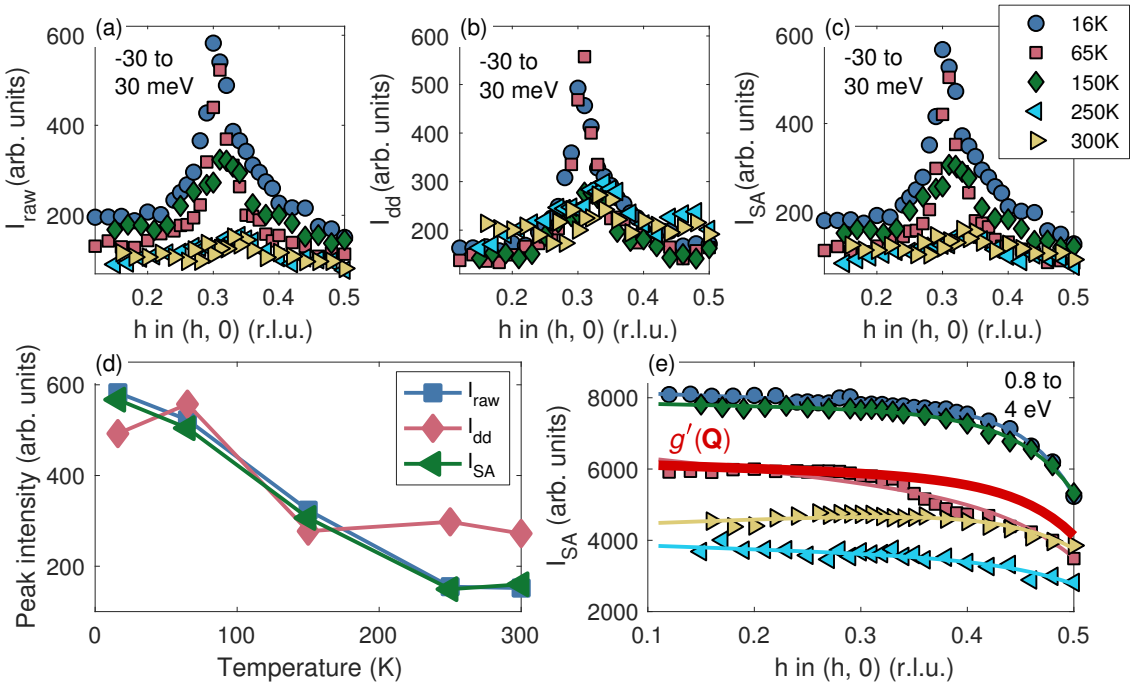

Figure 6.8: Comparison of the charge order intensity extracted from an integration over the elastic peak in RIXS data for various normalisation approaches. Data are integrated in the region –30 to 30 meV . Showing the maximum intensity extracted from (a) unnormalised data I_{raw}, (b) *dd*-normalised data I_{dd} and (c) self-absorption corrected data I_{SA}. Panel (d) shows the peak intensity as a function of temperature for the three methods. Panel (e) shows the wavevector dependence of the *dd* excitations g, integrated in the region 0.8 to 4 eV, showing the averaged fit $g'(\mathbf{Q})$ in red. Data are all collected in σ polarisation with grazing-out geometry.

be because the measurements are sensitive to small changes in scattered intensity resulting from small movements of the beam on the sample. This effect is particularly important as the samples are so small. Normalising to the *dd* excitations accounts for the small movements but the self-absorption correction does not. This reveals the importance of accurately normalising the data in the case where the important physics is captured within small changes in intensity.

In practice, it is necessary to correct the whole spectrum using the self-absorption calculation and then normalise to the *dd* intensity. This approach corrects for both the strong resonance effect and for anomalies which occur due to the beam moving slightly off of the sample. However, normalising to the *dd* intensity introduces the assumption that the total spectral weight of the *dd* excitations is constant in $\mathbf{Q}$. In fact it is clear from the raw and self-absorption corrected data that this is not the case. This means that a $\mathbf{Q}$-dependent factor, which we define as $g'(\mathbf{Q})$ is introduced into the data. To compensate for this, the intensity of the *dd*-excitations is modelled as an exponential function to approximate $g'(\mathbf{Q})$. The fits are plotted in Fig. 6.8 (e) where the average fit which approximates $g'(\mathbf{Q})$ is shown in red. Each dataset is then multiplied by $g'(\mathbf{Q})$ and therefore the total normalisation is defined as,

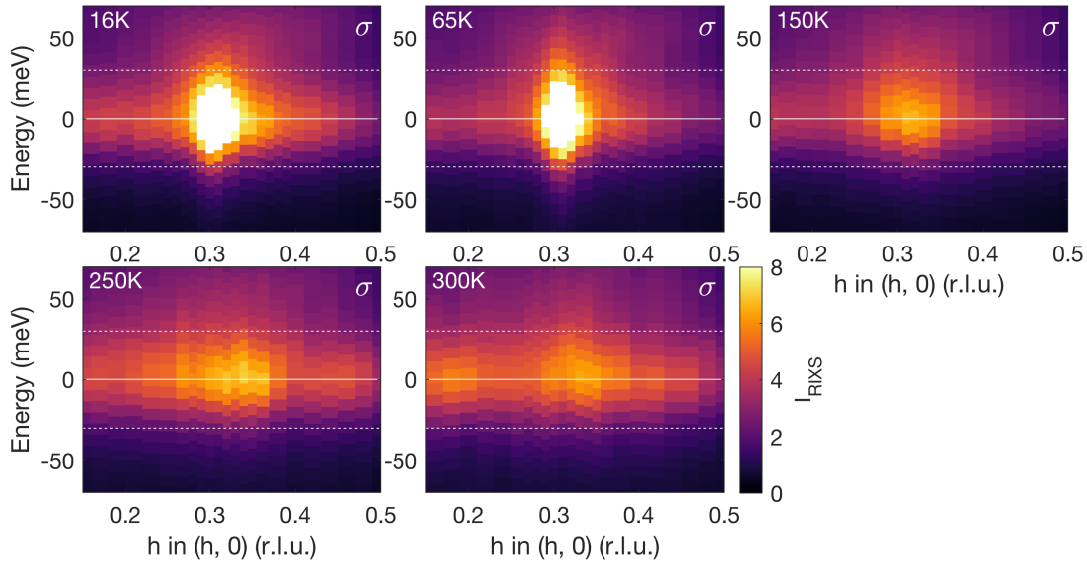

Figure 6.9: Normalised RIXS intensity as a function of wavevector and energy in the range of the charge order peak. Dashed white lines show the integration range used to plot the charge order intensity in Fig. 6.8.

$$I_{\mathrm{RIXS}} = \frac{I_{\mathrm{SA}} g'(\mathbf{Q})}{g(\epsilon, \epsilon', \mathbf{k}, \mathbf{k}')}. \tag{6.1}$$

It should be noted that while this normalisation procedure is sufficient to correct the charge order intensity, the intensity of the spin fluctuations still contain magnetic prefactors which contribute to the RIXS cross-section. The analysis in this chapter therefore does not consider the intensity of spin fluctuations.

6.3 Results: charge fluctuations

Following normalisation with Eqn. 6.1, the RIXS intensity I_{RIXS} is plotted in the region of the elastic peak in Fig. 6.9. The charge order peak is centred at $\mathbf{Q} = (0.31, 0)$ and E = 0 eV. The intensity of the peak is largest at 16 and 65 K and significantly suppressed at higher temperatures. The sharp charge order peak is rapidly suppressed with increasing temperature but a broader peak can be seen emerging which becomes stronger than in the low temperature data.

6.3.1 Data fitting

The data are modelled as in Chapters 4 and 5 with Gaussian functions to account for elastic and phonon peaks, a linear function to account for the background and a damped harmonic oscillator (Eqn. 4.35) to account for the spin fluctuations. At low $\mathbf{Q}$, where the pole weight approaches zero, the excitations become overdamped and the overdamped harmonic oscillator

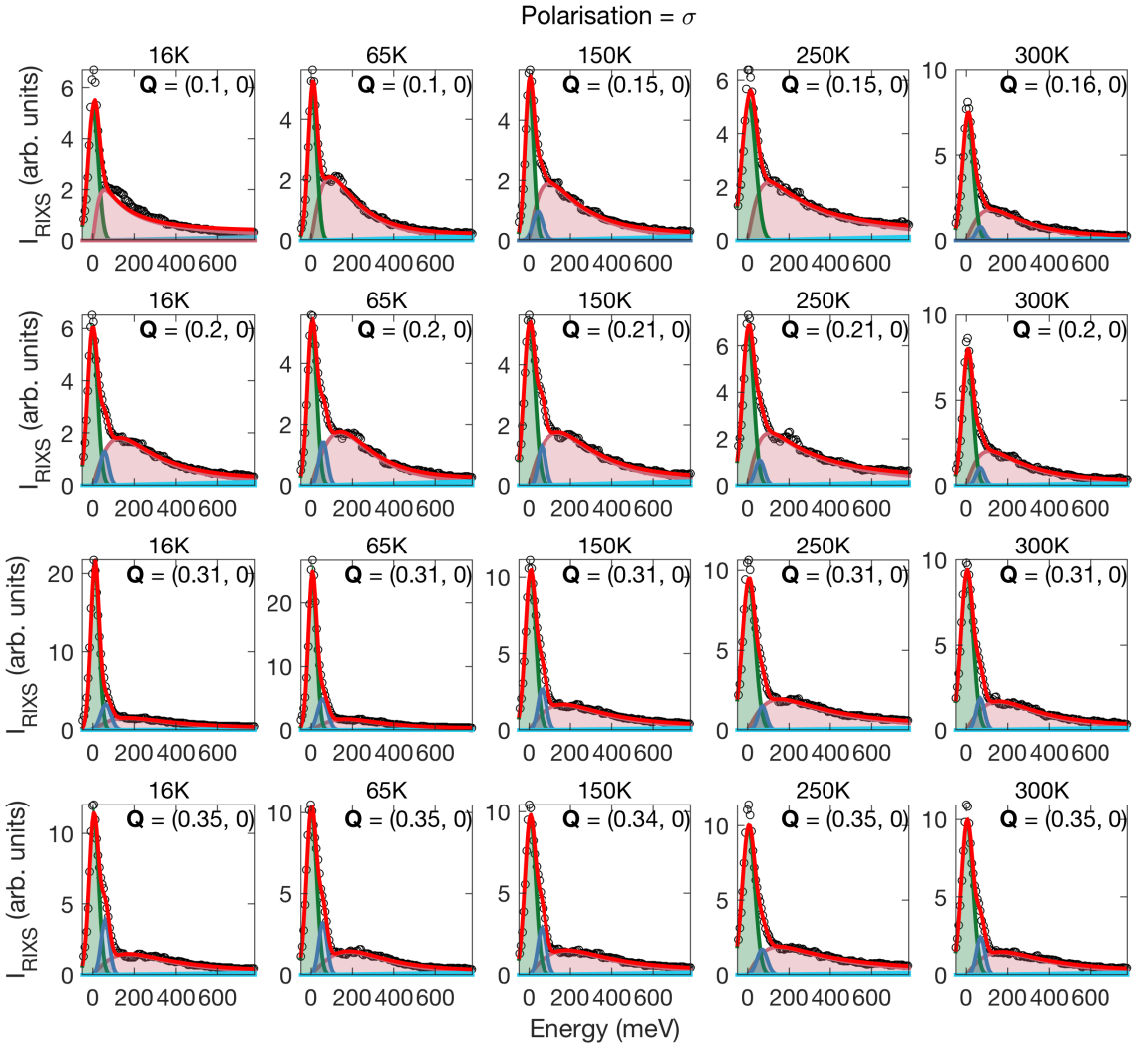

Figure 6.10: Example RIXS spectra on YBCO showing data in black, the total fit in red and components of the fit beneath: the elastic peak in green, magnon in pink, phonon in dark blue and linear background in light blue. Showing data used in the analysis of the charge order, measured in the $(h,0)$ orientation at 16, 65, 150, 250 and 300 K and with σ polarisation such that charge fluctuations are favoured.

(ODHO) function (Eqn. 5.3) is used to fit the data. Example fits are shown in Figs. 6.10 and 6.11 and the full dataset with fits is shown in Appendix A. The fits generally describe the data well.

6.3.2 Charge density wave peak strength

The intensity of the fitted elastic peak is plotted for each temperature in Fig. 6.12 (a). The elastic peak is broadened due to the resolution of the experiment but may also include quasielastic contributions from low energy phonons. Following the approach described in reference [136], the charge order peak in **Q** can be separated into a broad and narrow component which are modelled with Lorentzian functions. In the high temperature data, 250 K and 300 K, the narrow peak is assumed to be suppressed and only a single Lorentzian function is used in the fit.

The extracted parameters of the fitted Lorentzian peaks are plotted in Fig. 6.12 (b-d). The

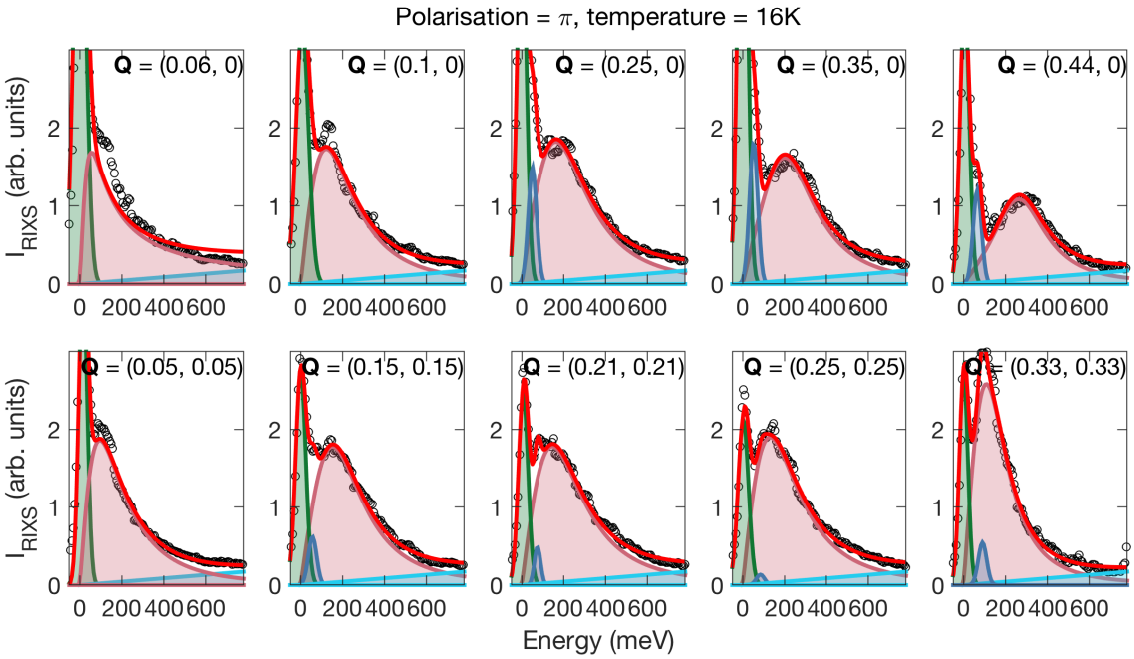

Figure 6.11: Example RIXS spectra on YBCO showing data in black, the total fit in red and components of the fit beneath, the components are indexed as in 6.10. Showing data used in the analysis of the spin fluctuations, measured in the $(h,0)$ and (h,h) directions at 16 K with π polarisation such that the magnetic excitations are favoured.

peak intensities plotted in panel (b) show that the narrow peak rapidly increases below 150 K but decreases slightly below T_c. This matches well with previous observations [74, 76, 259, 263, 137, 136] that the charge order is enhanced at low temperature and suppressed with the onset of superconductivity. The intensity of the broad peak is relatively flat with a slight increase above 150 K which may indicate its relationship to the pseudogap. The broad peak does not show evidence for suppression below T_c which could point to a different relationship with the superconductivity.

Panel (c) shows that the narrow peak is consistently seen at $\mathbf{Q} \sim 0.31$ as has been previously reported. The broad peak is centred at a slightly larger wavevector and there is a small shift in the position of the peak from $\mathbf{Q} \sim 0.33$ below $T^\star$ increasing to $\mathbf{Q} \sim 0.38$ at 16 K. This may reflect the influence of fitting two Lorentzian functions to the low temperature data, however, the data in panel (a) shows a shoulder at high-$\mathbf{Q}$ which shifts to lower wavevector as temperature increases.

Finally, the peak width (full width half maximum) shown in panel (d) illustrates that the broad peak is generally larger than the narrow peak. Panels (b-c) indicate that $T = 150$ K corresponds to a cross-over between the low and high temperature behaviour hence the error in extracting the width and position is large.

To verify that this behaviour exists in the raw data and is not an artefact from fitting, Fig.

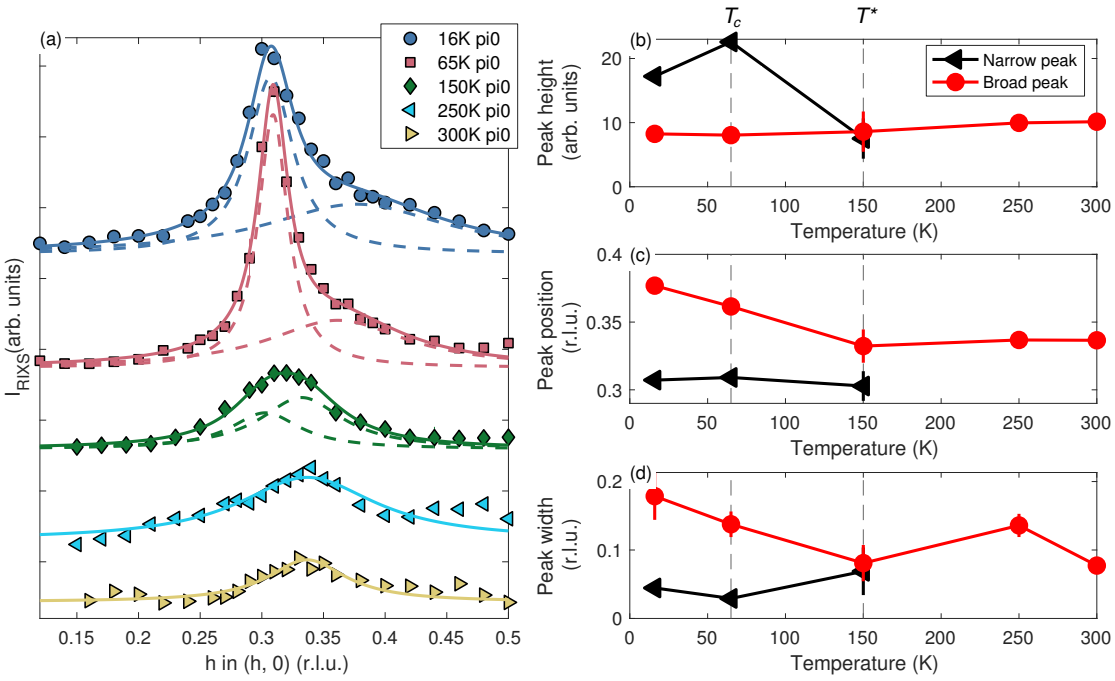

Figure 6.12: Characteristics of the charge density wave peak from fits to RIXS data showing (a) the CDW peak intensity as a function of wavevector with Lorentzian fits for five temperatures (the data are offset for clarity) and (b-d) the height, position and width of the peaks in **Q** as a function of temperature. Data are shown from experiments optimised to measure the charge order in LCO, with σ polarisation and along the $\mathbf{Q} = (h, 0)$ direction.

6.13 shows the RIXS spectra in a region 100 meV around the elastic peak for each temperature. The spectra are offset by **Q** to show the evolution of the charge order intensity as a function of wavevector. The sharp peak is clearly shown in the low temperature data with wavevector $\mathbf{Q} = 0.31$. The broad peak is clear in the high temperature data at $\mathbf{Q} = 0.34$ and also evident in the low temperature data as a shoulder to the sharp peak at $\mathbf{Q} \approx 0.38$.

6.3.3 Phonon anomalies

The phonon excitations that we measure in YBCO are not as well separated as those seen in previous IXS experiments [137] or as in the data presented in Chapters 4 and 5. However, the energy resolution of these experiments ($\Delta E \sim 45$ meV) is sufficient to observe a single phonon as shown in map plots in Fig. 6.14 which show some evidence of phonon softening close to $\mathbf{Q}_{\mathrm{CDW}}$. As in Chapter 5, it is assumed that the fitted phonon contains spectral weight from both the bond-stretching and bond-buckling phonon modes which are predicted to be present at the Cu L_3-edge in RIXS measurements [129]. Fig. 6.15 shows the phonon energy extracted from fits to the data. In data measured at temperatures below $T^\star$, the phonon intensity is suppressed by around 15 meV close to $\mathbf{Q} = 0.3$. As temperature increases, the suppression is no longer seen. This behaviour is in keeping with previous RIXS measurements of anomalous phonon behaviour

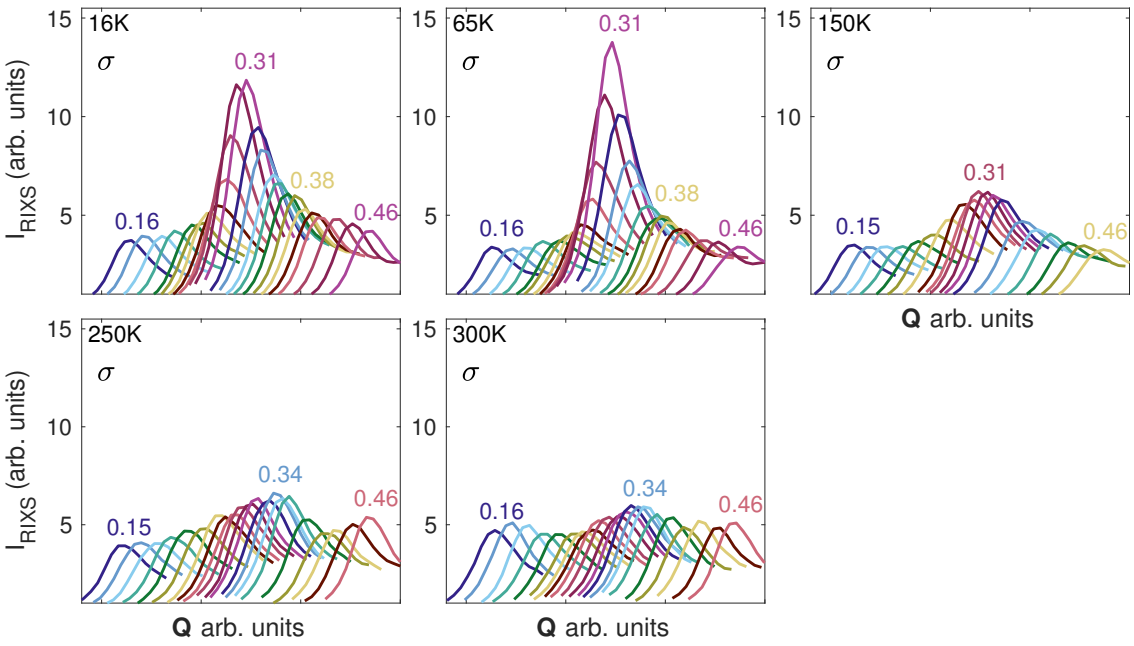

Figure 6.13: RIXS spectra ±50 meV around the elastic peak in YBCO showing the intensity of the charge order for different temperatures. The spectra are offset by their wavevector to show the evolution of the charge order with **Q**.

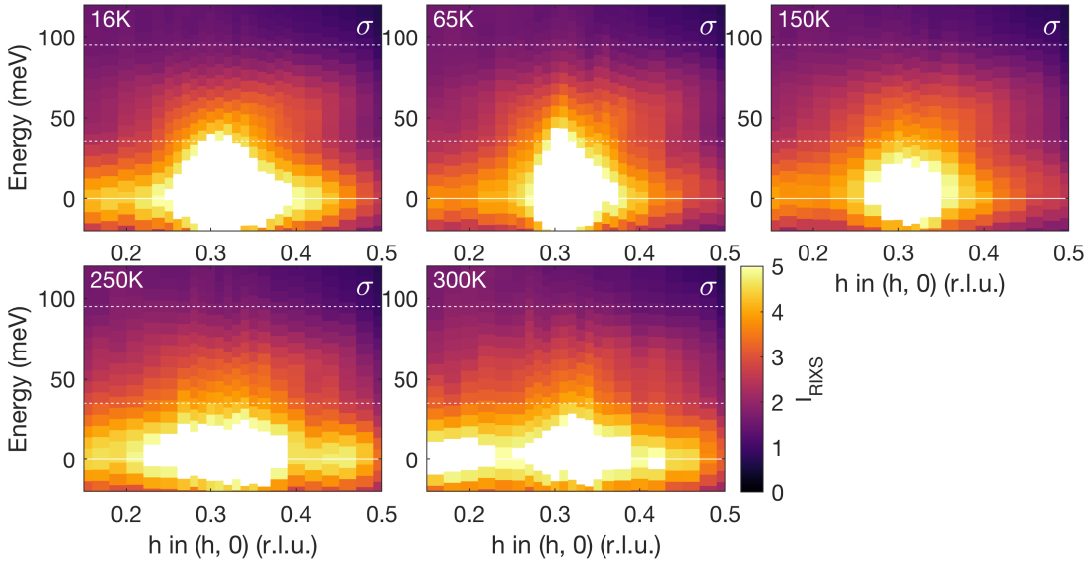

Figure 6.14: Normalised RIXS intensity as a function of wavevector and energy in the range of the charge order and phonons.

in charge ordered cuprates and is interpreted as being a signature of the charge order [112, 229]. However, as the phonon energy is not completely softened, as is the case for Kohn anomalies, it has been suggested that the phonons couple to the CDW fluctuations but the electron-phonon coupling does not drive CDW formation itself. The persistence of this behaviour to higher temperatures than the sharp CDW peak suggests that the phonons couple to the precursor CDW rather than to the full 3D order.

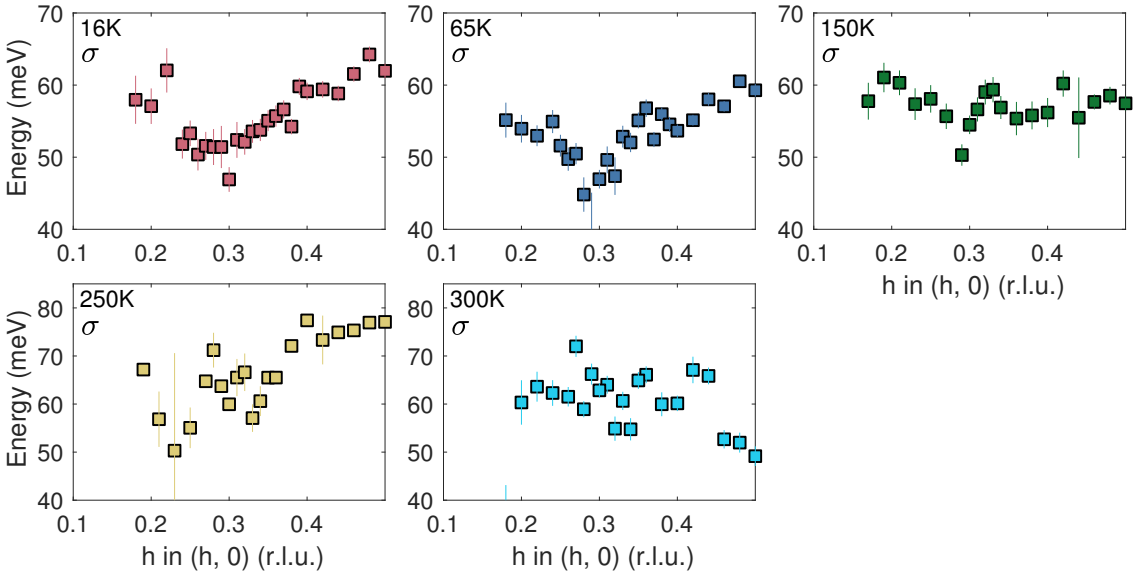

Figure 6.15: Energy dispersion of the phonon excitations for a range of temperatures. Data are extracted from fits to π polarised RIXS spectra as shown in Fig. 6.11.

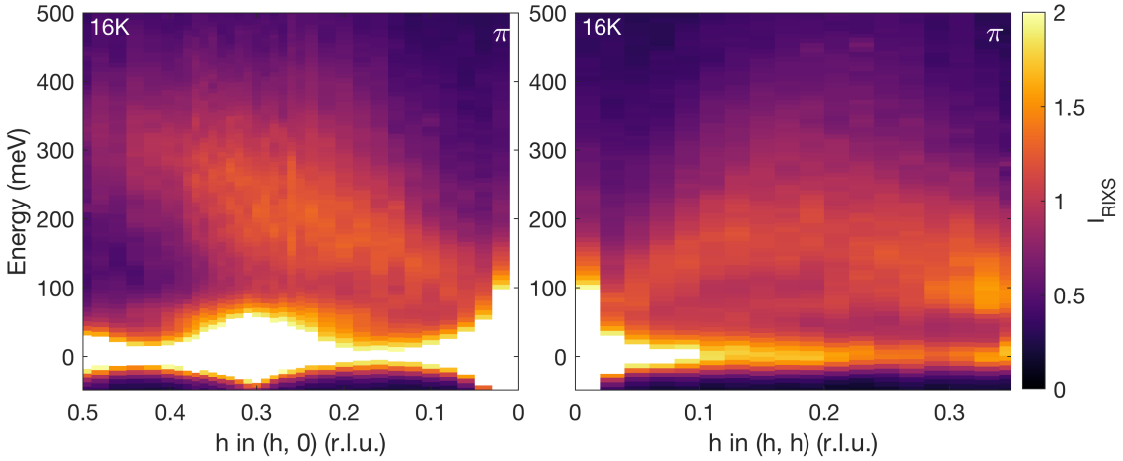

Figure 6.16: Normalised RIXS intensity as a function of wavevector and energy in the range of the spin fluctuations.

6.4 Results: spin fluctuations

Finally, this section focuses on the spin fluctuations measured in YBCO. Fig. 6.16 shows a normalised RIXS intensity map in the region associated with the spin fluctuations. In this instance the data have been corrected for the effects of self absorption assuming the polarisation of the photon is flipped from π to σ as is the case for the spin fluctuations. However, contributions from the RIXS cross-section are not accounted for hence the absolute intensity of the spin fluctuations in not considered in this Chapter. Fig. 6.16 shows that as well as clear charge order in the $(h,0)$ direction, strong dispersive spin fluctuations are also observed. The measurements match well with previous observations of the high energy spin fluctuations [239], however, we cannot resolve details of the low energy fluctuations from the elastic peak.

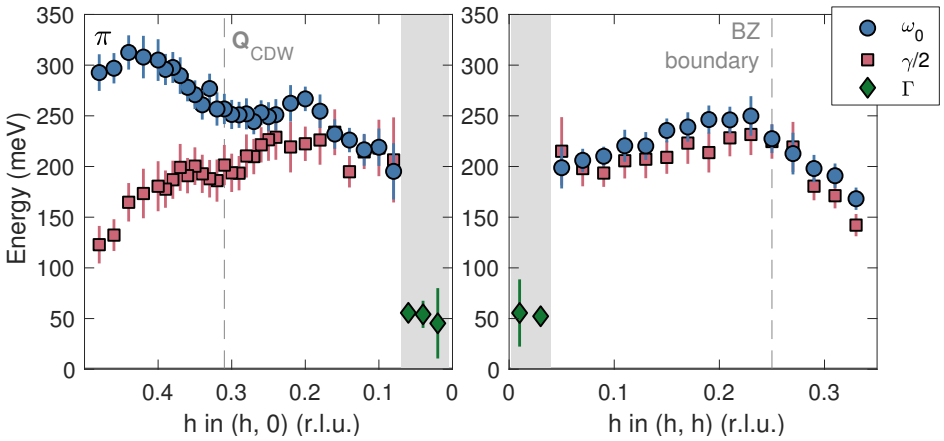

Figure 6.17: Parameters extracted from damped harmonic oscillator fits to RIXS data on the spin fluctuations in YBCO. The excitation pole position ω_0, in blue, is compared to the damping parameters $\gamma/2$ in red. The grey region indicates where the ODHO function is used to fit the data and therefore only the overdamped parameter Γ is shown.

Fig. 6.17 shows the parameters extracted from the DHO model of the RIXS data. The excitation pole weight ω_0 shows the characteristic anisotropic dispersion as described above. As in LSCO, we also see a peak in the damping parameter γ along the (h,h) direction which in YBCO is seen to be close to or slightly below $(1/4,1/4)$. This appears to support the conclusion in Chapter 5 that the damping is anisotropic.

However, the damping in $(h,0)$ is quite different to that seen in LSCO, where γ is relatively flat for all wavevectors, see Fig. 5.10. In YBCO, γ appears to show a broad peak around $\mathbf{Q} = 0.2$ and decrease towards the zone boundary. However, as the magnon pole energy decreases towards Γ, $\gamma/2$ is close to ω_0 up to $\mathbf{Q} = 0.2$. It should be noted that the total flux is lower than that used in Chapter 5 so the error associated with extracting the damping parameters is larger and the wavevector dependence trends are not so clear.

6.4.1 Interaction with charge order

Fig. 6.17 appears to show signatures of the influence of charge order on the spin fluctuations including a slight suppression of both ω_0 and γ close to $\mathbf{Q}_{\mathrm{CDW}} = (0.31,0)$. These signatures could point to the interaction of spin and charge fluctuations. However, we do not reproduce the measurements in NCCO and LBCO which showed enhanced spectral weight in the spin fluctuations at $\mathbf{Q}_{\mathrm{CDW}}$ as shown in Fig. 6.4 [282, 284]. In fact, the data plotted in Fig. 6.20 show that the spin fluctuation intensity actually appears to be somewhat suppressed at $\mathbf{Q} = (0.31,0)$ compared to wavevectors away from the charge order at $\mathbf{Q} = (0.2,0)$. However, the analysis in this chapter does not attempt to consider the prefactors to the RIXS intensity in YBCO and hence measurements of the spin fluctuation intensity do not reflect the underlying spin response.

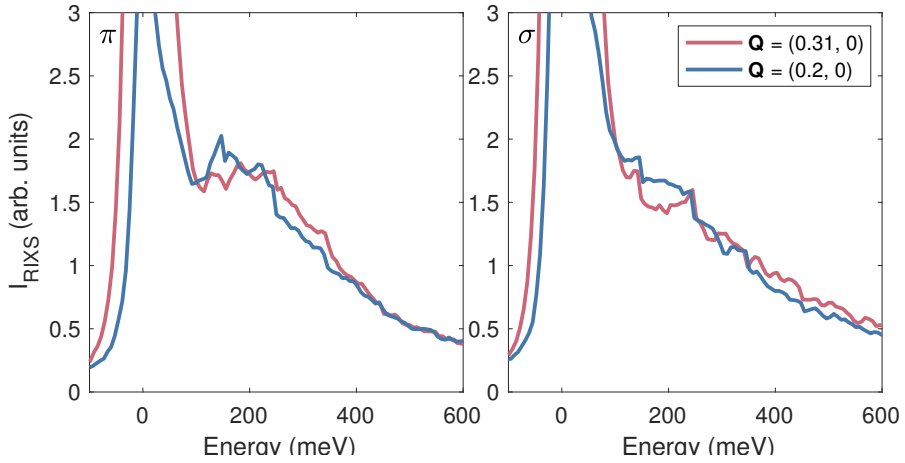

Figure 6.18: RIXS spectra close to (pink) and away from (blue) the charge ordering wavevector for data measured with π and σ polarisation.

Additionally, our measurements do not analyse the polarisation of the outgoing photon as in reference [284] and hence the effect on the spin-flip contribution may be hidden.

6.4.2 Resolution correction

At this point the impact of the energy resolution on the spectra is briefly considered. While the resolution of the experiments is expected to impact on the widths of all excitations described in this thesis, the energy resolution of the experiments in this chapter is worse ($\Delta E \sim 45$ meV) and so a survey of the impact on the damping parameter γ is particularly useful.

Fig. 6.19 shows example RIXS spectra following a procedure to account for the energy resolution in the DHO function which models the spin fluctuations. In this procedure, the modelled DHO function is subtracted from the RIXS intensity and replaced with the modelled function deconvolved with a Gaussian function of width of the energy resolution, $\Delta E \sim 45$ meV,

$$\chi''_{\text{corr}}(\mathbf{Q},\omega) = \sum_{\omega} e^{-\frac{\omega^2}{2\sigma^2}} \cdot \chi''(\mathbf{Q},\omega), \tag{6.2}$$

where σ is the HWHM of the total energy resolution established from scattering from a purely elastic reference just before the measurement at each $\mathbf{Q}$. The spectrum with the corrected DHO function, $\chi''_{\text{corr}}(\mathbf{Q},\omega)$, is referred to as the resolution corrected spectrum. Following this procedure, the spectra are fit with the same parameters and the damping parameter γ is extracted, as shown in the panels (b-c) and (e-f) of Fig. 6.19. The difference in γ between the uncorrected spectrum and the resolution corrected spectrum is found to be less than 1% suggesting that this effect cannot be responsible for the strongly enhanced and wavevector dependent γ which is seen in this Chapter and in Chapter 5.

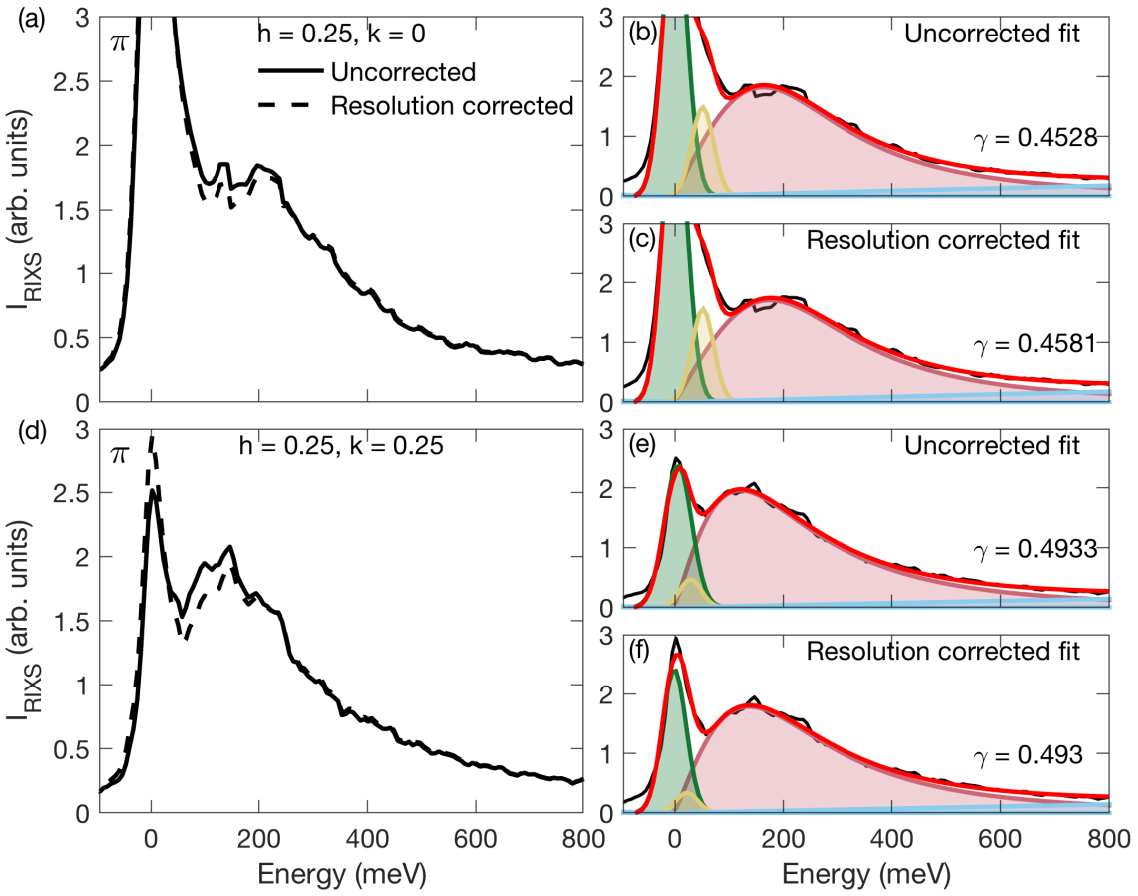

Figure 6.19: Comparison of un-deconvolved and resolution corrected RIXS spectra showing the effect for two wavevectors $\mathbf{Q} = (0.25, 0)$ and $(0.25, 0.25)$. Also showing fits to the un-deconvolved and deconvolved spectra and the resulting effect on γ.

6.5 Discussion and conclusions

It is generally accepted that charge fluctuations in cuprates are not the dominant mechanism behind electron pairing but that they do play some role as demonstrated by their effect on T_c. The dominant pairing mechanism is still up for debate but spin fluctuations, persisting beyond the AFM phase, are considered to be a good candidate. Both spin and charge fluctuations have been investigated in the RIXS measurements described in this chapter demonstrating the usefulness of RIXS as a technique and providing some new insights into the nature of the fluctuations, these include:

- Further evidence that charge density wave order is strongly enhanced below $T^\star$ and suppressed below T_c.
- The wavevector-dependent charge order can be separated into a broad and narrow component and the new results demonstrate the temperature dependence of the two peaks.
- Anomalous phonon behaviour is seen up to $T^\star$ and most strongly at T_c, perhaps demon-

strating a connection with superconductivity.

- Wavevector dependent damping is observed with similar characteristics as that reported in LSCO in Chapter 5
- Some signatures are reported of an interaction between the spin and charge fluctuations close to $\mathbf{Q}_{\mathrm{CDW}} = 0.31$.
- Technically, these results verify the importance of carefully considering the prefactors to the RIXS intensity. They demonstrate that a combination of normalisation with the *dd*-excitations and self-absorption correction can be useful for experiments performed with small sample sizes.

The following sections discuss these results in more detail.

6.5.1 Temperature dependence of charge order

Temperature dependent measurements are the principal tool used to understand charge order in this chapter. The measurements are performed at $T_c = 65$ K and $T^\star = 150$ K and explore a range well above and below these transitions. Arpaia *et al.* [136] set out new analysis which treats enhancement to the elastic spectral weight over a broad range of $\mathbf{Q}$, previously presumed to be a background effect, as a signature of charge order. Our measurements also show a second peak in the wavevector dependent elastic response as shown in Fig. 6.12 (a) particularly in the low temperature data. However, here we consider the possibility that the broad peak arises due to low energy phonon excitations. Devereaux *et al.* [129] predict that RIXS is sensitive to at least three phonons at the Cu L_3 edge including a longitudinal acoustic mode below 10 meV as shown in Fig. 4.8. As only one phonon is resolved and fit in this data, spectral weight from other phonon modes is likely to contribute to the elastic peak intensity and may be responsible for the broad peak. Separating the broad peak from the sharp low-temperature peak therefore gives insight into the behaviour of the charge order and the low energy phonon and their characteristics with temperature.

The most obvious characteristics are in the behaviour of the sharp peak which shows strong enhancement below $T^\star$ and slight suppression below T_c. The narrow peak has a roughly constant $\mathbf{Q}_{\mathrm{CDW}} = 0.31$ and peak width. These results fit in convincingly with other measurements of charge order in cuprates indicating strong 3D CDW order below $T^\star$ which competes with superconductivity.

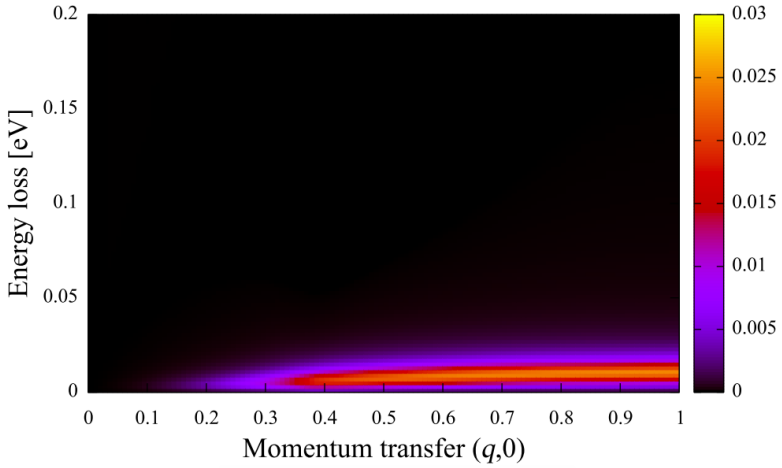

Figure 6.20: The low energy phonon mode predicted to contribute to the RIXS signal at the Cu L_3-edge. The intensity is in arbitrary units. Figure reproduced with permission from reference [129].

Contrastingly, while the intensity of the broad peak is relatively unchanged with temperature, it is observed at slightly higher wavevector, $\mathbf{Q} = 0.32$ which increases below T_c reaching nearly $\mathbf{Q} = 0.38$. Similar shifts have been reported in the wavevector of a broad peak in LBCO [267] and in the ordering wavevector of stripe order $La_{2-x}Sr_xNiO_4$ (LSNO) [286]. In these measurements, the wavevector shift is understood as a way of reducing entropy in a stripe-ordered system of doped holes [286, 267]. The entropy for N_c configurations of doped holes is computed as $S = k_B \ln N_c$. Miao *et al.* [267] describe the application of this model to stripe ordered LBCO where it is assumed that half filled stripes are insulating with zero entropy. They show that at zero temperature the charge ordering wavevector $\mathbf{Q}_{\mathrm{CDW}} = 2x$ and that as temperature changes, free energy is minimised by ordering at different wavevectors. It is not clear how this model could be extended to non stripe ordered YBCO. However, our measurements fit in well with the assumption that the broad peak comes from a low energy phonon. The longitudinal acoustic mode below 10 meV is expected to increase in intensity towards the zone boundary which could explain the broad peak seen in the elastic intensity.

The energy resolution of these measurements does not allow detailed characterisation of the phonon excitations. However, the anomalous softening of phonons close to $\mathbf{Q}_{\mathrm{CDW}}$ is seen up to approximately $T^\star$. As in previous work this is taken as an indicator of a gradual onset of CDW order in the pseudogap state. In combination with the results from the elastic part of the spectra, our results suggest that the phonon anomalies onset at higher temperature and may be considered a precursor to the CDW order. The precursor phase does not show strong evidence of competition with superconductivity which could support theories that charge fluctuations contribute to pairing.

6.5.2 The relationship between spin and charge fluctuations

The general characteristics of the spin fluctuations measured in this chapter are similar to those described in LSCO in Chapter 5. In particular they show a peak in the damping parameter γ along (h,h). This may lend additional support to theories based on the Hubbard model which consider spin fluctuations as the dominant mechanism in pairing.

However, the new measurements in YBCO show additional structure at the charge ordering wavevector which may point to an interaction between the spin and charge fluctuations. Our results show a slight suppression in both the damping and energy of the spin fluctuations at the ordering wavevector which could indicate competition between the two phases. Several studies have been considered to show signatures of a similar interaction [282, 283, 284]. Dean *et al.* [282] describe RIXS measurements on charge ordered LBCO and report enhanced intensity in the magnetic excitations at the charge ordering wavevector. They also report a slight decrease in the excitation FWHM in the same region which is qualitatively similar to our observations. This effect is explained as the result of the stripe order modulating the spin degrees of freedom. Similar effects are seen in polarised RIXS studies in NCCO [284]. However, the existence and origin of these effects remains ambiguous and are not seen in the higher resolution measurements on LSCO in Chapter 5.

Chapter 7

Conclusions

This thesis presents new resonant inelastic x-ray scattering (RIXS) measurements on the high-T_c cuprate superconductors, $La_{2-x}Sr_xCuO_4$ (LSCO) and $YBa_2Cu_3O_{6+x}$ (YBCO). These studies investigate spin and charge fluctuations with the aim of providing constraints on theories of pairing in high temperature superconductors. An additional result of this work is the characterisation of RIXS as a probe of spin and charge ordered systems, in particular investigating the prefactors to the RIXS intensity.

Chapter 4 is a broad study of the excitations in cuprate parent material La_2CuO_4 (LCO). The analysis begins with the simple case of the *dd* excitations between orbital states. The excitations measured with RIXS are compared to calculations based on a single-ion model within crystal field theory (CFT). These calculations are shown to well reproduce the energy, wavevector, geometry and polarisation dependent intensity of the measured excitations following correction for self-absorption effects. This approach is extended to the spin fluctuations where the local interactions are calculated with CFT and found to describe the shape of the measured magnetic excitations well. Dividing out the local interactions reveals the underlying long-range spin fluctuations from which the dynamic spin susceptibility is extracted.

The susceptibility measurements are scaled to previous measurements made with inelastic neutron scattering (INS) [44]. The region of the Brillouin zone probed by RIXS is smaller than INS, however, in the overlapping region, agreement is good. The results confirm the directional anisotropy in the energy and intensity of the spin fluctuations which verifies the need for beyond nearest neighbour exchange constants within spin-wave theory (SWT). Another key result of the neutron studies is the anomalous softening and broadening of the spin fluctuation response at $\mathbf{Q} = (1/2, 0)$. The RIXS measurements from $\mathbf{Q} = (0,0)$ to $(1/2,0)$ correspond to a region of suppression of the neutron cross-section, hence our results provide additional detail here.

Fig. 4.23 shows that the susceptibility deviates from SWT in the region $\mathbf{Q} = (1/4, 0)$ to $(1/2, 0)$ culminating in a suppression in the intensity by almost 50% compared to the intensity expected from SWT. Section 4.5.1 discusses some possible explanations for this within SWT, however, the most likely scenario is that the intensity is suppressed due to the creation of a spinon pair.

In Chapter 5, the measurements are extended to two doped compositions of LSCO $x = 0.12$ and 0.16. The susceptibility is analysed by comparison to the $x = 0$ composition which reveals the wavevector dependence of the susceptibility in doped cuprates measured with RIXS for the first time. The spin susceptibility is in fact shown to be enhanced in the doped compositions in comparison to the parent. This is partly a result of the definition of the imaginary part of the susceptibility, as shown in the Kramers-Kronig relation (Eqn. 2.26), $\chi'(\mathbf{Q}, \omega)$ is scaled by the excitation pole position, ω_0. In doped compositions, spectral weight is shifted to lower energies and hence the susceptibility is enhanced. However, the results show that spin fluctuations are still prominent in doped compositions despite the suppression of the antiferromagnetic (AFM) order. The doped compositions show significant enhancement approaching the repeating unit of the order, $\mathbf{Q}_{\mathrm{AFM}} = (1/2, 1/2)$. This behaviour is consistent with some predictions of spin fluctuation mediated theories based on the Hubbard model which predict that the region around $\mathbf{Q}_{\mathrm{AFM}} = (1/2, 1/2)$ is important for pairing [45, 52, 38].

Chapter 5 also discusses the characteristics of the spin fluctuations in LSCO parametrised within a damped harmonic oscillator (DHO) model. The results show an enhancement in the damping parameter, γ, along the (h, h) direction with a peak close to $\mathbf{Q} = (0.2, 0.2)$. This result is seen in high resolution scans along the high symmetry directions, as shown in Fig. 5.10, and in 3D maps produced from scans in a symmetrical portion of the Brillouin zone, as shown in Fig. 5.11. Chapter 6 discusses similar measurements in underdoped YBCO which also show a peak close to $(0.2, 0.2)$, however, the behaviour along $(h, 0)$ is more complex than in LSCO. These results appear to be phenomenologically similar to calculations based on a random phase approximation of itinerant quasiparticles [252, 253, 222] and others based on the Hubbard model [38].

In general our measurements lend support to some spin fluctuation mediated theories of pairing in cuprates pointing to the fact that spin fluctuations remain important into the doped phases. These theories sometimes consider charge fluctuations as an additional contributor to pairing, however, the relationship between the two ordered phases remains unclear. Chapter 6 presents a RIXS study on the charge-ordered composition of YBCO, $x = 0.67$. As reported previously in YBCO [136] and $La_{2-x}Ba_xCuO_4$ (LBCO) [229, 267], the wavevector dependent

charge order intensity can be separated into a narrow peak, which is interpreted as the well-studied 3D charge density wave, and a broad peak which persists to higher temperatures. The characteristics of the two peaks are similar to previous reports except it is seen to shift to higher wavevector below $T^\star$. Such behaviour has previously been attributed to an entropy reducing mechanism in striped compositions which could suggest the order in LBCO and YBCO are more similar than previously thought. However, we conclude that the broad peak is likely to contain intensity from the low energy acoustic mode phonon which is expected to increase in intensity at large wavevector as is seen in our results.

Phonon excitations are seen in all of the materials which have been studied. The high resolution study of LCO allows us to identify two phonon modes which are attributed to a bond-stretching and bond-buckling mode with energies $\sim$ 45 and 90 meV, approximately similar to previous measurements [212, 213, 133] and calculations [129] in the cuprates. However, the intensity dependence of the two modes is quite different to these previous studies with both showing an increase towards the zone boundary. This may indicate inaccuracies in the estimation of the prefactors to the RIXS intensity and further studies may be able to reconcile the results. In the doped compositions, the two higher energy phonons cannot be separately resolved and are modelled with a single Gaussian peak. In charge ordered YBCO, this phonon shows the characteristic softening at $\mathbf{Q}_{\mathrm{CDW}}$ at temperatures below $T^\star$. The low energy acoustic phonon which is seen in broad component of the elastic intensity appears to show a similar trend. These observations at temperatures higher than the sharp CDW peak lend weight to theories that consider anomalous phonon behaviour to be a precursor to charge order.

7.1 Future work

Recent RIXS measurements have established the power of scattered beam polarisation analysis in analysing the RIXS cross-section and its relationship to the susceptibility. This analysis depends on a graded multilayer mirror designed to deflect the scattered beam in the horizontal direction dependent on its linear polarisation [287]. The electric vector of σ polarised light is in plane with the multilayer and hence has higher reflectivity than π polarised light which has an electric vector oriented along the scattering plane.

The recent polarisation analysis performed by Peng *et al.* [161] and Fumagalli *et al.* [162] have been instrumental in the analysis in several parts of this thesis. Their analysis is used to justify the approximation that the magnetic excitations are mostly associated with spin-flip processes and hence can be attributed to single magnons. However, a more rigorous approach

would be to perform polarisation analysis and separately analyse the self-absorption. Scattered beam polarisation analysis is now possible at ID32 and is likely to be available at I21 in the near future.

Having verified the CFT approach of estimating the RIXS cross-section in LCO, several directions for future study are possible. An obvious extension to the work in this thesis would be to perform similar calculations in doped cuprates. The calculations become considerably more complex in doped systems due to the onset of electron correlations. However, Lau *et al.* [288] describe a method of reducing the size of the cluster by symmetry considerations to account for some correlation effects in a CuO_2 plaquette by exact diagonalisation. Cluster calculations based on a quantum chemical scheme have also successfully reproduced experimental measurements of excitations in cuprates [289]. Linking these sorts of calculations with RIXS would be a useful next step in isolating the susceptibility in cuprate systems.

Another area of future work would be to extend the calculations to multi-site excitations. The calculations described in Chapter 4 are performed on a single-ion basis and therefore interactions involving multiple sites, such as the creation of a two-magnon, are not fully described. To consider longer range interactions, cluster calculations could be used to construct interactions between multiple ions [171]. Again, this method becomes prohibitively computationally expensive when considering large numbers of electron correlations such as those that occur in the cuprates. However, several cluster models have been used to construct simplified versions of the interactions [290]. Future work could make use of these methods to fully describe the multimagnon cross-section. This, in combination with more accurate self-absorption correction would allow higher order contributions to the spin fluctuations to be more reliably characterised.

The results in Chapter 6 identify some new details of the charge order, of particular interest are the signatures indicating the influence of charge order on the spin fluctuations. Unfortunately, the resolution of these experiments ($\Delta E \sim 45$ meV) is the worst of all the measurements in this thesis and no such signatures are seen in LSCO. Higher resolution measurements focusing on the spin fluctuations in charge ordered YBCO may be able to verify this result and provide further details. Additionally, RIXS studies that can reliably extract the susceptibility in doped YBCO would also be useful to compare with LSCO.

Appendix A

Fitted data

A.1 Fitted simulated data

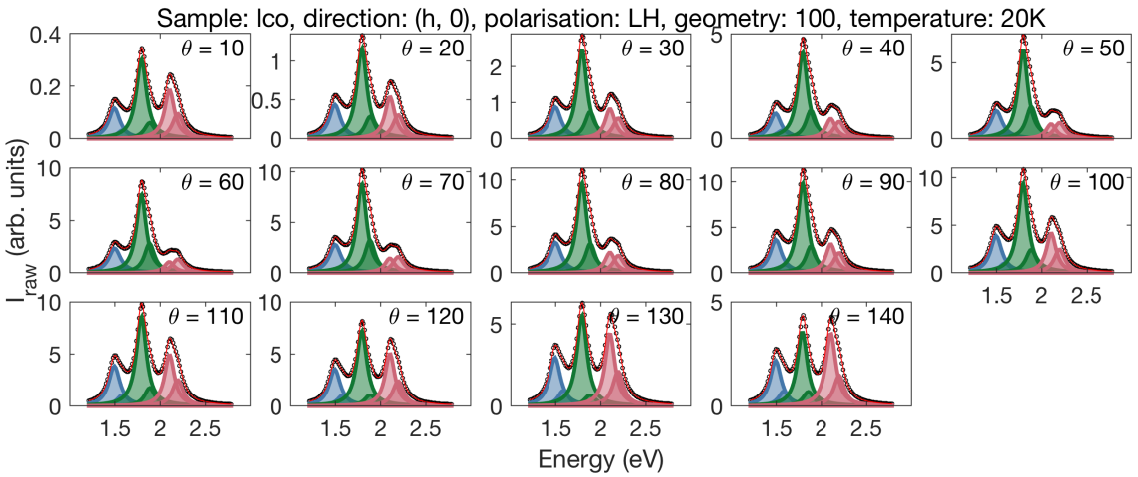

Figure A.1: Orbital intensity of the RIXS response in LCO for π-polarisation for spectra along the $(h,0)$ direction calculated from crystal field theory. The calculated data are fitted with six pseudo-Voigt functions.

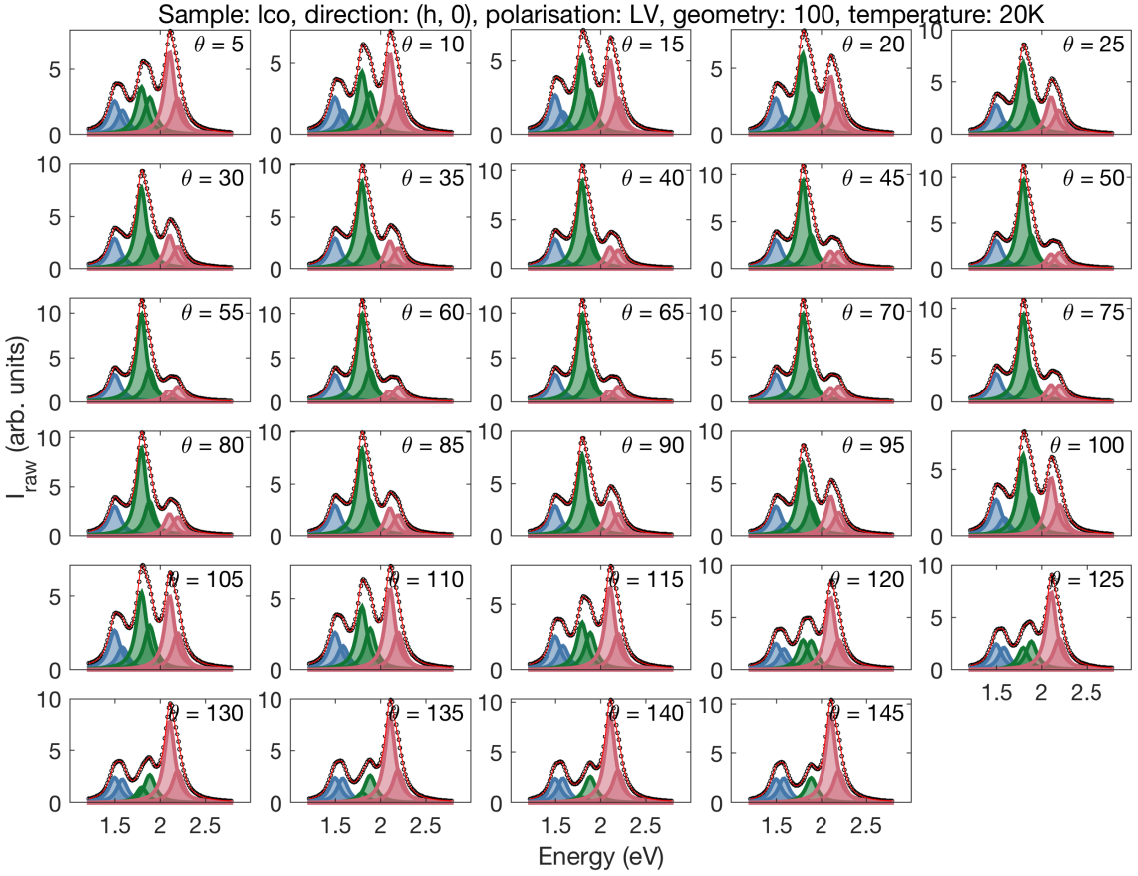

Figure A.2: Orbital intensity of the RIXS response in LCO for σ-polarisation for spectra along the $(h,0)$ direction calculated from crystal field theory. The calculated data are fitted with six pseudo-Voigt functions.

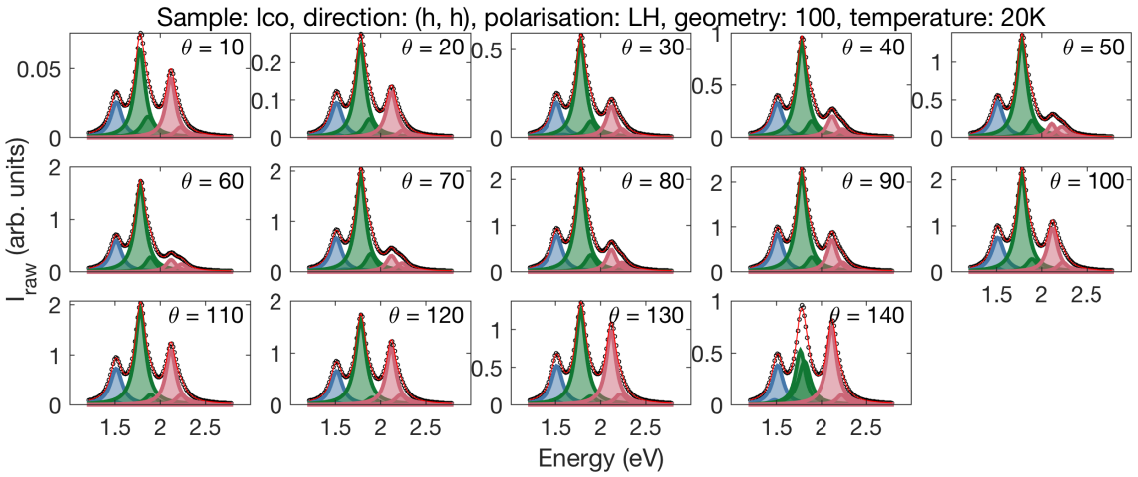

Figure A.3: Orbital intensity of the RIXS response in LCO for π-polarisation for spectra along the (h,h) direction calculated from crystal field theory. The calculated data are fitted with six pseudo-Voigt functions.

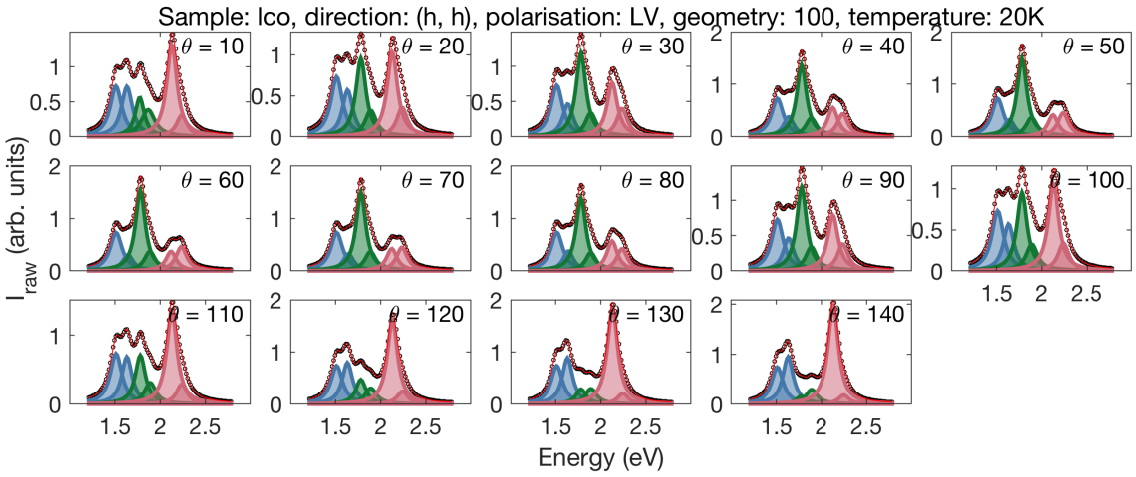

Figure A.4: Orbital intensity of the RIXS response in LCO for σ-polarisation for spectra along the (h,h) direction calculated from crystal field theory. The calculated data are fitted with six pseudo-Voigt functions.

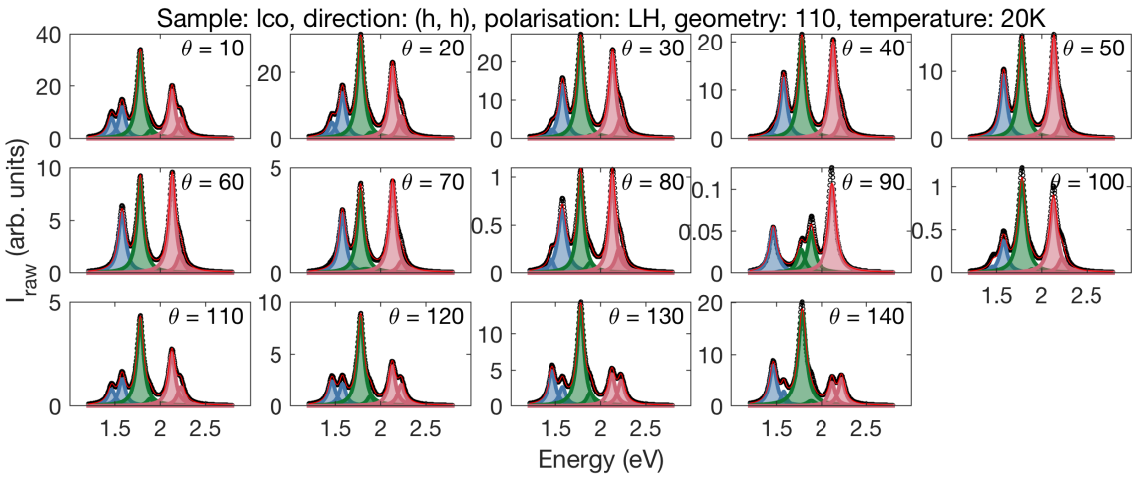

Figure A.5: Orbital intensity of the RIXS response in LCO for π-polarisation for spectra along the (h,h) direction in the LCO110 orientation calculated from crystal field theory. The calculated data are fitted with six pseudo-Voigt functions.

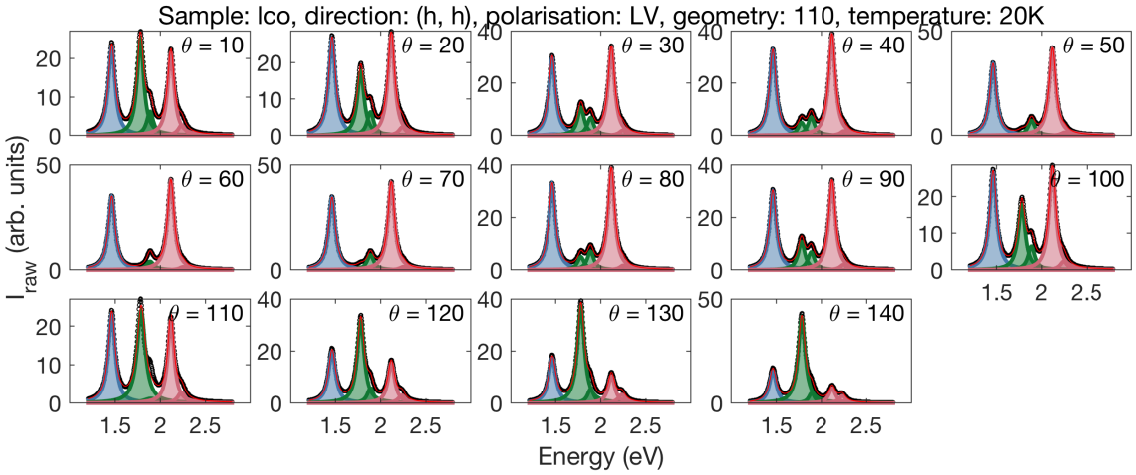

Figure A.6: Orbital intensity of the RIXS response in LCO for σ-polarisation for spectra along the (h,h) direction in the LCO110 orientation calculated from crystal field theory. The calculated data are fitted with six pseudo-Voigt functions.

A.2 Fitted RIXS data

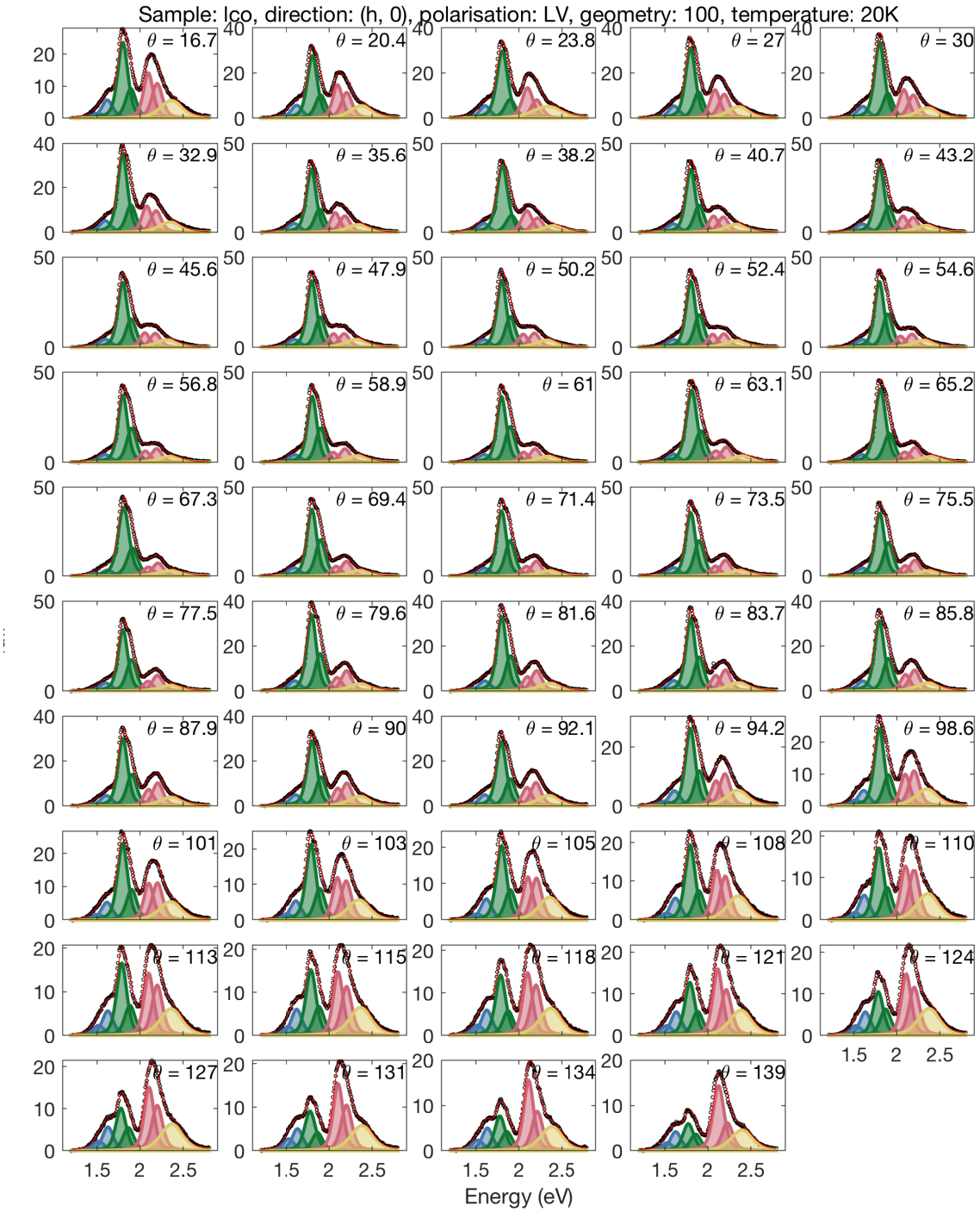

Figure A.7: Orbital intensity of the RIXS response in LCO from RIXS measurements of the *dd* excitations performed at I21 with σ-polarisation along the $(h,0)$ direction at 20 K. The data are fitted with seven pseudo-Voigt functions.

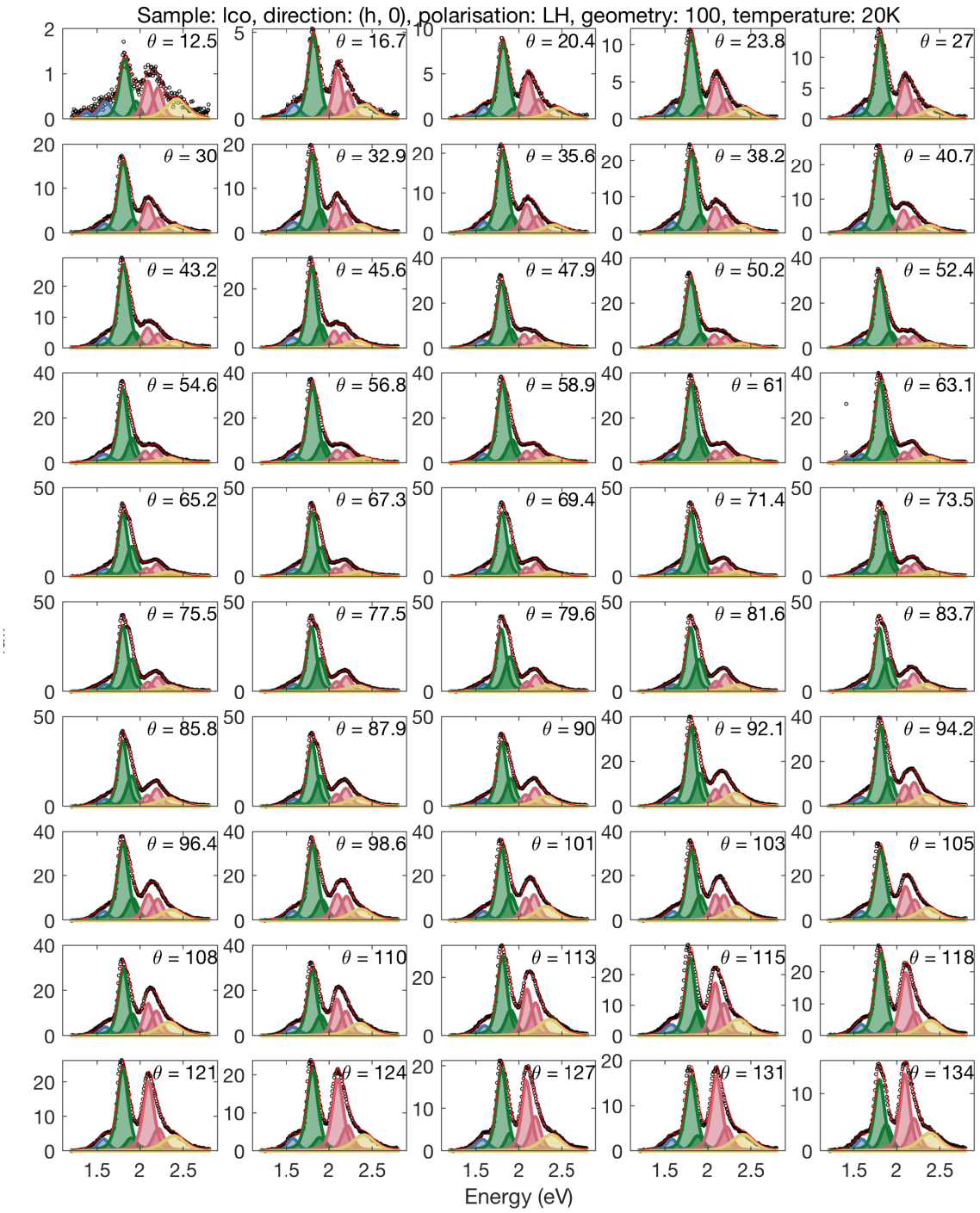

Figure A.8: Orbital intensity of the RIXS response in LCO from RIXS measurements of the *dd* excitations performed at I21 with π-polarisation along the $(h,0)$ direction at 20 K. The data are fitted with seven pseudo-Voigt functions.

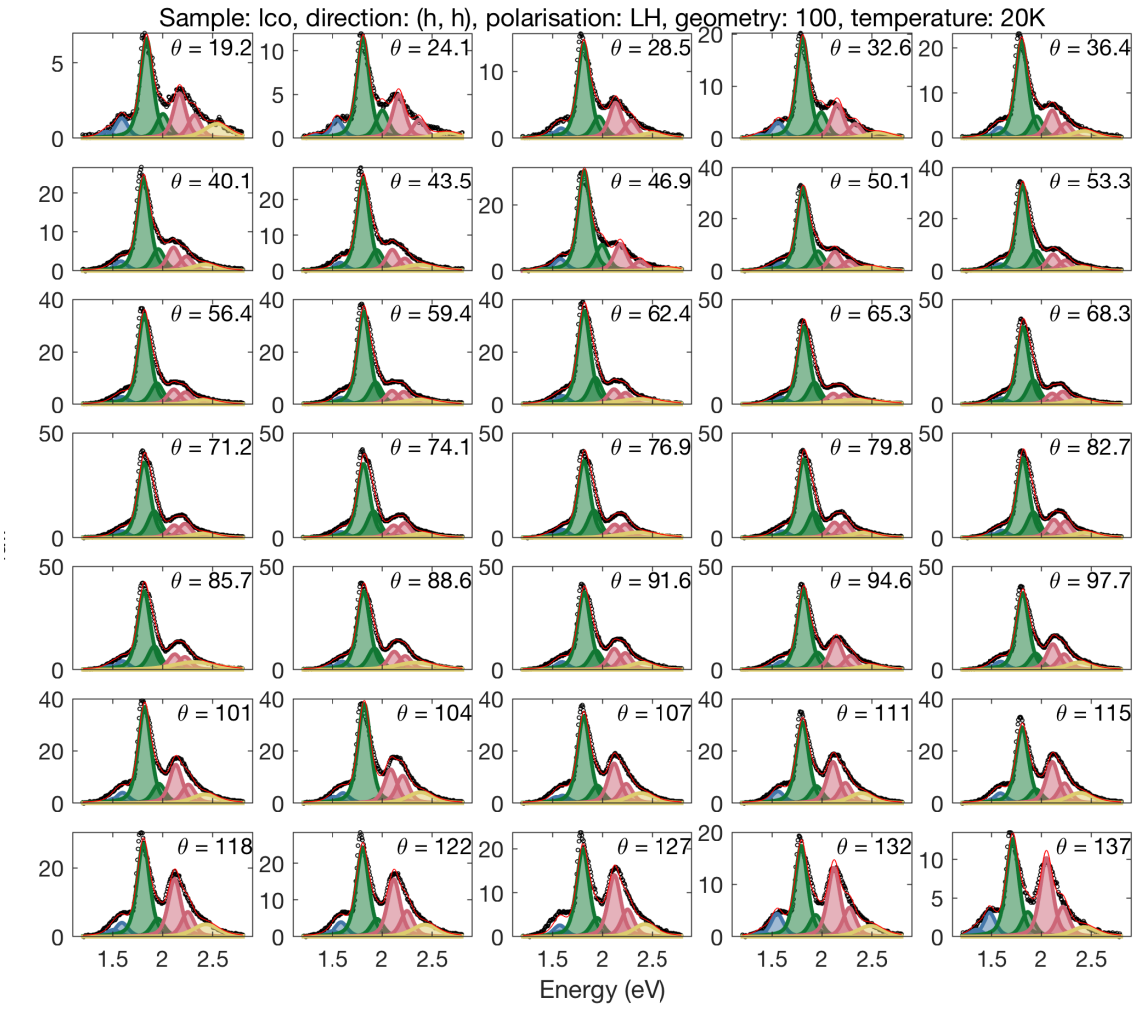

Figure A.9: Orbital intensity of the RIXS response in LCO from RIXS measurements of the *dd* excitations peformed at I21 with π-polarisation along the (h, h) direction at 20 K. The data are fitted with seven pseudo-Voigt functions.

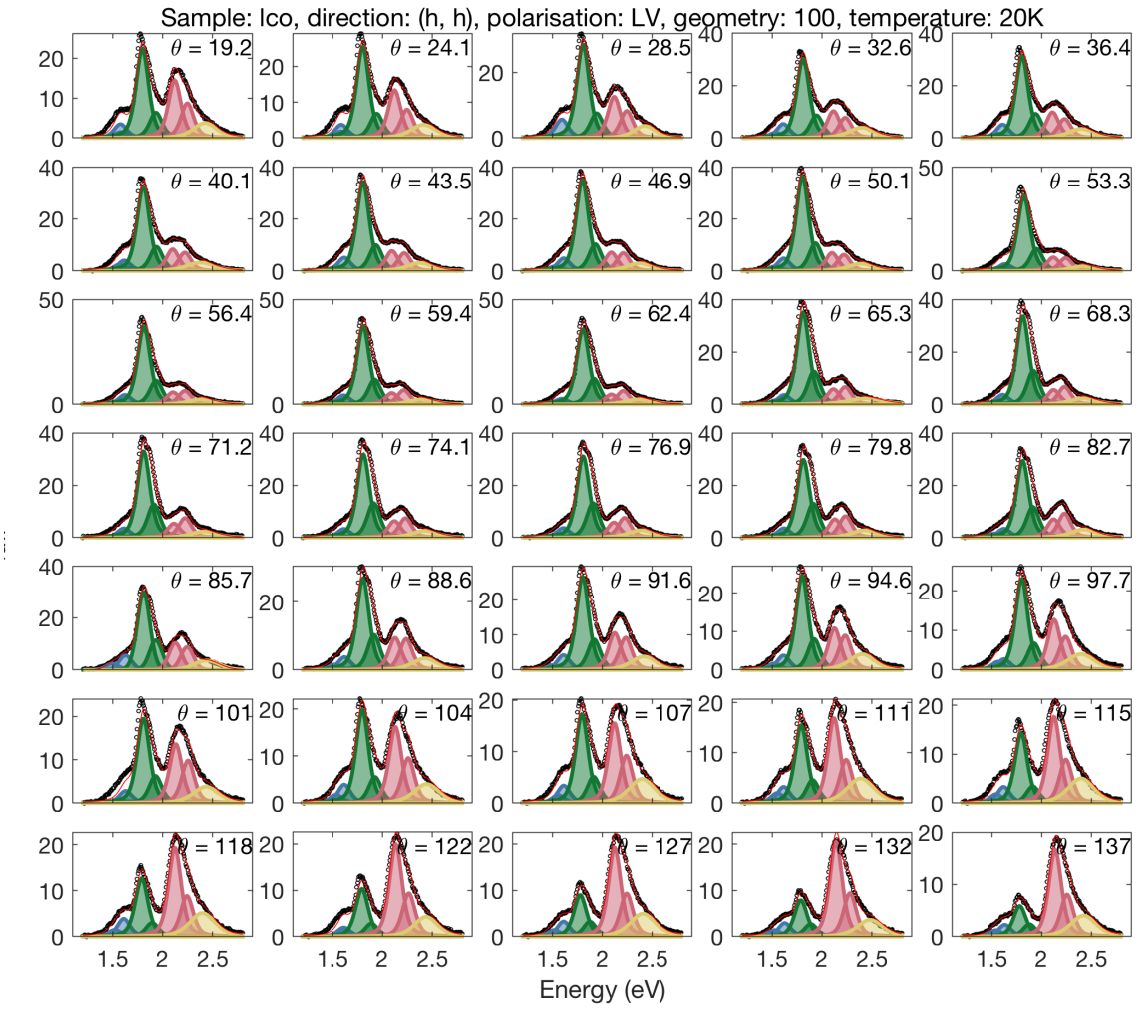

Figure A.10: Orbital intensity of the RIXS response in LCO from RIXS measurements of the *dd* excitations performed at I21 with σ-polarisation along the (h,h) direction at 20 K. The data are fitted with seven pseudo-Voigt functions.

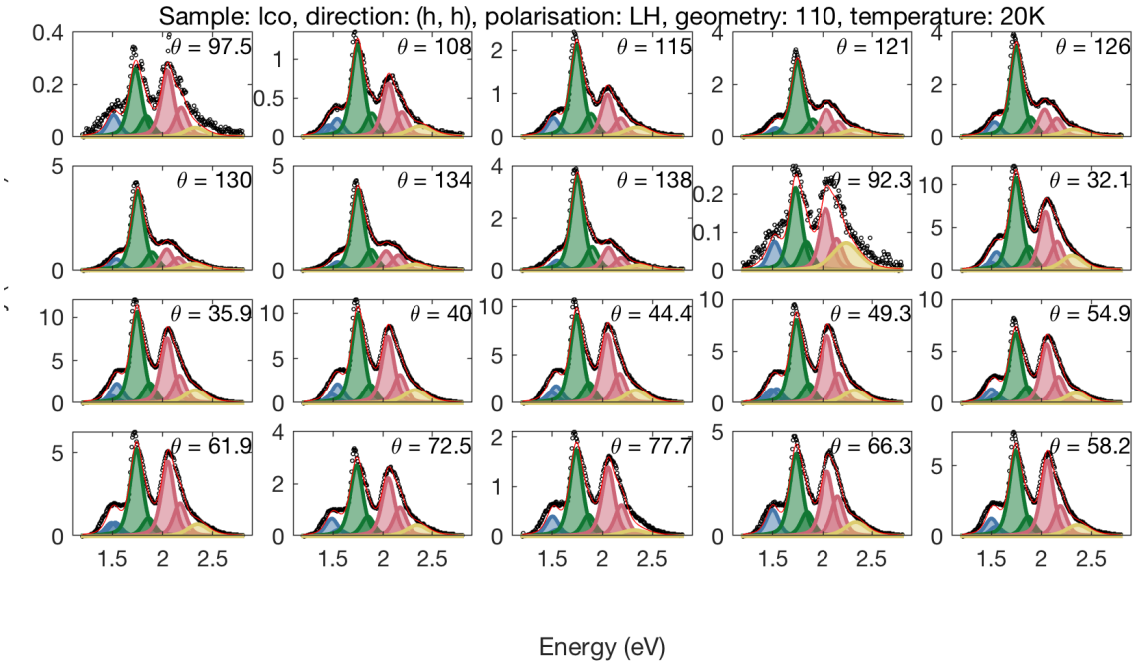

Figure A.11: Orbital intensity of the RIXS response in LCO from RIXS measurements of the *dd* excitations performed at I21 with π-polarisation along the (h,h) direction at 20 K in the LCO110 orientation. The data are fitted with seven pseudo-Voigt functions.

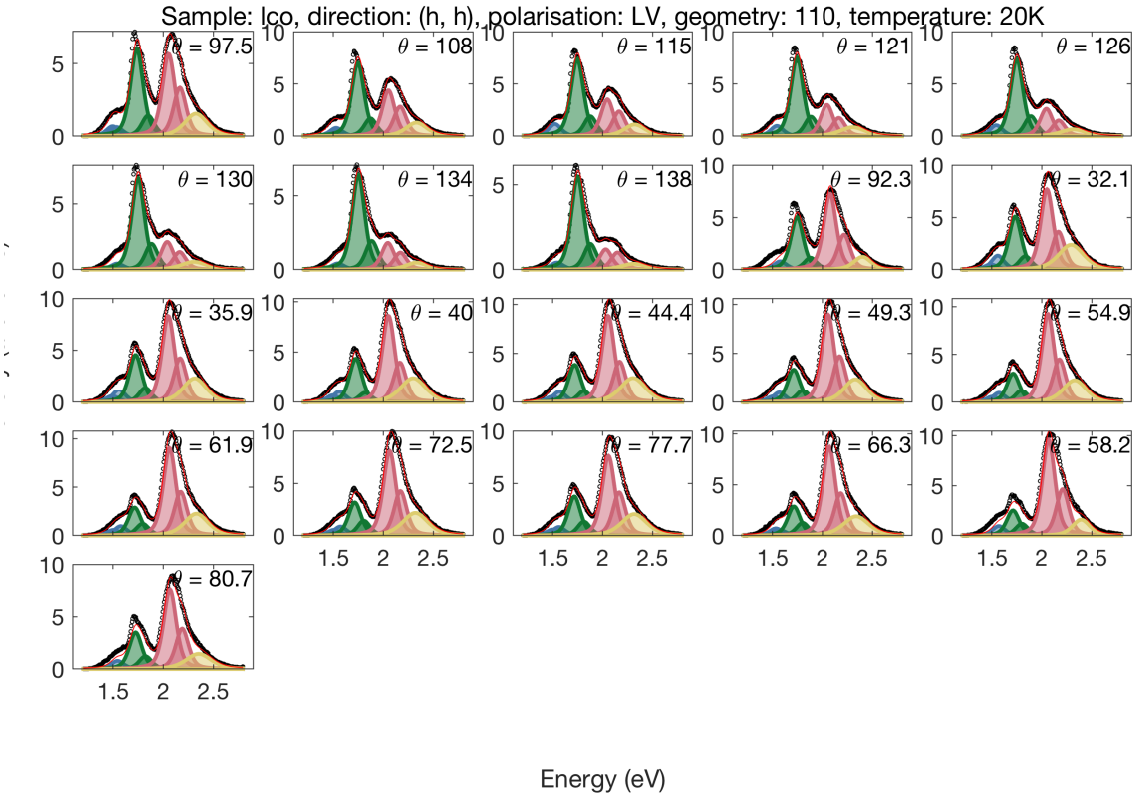

Figure A.12: Orbital intensity of the RIXS response in LCO from RIXS measurements of the *dd* excitations performed at I21 with σ-polarisation along the (h,h) direction at 20 K in the LCO110 orientation. The data are fitted with seven pseudo-Voigt functions.

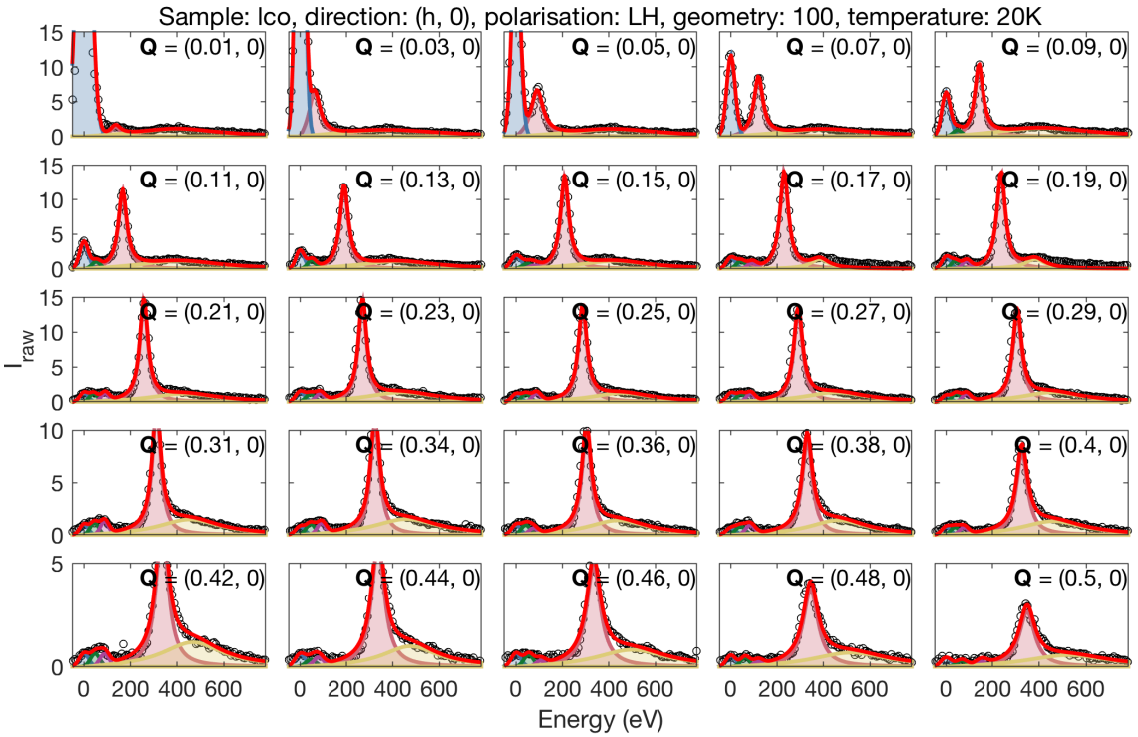

Figure A.13: Intensity of the RIXS response in LCO for RIXS measurements performed at I21 with π-polarisation along the $(h, 0)$ direction at 20 K. The data are fitted with a damped harmonic oscillator response function for the magnons (pink) and multimagnons (yellow), a Gaussian for the elastic peak (blue) and for the phonons (green and purple), the total fit is shown in red.

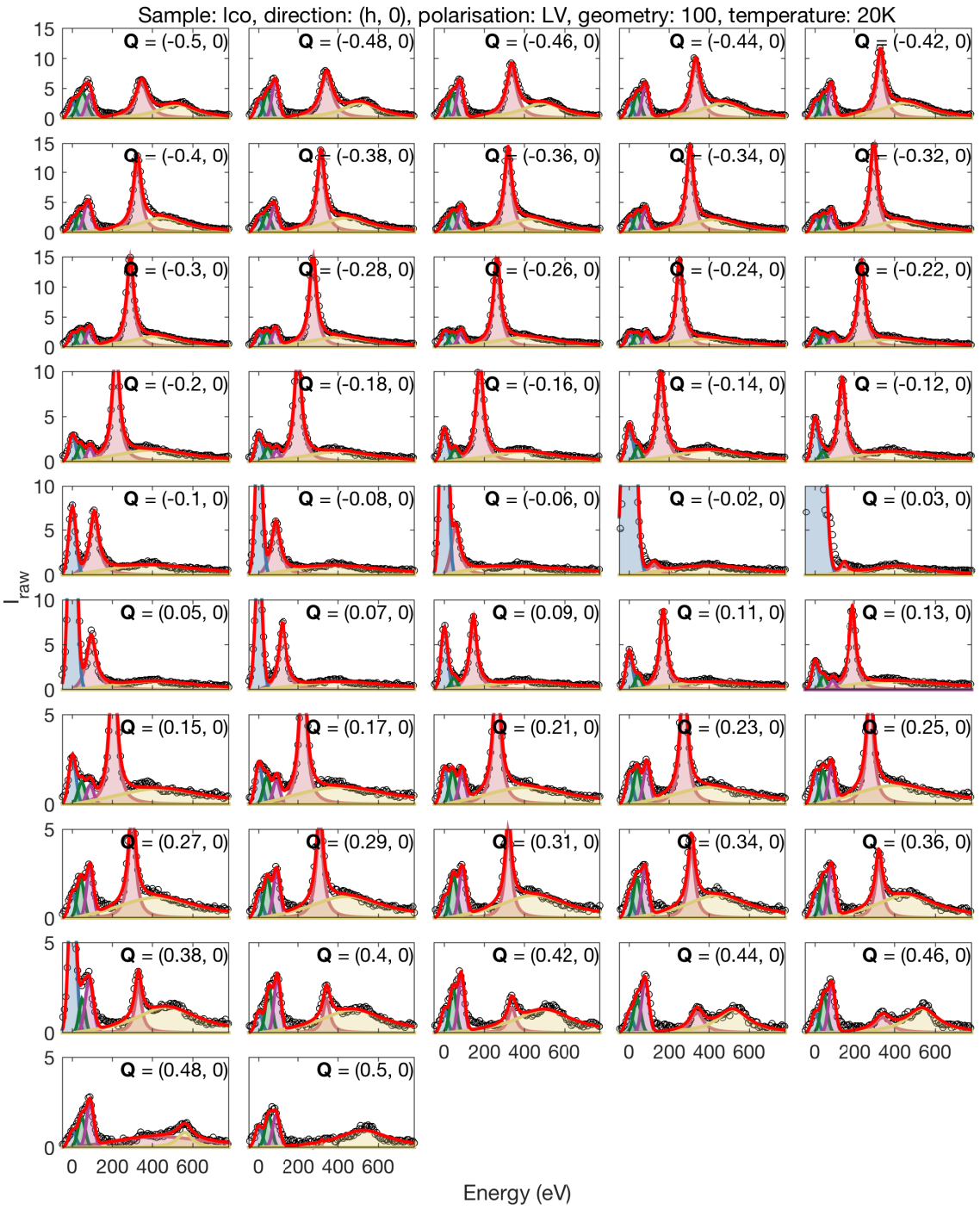

Figure A.14: Intensity of the RIXS response in LCO for RIXS measurements performed at I21 with σ-polarisation along the $(h, 0)$ direction at 20 K. The data are fitted as in Fig. A.13.

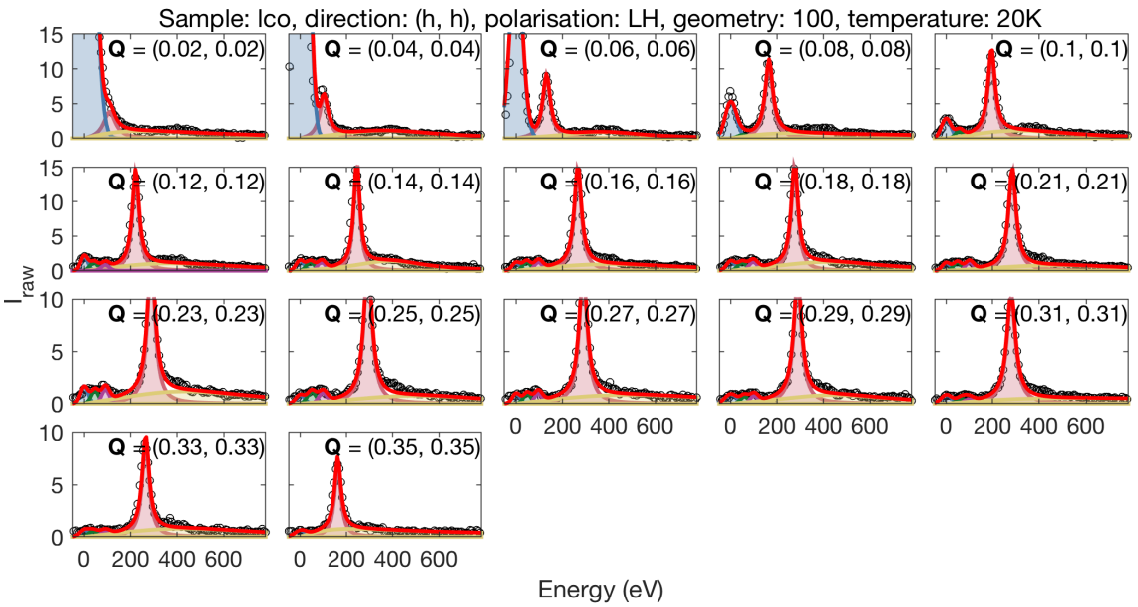

Figure A.15: Intensity of the RIXS response in LCO for RIXS measurements performed at I21 with π-polarisation along the (h, h) direction at 20 K. The data are fitted as in Fig. A.13.

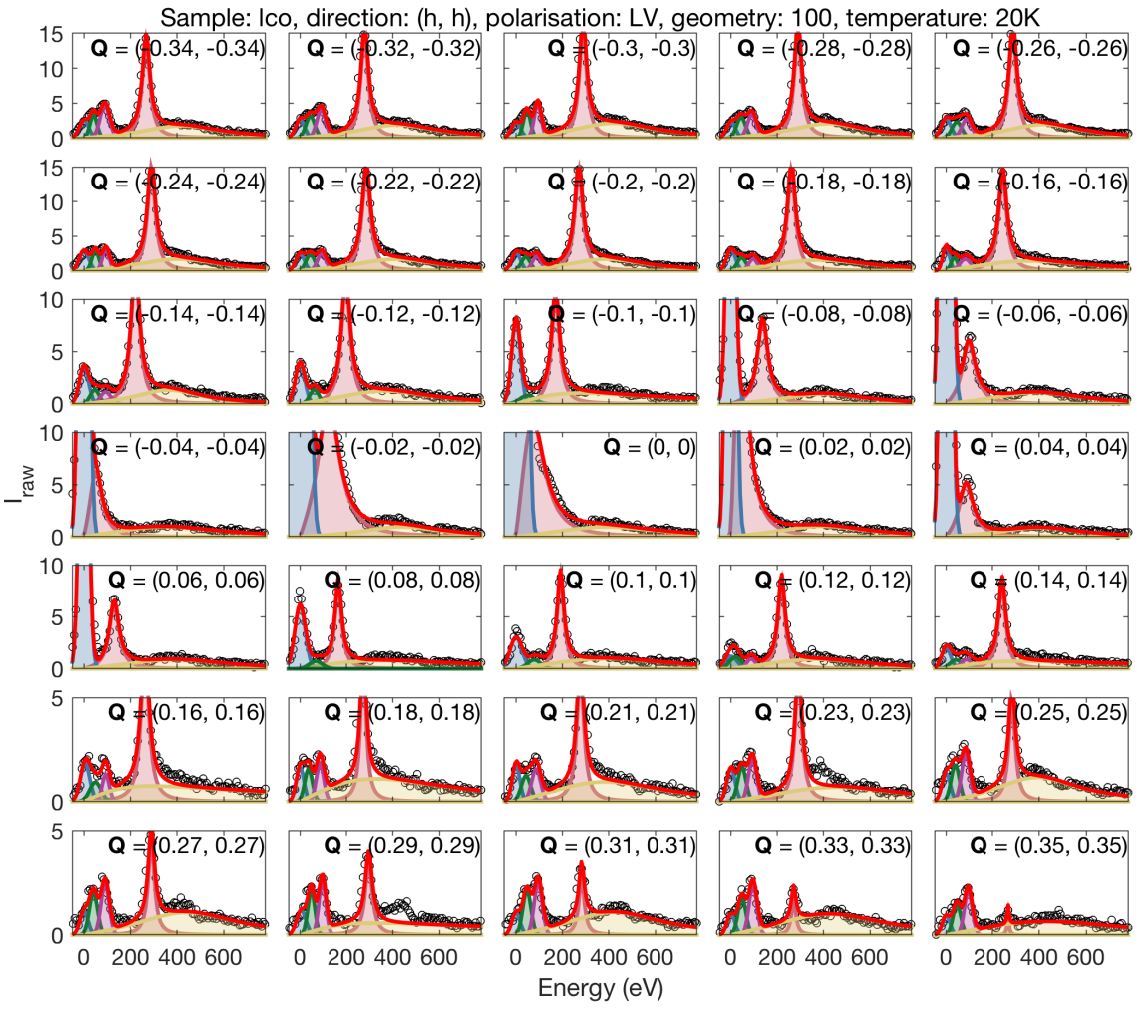

Figure A.16: Intensity of the RIXS response in LCO for RIXS measurements performed at I21 with σ-polarisation along the (h, h) direction at 20 K. The data are fitted as in Fig. A.13.

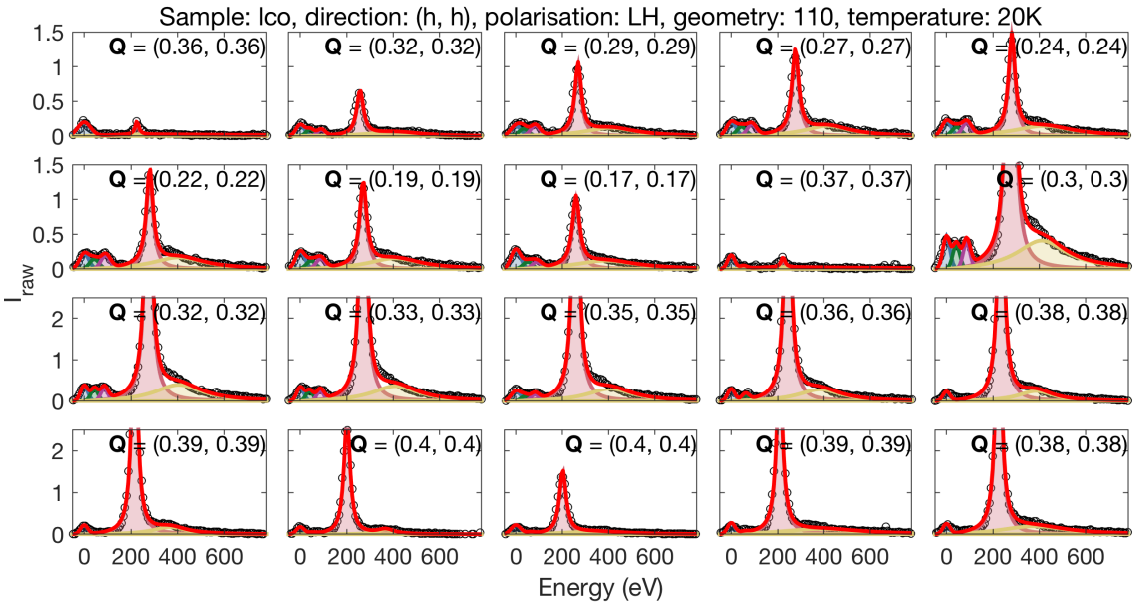

Figure A.17: Intensity of the RIXS response in LCO for RIXS measurements performed at I21 with π-polarisation along the (h,h) direction at 20 K in the LCO110 orientation. The data are fitted as in Fig. A.13.

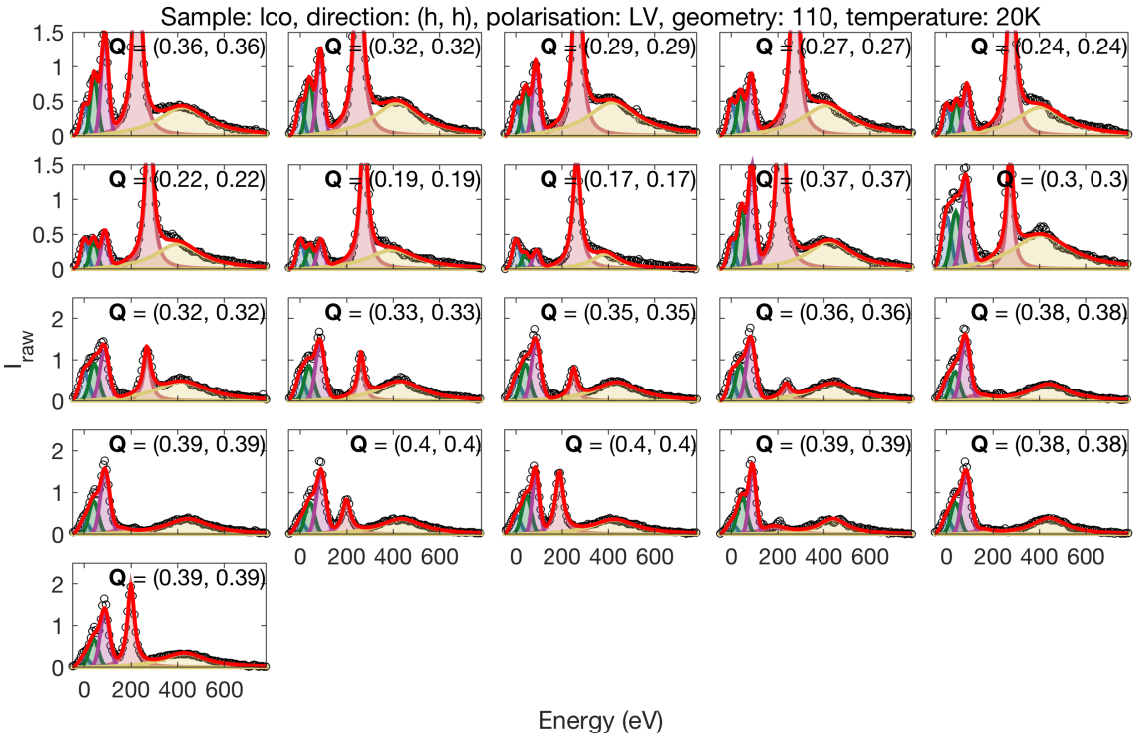

Figure A.18: Intensity of the RIXS response in LCO for RIXS measurements performed at I21 with σ-polarisation along the (h,h), at 20 K direction in the LCO110 orientation. The data are fitted as in Fig. A.13.

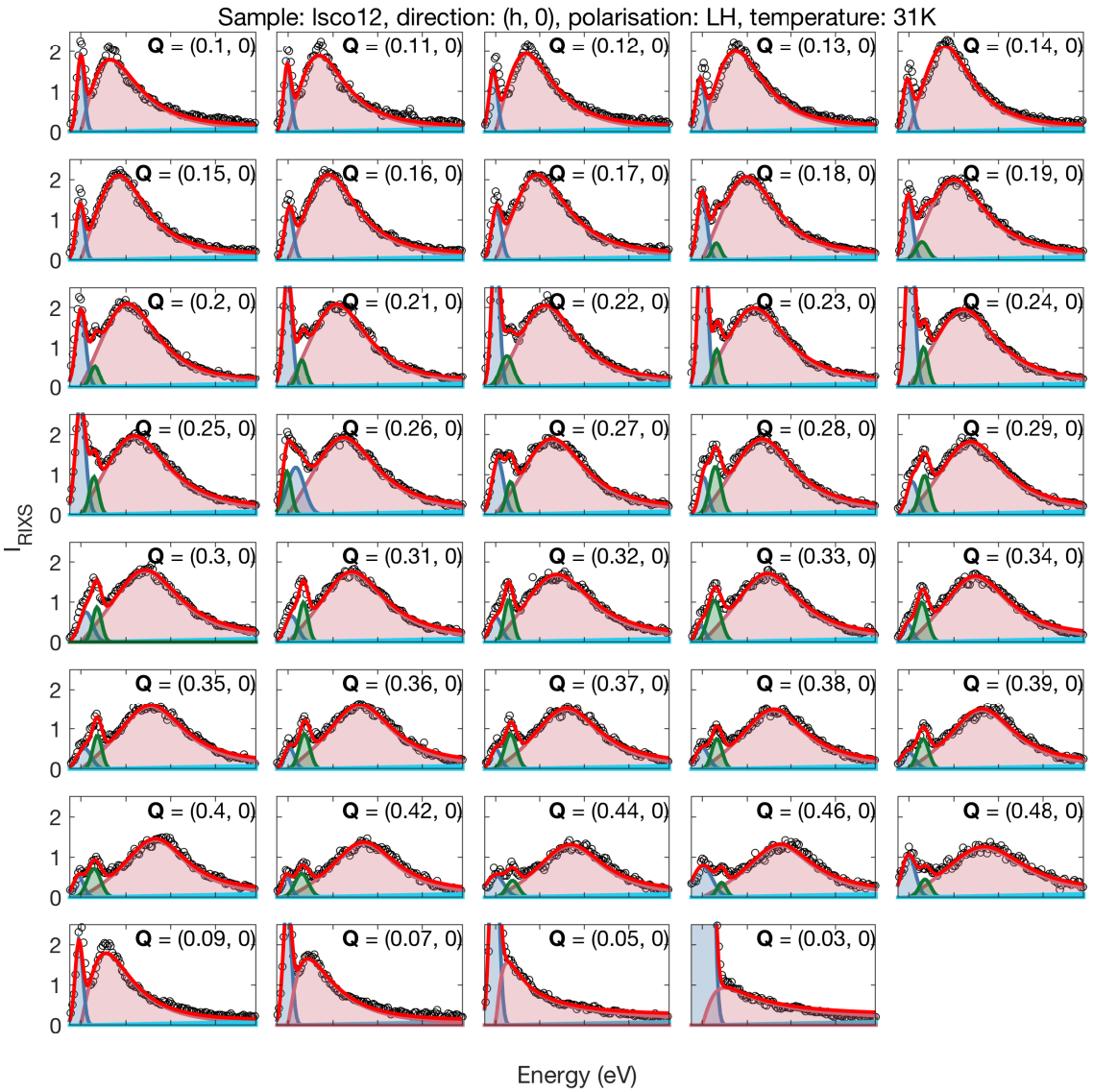

Figure A.19: Intensity of the RIXS response in LSCO ($x = 0.12$) for RIXS measurements performed at I21 with π-polarisation along the $(h, 0)$ direction at 31 K. The data are fitted with a damped harmonic oscillator response function (pink), Gaussian for the elastic peak (blue) and for the phonon (green) and a linear background (blue) with a fixed gradient, the total fit is shown in red.

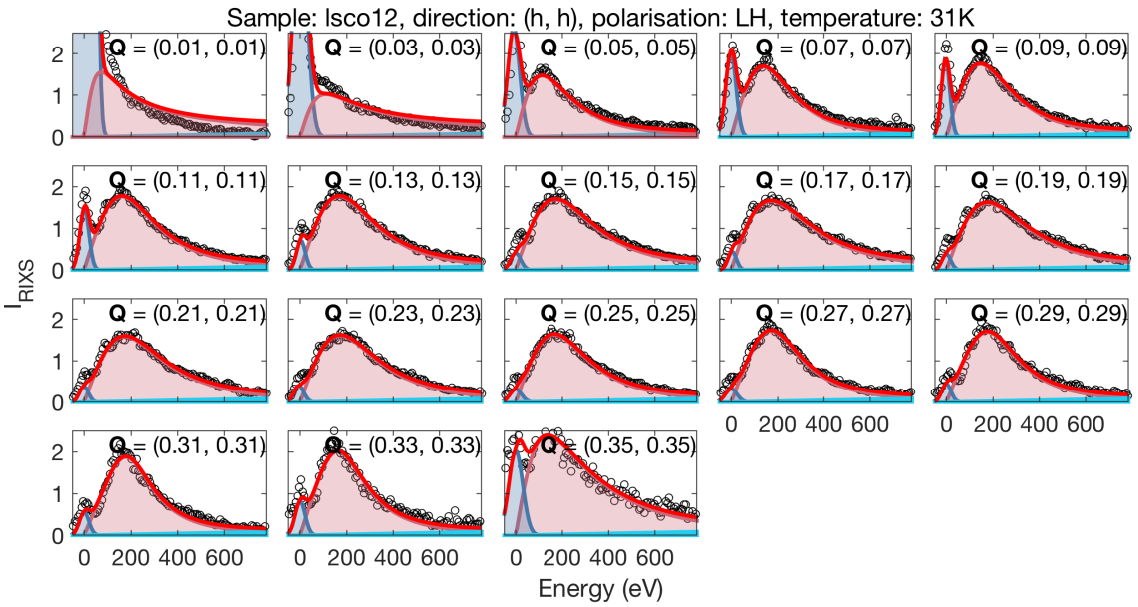

Figure A.20: Intensity of the RIXS response in LSCO ($x = 0.12$) for RIXS measurements performed at I21 with π-polarisation along the (h, h) direction at 31 K. The data are fitted as in Fig. A.19.

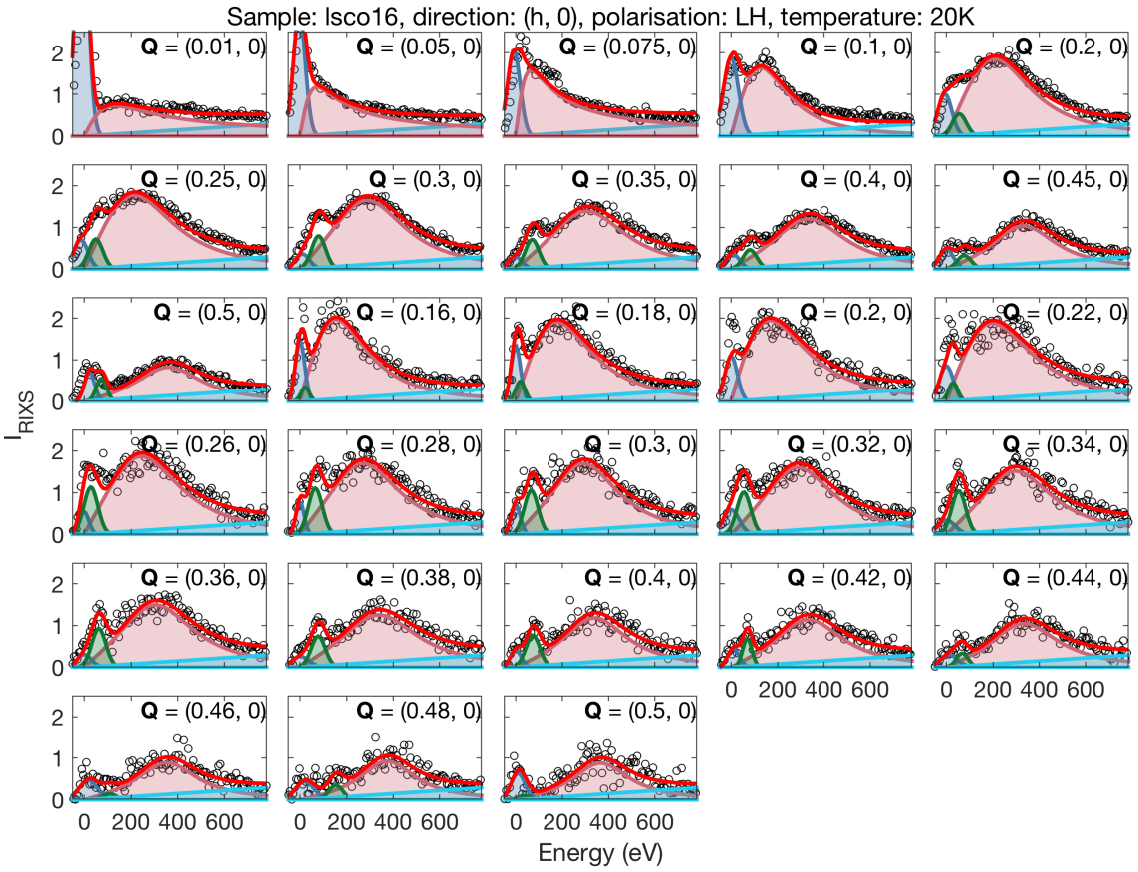

Figure A.21: Intensity of the RIXS response in LSCO ($x = 0.16$) for RIXS measurements performed at ID32 with π-polarisation along the $(h, 0)$ direction at 20 K. The data are fitted as in Fig. A.19.

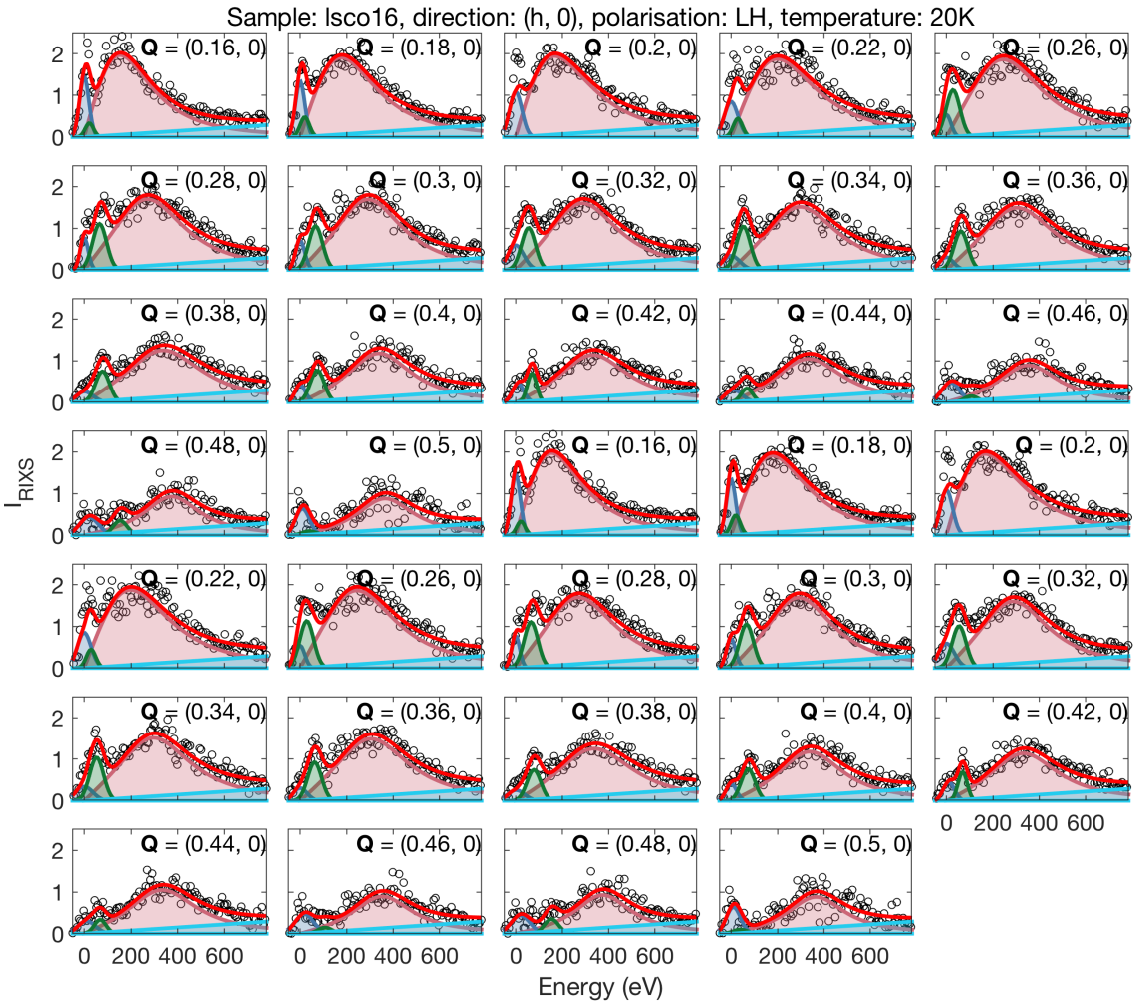

Figure A.22: Intensity of the RIXS response in LSCO ($x = 0.16$) for RIXS measurements performed at a repeat visit to ID32 with π-polarisation along the $(h, 0)$ direction at 20 K. The data are fitted as in Fig. A.19.

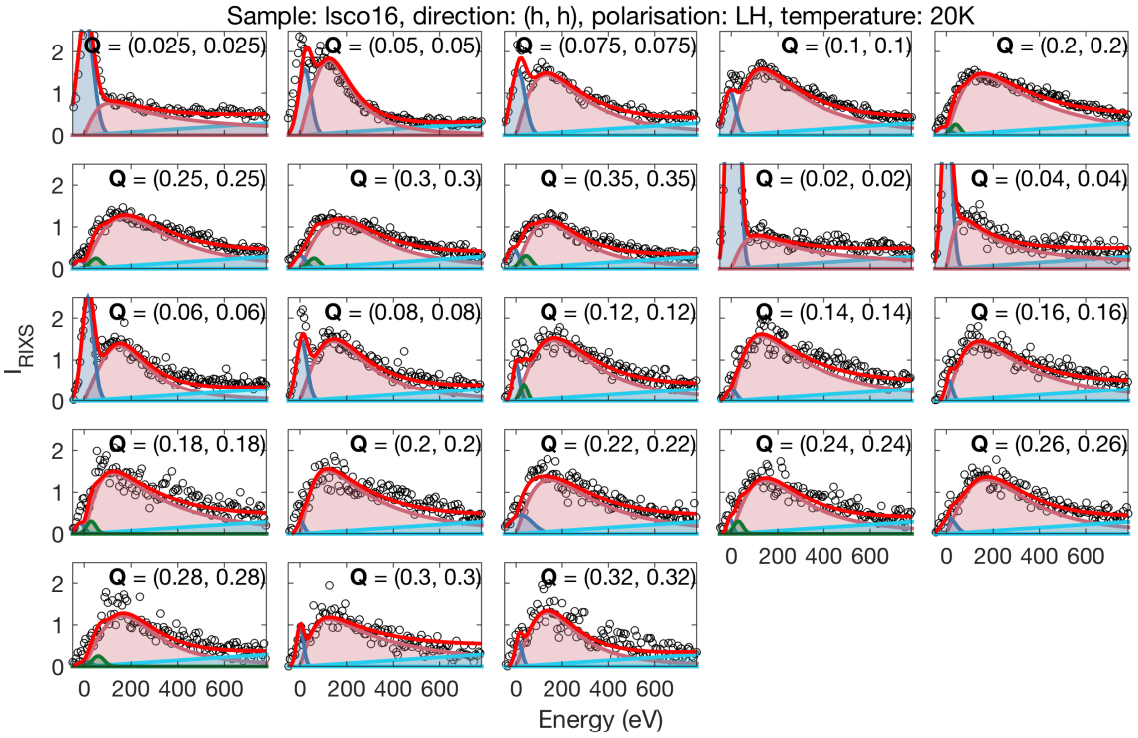

Figure A.23: Intensity of the RIXS response in LSCO ($x = 0.16$) for RIXS measurements performed at ID32 with π-polarisation along the (h, h) direction at 20 K. The data are fitted as in Fig. A.19.

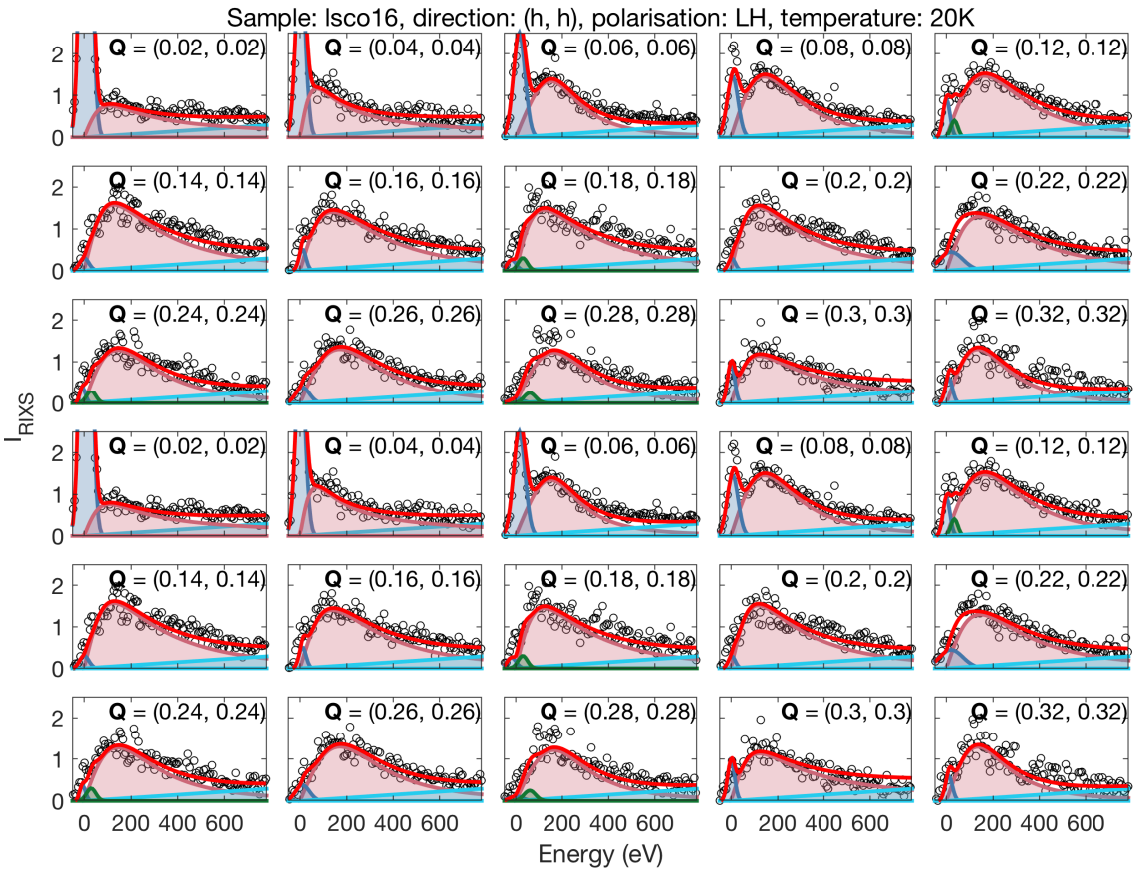

Figure A.24: Intensity of the RIXS response in LSCO ($x = 0.16$) for RIXS measurements performed at a repeat visit to ID32 with π-polarisation along the (h, h) direction at 20 K. The data are fitted as in Fig. A.19.

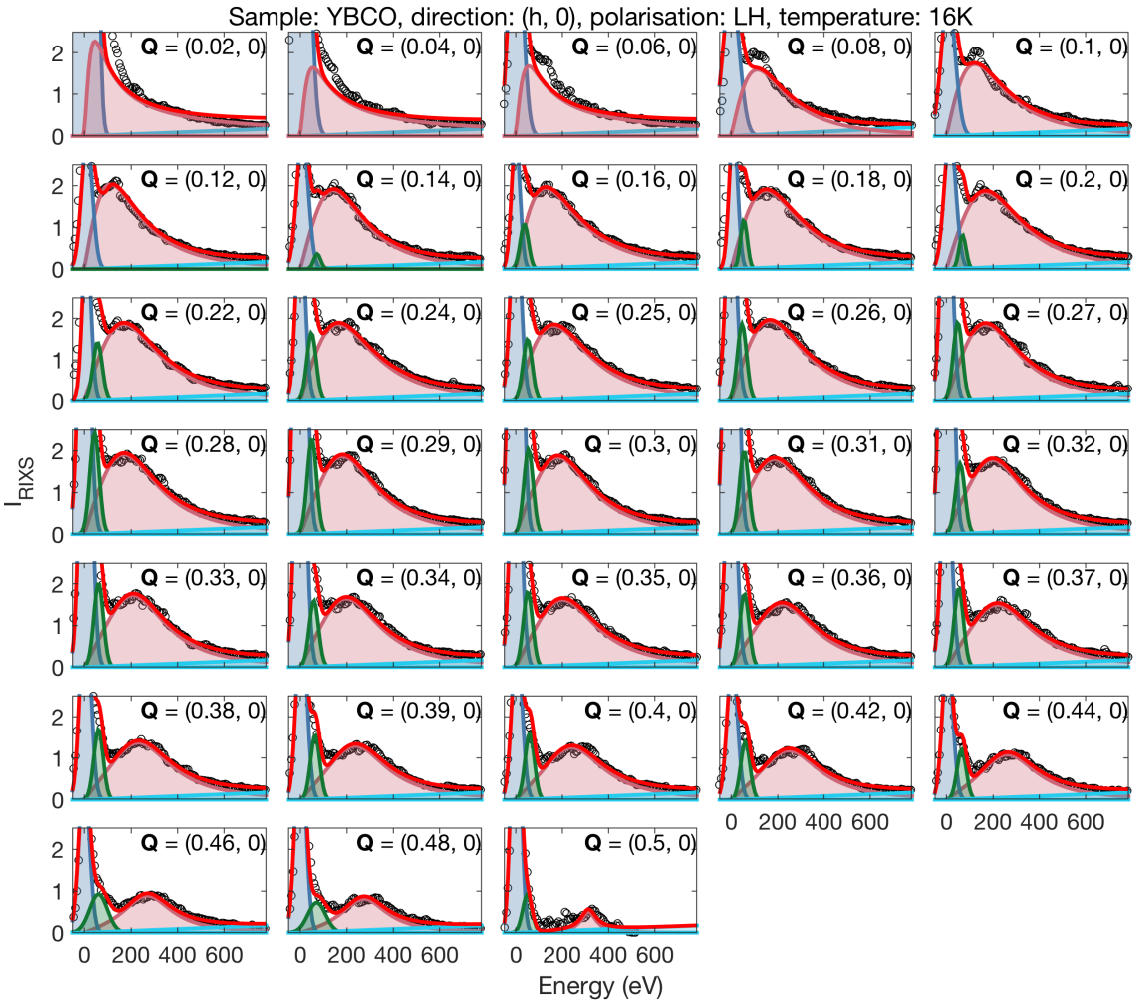

Figure A.25: Intensity of the RIXS response in YBCO ($x = 0.67$) for RIXS measurements performed at I21 with π-polarisation for $(h,0)$ at 16 K. The data are fitted as in Fig. A.19.

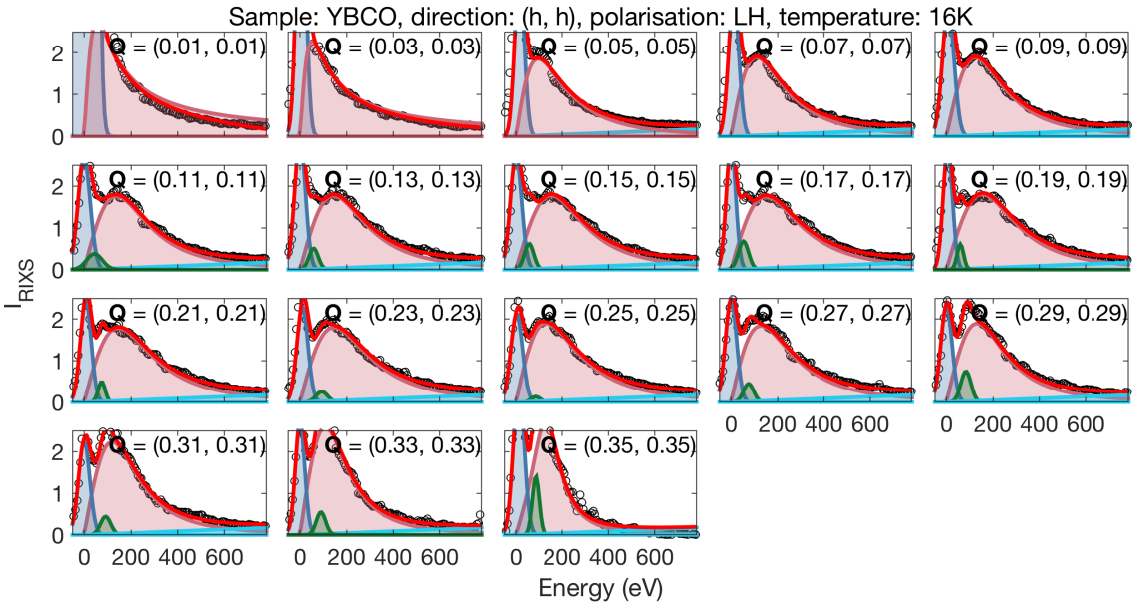

Figure A.26: Intensity of the RIXS response in YBCO ($x = 0.67$) for RIXS measurements performed at I21 with π-polarisation for (h,k) at 16 K. The data are fitted as in Fig. A.19.

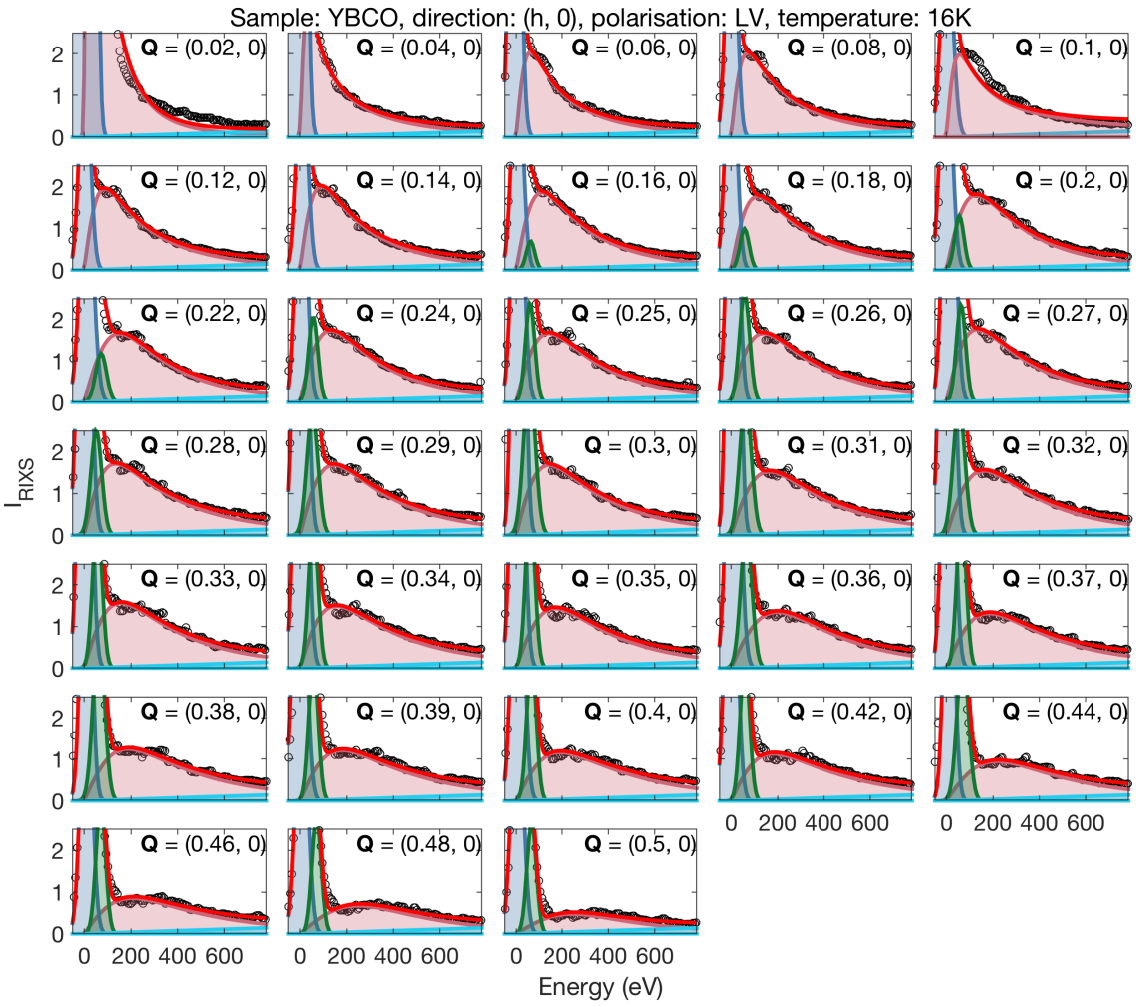

Figure A.27: Intensity of the RIXS response in YBCO ($x = 0.67$) for RIXS measurements performed at I21 with σ-polarisation for $(h,0)$ at 16 K. The data are fitted as in Fig. A.19.

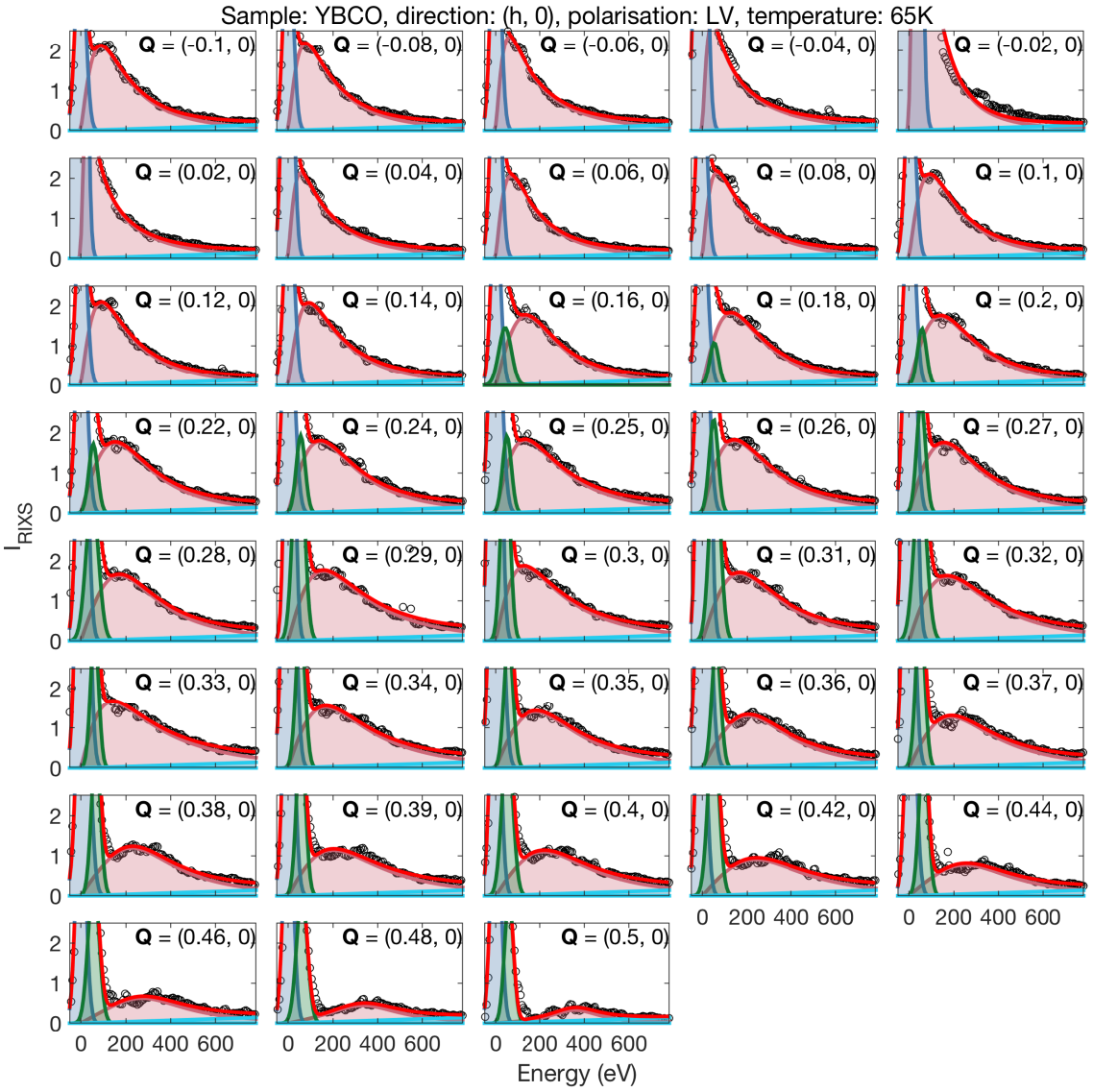

Figure A.28: Intensity of the RIXS response in YBCO ($x = 0.67$) for RIXS measurements performed at I21 with σ-polarisation for $(h,0)$ at 65 K. The data are fitted as in Fig. A.19.

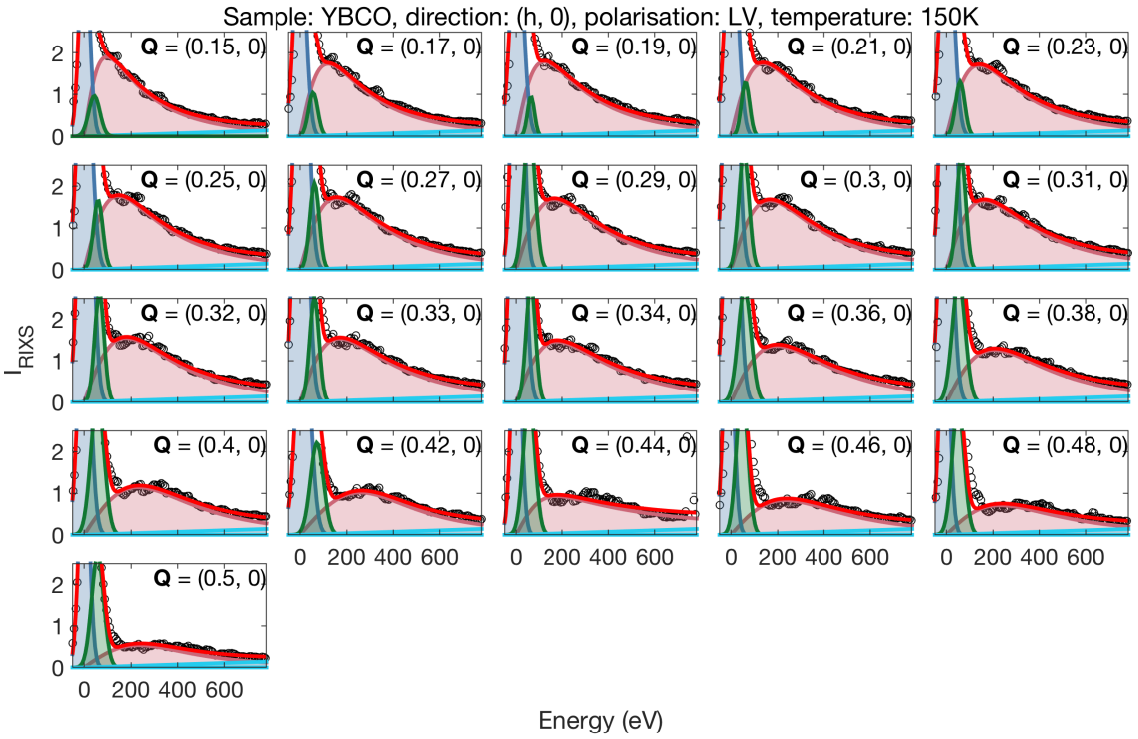

Figure A.29: Intensity of the RIXS response in YBCO ($x = 0.67$) for RIXS measurements performed at I21 with σ-polarisation for $(h,0)$ at 150 K. The data are fitted as in Fig. A.19.

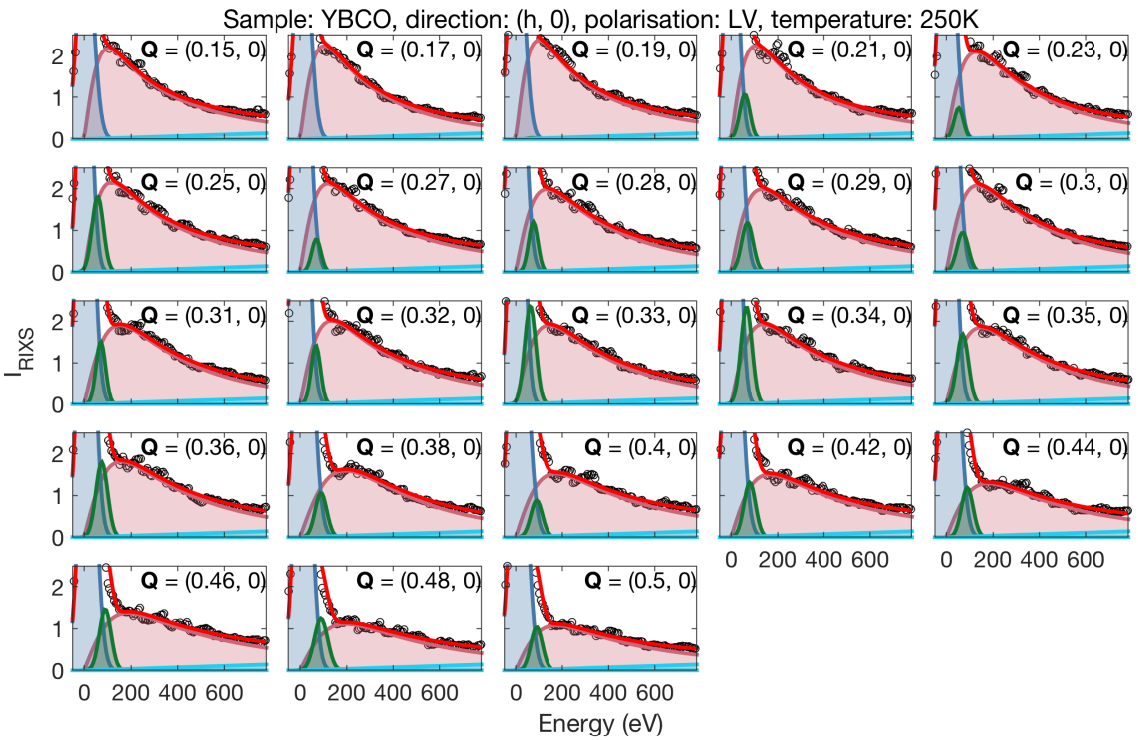

Figure A.30: Intensity of the RIXS response in YBCO ($x = 0.67$) for RIXS measurements performed at I21 with σ-polarisation for $(h,0)$ at 250 K. The data are fitted as in Fig. A.19.

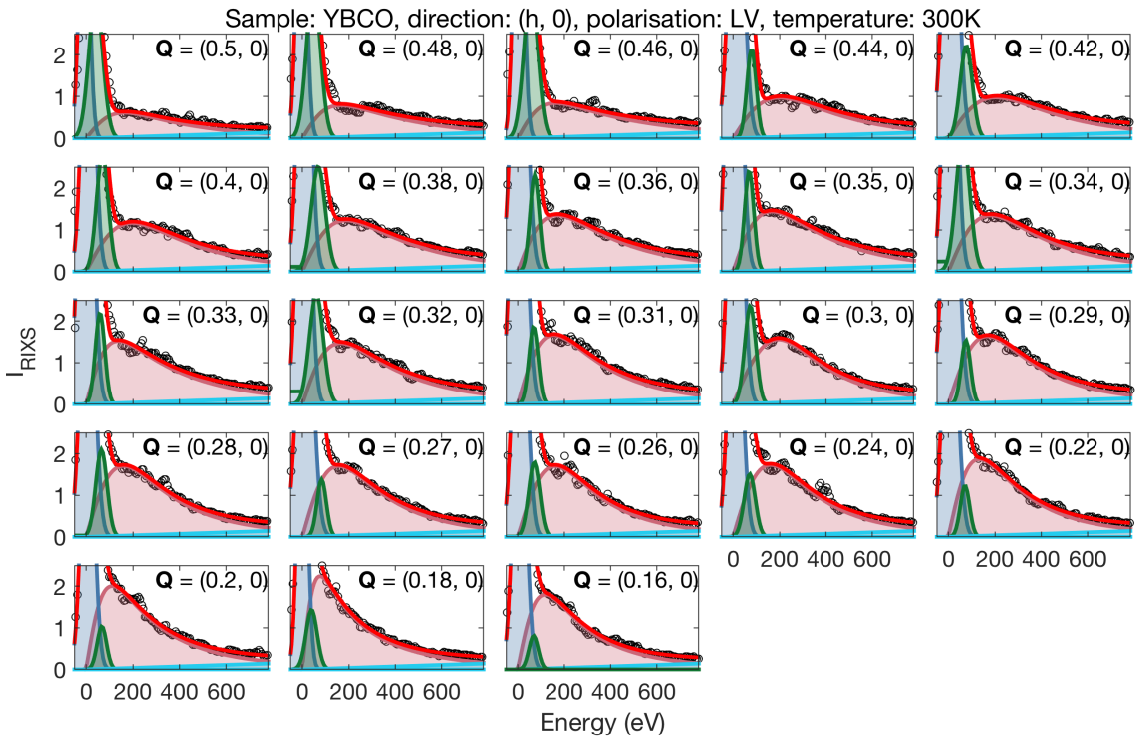

Figure A.31: Intensity of the RIXS response in YBCO ($x = 0.67$) for RIXS measurements performed at I21 with σ-polarisation for $(h,0)$ at 300 K. The data are fitted as in Fig. A.19.

Appendix B

Additional work

In addition to the work presented in this thesis, a portion of the PhD was spent studying disordered high entropy alloy (HEA) materials with Compton scattering. HEAs are alloys containing several metallic components in roughly equal proportions giving them a high level of disorder and entropy. While the electronic structure of perfect crystals can be well described by Bloch waves propagating in a periodic potential, the validity of this model in highly disordered systems remains unclear. In particular, concepts such as the Fermi surface become increasingly inexact in the case of disorder. This work comprises a Compton scattering study to investigate the effect of the disorder on the Fermi surface of a maximally disordered HEA system, $Ni_{0.25}Fe_{0.25}Co_{0.25}Cr_{0.25}$.

Compton scattering is an inelastic x-ray scattering effect which occurs at high incident energies, typically greater than 100 keV. In this limit, the scattering cross-section becomes proportional to the electron momentum density (EMD) of a system. The Hohenberg-Kohn theorems predict that the ground state of a quantum system is a unique functional of the charge density [291] which can be approximated from the EMD, making Compton scattering a useful probe of the ground state many-body wave function. Fermi surface features are indicated by jumps in the EMD allowing Compton scattering to map the Fermi surface of materials.

We performed Compton measurements at 15 directions in the Brillouin zone of NiFeCoCr with the aim of reconstructing the 1D EMD slices into the full 3D Fermi surface. I analysed this data to remove the effects of multiple scattering, detector efficiency and background and performed a basic reconstruction using the Cormack reconstruction algorithm [292]. I compared these data to calculations of the EMD and Fermi surface made using density functional theory. In these calculations the disorder was simulated using a supercell structure with random placement of the atoms [293].

The Fermi surface was subsequently reconstructed from the Compton data by Grazyna Kontrym-Sznajd and Malgorzata Samsel-Czekala using the lattice harmonic expansion method [294]. These results were compared to Korringa-Kohn-Rostoker (KKR) calculations performed by Stephen Dugdale. KKR is expected to capture both the chemical and magnetic disorder more precisely through the use of a mean-field coherent potential approximation (CPA) [295].

Both the measured data and calculations show a high level of smearing of the three Fermi surface sheets. The occupation $n(\mathbf{k})$ can be fit with three smeared step functions which reveal that the smearing extends to approximately 40% of $2\pi/a$. The fits can also be used to make an approximation of the mean-free-path and combined resistivity of the Fermi surface sheets of approximately 61 $\mu\Omega$cm. This work was subsequently written up and published in reference [296].

Bibliography

[1] Ashcroft N W and Mermin N D *Solid State Physics* (Harcourt College Publishers, 1976)

[2] Elliott S *The Physics and Chemistry of Solids* (Wiley, 1998)

[3] Willmott P *An Introduction to Synchrotron Radiation: Techniques and Applications* (Wiley, 2011)

[4] Onnes H K *Comm. Phys. Lab. Univ. Leiden* **122** 124 (1911)

[5] Bardeen J, Cooper L N and Schrieffer J R *Phys. Rev.* **106**(1) 162–164 (1957)

[6] Bednorz J G and Müller K A *Z. Phys. B* **64** 189–193 (1986)

[7] Nuñez-Regueiro M, Tholence J L, Antipov E V, Capponi J J and Marezio M *Science* **262** 97–99 (1993)

[8] Kamihara Y, Hiramatsu H, Hirano M, Kawamura R, Yanagi H, Kamiya T and Hosono H *Journal of the American Chemical Society* **128** 10012–10013 (2006)

[9] Johnson P D, Xu G and Yin W G *Iron-Based Superconductivity* Vol. 211 (Springer, 2015)

[10] Bauer E, Hilscher G, Michor H, Paul C, Scheidt E W, Gribanov A, Seropegin Y, Noël H, Sigrist M and Rogl P *Phys. Rev. Lett.* **92**(2) 027003 (2004)

[11] Riseborough P S, Schmiedeshoff G M and Smith J L *Heavy-Fermion Superconductors* , Chap. 19 1031–1154 (Springer, 2008)

[12] Schilling J S *Handbook of High-Temperature Superconductivity: High-Pressure Effects* , Chap. 11 (Springer, 2007)

[13] Drozdov A P, Eremets M I, Troyan I A, Ksenofontov V and Shylin S I *Nature* **525** 73–76 (2015)

[14] London F and Buckingham M *Superfluids: Macroscopic theory of superconductivity* Vol. 1 (Wiley, 1950)

[15] Deaver B S and Fairbank W M *Phys. Rev. Lett.* **7**(2) 43–46 (1961)

[16] Doll R and Näbauer M *Phys. Rev. Lett.* **7**(2) 51–52 (1961)

[17] Annett J *Superconductivity, Superfluids and Condensates* Oxford Master Series in Physics (Oxford University Press, 2004)

[18] Tinkham M *Introduction to superconductivity* (Courier Corporation, 2004)

[19] Bennemann K H and Ketterson J B *Superconductivity: Conventional and Unconventional Superconductors* Vol. 1 (Springer, 2008)

[20] Tsuei C C and Kirtley J R *Rev. Mod. Phys.* **72**(4) 969–1016 (2000)

[21] Cooper L N *Phys. Rev.* **104**(4) 1189–1190 (1956)

[22] Gor'kov L P *Sov. Phys. JETP* **9** 1364–1367 (1959)

[23] de Launay J *Phys. Rev.* **93**(4) 661–665 (1954)

[24] Alexandrov A S *Theory of superconductivity: from weak to strong coupling* (CRC Press, 2003)

[25] Gough C E, Colclough M S, Forgan E M, Jordan R G, Keene M, Muirhead C M, Rae A I M, Thomas N, Abell J S and Sutton S *Nature* **326** 855–855 (1987)

[26] Hoevers H, Bentum P V, Leemput L V D, Kempen H V, Schellingerhout A and Marel D V D *Physica C* **152** 105 – 110 (1988)

[27] Batlogg B, Cava R J, Jayaraman A, van Dover R B, Kourouklis G A, Sunshine S, Murphy D W, Rupp L W, Chen H S, White A, Short K T, Mujsce A M and Rietman E A *Phys. Rev. Lett.* **58**(22) 2333–2336 (1987)

[28] Bourne L C, Crommie M F, Zettl A, Loye H C z, Keller S W, Leary K L, Stacy A M, Chang K J, Cohen M L and Morris D E *Phys. Rev. Lett.* **58**(22) 2337–2339 (1987)

[29] Tsuei C C and Kirtley J R *Phase-Sensitive Tests of Pairing Symmetry in Cuprate Superconductors* , Chap. 16 869–921 (Springer, 2008)

[30] Van Harlingen D J *Rev. Mod. Phys.* **67**(2) 515–535 (1995)

[31] Warren W W, Walstedt R E, Brennert G F, Cava R J, Tycko R, Bell R F and Dabbagh G *Phys. Rev. Lett.* **62**(10) 1193–1196 (1989)

[32] Ding H, Bellman A F, Campuzano J C, Randeria M, Norman M R, Yokoya T, Takahashi T, Katayama-Yoshida H, Mochiku T, Kadowaki K, Jennings G and Brivio G P *Phys. Rev. Lett.* **76**(9) 1533–1536 (1996)

[33] Kordyuk A A *Low Temperature Physics* **41** 319–341 (2015)

[34] Coronado E, Tsukerblat B S and R G *Exchange Interactions I: Mechanisms* , Chap. 2 65–84 (Springer, 1996)

[35] Anderson P W *Phys. Rev.* **79**(2) 350–356 (1950)

[36] Anderson P W *Phys. Rev.* **83**(6) 1260–1260 (1951)

[37] Kivelson S A, Bindloss I P, Fradkin E, Oganesyan V, Tranquada J M, Kapitulnik A and Howald C *Rev. Mod. Phys.* **75**(4) 1201–1241 (2003)

[38] Huang E W, Scalapino D J, Maier T A, Moritz B and Devereaux T P *Phys. Rev. B* **96**(2) 020503 (2017)

[39] Moriya T, Takahashi Y and Ueda K *Journal of the Physical Society of Japan* **59** 2905–2915 (1990)

[40] Miyake K, Schmitt-Rink S and Varma C M *Phys. Rev. B* **34**(9) 6554–6556 (1986)

[41] Scalapino D J, Loh E and Hirsch J E *Phys. Rev. B* **34**(11) 8190–8192 (1986)

[42] Monthoux P, Pines D and Lonzarich G G *Nature* **450** 1177–1183 (2007)

[43] Coldea R, Hayden S M, Aeppli G, Perring T G, Frost C D, Mason T E, Cheong S W and Fisk Z *Phys. Rev. Lett.* **86**(23) 5377–5380 (2001)

[44] Headings N S, Hayden S M, Coldea R and Perring T G *Phys. Rev. Lett.* **105**(24) 247001 (2010)

[45] Scalapino D *Physics Reports* **250** 329 – 365 (1995)

[46] Moriya T and Ueda K *Rep. Prog. Phys.* **66** 1299–1341 (2003)

[47] Anderson P W *Science* **235** 1196–1198 (1987)

[48] Anderson P W, Lee P, Randeria M, Rice T, Trivedi N and Zhang F *Journal of Physics: Condensed Matter* **16** 755–769 (2004)

[49] Hsu T C *Phys. Rev. B* **41**(16) 11379–11387 (1990)

[50] Ho C M, Muthukumar V N, Ogata M and Anderson P W *Phys. Rev. Lett.* **86**(8) 1626–1629 (2001)

[51] Dalla Piazza B, Mourigal M, Christensen N B, Nilsen G J, Tregenna-Piggott P, Perring T G, Enderle M, McMorrow D F, Ivanov D A and Rønnow H M *Nat. Phys.* **11** 62 – 68 (2015)

[52] Scalapino D J *Rev. Mod. Phys.* **84**(4) 1383–1417 (2012)

[53] Lefmann K, Lake B, Aeppli G, Cheong S W, Christensen N B, Clausen K N, Hayden S, Mason T E, McMorrow D, Mook H A, Rønnow H M and Takagi H *Journal of Low Temperature Physics* **135** 621–664 (2004)

[54] Huang E W, Mendl C B, Liu S, Johnston S, Jiang H C, Moritz B and Devereaux T P *Science* **358** 1161–1164 (2017)

[55] Thorne R E *Physics Today* **49** 42–48 (1996)

[56] Peierls R E *Quantum theory of solids* (Clarendon Press, 1996)

[57] Grüner G *Rev. Mod. Phys.* **60**(4) 1129–1181 (1988)

[58] Fröhlich H *Proceedings of the Royal Society of London. Series A. Mathematical and Physical Sciences* **223** 296–305 (1954)

[59] Khomskii D I *Basic Aspects of the Quantum Theory of Solids: Order and Elementary Excitations* (Cambridge University Press, 2010)

[60] Bray J W, Interrante L, Jacobs I and Bonner J *The Spin-Peierls Transition* , Chap. 7 (Springer, 1983)

[61] Pouget J P *Comptes Rendus Physique* **17** 332–356 (2016)

[62] Overhauser A W and Arrott A *Phys. Rev. Lett.* **4**(5) 226–227 (1960)

[63] Blundell S *Am. J. Phys.* **71** 94 (2003)

[64] Overhauser A W *Phys. Rev.* **128**(3) 1437–1452 (1962)

[65] Monceau P *Advances in Physics* **61** 325–581 (2012)

[66] Moodenbaugh A R, Xu Y, Suenaga M, Folkerts T J and Shelton R N *Phys. Rev. B* **38**(7) 4596–4600 (1988)

[67] Schulz H *J. Phys. France* **50** 2833–2849 (1989)

[68] Zaanen J and Gunnarsson O *Phys. Rev. B* **40**(10) 7391–7394 (1989)

[69] Tranquada J, Sternlieb B, Axe J, Nakamura Y and Uchida S *Nature* **375** 561–563 (1995)

[70] Fujita M, Goka H, Yamada K and Matsuda M *Phys. Rev. Lett.* **88**(16) 167008 (2002)

[71] Tranquada J M *Physica B* **407** 1771 – 1774 (2012).
Proceedings of the International Workshop on Electronic Crystals (ECRYS-2011)

[72] Comin R and Damascelli A *Annu. Rev. Condens. Matter Phys.* **7** 369–405 (2016)

[73] Doiron-Leyraud N, Proust C, LeBoeuf D, Levallois J, Bonnemaison J B, Liang R, Bonn D A, Hardy W N and Taillefer L *Nature* **447** 565–568 (2007)

[74] Ghiringhelli G, Le Tacon M, Minola M, Blanco-Canosa S, Mazzoli C, Brookes N B, De Luca G M, Frano A, Hawthorn D G, He F, Loew T, Sala M M, Peets D C, Salluzzo M, Schierle E, Sutarto R, Sawatzky G A, Weschke E, Keimer B and Braicovich L *Science* **337** 821–825 (2012)

[75] Gabovich A M, Voitenko A I, Ekino T, Li M S, Szymczak H and Pękała M *Adv. Cond. Matter. Phys.* **2010** 681070 (2010)

[76] Chang J, Blackburn E, Holmes A T, Christensen N B, Larsen J, Mesot J, Liang R, Bonn D A, Hardy W N, Watenphul A, Zimmermann M v, Forgan E M and Hayden S M *Nature Physics* **8** 871 – 876 (2012)

[77] Croft T P, Lester C, Senn M S, Bombardi A and Hayden S M *Phys. Rev. B* **89**(22) 224513 (2014)

[78] Comin R, Frano A, Yee M M, Yoshida Y, Eisaki H, Schierle E, Weschke E, Sutarto R, He F, Soumyanarayanan A, He Y, Le Tacon M, Elfimov I S, Hoffman J E, Sawatzky G A, Keimer B and Damascelli A *Science* **343** 390–392 (2014)

[79] da Silva Neto E H, Comin R, He F, Sutarto R, Jiang Y, Greene R L, Sawatzky G A and Damascelli A *Science* **347** 282–285 (2015)

[80] Chaix L, Huang E W, Gerber S, Lu X, Jia C, Huang Y, McNally D E, Wang Y, Vernay F H, Keren A, Shi M, Moritz B, Shen Z X, Schmitt T, Devereaux T P and Lee W S *Phys. Rev. B* **97**(15) 155144 (2018)

[81] Xu Z, Schneeloch J A, Yi M, Zhao Y, Matsuda M, Pajerowski D M, Chi S, Birgeneau R J, Gu G, Tranquada J M and Xu G *Phys. Rev. B* **97**(21) 214511 (2018)

[82] Lee S, de la Peña G, Sun S X L, Mitrano M, Fang Y, Jang H, Lee J S, Eckberg C, Campbell D, Collini J, Paglione J, de Groot F M F and Abbamonte P *Phys. Rev. Lett.* **122**(14) 147601 (2019)

[83] Moll P J W, Zeng B, Balicas L, Galeski S, Balakirev F F, Bauer E D and Ronning F *Nature Communications* **6** 6663 (2015)

[84] Gray K E and Kim D H *Phys. Rev. Lett.* **70**(11) 1693–1696 (1993)

[85] Di Castro C, Raimondi R, Castellani C and Varlamov A A *Phys. Rev. B* **42**(16) 10211–10219 (1990)

[86] Hirayama M, Yamaji Y, Misawa T and Imada M *Phys. Rev. B* **98**(13) 134501 (2018)

[87] Keimer B, Kivelson S A, Norman M R, Uchida S and Zaanen J *Nature* **518** 179–186 (2015)

[88] Park H, Haule K and Kotliar G *Phys. Rev. Lett.* **101**(18) 186403 (2008)

[89] Gull E, Werner P, Wang X, Troyer M and Millis A J *EPL* **84** 37009 (2008)

[90] Balzer M, Kyung B, Sénéchal D, Tremblay A M S and Potthoff M *EPL* **85** 17002 (2009)

[91] Ferrero M, Cornaglia P S, Leo L D, Parcollet O, Kotliar G and Georges A *EPL* **85** 57009 (2009)

[92] Comanac A, de'Medici L, Capone M and Millis A J *Nature Physics* **4** 287–290 (2008)

[93] Balakirev F F, Betts J B, Migliori A, Ono S, Ando Y and Boebinger G S *Nature* **424** 912–915 (2003)

[94] Michon B, Girod C, Badoux S, Kačmarčík J, Ma Q, Dragomir M, Dabkowska H A, Gaulin B D, Zhou J S, Pyon S, Takayama T, Takagi H, Verret S, Doiron-Leyraud N, Marcenat C, Taillefer L and Klein T *Nature* **567** 218–222 (2019)

[95] Keimer B, Aharony A, Auerbach A, Birgeneau R J, Cassanho A, Endoh Y, Erwin R W, Kastner M A and Shirane G *Phys. Rev. B* **45**(13) 7430–7435 (1992)

[96] Kastner M A, Birgeneau R J, Shirane G and Endoh Y *Rev. Mod. Phys.* **70**(3) 897–928 (1998)

[97] Radaelli P G, Hinks D G, Mitchell A W, Hunter B A, Wagner J L, Dabrowski B, Vandervoort K G, Viswanathan H K and Jorgensen J D *Phys. Rev. B* **49**(6) 4163–4175 (1994)

[98] Reehuis M, Ulrich C, Prokeš K, Gozar A, Blumberg G, Komiya S, Ando Y, Pattison P and Keimer B *Phys. Rev. B* **73**(14) 144513 (2006)

[99] Headings N S *Neutron Scattering Measurements of Spin Fluctuations in Two-Dimensional Magnets and High-Tc Superconductors* Ph.D. thesis University of Bristol (2010)

[100] Zimmermann M v, Schneider J R, Frello T, Andersen N H, Madsen J, Käll M, Poulsen H F, Liang R, Dosanjh P and Hardy W N *Phys. Rev. B* **68**(10) 104515 (2003)

[101] Bannett Y B and Freund I *Phys. Rev. Lett.* **34**(6) 372–376 (1975)

[102] Eisenberger P, Platzman P M and Winick H *Phys. Rev. B* **13**(6) 2377–2380 (1976)

[103] Eisenberger P, Platzman P M and Winick H *Phys. Rev. Lett.* **36**(11) 623–626 (1976)

[104] Ament L J P, van Veenendaal M, Devereaux T P, Hill J P and van den Brink J *Rev. Mod. Phys.* **83**(2) 705–767 (2011)

[105] Ghiringhelli G, Brookes N B, Annese E, Berger H, Dallera C, Grioni M, Perfetti L, Tagliaferri A and Braicovich L *Phys. Rev. Lett.* **92**(11) 117406 (2004)

[106] Ament L J P, Ghiringhelli G, Sala M M, Braicovich L and van den Brink J *Phys. Rev. Lett.* **103**(11) 117003 (2009)

[107] Braicovich L, Ament L J P, Bisogni V, Forte F, Aruta C, Balestrino G, Brookes N B, De Luca G M, Medaglia P G, Granozio F M, Radovic M, Salluzzo M, van den Brink J and Ghiringhelli G *Phys. Rev. Lett.* **102**(16) 167401 (2009)

[108] Le Tacon M, Ghiringhelli G, Chaloupka J, Sala M M, Hinkov V, Haverkort M W, Minola M, Bakr M, Zhou K J, Blanco-Canosa S, Monney C, Song Y T, Sun G L, Lin C T, De Luca G M, Salluzzo M, Khaliullin G, Schmitt T, Braicovich L and Keimer B *Nat. Phys.* **7** 725–730 (2011)

[109] Dean M P M, Dellea G, Springell R S, Yakhou-Harris F, Kummer K, Brookes N B, Liu X, Sun Y J, Strle J, Schmitt T, Braicovich L, Ghiringhelli G, Božović I and Hill J P *Nat. Mater.* **12** 1019 – 1023 (2013)

[110] Dean M *J. Magn. Magn. Mater.* **376** 3 – 13 (2015)

[111] Meyers D, Miao H, Walters A C, Bisogni V, Springell R S, d'Astuto M, Dantz M, Pelliciari J, Huang H Y, Okamoto J, Huang D J, Hill J P, He X, Božović I, Schmitt T and Dean M P M *Phys. Rev. B* **95**(7) 075139 (2017)

[112] Chaix L, Ghiringhelli G, Peng Y Y, Hashimoto M, Moritz B, Kummer K, Brookes N B, He Y, Chen S, Ishida S, Yoshida Y, Eisaki H, Salluzzo M, Braicovich L, Shen Z X, Devereaux T P and Lee W S *Nat. Phys.* **13** 952–956 (2017)

[113] Lovesey S and Collins S *X-ray Scattering and Absorption by Magnetic Materials* Oxford science publications (Clarendon Press, 1996)

[114] Gibbs D, Harshman D R, Isaacs E D, McWhan D B, Mills D and Vettier C *Phys. Rev. Lett.* **61**(10) 1241–1244 (1988)

[115] Blume M *Journal of Applied Physics* **57** 3615–3618 (1985)

[116] Hill J P and McMorrow D F *Acta Crystallographica Section A* **52** 236–244 (1996)

[117] De Groot F and Kotani A *Core level spectroscopy of solids* (CRC Press, 2008)

[118] Kotani A and Shin S *Rev. Mod. Phys.* **73**(1) 203–246 (2001)

[119] Sala M M, Bisogni V, Aruta C, Balestrino G, Berger H, Brookes N B, de Luca G M, Castro D D, Grioni M, Guarise M, Medaglia P G, Granozio F M, Minola M, Perna P, Radovic M, Salluzzo M, Schmitt T, Zhou K J, Braicovich L and Ghiringhelli G *New J. Phys.* **13** 043026 (2011)

[120] Jia C J, Chen C C, Sorini A P, Moritz B and Devereaux T P *New Journal of Physics* **14** 113038 (2012)

[121] Jia C J, Nowadnick E A, Wohlfeld K, Kung Y F, Chen C C, Johnston S, Tohyama T, Moritz B and Devereaux T P *Nature Communications* **5** 3314 (2014)

[122] Jia C, Wohlfeld K, Wang Y, Moritz B and Devereaux T P *Phys. Rev. X* **6**(2) 021020 (2016)

[123] van den Brink J and van Veenendaal M *Journal of Physics and Chemistry of Solids* **66** 2145 – 2149 (2005).
5th International Conference on Inelastic X-ray Scattering (IXS 2004)

[124] van den Brink J and van Veenendaal M *EPL* **73** 121–127 (2006)

[125] Ament L J P, Forte F and van den Brink J *Phys. Rev. B* **75**(11) 115118 (2007)

[126] Kim J, Ellis D S, Zhang H, Kim Y J, Hill J P, Chou F C, Gog T and Casa D *Phys. Rev. B* **79**(9) 094525 (2009)

[127] Ishii K *Resonant Inelastic X-Ray Scattering in Strongly Correlated Copper Oxides* , Chap. 6 197–241 (Berlin, Heidelberg: Springer, 2017)

[128] Tanaka S and Kotani A *J. Phys. Soc. Jpn.* **62** 464–467 (1993)

[129] Devereaux T P, Shvaika A M, Wu K, Wohlfeld K, Jia C J, Wang Y, Moritz B, Chaix L, Lee W S, Shen Z X, Ghiringhelli G and Braicovich L *Phys. Rev. X* **6**(4) 041019 (2016)

[130] Ament L J P, van Veenendaal M and van den Brink J *EPL* **95** 27008 (2011)

[131] Yavaş H, van Veenendaal M, van den Brink J, Ament L J P, Alatas A, Leu B M, Apostu M O, Wizent N, Behr G, Sturhahn W, Sinn H and Alp E E *Journal of Physics: Condensed Matter* **22** 485601 (2010)

[132] Rossi M, Arpaia R, Fumagalli R, Moretti Sala M, Betto D, Kummer K, De Luca G M, van den Brink J, Salluzzo M, Brookes N B, Braicovich L and Ghiringhelli G *Phys. Rev. Lett.* **123**(2) 027001 (2019)

[133] Braicovich L, Rossi M, Fumagalli R, Peng Y, Wang Y, Arpaia R, Betto D, De Luca G M, Di Castro D, Kummer K *et al. arXiv preprint* (2019)

[134] Wakimoto S, Kimura H, Ishii K, Ikeuchi K, Adachi T, Fujita M, Kakurai K, Koike Y, Mizuki J, Noda Y, Yamada K, Said A H and Shvyd'ko Y *Phys. Rev. Lett.* **102**(15) 157001 (2009)

[135] Miao H, Lorenzana J, Seibold G, Peng Y Y, Amorese A, Yakhou-Harris F, Kummer K, Brookes N B, Konik R M, Thampy V, Gu G D, Ghiringhelli G, Braicovich L and Dean M P M *Proc. Natl. Acad. Sci. U.S.A.* **114** 12430–12435 (2017)

[136] Arpaia R, Caprara S, Fumagalli R, De Vecchi G, Peng Y Y, Andersson E, Betto D, De Luca G M, Brookes N B, Lombardi F, Salluzzo M, Braicovich L, Di Castro C, Grilli M and Ghiringhelli G *Science* **365** 906–910 (2019)

[137] Le Tacon M, Bosak A, Souliou S M, Dellea G, Loew T, Heid R, Bohnen K P, Ghiringhelli G, Krisch M and Keimer B *Nat. Phys.* **10** 52–58 (2013)

[138] Comin R, Sutarto R, da Silva Neto E H, Chauviere L, Liang R, Hardy W N, Bonn D A, He F, Sawatzky G A and Damascelli A *Science* **347** 1335–1339 (2015)

[139] Tsutsui K, Tohyama T and Maekawa S *Phys. Rev. Lett.* **83**(18) 3705–3708 (1999)

[140] de Groot F M F, Kuiper P and Sawatzky G A *Phys. Rev. B* **57**(23) 14584–14587 (1998)

[141] van Veenendaal M *Phys. Rev. Lett.* **96**(11) 117404 (2006)

[142] Haverkort M W *Phys. Rev. Lett.* **105**(16) 167404 (2010)

[143] Braicovich L, van den Brink J, Bisogni V, Sala M M, Ament L J P, Brookes N B, De Luca G M, Salluzzo M, Schmitt T, Strocov V N and Ghiringhelli G *Phys. Rev. Lett.* **104**(7) 077002 (2010)

[144] van den Brink J *Europhysics Letters (EPL)* **80** 47003 (2007)

[145] Forte F, Ament L J P and van den Brink J *Phys. Rev. B* **77**(13) 134428 (2008)

[146] Harada Y, Okada K, Eguchi R, Kotani A, Takagi H, Takeuchi T and Shin S *Phys. Rev. B* **66**(16) 165104 (2002)

[147] Hill J P, Blumberg G, Kim Y J, Ellis D S, Wakimoto S, Birgeneau R J, Komiya S, Ando Y, Liang B, Greene R L, Casa D and Gog T *Phys. Rev. Lett.* **100**(9) 097001 (2008)

[148] Bisogni V, Moretti Sala M, Bendounan A, Brookes N B, Ghiringhelli G and Braicovich L *Phys. Rev. B* **85**(21) 214528 (2012)

[149] Brookes N B, Ghiringhelli G, Glatzel P and Sala M M *Synchrotron Radiat. News* **31** 26–30 (2018)

[150] Ghiringhelli G, Piazzalunga A, Dallera C, Trezzi G, Braicovich L, Schmitt T, Strocov V N, Betemps R, Patthey L, Wang X and Grioni M *Review of Scientific Instruments* **77** 113108 (2006)

[151] Braicovich L, Brookes N B, Ghiringhelli G, Minola M, Monaco G, Sala M M and Simonelli L *Synchrotron Radiat. News* **25** 9–15 (2012)

[152] Jarrige I, Bisogni V, Zhu Y, Leonhardt W and Dvorak J *Synchrotron Radiation News* **31** 7–13 (2018)

[153] Huang D J and Chen C T *Synchrotron Radiation News* **31** 3–6 (2018)

[154] Kao K Y, Hua C Y, Fung H S, Lin S W, Chao H Y, Yeh S C, Chung S C, Huang D J and Chen C T *AIP Conference Proceedings* **2054** 060005 (2019)

[155] See https://www.maxiv.lu.se/accelerators-beamlines/beamlines/veritas/

[156] See https://www.diamond.ac.uk/Instruments/Magnetic-Materials/I21

[157] Achkar A J, Regier T Z, Wadati H, Kim Y J, Zhang H and Hawthorn D G *Phys. Rev. B* **83**(8) 081106 (2011)

[158] Minola M, Dellea G, Gretarsson H, Peng Y Y, Lu Y, Porras J, Loew T, Yakhou F, Brookes N B, Huang Y B, Pelliciari J, Schmitt T, Ghiringhelli G, Keimer B, Braicovich L and Le Tacon M *Phys. Rev. Lett.* **114**(21) 217003 (2015)

[159] Achkar A J, He F, Sutarto R, McMahon C, Zwiebler M, Hücker M, Gu G D, Liang R, Bonn D A, Hardy W N, Geck J and Hawthorn D G *Nat. Mater.* **15** 616–620 (2016)

[160] Maslen E N *X-ray absorption* , Chap. 6.3 599–608 (American Cancer Society, 2006)

[161] Peng Y Y, Huang E W, Fumagalli R, Minola M, Wang Y, Sun X, Ding Y, Kummer K, Zhou X J, Brookes N B, Moritz B, Braicovich L, Devereaux T P and Ghiringhelli G *Phys. Rev. B* **98**(14) 144507 (2018)

[162] Fumagalli R, Braicovich L, Minola M, Peng Y Y, Kummer K, Betto D, Rossi M, Lefrançois E, Morawe C, Salluzzo M, Suzuki H, Yakhou F, Le Tacon M, Keimer B, Brookes N B, Sala M M and Ghiringhelli G *Phys. Rev. B* **99**(13) 134517 (2019)

[163] Comin R, Sutarto R, He F, da Silva Neto E H, Chauviere L, Fraño A, Liang R, Hardy W N, Bonn D A, Yoshida Y, Eisaki H, Achkar A J, Hawthorn D G, Keimer B, Sawatzky G A and Damascelli A *Nature Materials* **14** 796–800 (2015)

[164] Lyons K B, Fleury P A, Schneemeyer L F and Waszczak J V *Phys. Rev. Lett.* **60**(8) 732–735 (1988)

[165] Hayden S M, Aeppli G, Mook H A, Perring T G, Mason T E, Cheong S W and Fisk Z *Phys. Rev. Lett.* **76**(8) 1344–1347 (1996)

[166] Dai P, Mook H A, Hunt R D and Doğan F *Phys. Rev. B* **63**(5) 054525 (2001)

[167] Stock C, Buyers W J L, Cowley R A, Clegg P S, Coldea R, Frost C D, Liang R, Peets D, Bonn D, Hardy W N and Birgeneau R J *Phys. Rev. B* **71**(2) 024522 (2005)

[168] Lipscombe O J, Hayden S M, Vignolle B, McMorrow D F and Perring T G *Phys. Rev. Lett.* **99**(6) 067002 (2007)

[169] Vaknin D, Sinha S K, Moncton D E, Johnston D C, Newsam J M, Safinya C R and King H E *Phys. Rev. Lett.* **58**(26) 2802–2805 (1987)

[170] Vilk Y and Tremblay A M *J. Phys. I France* **7** 1309–1368 (1997)

[171] Haverkort M *Spin and orbital degrees of freedom in transition metal oxides and oxide thin films studied by soft x-ray absorption spectroscopy* Ph.D. thesis Universität zu Köln (2005)

[172] Minola M *Magnetic, orbital and charge fluctuations in layered cuprates studied by resonant soft x-ray scattering* Ph.D. thesis Politecnico di Milano (2013)

[173] Glawion S, Heidler J, Haverkort M W, Duda L C, Schmitt T, Strocov V N, Monney C, Zhou K J, Ruff A, Sing M and Claessen R *Phys. Rev. Lett.* **107**(10) 107402 (2011)

[174] Haverkort M W, Zwierzycki M and Andersen O K *Phys. Rev. B* **85**(16) 165113 (2012)

[175] Kim Y J, Hill J P, Benthien H, Essler F H L, Jeckelmann E, Choi H S, Noh T W, Motoyama N, Kojima K M, Uchida S, Casa D and Gog T *Phys. Rev. Lett.* **92**(13) 137402 (2004)

[176] Lu Y, Höppner M, Gunnarsson O and Haverkort M W *Phys. Rev. B* **90**(8) 085102 (2014)

[177] Haverkort M W, Sangiovanni G, Hansmann P, Toschi A, Lu Y and Macke S *EPL* **108** 57004 (2014)

[178] Anderson P W *Phys. Rev.* **86**(5) 694–701 (1952)

[179] Kubo R *Phys. Rev.* **87**(4) 568–580 (1952)

[180] Oguchi T *Phys. Rev.* **117**(1) 117–123 (1960)

[181] Cheong S W, Thompson J D and Fisk Z *Phys. Rev. B* **39**(7) 4395–4398 (1989)

[182] Moriya T *Phys. Rev.* **120**(1) 91–98 (1960)

[183] Silva Neto M B, Benfatto L, Juricic V and Morais Smith C *Phys. Rev. B* **73**(4) 045132 (2006)

[184] Shirane G, Endoh Y, Birgeneau R J, Kastner M A, Hidaka Y, Oda M, Suzuki M and Murakami T *Phys. Rev. Lett.* **59**(14) 1613–1616 (1987)

[185] Endoh Y, Yamada K, Birgeneau R J, Gabbe D R, Jenssen H P, Kastner M A, Peters C J, Picone P J, Thurston T R, Tranquada J M, Shirane G, Hidaka Y, Oda M, Enomoto Y, Suzuki M and Murakami T *Phys. Rev. B* **37**(13) 7443–7453 (1988)

[186] Birgeneau R J, Gabbe D R, Jenssen H P, Kastner M A, Picone P J, Thurston T R, Shirane G, Endoh Y, Sato M, Yamada K, Hidaka Y, Oda M, Enomoto Y, Suzuki M and Murakami T *Phys. Rev. B* **38**(10) 6614–6623 (1988)

[187] Sato M, Shamoto S, Tranquada J M, Shirane G and Keimer B *Phys. Rev. Lett.* **61**(11) 1317–1320 (1988)

[188] Rossat-Mignod, J, Burlet, P, Jurgens, M J, Vettier, C, Regnault, L P, Henry, J Y, Ayache, C, Forro, L, Noel, H, Potel, M, Gougeon, P and Levet, J C *J. Phys. Colloques* **49** C8–2119–C8–2124 (1988)

[189] Jurgens M, Burlet P, Vettier C, Regnault L, Henry J, Rossat-Mignod J, Noel H, Potel M, Gougeon P and Levet J *Physica B* **156-157** 846 – 850 (1989)

[190] Tranquada J M, Shirane G, Keimer B, Shamoto S and Sato M *Phys. Rev. B* **40**(7) 4503–4516 (1989)

[191] Aeppli G, Hayden S M, Mook H A, Fisk Z, Cheong S W, Rytz D, Remeika J P, Espinosa G P and Cooper A S *Phys. Rev. Lett.* **62**(17) 2052–2055 (1989)

[192] Hayden S M, Aeppli G, Mook H A, Cheong S W and Fisk Z *Phys. Rev. B* **42**(16) 10220–10225 (1990)

[193] Hayden S M, Aeppli G, Osborn R, Taylor A D, Perring T G, Cheong S W and Fisk Z *Phys. Rev. Lett.* **67**(25) 3622–3625 (1991)

[194] Hayden S, Aeppli G, Dai P, Mook H, Perring T, Cheong S W, Fisk Z, Doğan F and Mason T *Physica B* **241-243** 765 – 772 (1997).
Proceedings of the International Conference on Neutron Scattering

[195] Roger M *Journal of Magnetism and Magnetic Materials* **31-34** 727 – 732 (1983)

[196] Roger M *Journal of Physics and Chemistry of Solids* **66** 1412 – 1416 (2005)

[197] Toader A M, Goff J P, Roger M, Shannon N, Stewart J R and Enderle M *Phys. Rev. Lett.* **94**(19) 197202 (2005)

[198] Goff J P, Toader A M, Roger M, Shannon N, Stewart J R, Enderle M and Fåk B *Journal of Magnetism and Magnetic Materials* **310** 1663–1665 (2007)

[199] Ino A, Kim C, Mizokawa T, Shen Z X, Fujimori A, Takaba M, Tamasaku K, Eisaki H and Uchida S *J. Phys. Soc. Jpn.* **68** 1496–1499 (1999)

[200] Damascelli A, Hussain Z and Shen Z X *Rev. Mod. Phys.* **75**(2) 473–541 (2003)

[201] Yoshida T, Zhou X J, Sasagawa T, Yang W L, Bogdanov P V, Lanzara A, Hussain Z, Mizokawa T, Fujimori A, Eisaki H, Shen Z X, Kakeshita T and Uchida S *Phys. Rev. Lett.* **91**(2) 027001 (2003)

[202] Yoshida T, Zhou X J, Tanaka K, Yang W L, Hussain Z, Shen Z X, Fujimori A, Sahrakorpi S, Lindroos M, Markiewicz R S, Bansil A, Komiya S, Ando Y, Eisaki H, Kakeshita T and Uchida S *Phys. Rev. B* **74**(22) 224510 (2006)

[203] Pickett W E *Rev. Mod. Phys.* **61**(2) 433–512 (1989)

[204] Pavarini E, Dasgupta I, Saha-Dasgupta T, Jepsen O and Andersen O K *Phys. Rev. Lett.* **87**(4) 047003 (2001)

[205] Delannoy J Y P, Gingras M J P, Holdsworth P C W and Tremblay A M S *Phys. Rev. B* **79**(23) 235130 (2009)

[206] Laughlin R B *Journal of Low Temperature Physics* **99** 443–466 (1995)

[207] Sandvik A W and Singh R R P *Phys. Rev. Lett.* **86**(3) 528–531 (2001)

[208] Little W, Holcomb M, Ghiringhelli G, Braicovich L, Dallera C, Piazzalunga A, Tagliaferri A and Brookes N *Physica C* **460–462** 40–43 (2007).
Proceedings of the 8th International Conference on Materials and Mechanisms of Superconductivity and High Temperature Superconductors

[209] Abbamonte P, Burns C A, Isaacs E D, Platzman P M, Miller L L, Cheong S W and Klein M V *Phys. Rev. Lett.* **83**(4) 860–863 (1999)

[210] Ishii K, Tohyama T, Asano S, Sato K, Fujita M, Wakimoto S, Tustsui K, Sota S, Miyawaki J, Niwa H, Harada Y, Pelliciari J, Huang Y, Schmitt T, Yamamoto Y and Mizuki J *Phys. Rev. B* **96**(11) 115148 (2017)

[211] Dean M P M, Springell R S, Monney C, Zhou K J, Pereiro J, Božović I, Dalla Piazza B, Rønnow H M, Morenzoni E, van den Brink J, Schmitt T and Hill J P *Nat. Mater.* **11** 850–854 (2012)

[212] Pintschovius L *Phys. Status Solidi B* **242** 30–50 (2005)

[213] Reznik D *Physica C* **481** 75 – 92 (2012).
Stripes and Electronic Liquid Crystals in Strongly Correlated Materials

[214] Lee W S, Johnston S, Moritz B, Lee J, Yi M, Zhou K J, Schmitt T, Patthey L, Strocov V, Kudo K, Koike Y, van den Brink J, Devereaux T P and Shen Z X *Phys. Rev. Lett.* **110**(26) 265502 (2013)

[215] Johnston S, Monney C, Bisogni V, Zhou K J, Kraus R, Behr G, Strocov V N, Málek J, Drechsler S L, Geck J, Schmitt T and van den Brink J *Nature Communications* **7** 10563 (2016)

[216] Song J and Annett J F *Phys. Rev. B* **51**(6) 3840–3849 (1995)

[217] Bulut N and Scalapino D J *Phys. Rev. B* **54**(21) 14971–14973 (1996)

[218] Gadermaier C, Alexandrov A S, Kabanov V V, Kusar P, Mertelj T, Yao X, Manzoni C, Brida D, Cerullo G and Mihailovic D *Phys. Rev. Lett.* **105**(25) 257001 (2010)

[219] Johnston S, Vernay F, Moritz B, Shen Z X, Nagaosa N, Zaanen J and Devereaux T P *Phys. Rev. B* **82**(6) 064513 (2010)

[220] Tanaka I and Kojima H *Nature* **337** 21–22 (1989)

[221] Lamsal J and Montfrooij W *Phys. Rev. B* **93**(21) 214513 (2016)

[222] Monney C, Schmitt T, Matt C E, Mesot J, Strocov V N, Lipscombe O J, Hayden S M and Chang J *Phys. Rev. B* **93**(7) 075103 (2016)

[223] Chaikin P M and Lubensky T C *Principles of Condensed Matter Physics* (Cambridge University Press, 1995)

[224] Peng Y Y, Salluzzo M, Sun X, Ponti A, Betto D, Ferretti A M, Fumagalli F, Kummer K, Le Tacon M, Zhou X J, Brookes N B, Braicovich L and Ghiringhelli G *Phys. Rev. B* **94**(18) 184511 (2016)

[225] Dalla Piazza B *Theories of Experimentally Observed Excitation Spectra of Square Lattice Antiferromagnets* Ph.D. thesis EPFL (2014)

[226] Coldea R, Tennant D A and Tylczynski Z *Phys. Rev. B* **68**(13) 134424 (2003)

[227] Lake B, Tennant D A, Frost C D and Nagler S E *Nat. Mater.* **4** 329–334 (2005)

[228] Kotliar G and Liu J *Phys. Rev. B* **38**(7) 5142–5145 (1988)

[229] Miao H, Ishikawa D, Heid R, Le Tacon M, Fabbris G, Meyers D, Gu G D, Baron A Q R and Dean M P M *Phys. Rev. X* **8**(1) 011008 (2018)

[230] Chaplot S L, Reichardt W, Pintschovius L and Pyka N *Phys. Rev. B* **52**(10) 7230–7242 (1995)

[231] Reznik D, Pintschovius L, Fujita M, Yamada K, Gu G D and Tranquada J M *Journal of Low Temperature Physics* **147** 353–364 (2007)

[232] Jiang H C and Devereaux T P *Science* **365** 1424 (2019)

[233] Vignolle B, Hayden S M, McMorrow D F, Rønnow H M, Lake B, Frost C D and Perring T G *Nat. Phys.* **3** 163 – 167 (2007)

[234] Lipscombe O J, Vignolle B, Perring T G, Frost C D and Hayden S M *Phys. Rev. Lett.* **102**(16) 167002 (2009)

[235] Matsuda M, Fujita M, Yamada K, Birgeneau R J, Kastner M A, Hiraka H, Endoh Y, Wakimoto S and Shirane G *Phys. Rev. B* **62**(13) 9148–9154 (2000)

[236] Christensen N B, McMorrow D F, Rønnow H M, Lake B, Hayden S M, Aeppli G, Perring T G, Mangkorntong M, Nohara M and Takagi H *Phys. Rev. Lett.* **93**(14) 147002 (2004)

[237] Arai M, Nishijima T, Endoh Y, Egami T, Tajima S, Tomimoto K, Shiohara Y, Takahashi M, Garrett A and Bennington S M *Phys. Rev. Lett.* **83**(3) 608–611 (1999)

[238] Dai P, Mook H A, Hayden S M, Aeppli G, Perring T G, Hunt R D and Doğan F *Science* **284** 1344–1347 (1999)

[239] Hayden S M, Mook H A, Dai P, Perring T G and Doğan F *Nature* **429** 531–534 (2004)

[240] Wakimoto S, Yamada K, Tranquada J M, Frost C D, Birgeneau R J and Zhang H *Phys. Rev. Lett.* **98**(24) 247003 (2007)

[241] Hirsch J E *Phys. Rev. B* **31**(7) 4403–4419 (1985)

[242] Takigawa M and Mitzi D B *Journal of Low Temperature Physics* **95** 89–93 (1994)

[243] Perkins J D, Graybeal J M, Kastner M A, Birgeneau R J, Falck J P and Greven M *Phys. Rev. Lett.* **71**(10) 1621–1624 (1993)

[244] Moler K A, Baar D J, Urbach J S, Liang R, Hardy W N and Kapitulnik A *Phys. Rev. Lett.* **73**(20) 2744–2747 (1994)

[245] Volovik G *JETP* **58** 469–469 (1993)

[246] James A J A, Konik R M and Rice T M *Phys. Rev. B* **86**(10) 100508 (2012)

[247] Eremin M V, Shigapov I M and Thuy H T D *Journal of Physics: Condensed Matter* **25** 345701 (2013)

[248] Spanu L, Lugas M, Becca F and Sorella S *Phys. Rev. B* **77**(2) 024510 (2008)

[249] Demler E, Hanke W and Zhang S C *Rev. Mod. Phys.* **76**(3) 909–974 (2004)

[250] Croft T P *X-ray and Neutron Scattering Studies of High-Tc Cuprate Superconductors* Ph.D. thesis University of Bristol (2016)

[251] Minola M, Lu Y, Peng Y Y, Dellea G, Gretarsson H, Haverkort M W, Ding Y, Sun X, Zhou X J, Peets D C, Chauviere L, Dosanjh P, Bonn D A, Liang R, Damascelli A, Dantz M, Lu X, Schmitt T, Braicovich L, Ghiringhelli G, Keimer B and Le Tacon M *Phys. Rev. Lett.* **119**(9) 097001 (2017)

[252] Dean M P M, James A J A, Walters A C, Bisogni V, Jarrige I, Hücker M, Giannini E, Fujita M, Pelliciari J, Huang Y B, Konik R M, Schmitt T and Hill J P *Phys. Rev. B* **90**(22) 220506 (2014)

[253] Guarise M, Piazza B D, Berger H, Giannini E, Schmitt T, Rønnow H M, Sawatzky G A, van den Brink J, Altenfeld D, Eremin I and Grioni M *Nat. Commun.* **5** 5760 (2014)

[254] Kivelson S A, Fradkin E and Emery V J *Nature* **393** 550–553 (1998)

[255] Kato M, Machida K, Nakanishi H and Fujita M *Journal of the Physical Society of Japan* **59** 1047–1058 (1990)

[256] Wu T, Mayaffre H, Krämer S, Horvatić M, Berthier C, Hardy W N, Liang R, Bonn D A and Julien M H *Nature* **477** 191 – 194 (2011)

[257] LeBoeuf D, Krämer S, Hardy W N, Liang R, Bonn D A and Proust C *Nature Physics* **9** 79–83 (2012)

[258] Sebastian S E, Harrison N and Lonzarich G G *Philosophical Transactions of the Royal Society A: Mathematical, Physical and Engineering Sciences* **369** 1687–1711 (2011)

[259] Achkar A J, Sutarto R, Mao X, He F, Frano A, Blanco-Canosa S, Le Tacon M, Ghiringhelli G, Braicovich L, Minola M, Moretti Sala M, Mazzoli C, Liang R, Bonn D A, Hardy W N, Keimer B, Sawatzky G A and Hawthorn D G *Phys. Rev. Lett.* **109**(16) 167001 (2012)

[260] Gerber S, Jang H, Nojiri H, Matsuzawa S, Yasumura H, Bonn D A, Liang R, Hardy W N, Islam Z, Mehta A, Song S, Sikorski M, Stefanescu D, Feng Y, Kivelson S A, Devereaux T P, Shen Z X, Kao C C, Lee W S, Zhu D and Lee J S *Science* **350** 949–952 (2015)

[261] Jang H, Lee W S, Nojiri H, Matsuzawa S, Yasumura H, Nie L, Maharaj A V, Gerber S, Liu Y J, Mehta A, Bonn D A, Liang R, Hardy W N, Burns C A, Islam Z, Song S, Hastings J, Devereaux T P, Shen Z X, Kivelson S A, Kao C C, Zhu D and Lee J S *Proceedings of the National Academy of Sciences* **113** 14645–14650 (2016)

[262] Putzke C, Ayres J, Buhot J, Licciardello S, Hussey N E, Friedemann S and Carrington A *Phys. Rev. Lett.* **120**(11) 117002 (2018)

[263] Blackburn E, Chang J, Hücker M, Holmes A T, Christensen N B, Liang R, Bonn D A, Hardy W N, Rütt U, Gutowski O, Zimmermann M v, Forgan E M and Hayden S M *Phys. Rev. Lett.* **110**(13) 137004 (2013)

[264] Yao H, Lee D H and Kivelson S *Phys. Rev. B* **84**(1) 012507 (2011)

[265] Laliberté F, Chang J, Doiron-Leyraud N, Hassinger E, Daou R, Rondeau M, Ramshaw B J, Liang R, Bonn D A, Hardy W N, Pyon S, Takayama T, Takagi H, Sheikin I, Malone L, Proust C, Behnia K and Taillefer L *Nature Communications* **2** 432 (2011)

[266] Gannot Y, Ramshaw B J and Kivelson S A *Physical Review B* **100** (2019)

[267] Miao H, Fumagalli R, Rossi M, Lorenzana J, Seibold G, Yakhou-Harris F, Kummer K, Brookes N B, Gu G D, Braicovich L, Ghiringhelli G and Dean M P M *Phys. Rev. X* **9**(3) 031042 (2019)

[268] Caprara S, Di Castro C, Seibold G and Grilli M *Phys. Rev. B* **95**(22) 224511 (2017)

[269] Sachdev S and La Placa R *Phys. Rev. Lett.* **111**(2) 027202 (2013)

[270] Pintschovius L, Reichardt W, Kläser M, Wolf T and v Löhneysen H *Phys. Rev. Lett.* **89**(3) 037001 (2002)

[271] Reznik D, Pintschovius L, Ito M, Iikubo S, Sato M, Goka H, Fujita M, Yamada K, Gu G D and Tranquada J M *Nature* **440** 1170–1173 (2006)

[272] Raichle M, Reznik D, Lamago D, Heid R, Li Y, Bakr M, Ulrich C, Hinkov V, Hradil K, Lin C T and Keimer B *Phys. Rev. Lett.* **107**(17) 177004 (2011)

[273] Pailhès S, Sidis Y, Bourges P, Hinkov V, Ivanov A, Ulrich C, Regnault L P and Keimer B *Phys. Rev. Lett.* **93**(16) 167001 (2004)

[274] Tanamoto T, Kohno H and Fukuyama H *Journal of the Physical Society of Japan* **61** 1886–1890 (1992)

[275] Carbotte J P, Schachinger E and Basov D N *Nature* **401** 354–356 (1999)

[276] Pintschovius L, Endoh Y, Reznik D, Hiraka H, Tranquada J, Reichardt W, Bourges P, Sidis Y, Uchiyama H, Masui T and Tajima S *Physica C* **412–414** 70–75 (2004)

[277] Reznik D, Bourges P, Pintschovius L, Endoh Y, Sidis Y, Masui T and Tajima S *Phys. Rev. Lett.* **93**(20) 207003 (2004)

[278] Mook H A, Yethiraj M, Aeppli G, Mason T E and Armstrong T *Phys. Rev. Lett.* **70**(22) 3490–3493 (1993)

[279] Rossat-Mignod J, Bourges P, Onufrieva F, Regnault L, Henry J, Burlet P and Vettier C *Physica B* **199-200** 281 – 283 (1994)

[280] Fong H F, Bourges P, Sidis Y, Regnault L P, Bossy J, Ivanov A, Milius D L, Aksay I A and Keimer B *Phys. Rev. B* **61**(21) 14773–14786 (2000)

[281] Hinkov V, Bourges P, Pailhès S, Sidis Y, Ivanov A, Frost C D, Perring T G, Lin C T, Chen D P and Keimer B *Nature Physics* **3** 780–785 (2007)

[282] Dean M P M, Dellea G, Minola M, Wilkins S B, Konik R M, Gu G D, Le Tacon M, Brookes N B, Yakhou-Harris F, Kummer K, Hill J P, Braicovich L and Ghiringhelli G *Phys. Rev. B* **88**(2) 020403 (2013)

[283] Hücker M, Christensen N B, Holmes A T, Blackburn E, Forgan E M, Liang R, Bonn D A, Hardy W N, Gutowski O, Zimmermann M v, Hayden S M and Chang J *Phys. Rev. B* **90**(5) 054514 (2014)

[284] da Silva Neto E H, Minola M, Yu B, Tabis W, Bluschke M, Unruh D, Suzuki H, Li Y, Yu G, Betto D, Kummer K, Yakhou F, Brookes N B, Le Tacon M, Greven M, Keimer B and Damascelli A *Phys. Rev. B* **98**(16) 161114 (2018)

[285] Barthélemy M C *Studies of Charge Density Waves in Cuprate Superconductors* Ph.D. thesis University of Bristol (2019)

[286] Ishizaka K, Arima T, Murakami Y, Kajimoto R, Yoshizawa H, Nagaosa N and Tokura Y *Phys. Rev. Lett.* **92**(19) 196404 (2004)

[287] Braicovich L, Minola M, Dellea G, Le Tacon M, Moretti Sala M, Morawe C, Peffen J C, Supruangnet R, Yakhou F, Ghiringhelli G and Brookes N B *Review of Scientific Instruments* **85** 115104 (2014)

[288] Lau B, Berciu M and Sawatzky G A *Phys. Rev. Lett.* **106**(3) 036401 (2011)

[289] Hozoi L, Siurakshina L, Fulde P and van den Brink J *Scientific Reports* **1** 65 (2011)

[290] Eskes H, Tjeng L H and Sawatzky G A *Phys. Rev. B* **41**(1) 288–299 (1990)

[291] Hohenberg P and Kohn W *Phys. Rev.* **136**(3B) B864–B871 (1964)

[292] Cormack A M *J. Appl. Phys* **34** 2722–2727 (1963)

[293] Zunger A, Wei S H, Ferreira L G and Bernard J E *Phys. Rev. Lett.* **65**(3) 353–356 (1990)

[294] Kontrym-Sznajd G and Samsel-Czekała M *Applied Physics A* **70** 89–92 (2000)

[295] Gyorffy B L, Pindor A J, Staunton J, Stocks G M and Winter H *Journal of Physics F: Metal Physics* **15** 1337–1386 (1985)

[296] Robarts H C, Millichamp T E, Lagos D A, Laverock J, Billington D, Duffy J A, O'Neill D, Giblin S R, Taylor J W, Kontrym-Sznajd G, Samsel-Czekała M, Bei H, Mu S, Samolyuk G D, Stocks G M and Dugdale S B *Phys. Rev. Lett.* **124**(4) 046402 (2020)